Characterization of Nanoparticle Emissions from Diesel and Advanced Dual Fuel Compression Ignition Engines

A Thesis Submitted
In Partial Fulfillment of the Requirements
for the Degree of

Doctor of Philosophy

by

Sahil Rana

2016 MEZ0023

DEPARTMENT OF MECHANICAL ENGINEERING
INDIAN INSTITUTE OF TECHNOLOGY ROPAR
April 2024

Sahil Rana: *Characterization of Nanoparticle Emissions From Diesel and Advanced Dual Fuel Compression Ignition Engines*

DEDICATED

TO

FAMILY & FRIENDS

DECLARATION

I hereby declare that the work which is being presented in the thesis entitled "**Characterization of Nanoparticle Emissions from Diesel and Advanced Dual Fuel Compression Ignition Engines"** has been solely authored by me. It presents the result of my own independent investigation/research conducted during the time period from **January 2017** to **August 2023** under the supervision of **Dr. Rakesh Kumar Maurya**, Associate Professor Department of Mechanical Engineering IIT Ropar. To the best of my knowledge, it is an original work, both in terms of research content and narrative, and has not been submitted or accepted elsewhere, in part or in full, for the award of any degree, diploma, fellowship, associateship, or similar title of any university or institution. Further, due credit has been attributed to the relevant state-of-the-art and collaborations (if any) with appropriate citations and acknowledgments, in line with established ethical norms and practices. I also declare that any idea/data/fact/source stated in my thesis has not been fabricated/ falsified/ misrepresented. All the principles of academic honesty and integrity have been followed. I fully understand that if the thesis is found to be unoriginal, fabricated, or plagiarized, the Institute reserves the right to withdraw the thesis from its archive and revoke the associated Degree conferred. Additionally, the Institute also reserves the right to appraise all concerned sections of society of the matter for their information and necessary action (if any). If accepted, I hereby consent for my thesis to be available online in the Institute's Open Access repository, inter-library loan, and the title & abstract to be made available to outside organizations.

Signature :

Name: Sahil Rana
Entry Number: 2016 MEZ0023
Program: PhD
Department: Mechanical Engineering
Indian Institute of Technology Ropar
Rupnagar, Punjab 140001

Date:

ACKNOWLEDGMENTS

As another phase of life is ready to dawn with the submission of my PhD thesis, there have been numerous helping hands and genuine advice behind the successful completion of my work. First and foremost, I express my sincere gratitude and respect to my thesis supervisor **Dr. Rakesh Kumar Maurya,** Associate Professor, Department of Mechanical Engineering, IIT Ropar, for his valuable guidance, constant encouragement throughout this study and untiring help, without which this research would not have attained its shape. Without his guidance and support this thesis would not have been possible. I would also like to thank **Dr. Mohit Raj Saxena, Senior Research Associate, CSIR Pool Scientist** for his support and encouragement throughout the research work.

It was my pleasure to be associated with Advanced Engine and Fuel Research Laboratory IIT Ropar. I would like to thank my colleagues in the lab: Dr. Ajay Singh, Neeraj Kumar Yadav, Ratnesh Kumar Yadav, Saket Kumar, Avdhoot Abaso Mohite, Pankaj Gupta, Shivraj Anand Karenawar, Rajat Prashar, Amit Singh Chandel, and Kamal S Kumar.

I extent my gratefulness to **Prof. Sarit Kumar Das**, former director IIT Ropar, and **Prof. Rajiv Ahuja**, Director, IIT Ropar for their excellent and strategic administration and research-friendly environment provided to me during my stay at IIT Ropar.

I extend my deepest gratitude to my parents for their invaluable love, affection, encouragement, and support. I feel proud and blessed with such caring parents. I offer greatest thanks to my wife for her contribution of patience, encouragement, and love. Thanks for being there and bring happiness to my life.

CERTIFICATE

This is to certify that the thesis entitled **“Characterization of Nanoparticle Emissions from Diesel and Advanced Dual Fuel Compression Ignition Engines”** submitted by **Sahil Rana (2016MEZ0023)** for the award of the degree of **Doctor of Philosophy** of Indian Institute of Technology Ropar, is a record of bonafide research work carried out under my guidance and supervision. To the best of my knowledge and belief, the work presented in this thesis is original and has not been submitted, either in part or full, for the award of any other degree, diploma, fellowship, associateship, or similar title of any university or institution.

In our opinion, the thesis has reached the standard fulfilling the requirements of the regulations relating to the Degree.

Signature :
Dr. Rakesh Kumar Maurya
Associate Professor
Department of Mechanical Engineering
Indian Institute of Technology Ropar
Rupnagar, Punjab 140001
Date:

LAY SUMMARY

Transportation is the backbone of every society and its progress. Mainly due to the use of fossil fuels, this comes at a high cost for the earth and human health because of harmful local emissions. Diesel and gasoline engines are the most common internal combustion engines used in the transportation sector. Diesel engines are more efficient than spark ignition engines because they operate at significantly high compression ratios and lean fuel-air mixtures. However, diesel engines cause environmental pollution owing to their high NOx and soot emissions. Epidemiology and toxicological studies have confirmed that long-term exposure to particulate matter emissions from diesel engines adversely affects human health. Therefore, regulatory and government bodies worldwide have implemented strict emission regulations. Innovative in-cylinder combustion strategies and exhaust emission aftertreatment technologies are developed to comply with stringent emission regulations. Aftertreatment technologies increase fuel consumption, operational cost, and engine complexity and require frequent maintenance. Therefore, in-cylinder technologies for emission reduction have been the research focus. Low-temperature combustion (LTC) strategies such as reactivity controlled compression ignition (RCCI) have the potential to achieve simultaneously low emissions of both nitrogen oxides (NOx) and particulate matter (PM) while maintaining high thermal efficiency without the need for a costly after-treatment system. This study investigates the PM characteristics of diesel and RCCI engines. An adequate understanding of the formation of polyaromatic hydrocarbon (PAH) species which are precursors for particle formation in diesel engines is essential for minimizing particulate matter emissions. Therefore, in this thesis work, a numerical investigation is conducted to understand the effect of injection timing and injection pressure (relevant to diesel and RCCI combustion strategy) on in-cylinder soot precursor formation and particle emission characteristics using a detailed soot model. Experimental analysis is done to study the PM characteristics of RCCI engines.

To study the RCCI combustion concept, several modifications, and suitable instrumentation were carried out in the existing single-cylinder diesel engine. Gasoline, methanol, and CNG are used as low reactivity fuel, and diesel is used as high reactivity fuel. The effect of the in-cylinder heat release feature on particle emissions was investigated for RCCI engines. Later, empirical correlations were developed to study the relationship between heat release features and particle emissions for RCCI engines. For characterizing particle emissions from RCCI engines, a thermodesorption system was developed and tested in the laboratory. Results show that advancing injection timing and increasing injection pressure reduce the PAH species formation at injection timing employed in diesel injection strategy. It is observed that acetylene mass fraction start rising after the start of combustion and then decreases and remain constant at injection timings employed in RCCI experiments (30°bTDC) in this study.

Developed empirical correlations show a good correlation between diesel injection timing and heat release feature to estimate particle emissions from RCCI engine. The developed thermodesorption system was effective in removing volatile particles emitted from the RCCI engine.

Abstract

Diesel engines are widely used for transportation and power generation due to their high fuel efficiency, torque output, durability, and reliability. Major problems with diesel engines are emissions of particulate matter and NOx, which negatively affect human health and the environment. Stringent emissions norms are therefore introduced for diesel engines to limit the pollutants from diesel engines. NOx and PM emitted by diesel engines are significant issues to solve because of the NOx-PM trade-off, in which simultaneous reduction of these two pollutants is highly challenging. Revolutionary in-cylinder combustion strategies and emissions after-treatment systems are required for diesel engines to meet stringent emission norms such as Euro VI. Emissions after treatment systems require frequent maintenance, increasing overall vehicle cost and fuel consumption. Thus, to reduce after-treatment costs and fuel consumption, it is necessary to avoid the generation of these pollutants during combustion. Reactivity-controlled compression ignition is a dual fuel low-temperature combustion strategy that has the potential for simultaneous reduction of NOx and PM emissions with high thermal efficiency without the need for a costly after-treatment system. This study investigates PM characteristics of diesel and RCCI engines. A numerical investigation is conducted to understand the effect of injection timing and injection pressure (relevant to diesel and RCCI combustion strategy) on in-cylinder soot precursor formation and incylinder particle emission characteristics using a detailed soot model based on method of moments available in ANSYS FORTE CFD software. For the experimental study of RCCI combustion concept, suitable hardware, and instrumentation was done on existing automotive single-cylinder diesel engine. Gasoline, methanol, and CNG are used as low reactivity fuel, and diesel is used as high reactivity fuel. The low-reactivity fuel is injected in the intake manifold using a solenoid-based port fuel injector developed in the laboratory. High reactivity fuel (HRF) is injected using the common rail direct injection (CRDI) technique. An open ECU is used to vary the diesel injection timing. RCCI combustion mode experiments were conducted at 1.5 bar (lower engine load) and 3 bar BMEP (medium engine load) at constant 1500 rpm. For the characterization of solid particle emissions from RCCI engines, a thermodesorption system was developed in the laboratory for particulate sampling.

The main objective of the research is to investigate the PM characteristics of diesel and RCCI engines. The impact of injection timings and injection pressure relevant to diesel and RCCI combustion strategy on soot precursor species mass fraction, particle number density, size and volume fraction is investigated. The results show that soot precursor species mass fraction and particle number density decreased with advanced injection timing from 6° bTDC to 18° bTDC and increased injection pressure from 500 bar to 1000 bar. It is observed that acetylene mass fraction start rising after the start of combustion and then decreases and remain constant at injection timings employed in RCCI experiments (30°bTDC). The impact of low-temperature heat release (LTHR) and high-temperature heat release (HTHR) on particle emission was investigated for RCCI engines with single and double injection strategies and different port fuel-injected CNG mass at low and medium engine loads. Later, empirical correlations were developed to study the relationship between LTHR, HTHR, and particle emissions. Results show that the amount and location of LTHR and HTHR significantly influence the formation of particle number emission in RCCI combustion. The developed empirical correlations show a good correlation between diesel SOI and the ratio of HTHR to LTHR to estimate total particle number concentration. Solid particle emissions from the RCCI engine were investigated with a developed thermodesorption system at different premixing ratios. The bimodal shape of the particle size distribution curve was changed to a unimodal shape when sampling was performed with a thermodesorption system for both gasoline diesel and CNG diesel RCCI operation. Thermodesorption system showed high volatile particle removal efficiency for gasoline diesel RCCI operation compared to CNG diesel RCCI operation.

LIST OF PUBLICATIONS

Journal papers

1. Rana, S., Saxena, M. R., & Maurya, R. K. (2021). Development and characterization of aerosol conditioning devices for solid ultrafine particle measurement from diesel engines: A review. SAE Technical Paper, 01-0615.

2. Rana, S., Saxena, M. R., & Maurya, R. K. (2022). A review on morphology, nanostructure, chemical composition, and number concentration of diesel particulate emissions. *Environmental Science and Pollution Research*, 1-58.

3. Saxena, M. R., Rana, S., & Maurya, R. K. (2022). Analysis of Low-and High-Temperature Heat Release in Dual-Fuel RCCI Engine and Its Relationship with Particle Emissions. *Journal of Energy Resources Technology*, *144*(9), 091201.

4. Rana, S., Saxena, M. R., Maurya, R. K., & Shukla, P. C. (2022). Numerical Investigation on the Effect of Fuel Injection Timing on Soot Particle Size and Number Characteristics of Diesel Engine (No. 2022-01-1053). *SAE Technical Paper*.

5. Saxena, M.R., Rana, S., & Maurya, R.K. Experimental investigation on the effect of in-cylinder heat release features on particle emissions characteristics of CNG-diesel RCCI engine. *Int. J. Environ. Sci. Technol.* (2023).

6. Rana, S., Saxena, M.R., . & Maurya, R.K. Experimental Investigation of Solid Particle emissions from RCCI Engine using Insitu Developed Thermodesorption system (Revision Submitted in Journal of Traffic and Transportation Engineering).

TABLE OF CONTENTS

LIST OF FIGURES

LIST OF TABLES

ABBREVIATIONS AND NOTATIONS

AHRR	Apparent heat release rate
AMPs	Accumulation mode particles
BMEP	Brake mean effective pressure
BEVs	Batter electric vehicles
bTDC	Before top dead center
CI	Compression ignition
CH_4	Methane
CI	Compression ignition
CAD	Crank angle degrees
CA_{10}	Crank angle at which 10% heat is released
CA_{50}	Crank angle at which 50% heat is released
CNG	Compressed natural gas
CFD	Computational fluid dynamics
DAQ	Data acquisition system
d_p	Particle diameter
ESC	European stationary cycle
ELR	European load response
ETC	European test cycle
FSN	Filter smoke number
GHG	Greenhouse gases
GD RCCI	Gasoline diesel reactivity controlled compression ignition
HTHRR	High temperature heat release rate
h_x	Mass transfer coefficient
LTHRR	Low temperature heat release rate
LRF	Low reactivity fuel
MD RCCI	Methanol diesel reactivity controlled compression ignition
m_c	Port injected CNG mass
NOx	Nitrogen oxide
NMPs	Nucleation mode particles
OECD	Organization for economic cooperation and development
PM	Particulate matter
PN	Particle number
PSD	Particle size distribution
PID	Proportional integral derivative

PAH	Polyaromatic hydrocarbons
PLIF	Planar laser induced fluorescence
P_{diff}	Penetration fraction
RCCI	Reactivity controlled compression ignition
ROHR	Rate of heat release
r_p	Premixing ratio
SOI	Start of injection
SOC	Start of combustion
Sh	Sherwood number
THC	Total hydrocarbons
WHSC	World harmonized stationary cycle
WHTC	World harmonized transient cycle
η_p	Penetration efficiency
η_v	Volatile particle removal efficiency

Chapter 1

Introduction

Transportation requirement is rapidly increasing with the development of modern society. Currently transportation sector is dominated by automobiles powered by internal combustion engines running on fossil fuels. According to the international transport forum, by 2050 the demand for transportation could double or even quadruple which will increase the requirement for fossil fuels in the coming years. Rapid increase in the number of vehicles leads to a drastic increase in pollutant emissions in the earth atmosphere. An increase in vehicular emissions and rapid depletion of fossil fuel reserves demand for the development of efficient and cleaner engines. Diesel engines are a preferred choice for medium and heavy-duty applications due to their high fuel conversion efficiency as it is operated at high compression ratio, on leaner fuel air mixtures and unthrottled. However, diesel engines emit higher NOx and PM, and there exists a trade off in the emission of two species. To meet future emission legislations, a combination of incylinder strategies as well as exhaust aftertreatment devices is proposed for emission reduction. Employing currently available aftertreatment devices has limitations of higher cost, fuel economy penalties, durability issues and larger space requirements. Thus, there is a need for drastic improvement in incylinder strategies to achieve lower fuel consumption along with a decrease in emissions which can reduce dependency on aftertreatment devices. Therefore, several advanced low temperature combustion (LTC) strategies have been developed to reduce the harmful emissions of diesel engines. These LTC strategies, such as homogeneous charge compression ignition (HCCI), premixed charge compression ignition (PCCI), and reactivity controlled compression ignition (RCCI), can reduce engine-out nitrogen oxide (NOx) and soot emission simultaneously. Lower combustion temperature result in NOx reduction due to the high activation energy of the NO formation reactions. Also due to long ignition delay period, there is sufficient time for fuel and air mixing prior to the start of combustion. This reduces fuel rich regions inside the engine cylinder and soot formation is inhibited. However, LTC investigations exhibit several drawbacks of HCCI and PCCI combustion, such as lack of combustion control and other operational issues at high loads, making their application in production grade engines challenging.

RCCI combustion strategy exhibits encouraging result in combustion control, engine performance, and applicability at high engine loads. With RCCI combustion strategy, engine out NOx levels below the limits proposed by emissions regulations, together with ultra low soot emissions can be achieved without the need for aftertreatment devices. The goal of this dissertation is to study the PM characteristics of diesel engines and RCCI engines. A numerical investigation is conducted to study the incylinder formation polyaromatic hydrocarbons and PM characteristics at different engine operating parameters using ANSYS FORTE CFD

Software. Experimental investigation is conducted on modified single-cylinder diesel engines to study the influence of heat release features on particle emissions from RCCI engines utilizing gasoline, methanol, and CNG as low reactivity fuels and diesel as high reactivity fuel. Later, empirical correlations are developed for the estimation of particle emissions from RCCI engines. For the characterization of solid particle emissions from RCCI engines, a thermosdesorption system is developed and tested in the laboratory. Effect of thermodesorption system on particle emissions from RCCI engines is studied at different premixing ratios. This chapter starts with a description of motivations for engine research which focuses on air pollution, health impacts, and emission regulations. Then combustion process in diesel engines and its advantages and challenges are discussed. Further, reactivity-controlled compression ignition (RCCI) is discussed. Combustion process in RCCI engines is discussed together with their advantages and challenges. At last research objectives and thesis organization are discussed in this chapter.

1.1 Motivation for Engine Research

The existence of an efficient transport infrastructure is crucial for the growth of the global economy and society [1.1-1.2]. Throughout history, transportation has been a spur to expansion, better transport allows more trade and a greater spread of people. Internal combustion engines are prime movers for vehicles, ships, construction equipment, and agricultural machines. Vast majority of engines are reciprocating piston engines are powered by the combustion of petroleum-based fossil fuels due to their plentiful supply, convenience, and affordability [1.3]. It is anticipated that internal combustion engines using liquid fuels generated from petroleum (crude oil) are likely to power most of the transportation (around 90% share) in the future [1.3]. The IC engines are well accepted and the most significant prime movers since last century due to their performance, economy, durability, controllability, and lack of other alternatives.

Increased mechanization of the world has led to a steep rise in the demand for fossil fuels and an increase in the number of automotive vehicles [1.1-1.3]. The transportation sector consumes 20% of the total energy globally and there will be rise 40% rise in worldwide energy consumption for the transport sector primarily in non-OECD nations such as India and China [1.2]. Compared to now the global demand for transport energy could be 40-50% higher shortly [1.2], [1.3]. According international energy outlook fuel demand is expected to rise over the next three decades and fossil fuel share 78% of energy use in 2040 [1.5 - 1.6]. Increasing demand for transport energy has resulted in a drastic increase in pollutant and green house gaseous emissions in the earth's atmosphere, which has led to the enforcement of strict emission regulations around the world [1.7]. Also, the oil resources of the earth will however not last forever, therefore prices of crude oil have increased substantially over the last decade. As a result of strict emission norms and rising oil prices, reciprocating IC engine vehicles are anticipated to become more efficient and cleaner [1.7-1.8].

In recent years, the energy landscape has boomed, giving rise to fresh possibilities like fuel cells, and electric and hybrid vehicles [1.9-1.11]. These are aimed at reducing the negative impact of emissions from the transportation sector, which accounts for 16% of global greenhouse gas emissions (GHG) emissions [1.10]. Battery electric vehicles (BEVs) are environment friendly in terms of local pollution but these can generate global pollution due to the production of electricity from coal in some developing and developed countries [1.10-1.11]. Promoting BEVs may therefore be unproductive unless enough carbon is removed from the power producing process [1.12]. Also, hybrid electric vehicles are better suited for short distance travel in the light-duty vehicle category. BEVs have a considerable negative influence on human toxicity, fresh water ecotoxicity, and fresh water eutrophication even when power generation is decarbonized, mostly due to the manufacture of metals needed for batteries [1.12]. Additionally, modern batteries still have a lower volumetric and gravimetric density than the gasoline used in IC engines [1.13]. A study calculated the degree of viability (a non-dimensional term) denoted by φ which is the ratio of the emission index of the electric vehicle and the emission index of internal combustion engine. It was found that shifting from conventional vehicles to electric vehicles will lead to a decrease in CO and CO_2 emissions by 60% and 17% per unit vehicle respectively. However, this reduction will be greater in the city core while the emission in the urban periphery is likely to be greater. This situation will arise because of an increase in load demand as a result of electric vehicles on thermal power plants which are situated in the outskirts of urban areas. This in turn may not have a positive impact on rural/ suburban population of the region [1.10]. According to a study, alternative transportation energy sources cannot develop quickly enough to substantially replace petroleum-based liquid fuels in the next decades. India is majorly dependent on coal for electricity generation and the use of electric vehicles on a large scale will put an extra burden on power generation. In addition, the current quality of coal is poorer as compared to other countries which results in higher levels of emissions almost the double global average [1.11]. A study suggested that the intricate interaction between several change-causing factors is what will determine how transportation energy will evolve [1.12]. Energy security, local pollution difficulties, climate change concerns, support for farmers, growth in rural jobs, and aspirations for leadership in newer technologies are just a few of the variables driving energy policy. This study concludes that transportation policy should be based on a balanced approach using all available technologies considering local and global environment and greenhouse gas impacts, security of supply, and social, economic, political, and ethical impacts [1.12].

Therefore, combustion engines are expected to be around for several decades or may even centuries to come, as long as more fuel efficient and cleaner alternative is made available [1.13-1.14]. Hence research focusing on improving fuel conversion efficiency and reducing harmful emissions from IC engines is justified and required in current scenario [1.13]. Over the years, improving the performance in terms of fuel conversion efficiency and power density of IC engines has been major driving force for research and development (R&D). Exhaust emissions from automobiles were recognized as major contributor to urban pollution for the first time in California during the 1950s. Now the user of IC engines is aware of the air pollution from the vehicles, and consequently, they demand compliance to environmental consideration and regulatory legislations prevailing around the world. The main governing factors for engine research are described in the next subsections.

1.1.1 Environmental Concerns

The world is facing crisis twin crisis of depletion of fossil fuel reserves and degradation of environment conditions. Environment pollution is a key public health issue in most cities. Epidemiological studies show that air pollution is one of the greatest risks to human health. According to the world health organization (WHO) combined effect of ambient air pollution and household air pollution led to 6.7 million premature deaths worldwide. Major environmental concerns that appear due to heavy use of combustion engines is global warming, photochemical smog, particulate matter, acid rains, and ozone depletion. Currently global warming is important environmental challenge [1.14]. Global warming occurs due to thermal energy imbalance because of heat trapped in earth's environment by greenhouse gases. The major green house gases produced due to human activities are carbon dioxide (CO_2) methane (CH_4), nitrous oxides and fluorinated compounds. Internal combustion engines operating on fossil fuels provide about 25% of the world power and in doing so produce 10% of greenhouse gases [1.7]. Photochemical smog is a mixture of pollutants that are formed when nitrogen oxides (NOx) and volatile organic compounds (VOC) react to sunlight creating brown haze above cities. Nitrogen oxides are produced mainly from the combustion of fossil fuels particularly in power stations and motor vehicles [1.14-1.15]. VOCs are produced mainly from incomplete combustion of fossil fuels. Therefore, it is required to build technologies that reduce emissions of NOx and unburned hydrocarbons. Acid rain results when sulfur dioxide (SO_2) and nitrogen oxides (NOx) are emitted into the atmosphere and transported by wind and air currents. It has a negative effect on soil, forest, stream, and lakes. Emissions of sulfur dioxide and NOx from the combustion of fossil fuels contribute to acid rain [1.14].

Particulate matter (PM) is the major component of air pollution and has its genesis from anthropogenic origins such as building machinery, automobiles, agricultural machinery, and industrial activities [1.15-1.16]. Solid particles emitted from automotive engines comprise of carbonaceous matter (soot) comprising a small fraction of inorganic matter [1.16]. One of the main sources of soot particles in the atmosphere are diesel engines. Soot particles are primarily carbonaceous soot agglomerates formed due to diffusion controlled heterogeneous combustion of the locally rich fuel air mixture in diesel combustion [1.16]. The California air resource board (CARB) has defined diesel PM as an 'air toxic' and estimated that in 2003, diesel PM was responsible for approximately 70% of the cancer cases attributed to all air toxics.

Particles are classified according to their size by aerodynamic diameter: nanoparticles (aerodynamic diameter < 50 nm), ultrafine particles (aerodynamic diameter < 100 nm), and fine particles (aerodynamic diameter < 2.5 μm designated as PM 2.5) [1.17]. The aerodynamic diameter of a particle is defined as that of a sphere, whose density is $1g/cm^3$, which settles in still air at the same velocity as the particle in question. The diameter is obtained from aerodynamic classifiers such as cascade impactors. In metropolitan regions, transportation plays a crucial role in ultrafine particles. The Royal Society held a multidisciplinary meeting in London in march 2000, they claimed that ultrafine particles (UFP) make up a relatively small percentage of the mass in the atmosphere, however, they make up a sizable part in terms of both number and surface area [1.7]. Larger particles pose no significant hazard to human health since the body can protect itself against them. Smaller particles less than 2.5 μm are the main concern because they take a long time to settle and remain air borne for a long time. Therefore, small soot particles can reach human respiratory system. Particles smaller than 1μm are too small to be trapped by upper portion of the lungs, and they penetrate deep into lungs. The ultra-fine soot particles are more toxic as they have more defects in soot nanostructure and high surface reactivity [1.16]. High correlation was found between organic fractions of diesel PM such as PAH with variation in cytotoxicity and gene expression [1.16]. Epidemiological studies show that airborne PM, in which diesel PM is the main component, contributes to respiratory mortality and morbidity [1.16 - 1.18]. Diesel exhaust particles can alter the expression patterns of peroxiredoxins genes in bronchial epithelial pathways which affect the cellular functions according to a recent study [1.16]. In an invitro toxicity assessment study, it was found that exposure of human epithelial cells to quasi ultrafine particles from diesel engines altered the global gene expression [1.16]. A health study on particles suggests that the particle number concentration and surface areas correlate better with inflammatory response than particle mass [1.17]. Additionally, diesel PM affects the environment by causing visibility reduction, and diesel black carbon (soot) a component of diesel PM is a potent contributor to global warming. Therefore, it is important to develop engine technologies that employ premix flame and emit a small number of particles.

1.1.2 Emission Regulations

The use of fossil fuels in IC engines has an impact on the local and global environment. The environment and human health are negatively affected by the pollutants released by IC engines. Health and other hazards of pollutants depend on their concentration as well as the time of exposure to the human body. Government worldwide has imposed increasingly stringent restrictions on emission levels to reduce the effect of pollutants on human health and the environment [1.19-1.22]. Vehicular exhaust emission standards are expressed in terms of pollutant mass per km distance travelled (g/km) [1.14]. For heavy duty vehicle engines, emissions limits are specified in terms of mass of emission per unit work output (g/KWh) [1.23-1.25]. The new production vehicles and engines are tested for compliance with the emission standards in a government-approved laboratory. For emission certification, vehicles and engines are run on a specified driving schedule of speed and loads which are commonly known as driving cycles. The test-driving cycle comprise of cold start period, idling, moderate acceleration, deacceleration and cruise mode [1.25]. For heavy duty vehicles, engines are tested for various load and speed condition for steady state test cycle. Engines are also evaluated for transient cycles to make the test more relevant to real-world driving situations. Emission legislation includes pollutant species such as NOx, unburned hydrocarbons, CO, and particulate matter [1.25]. These pollutants are called regulated pollutants. However, NOx and PM have been a challenge for diesel engines due to their heterogeneous nature of combustion. Since ultrafine PM have a negative impact on human health an environment, tighter PM standards have been created and implemented [1.26]. Particle number limits are also supported by research in Europe that has found significant health impact from exposure of high particle counts. The limit of particle mass in Euro-VI for diesel engines has been cut down to 96% compared to Euro-I emission standards. In India BS VI emissions norms were implemented nationwide from April 2020. PN restrictions of 6×10^{11} have been introduced for both gasoline and diesel vehicles, although they have not yet been put into practice [1.26]. As per BS VI emission norms, the NOx from diesel engines is to be reduced by 70%, and particulate by 80% [1.26].

A number-based engine exhaust particle control has been created with a target size of solid particles greater than 23 nm [1.26]. The European Union established the particle measurement program (PMP) to monitor ultrafine particles generated by engines under the regulatory framework. Measurement sensitivity and accuracy are the main concerns due to the low magnitude of the particle mass limits [1.26]. This has led to the introduction of particle number limits to measure low particulate emissions from modern diesel engines [1.26]. A particulate number (PN) standard was introduced in 2011 with Euro-V (b) for diesel engines and in 2014 with Euro-VI for petrol engines. A solid particle number (SPN) concentration limit of 6×10^{11} particles/km was included in the Euro-V/VI standards for light-duty vehicles [1.26]. The Euro-VI standard for heavy-duty diesel vehicles included an SPN concentration limit as well with proposed limits of 8×10^{11} particles/ kWh for the stationary cycle and 6×10^{11} particles / kWh for the transient cycle [1.26]. The SPN method is based on the findings of the particle measurement program in which the exhaust gas enters a volatile particle remover (VPR) which consists of a hot dilutor (> 150 °C) and evaporation tube (ET) at 350 °C followed by a dilutor at ambient temperature. At the exit of VPR, a condensation particle counter measures particle > 23 nm (50% cut -point) [1.26]. Euro 5 and Euro 6 emission norms for light duty and heavy-duty vehicles are presented in Table 1.1 and Table 1.2.

Table 1.1 The light duty Euro 5 and Euro 6 vehicle emission standards on the new European driving cycle (NEDC) [1.14]

Pollutant	Euro 5 Light Duty		Euro 6 Light Duty	
	Gasoline	Diesel	Gasoline	Diesel
CO (g/km)	1.0	0.5	1.0	0.5
HC (g/km)	0.1	-	-	-
HC+NOx (g/km)	-	0.23	-	0.17
NOx (g/km)	0.06	0.18	0.06	0.08
PM (g/km)	0.005	0.005	0.005	0.005
PN (#/km)	-	6.0×10^{11}	6.0×10^{11}	6.0×10^{11}

Table 1.2 Euro 5 and Euro 6 vehicle emission standards for heavy duty diesel engines [1.14]

Pollutant	Euro 5	Euro 6	
CO (g/kwh)	1.5	1.5	4.0
HC(g/kwh)	0.46	0.13	0.16
CH_4(g/kwh)	-	-	0.5
NOx(g/kwh)	2.0	0.4	0.46
PM(g/kwh)	0.02	0.01	0.01
PN (#/kwh)	-	8.0×10^{11}	8.0×10^{11}
Smoke (1/m)	0.5	-	-
Ammonia (ppm)	-	10	10
Test cycle	ESC and ELR	WHSC	WHTC

1.1.3 Fuel Challenge

Automotive engines and fuels are facing challenges to reduce emissions for improving local air quality as well as reduce CO_2 emissions to reduce global warming [1.25]. Oil provides 33% of world energy and transportation engines account for 60% of 70 million barrels of crude oil used each day. This heavy consumption of fossil fuels results in emissions of large quantities of CO_2 emissions which is identified as greenhouse gas. Internal combustion engines operating on fossil fuels provide 25% of the world's power and produce 10% of the total world's greenhouse gases. To solve this problem, the IEA's roadmap calls for new road vehicles worldwide to consume 30 to 50 percent less fuel per km by 2030 [1.25]. All these goals simulate new developments in both conventional and alternative engines as well as fuels. Grand challenges in IC engine research are to develop technologies for maximizing engine efficiency, minimizing exhaust emissions, and optimizing tolerance for the utilization of a wide variety of fuels. To address these challenges, there are four possible approaches (i) improvement of conventional engines (ii) improvement of conventional fuels (iii) development of alternative engines (iv) utilization of alternative fuels and their combination [1.25]. Over the century, there have been significant developments in conventional engines and fuel technology to improve their performance to the present level. Another possible approach is to explore new engine concepts that use alternative fuels (such as biodiesel, alcohol, natural gas, etc.) to meet future emission legislation. The use of alternative fuels results in reducing the reliance on fossil fuels as well as increasing engine efficiency [1.25].

Due to concerns regarding environmental effects and strict emission regulations, research for next-generation combustion mode for IC engines has gained attention worldwide which can simultaneously reduce exhaust emissions and substantially improve thermal efficiency. RCCI is a promising strategy to meet current and future emission norms and regulations without relying on NOx and soot after treatment. Aside from the ability to meet NOx and soot emission incylinder, RCCI offers high thermal efficiency over a wide range of engine loads. This research mainly focuses on the characterization of PM emissions from diesel engines and RCCI engines. RCCI combustion is explored with conventional as well as alternative low-reactivity fuels.

1.2 Combustion and PM Characteristics of Diesel Engines

Internal combustion engines are heat engines that convert chemical energy bound in the fuel into mechanical energy. In IC engines, fuel is burned inside combustion chamber and combustion products directly apply force on the piston [1.23]. The most frequent used types of IC engine in automotive vehicles are compression ignition (CI) and spark ignition engines (SI). The majority of CI and SI engines are four stroke cycle of CI and SI engines namely intake stroke, compression stroke, power stroke, and exhaust stroke. CI engines and SI engines have different charge preparation and combustion characteristics, but the fundamentals of the engine cycle are the same for each. Diesel CI engines are a preferred choice for medium and heavy-duty applications due to their high fuel conversion efficiency, as it is operated at high compression ratio, on lean air fuel mixture and unthrottled. In this section combustion characteristics of compression ignition engines is discussed [1.25].

In DI diesel engines, the fuel is sprayed at high pressure directly into the main combustion chamber where it ignites by mixing with hot air produced by isentropic compression [1.24]. Diesel is injected during the end of compression stroke utilizing a fuel injector into hot and dense air. Based on the observation of combustion photography and measured combustion pressure – time history, diesel combustion process comprises of three distinct phases : ignition delay, premixed combustion and mixing controlled combustion [1.24]. Figure 1.1 shows the heat release curve for conventional diesel depicting different phases of combustion. Upon injection, the liquid fuel goes through a process that includes atomization into tiny droplets, vaporization and mixing with hot air, and precombustion reactions that result in autoignition, which initiates combustion [1.24]. The time between start of injection and start of combustion is called ignition delay. The combustion starts at multiple sites in the rich premixed region of the spray and then spreads along the edge of the spray rapidly burning the fuel vapor mixture around the spray core and leading edge of the spray during the ignition delay period. During the premixed combustion period, pressure and temperature increase rapidly in the cylinder. The fuel injection continues even after the start of combustion [1.24]. The rate of combustion of fuel after the start of combustion is governed by rate of atomization, vaporization, and mixing with air. As the incylinder temperature and pressure are much higher than start of combustion, therefore vaporization of the fuel droplets is faster, and rate of fuel air mixing control the combustion. This phase of combustion is called mixing controlled combustion phase [1.24]. The combustion of fuel continues even after the end of injection and the overall combustion period is much longer than the fuel injection period. Heat release rate decreases fast and gradually reduces to zero because of dissipation of spray turbulence. The fuel distribution in the cylinder is not uniform, and the local fuel-air ratio also varies from rich at the center of the spray to lean at the edges of the spray. At high combustion temperature (2000 -2500 °C), carbon particles in the diffusion flames have sufficient luminosity and appear as yellow regions [1.25]. Over the past decades, diesel combustion has advanced significantly due to improvements in high pressure common rail injection system. Modern diesel engines with high injection pressure fuel injection system show a small portion of premixed heat release due to enhanced fuel-air mixing and a decrease in ignition delay period [1.25].

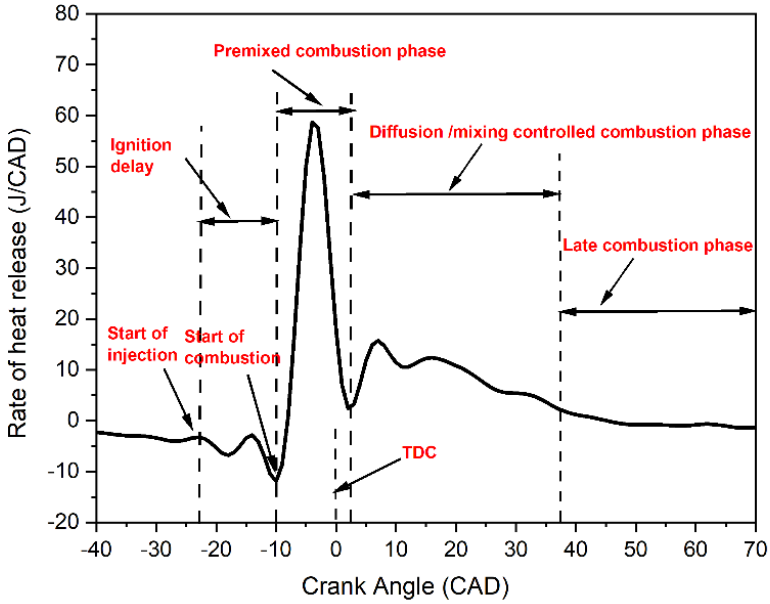

Figure 1.1 Heat release rate diagram for DI diesel engine identifying different phases of combustion

Studies of diesel engine using optical diagnostics to visualize fuel spray and flame behavior, combined with analysis of incylinder pressure data have led to a widely accepted descriptive model of the compression ignition engine combustion process. A model for DI diesel combustion based on laser sheet imaging was conceptualized by Dec and coworkers [1.27]. According to this model during the ignition delay period the spray penetrates the combustion chamber, entraining surrounding hot air. The fuel droplets evaporate forming a fuel rich mixture $(\varphi \approx 2-4)$ mixture which after few crank angle degrees, starts to react chemically, emit chemiluminescence and release 20% of its chemical energy [1.27]. During the first part of the premixed phase following autoignition, the fuel breaks down and large quantities of polycyclic aromatic hydrocarbons (PAH) form almost uniformly across the entire cross section of the leading portion of the jet. The formation of PAH coincides with sudden increase in the combustion rate indicating that a premixed burn spike consists of the combustion of this fuel rich mixture. These PAH molecules upon coagulation and condensation reactions form soot particles inside diffusion flames. Soot particles start forming throughout the cross-section of the downstream region of the jet from fuel rich premixed combustion. After the premixed burn, fuel droplets and products of fuel rich combustion are consumed through diffusion combustion and a diffusion flame rapidly surrounds the jet. The highest temperature is reached in the diffusion flame which leads to formation of nitrogen oxide [1.27].

Conventional diesel fueled compression ignition engines produce harmful pollutants such as nitrogen oxides (NOx), soot and particulate matter (PM). PM emissions from diesel engines consist of highly agglomerated solid carbonaceous material and ash, and volatile organic and sulfur compounds. Epidemiology studies have suggested a link between the increase of vehicular particulate emissions and negative impact on human health. PM emissions from diesel engines have been recognized as one of the important hazardous sources for human respiratory diseases. Due to increasing evidence of the impact of ultrafine PM regulations have been developed and imposed. Moreover, number-based PM legislations have been introduced on the top of stringent mass-based PM regulations. The European union established the particle measurement program (PMP) to measure ultrafine particles emitted by engines in regulatory framework, and a number-based engine exhaust particle regulation has been established targeting solid particles larger than 23nm. The newly established number-based PM emission regulations also arouse the need for PM emission characteristics in term of PM size and number on top of PM mass measurement

Soot particle formation in diesel engine encompasses complex physical and chemical processes whose understanding form the foundation of soot modelling in diesel combustion [1.28]. Inception is the first step in soot particle formation in which primary soot particles are formed through nucleation from gas phase precursors. These primary soot particles undergo surface reactions resulting in soot particle growth or oxidation. The gas phase species can also condense on soot particle surface [1.28]. In due course of time, these particles coagulate with each other leading to formation of larger particles. Accurate kinetic schemes are important to predict the gas phase species taking part in all processes leading to soot formations. The widely accepted gas phase species are PAH (polycyclic aromatic hydrocarbons) for soot precursors; acetylene for surface growth ; O_2 and OH for oxidation [1.29]. The precursors used in soot models have evolved over years from fuel vapor, acetylene to higher PAH species. Surface growth is generally modeled using the hydrogen abstraction carbon addition mechanism and the collision processes are represented by smoluchowski equation [1.29].

Quantitative and qualitative prediction of soot formation and oxidation in diesel engines can be done through four type of modelling approaches: empirical models, semi empirical models, phenomenological models and, detailed soot models [1.28-1.29]. The empirical soot models employ correlation of experimental data for soot mass numerical calculations. Semi empirical models calculate the functional relationship between in-cylinder soot and time based on physical process and parameters such as soot particle number density, species mass fraction and, soot volume fractions [1.28]. The soot particle size classes are however neglected by these models. These models solve the rate equations for soot particle formation and oxidation. These are used in engine CFD codes with change in activation energy parameters. The phenomenological soot models predict the intermediate species between conversion of fuel to soot. These models also include various particle formation processes such as soot particle nucleation or inception, particle coagulation, surface growth and oxidation [1.28]. Additionally, they also include chemical reaction rates for intermediate chemical species formation and oxidation. Such models have been successfully employed in engine CFD codes. In such multi step phenomenological models detailed chemical kinetic mechanism are employed to predict intermediate soot precursors species such as acetylene and PAH [1.29]. Physical and chemical phenomena for soot particle formation and oxidation were also included in these models. Soot parameters such as particle number density and mass can be calculated by solving the transport equations [1.28].

In detailed soot models complete description of particle size distribution function is provided. In these models chemical kinetics is coupled with the soot particle dynamics. Therefore, these models provide more details about the soot parameters relevant to engine operating conditions. This requires an efficient particle dynamics model and detailed soot chemistry. They are of three types: (1) Stochastic method (2) Sectional method and (3) Method of moments [1.28], [1.30]. In stochastic method growth molecules and particles are tracked using Monte-Carlo methods. In these three detailed soot models stochastic method is most accurate for predicting soot particle dynamics. It assumes a certain number of stochastic particles and handle the particle dynamics with probability methods. These detailed soot models estimate the global soot quantities such as mass, number density, volume fraction and surface area. In addition to these quantities these models also reveal the soot physical and chemical properties such as morphology and chemical composition [1.31]. However computational cost increases when this method is coupled with CFD codes. In the literature this method is only used as a post processing tool to investigate the distribution of soot particles in the direct injection engine exhaust [1.31]. Sectional method is another detailed soot modelling technique [1.32-1.33]. In this method, discretization of particle size distribution function is performed into number of sections and then the population balance equations are converted into coupled ordinary differential equations (ODEs). The time evolution of particles is then calculated with these coupled ODEs in each section to obtain the particle size distribution function. This method is simple to use in CFD codes but large number of sections are required obtain the complete particle size distribution function which results in high computational time and hence not adaptable for computational fluid dynamic engine simulations [1.34]. A detailed soot model was developed by Frenklach and Wang which operated on the method of moments. Methods of moments is lucrative method for detailed soot modelling due to its high computational efficiency [1.35]. In method of moments the PBE is transformed into moment equations and only few moments describe the soot particle characteristics such as number density and mass. By knowing the moments, the particle size distribution can be estimated. This method has been successfully implemented in engine CFD codes for prediction of soot particle size, mass, and number.

Hong et al. [1.36] implemented method of moments in KIVA CFD code to estimate the soot particle formation and soot particle transport process. This model employed skeletal chemistry for n heptane combustion and connects acetylene chemistry to soot particle inception process. The results for soot mass predicted were in agreement experimental results for varied injection timings and two EGR levels [1.36]. Zhong et al. [1.37] conducted soot and PAH modelling with method of moments. The turbulent diffusion flame and PAH formation were modelled using the reduced mechanism based on the detailed mechanism using fixed wall temperature as boundary conditions. Comparison of the simulation results with limited experimental data shows that chemical mechanism and soot model are realistic and correctly describe the basic physics of diesel combustion but require further development to improve their accuracy [1.37]. Zhao et al. [1.38] investigated soot particle number characteristics in term of particle dynamics, particle size and number density of a single cylinder diesel engine by integrating multi step phenomenological soot model into KIVA CHEMKIN CFD code. The predicted histogram of soot particle number along with size distribution contribute to dominant factors that affect soot formation. The results showed that predicted soot particle size was large for heavy soot conditions as compared to low soot conditions. Duvvuri et al . [1.39] investigated the soot particle size distribution inside a heavy duty and a light duty diesel engine and validating the results for variation of injection pressure using sectional soot model. Numerical results show good qualitative trends for soot PSD at exhaust conditions. This improved method of prediction of soot mass and PSD helps to design engines to meet Euro 6 emissions norms. Arad et al. [1.40] proposed a phenomenological soot model for biodiesel blends in diesel engines. According to this study, experimental soot reduction potentials of biodiesel blending for B20, B50, and biodiesel were 12.0%, 27.3%, and 47.2%, respectively. The respective computational soot reduction potentials were 34.8%, 36.2%, and 43.4%. Dong et al. [1.41] developed a practical soot model to describe the soot behaviors for diesel surrogate fuel comprising large n alkanes, isoalkanes, cyclopraffins, and aromatic hydrocarbons, as well as oxygenated fuels including alcohols and ethers. An efficient moment projection method was employed to describe the soot particle dynamics by directly solving the moment transport equations and tracking the number of soot particles. Results from this study indicate that the present model can satisfactorily reproduce soot characteristics of different fuels with distinct soot formation and oxidation characteristics. Puduppakam et al . [1.42] validated soot chemistry in ANSYS Model fuel library (MFL) for a variety of fuels, including n-heptane, n dodecane, methylcyclohexane, and toluene by using reduced chemical mechanism. The model was validated for various fuels in a wide range of operating conditions in flow reactors, shock tubes, stagnation flames, and engines. It was found that the involvement of multiple soot precursors in soot nucleation and PAH condensation is necessary to describe the soot characteristics for various fuels. Pan et al. [1.43] implemented a modified phenomenological soot model including key steps for soot formation, such as particle inception and surface growth in KIVA 3V for use in glow plug assisted natural gas direct injection engine. The kinetic model and modified soot model were compared with experimental data to validate their reliability and a good agreement was found between experimental and computational results. Wu et al. [1.44] investigated soot particle dynamics of diesel engine using the moment of projection method. It was found that the inclusion of a detailed soot model in the engine code induces and additional CPU cost of only 20% which is a relatively minor increase compared to the treatment of soot particle dynamics using stochastic methods. . Zhou et al. [1.45] developed a phenomenological model to simulate soot formation and oxidation and reveal the mechanism behind those processes in separated swirl combustion system. It was found that soot mas was lower in separated swirl combustion system than in double swirl combustion system due to lower soot formation rates and higher soot oxidation rate. Duvvuri et al. [1.46] evaluated soot model based on methods of moments by comparing simulations with the experimental data for varying operating conditions of heavy-duty optical engine. Results show that soot mass modeled by the method of moments has shown less sensitivity to the involved soot model constants and a good agreement for temporal evolution and spatial soot distribution for the considered cases. Li et al. [1.47] developed a reduced n-heptane/toluene (TRF)-polycyclic aromatic hydrocarbon (PAH) chemistry mechanism to simulate the combustion process of diesel fuel. Experimental results from an optical spray chamber, an optical diesel engine, and a heavy-duty metal diesel engine were used to assess the predictive power of the proposed soot model. The obtained results show that the numerical simulation results of the proposed soot model agree fairly well with those experimental data. Zhao et al. [1.48] conducted numerical analysis of fuel structures on soot particle mass and size using a multi step phenomenological soot particle model. It was found from the study that the reduction of exhaust soot from biodiesel combustion, compared to diesel fuel, was attributed to the suppressed soot precursors formation and lower number of particles in total. However, it was concluded that biodiesel fuel with higher unsaturated FAMEs (more double carbon bonds) contributed more to the formation of soot precursors, thus producing a higher amount of soot particles in mass and numbers as a consequence of accelerated soot particle nucleation and soot surface growth.

Martos et al. [1.49] proposed a new semi-empirical model that predicts incylinder soot primary particle growth from engine fueled with alcohol- diesel fuel blends. The model uses the macroscopic experimental measurement of engine parameters such as instantaneous incylinder pressure. They also developed an empirical correlation to predict the mean soot primary particle size as a function of alcohol diesel fuel blend properties and fuel/air ratio. Li et al. [1.50] investigated the effect of octanol addition to biodiesel on characteristics of soot formation and oxidation by performing a modelling study of the compression ignition engine fueled by octanol/biodiesel blends. It was found that a higher ratio of octanol led to the formation of fuel-rich zones within the bowl of the cylinder due to the increased viscosity of blends which increased the production of acetylene and a greater number of soot particles.

1.3 Advantages and Challenges with Conventional Diesel Engines

This section describes the potential advantages and scientific challenges of conventional diesel engines.

1.3.1 Advantages of Conventional Diesel Engines

- Diesel engines are currently the most fuel-efficient engines due to their high compression ratio, high specific heat ratio, and near zero throttling and pumping losses relative to conventional gasoline engines [1.14], [1.15].
- They are more rugged and reliable [1.15].
- There are no spark plugs as fuel autoignites. The absence of a spark plug of spark wires lowers maintenance cost [1.15].
- These engines emit less CO_2 emissions as compared to spark ignition engines [1.15].
- In diesel engines, less frequent overheat conditions occur during long idling running due to lower heat losses. These engines can operate at idling speeds for extended periods in sectors like agricultural, marine applications, and trains [1.15].
- Diesel engines can have generous intake pressure boosting by turbocharging without any knock limitation, which further increases efficiency and power density [1.15].

1.3.2 Challenges with Conventional Diesel Engines

- High PM and NOx emissions due to their operation in high combustion temperature and fuel rich regions.
- NOx-PM trade-off
- Aftertreatment systems require frequent maintenance, increased vehicle production and operational cost, fuel consumption, and complexity.

1.4 Combustion and PM Characteristics of RCCI Engines

In recent times advanced combustion strategies for CI engines have drawn great interest from the engine research community for simultaneous incylinder reduction of NOx and soot emissions without need of costly aftertreatment system [1.51]. These are premixed low temperature combustion (LTC) strategies that relies on using high rates of exhaust gas recirculation (EGR) and long fuel air mixing time. Long fuel air mixing time leads to lower local flame temperature and fuel rich zones in combustion chamber resulting in a simultaneous reduction of NOx and soot emissions. Lower flame temperature results in NOx reduction due to the high activation energy of NO formation reactions. Long ignition delay provide adequate time for fuel and air mixing before the start of combustion. This leads to less fuel-rich regions in the combustion chamber which reduces soot formation. Many researchers have shown that homogeneous charge compression ignition (HCCI) and premixed charge compression ignition (PCCI) concepts are promising techniques for simultaneous NOx and soot emissions [1.52]. These strategies address the soot - NOx trade-off challenge of conventional diesel combustion and maintain conventional diesel-like efficiency [1.52]. Despite their emission benefits, these combustion concepts present some practical issues that must be overcome before they can be implemented in CI engines [1.52]. The most relevant limitations consist of achieving appropriate combustion phasing, the cycle-to-cycle control of the combustion process, the noise, and the operation at high load conditions [1.52].

To overcome the HCCI and PCCI combustion concepts drawbacks, different strategies have been proposed in the last few years. Some of these strategies are control of intake air temperature, use of different injection strategies, and the control of intake oxygen concentration [1.52-1.55]. These strategies aim to compensate the high reactivity of diesel fuel by modifying gas properties. Recent investigations tried to overcome the challenges of previously described combustion concepts by modifying fuel properties, reducing fuel reactivity to slow down the chemical reaction rates, and delay autoignition [1.55]. Inagaki et al. [1.56] investigated dual fuel, premixed charge compression ignition (PCI) combustion controlled by two fuels with different ignitability to achieve drastically low smoke and NOx emissions. This study concluded that ignition timing of PCI combustion can be controlled by changing the ratio of the amount of injected fuels and combustion proceeds very mildly by making spatial stratification of ignitability in the cylinder even without EGR, preventing the whole mixture from autoigniting simultaneously [1.56]. Learning from this research, reactivity controlled compression ignition (RCCI) combustion concept was developed by Kokjohn et al. [1.57].

Reactivity controlled compression ignition (RCCI) strategy is a dual fuel partially premixed compression ignition, and it employs two fuels of different reactivities. In this strategy, two fuels of different autoignition reactivities (high and low reactivity) are used for premixed charge preparation by incylinder fuel blending. This strategy adopts multiple injection strategies and an appropriate level of EGR for controlling the incylinder reactivity to optimize the combustion phasing and combustion duration, which leads to higher thermal efficiency along with simultaneous reduction of NOx and soot emissions to ultra-low levels. The low-reactivity fuel (gasoline) is injected through port fuel injector in the intake manifold and premixed with intake air in the engine cylinder during the suction stroke of the engine cycle. The high reactivity fuel (HRF) is injected during the compression stroke through single, double, and triple injections. The early injected high reactivity fuel targets the squish region while late injected high reactivity fuel acts as an ignition source. The process of incylinder blending develops reactivity gradients in the combustion chamber. The stratification of fuel reactivity results in broader combustion events and reduced pressure rise rates compared to fully premixed HCCI combustion. Figure 1.2 shows a representative RCCI rate of heat release trace with distinct low temperature heat release (LTHR) and high temperature heat release (HTHR). Ignition processes that produce ROHR trace of this type are described as two stage ignition processes. LTHR occurs through cool flame reaction from diesel fuel, HTHR occur through high temperature oxidation of CO formed from the oxidation of diesel fuel and gasoline break down [1.58].

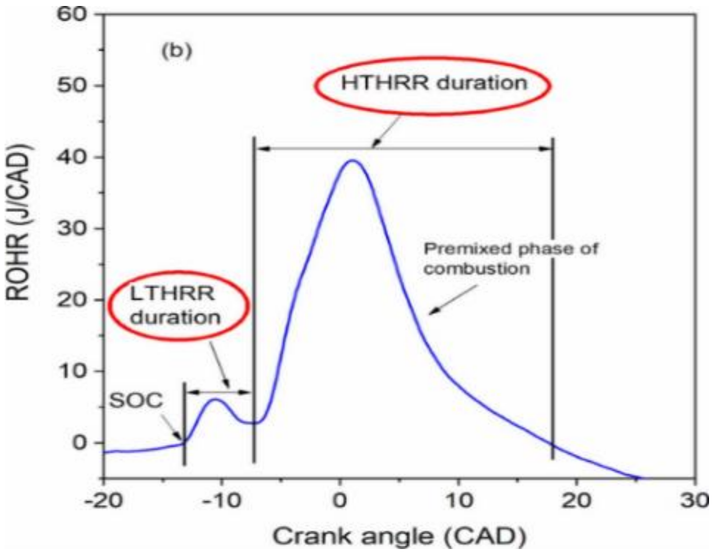

Figure 1.2 Heat release rate curve of RCCI combustion [1.58]

Multiple studies have investigated the effects of low and high reactivity fuels on RCCI combustion. These studies found that combustion phasing is effectively controlled by mixture stratification, which is affected by premixing ratio, diesel injection timing and diesel injection strategy [1.59-1.61]. Kokjohn et al. [1.60] compared RCCI and conventional diesel combustion and found reduction in NOx by three orders of magnitude, a reduction in soot by factor of six, and an increase in gross indicated efficiency of 16.4 percent. Simulations results of the studies showed that improvement in fuel conversion efficiency is due to both reduction in heat transfer losses and improved control over start and end of combustion. Despite its advantages, there are several limitations of RCCI combustion when operating at low load or high load due to low combustion efficiency, excessive pressure rise rate, and mechanical constraints. Several studies have been conducted to find the solutions to these limitations [1.61 -1.65]. Hanson et al. [1.61] investigated dual fuel and single fuel RCCI combustion with ignition improver at load of 2 and 4.5 bar IMEP and various engine speeds. It was found that at 4.5 bar IMEP operating condition it was possible to achieve 54% gross indicated thermal efficiency with NOx and PM emissions below US EPA 2010 limits. The results also show that it is possible to operate at a near idle load of 2 bar gross IMEP load with a gross indicated thermal efficiency of 49% at 1300 rev/min and 44% at 800 rev/min [1.61]. Splitter et al. [1.62] investigated effect of single and double injection strategy on RCCI combustion at low load. The results from this study show that double injection strategy reduced HC and CO emissions by 40% and thermal efficiency increased by 1%. Molina et al. [1.65] investigated suitable strategies to extend the RCCI operation from low load to full load. Results from this study show that double injection strategies should be used for RCCI operation from low to mid load. However, for high to full load operation single injection strategies should be used to avoid excessive pressure rise rates. Mikulski et al. [1.66] investigated variable valve actuation approaches to increase the load range and improve combustion efficiency of RCCI engine. It was shown that a heavy duty engine can run in natural gas diesel RCCI mode in full load range with CH_4 emissions within Euro 6 limits.

Researchers also investigated alternative fuels such as CNG, alcohols, hydrogen as low reactivity fuel in RCCI engines [1.66-1.72]. Doosje et al. [1.67] investigated RCCI operating limits and found that in the engine speed range (1200-1800 rpm) RCCI operation with Euro 6 engine out NOx and soot emissions was achieved between 2 and 9 bar BMEP without EGR. Mikulski et al. [1.67] investigated the influence of low reactivity fuel stratification on performance and emissions of dual fuel natural gas RCCI engine. It was found that low reactivity fuel stratification is a promising strategy to improve efficiency and reduce hydrocarbon emissions at part load RCCI. Gharehghani et al. [1.72] investigated the addition of ozone to NG/ diesel fueled RCCI engines using experiments and numerical methods. It was found that the addition of ozone by a distinct quantity not only can enhance the combustion phasing controllability but also extend the operating range of the RCCI engine in both lower intake air temperature and the lower fraction of high reactive fuel. Ganesan et al. [1.73] investigated the combined effect of the split injection technique and RCCI dual-fuel combustion in a single-cylinder CRDI research engine operated with waste cooking oil (WCO) biofuel and methanol. Results show a decrease in NOx emissions with RCCI dual-fuel combustion mode. Also, smoke emissions were reduced from 19% to 46%. Panda et al. [1.74] investigated the conventional dual fuel mode and RCCI modes using methanol and diesel at an IMEP of 5 bar and a speed of 1500 rpm. Results show a reduction in NO emissions by 95% in the RCCI mode compared to the dual fuel mode and soot emissions is reduced by about 78%. Thomas et al. [1.75] investigated low-temperature reactivity-controlled compression ignition engines using biodiesel as high-reactivity fuel and n hexanol as low-reactivity fuel with double injection strategies. It was found that smoke and NO emissions were reduced with advanced pilot injection. A maximum reduction in NO emissions by 96% and smoke emissions by 80% were observed with 25 % EGR as compared to diesel mode.

Duan et al . [1.76] investigated the combustion characteristics of Hydrogen (H_2)/diesel RCCI engines. The results showed that under a single DI strategy, the maximum indicated thermal efficiency (ITE) of H_2 RCCI is considerably higher than that of gasoline RCCI. Under the double injection strategy, the ignition and combustion of H_2 are more sensitive to intake boost than gasoline in RCCI. An increased premixed ratio can effectively improve combustion stability, indicated thermal efficiency (ITE), nitrogen oxides (NOx), and soot simultaneously with a reduced peak pressure rise rate for H2/diesel RCCI engines. Wang et al. [1.77] investigated the combustion and emission characteristics of the PODE/ methanol RCCI engine. The results showed that with an increase in EGR ratio, the combustion process becomes smoother. With the increase in EGR ratio from 0% to 30%, NOx production gradually reduced by 47.3%, ringing intensity (RI) and maximum pressure rise rate (MPRR) decreased by 1.31 MW/m^2 and 0.37 MPa/° CA, respectively, and brake thermal efficiency decreases from 45.45% to 43.19%. Liu et al . [1.78] investigated the RCCI engine fueled with E10 and HCB achieved reliable ignition at low loads with a higher premixed energy ratio. It was found that increasing the premixed ratio (90%) can result in better flame propagation, cleaner combustion, and an IMEP of about 0.21 MPa at low load. Increasing the premixed energy from 70% to 90% significantly reduced the high temperature and soot concentration regions resulting in a significant decrease in the integrated KL factor by 75.69% and 96.41% respectively. Sun et al. [1.79] conducted experiments using coal to liquid fuel (CTL) and conventional diesel as pilot fuel and gasoline as the premixed fuel was carried out on modified dual-fuel engines. The results from this study show that gasoline/CTL reactivity controlled compression ignition (RCCI) mode and gasoline/diesel RCCI mode contain low temperature heat release (LTHR) and high temperature heat release (HTHR) phases. Under optimum conditions, the gasoline/CTL RCCI mode achieves higher thermal efficiency and generates lower CO, HC, and particle emissions.

Particle emissions can be affected by many factors under RCCI combustion mode, especially those which can vary the distribution and stratification of the mixture. Since the physical and chemical characteristics of different fuels have a crucial impact on combustion and emission characteristics, various low reactivity fuels (LRFs) have been extensively explored by researchers over the years. Benajes et al. [1.80] investigated dual mode dual fuel combustion concept that combines fully and highly premixed RCCI regime for low and medium engine loads and changes to dual fuel combustion at greater engine loads. The highly premixed reactivity-controlled compression ignition regime showed a transitional particle size distribution with peaks of mobility diameter around 20 nm and 80 nm. It was discovered that fully premixed RCCI combustion was dominated by small particles (less than 30 nm in diameter) and that the dual fuel dual mode displayed larger sized particles similar to diesel soot particles, which are nearly 100 nm in mobility diameter [1.80]. Gracia et al. [1.81] investigated particulate emissions of a modified medium duty engine working in dual mode dual fuel combustion concept with objective to maintain ultra-low NOx and very low soot emission generation on RCCI combustion mode. The study found that premixed RCCI combustion generated particles between diameter 5nm and 40 nm. In diffusion combustion regime larger particles around 80 nm and 200 nm consisting of solid black carbon are generated due to fuel rich incylinder charge and higher temperature that decreases the gas to particle conversion. RCCI combustion mode generated particle mass around 4 mg/kWh due to premixed combustion while diffusive combustion mode generated particle mass around 50 mg/kWh [1.75]. Agarwal et al. [1.82] compared the particulate matter characteristics of CI, PCCI and RCCI combustion strategies on a single cylinder diesel engine. A significant result of this study was the relative higher concentration of accumulation mode particles (AMP) compared to nucleation mode particles (NMP) in the exhaust of the RCCI combustion. In comparison to other combustion techniques (CI and PCCI), it was discovered that the RCCI combustion approach was dominant in the reduction of PM and NOx. Geng et al. [1.83] investigated the effect of diesel/ methanol dual fuel combustion on dry soot and PM (particulate matter) emission characteristics of a 6-cylinder turbocharged, intercooler HD (heavy duty) diesel engine modified to diesel methanol dual fuel combustion mode. It was found that dry soot emissions decrease with increase in methanol at low and medium loads, while there is an increase in PM emissions at higher load. Wu et al. [1.84] investigated the effect of premixing ratio and diesel late injection timing on methanol/diesel dual fuel engine PM emissions. It was found that an increase in the premixing ratio leads to a decrease in accumulation mode particle (AMPs). Lee et al. [1.85] investigated the effect of the premixing ratio on combustion and emission characteristics of ethanol diesel dual fuel RCCI engine through a double direct injection strategy. Results show that total mass of PM emissions decreased with increase in ethanol fraction due to less accumulation mode particles produced, however number of nucleation mode particles increased. Iorio et al. [1.86] investigated the PM characteristics of methane diesel RCCI engine. Results from the study show that RCCI combustion mode emits fewer particles due to the absence of C-C bond and lower C/H ratio in methane chemical structure. Qian et al. [1.87] investigated the effect of premixing ratio and main direct injection timing on particulate emission characteristics of RCCI engine. The results from the study show that the particles emitted from biogas/diesel RCCI combustion mode are primarily nucleation mode particles. With an increase in the premixing ratio, the particle number and surface area concentration increase significantly. With the advance of main direction injection timing, the particle number and volume concentration also show a notable increase. Han et al. [1.88] investigated the particle emission characteristics of RCCI engine with variations in premixing ratio and total cycle energy. Results show that an increase in premixing ratio resulted in a decrease in nucleation mode particle number (NMPn) and nucleation mode particle mass (NMPm) and an increase in accumulation mode particle number (AMPn) and accumulation mode particle mass (AMPm). It was also observed that an increase in ethanol addition leads to higher AMPn and AMPm and lower NMPn and NMPm. Saxena et al. [1.89] investigated the effect of port fuel injected gasoline mass and diesel injection timings on particle emissions and unregulated emission characteristics of gasoline diesel RCCI engine. Results show that advanced diesel injection timing and increase in port injected mass lead to higher particle emissions as well as saturated, unsaturated hydrocarbon and formaldehyde emissions. Pan et al. [1.90] investigated the combustion and emissions of iso butanol/ diesel RCCI under low load and compared its results with gasoline diesel/ RCCI. Results show that NOx and particle emissions of isobutanol/ diesel RCCI combustion are lower than those of gasoline/diesel RCCI mode.

While initial RCCI studies were encouraging, further improvements have been undertaken to assess its ability to achieve future emissions reduction and assess its commercialization in automotive, stationary, and marine applications (using natural gas diesel for mid-speed marine engines). Recent emissions legislation in the marine sector has emphasized the need to reduce nitrogen dioxide (NOx) as well as Sulphur emissions. The fulfillment of emission legislation limits with conventional marine diesel oil require complex and expensive aftertreatment system. Milkulski et al. [1.91] conducted first study to evaluate natural gas RCCI combustion for mid-speed marine engines. The study found that the best point indicated thermal efficiency of 47.8% is achievable using RCCI mode on stock engine hardware while meeting IMO Tier III's NOx limit. RCCI also provides additional methane and CO reductions with performance similar to best contemporary marine engines. The study concluded that RCCI combustion can meet Europe's new rigorous stage V limits, offering significant improvement in a marine engine's GHG foot print. Valladolid et al. [1.92] carried out experimental study in an dual fuel single cylinder marine engine to evaluate different diesel equivalence ratio distributions in the combustion chamber and to get the deeper insight into the interaction between the high reactivity (diesel) and the low reactivity (natural gas) during ignition process. The results from this study show that local pilot fuel distribution as way to control combustion phasing and consequently its impact on combustion instability, emissions, and knock conditions. Stable combustion with engine out NOx level below legislation has been achieved without the need for an aftertreatment system with appropriate high reactivity fuel (HRF) distribution control. RCCI combustion is not only useful in mobile applications but also, they can be used in stationary applications such as power generators, particularly in hybrid configurations combined with fuel cells and electric motors. Taghavifar et al. [1.93] investigated RCCI / battery hybrid electric vehicles (HEVs) with diesel and hydrogen. The findings indicate that the battery SOC is preserved in better condition when RCCI engine mode is coupled in hybrid vehicle. It was also found that HEV releases considerably low NOx compared to DCI and more NOx compared to D100 (conventional pure diesel injection case) and D50M50 (direct injection of 50% diesel with 50% methanol).

For the fundamental investigation of RCCI combustion strategy researchers used advanced optical techniques in order to understand the incylinder process including charge stratifications, reactivity gradients, autoignition, flame propagation. Kokjohn et al. [1.94] investigated the RCCI combustion process using optical diagnostics techniques. High speed chemiluminescence imaging and toluene fuel tracer PLIF were used to explore fuel reactivity stratification as a method to control heat release rate for PCI combustion. A sweep of injection timing was used to vary the fuel reactivity stratification inside the combustion chamber. At very early injection timings (145°bTDC), the chemiluminescence imaging showed HCCI like combustion with random ignition location and rapid combustion zones. The fuel tracer imaging showed that the fuel distribution for the early injection timing case has only a weak spatial gradient of reactivity. Retarded injection timing to 50° bTDC resulted in a significant reduction in the peak heat release rate. At this mid-range injection timing, the chemiluminescence imaging showed ignition occurring in the downstream portion of the jet and a controlled reaction zone growth toward the common rail injector (toward the center of the combustion chamber). Consistent with the observed ignition location and reaction zone growth, the fuel tracer fluorescence imaging showed that the region with the highest fuel reactivity was located near the cylinder liner, and the reactivity decreased close to the center of the combustion chamber [1.94]. This reduction in peak HRR appears to be the result of increased fuel reactivity stratification [1.94]. Similar to the early injection timing case, the case with near TDC injection of n-heptane (SOI = 15° bTDC) showed violent combustion in the early part of heat release. The combustion luminosity imaging showed that ignition occurs in the downstream portion of n-heptane jet and very quickly luminosity was observed throughout the entire n-heptane jet (the entire jet ignites instantaneously) [1.94]. The fuel tracer fluorescence imaging showed bimodal distribution in both equivalence ratio and primary reference fuel (PRF number). Ignition delay calculations suggest that the rapid energy release inside the jet is due to limited mixing time that yields over stratified charge where much of the fuel mass is located in the region of nearly constant ignition delay [1.94]. Kokjohn et al. [1.95] investigated the combustion process in RCCI engine using a combination of optical diagnostics and chemical kinetics to explain the role of equivalence ratio temperature, and, fuel reactivity stratification for heat release control. The chemiluminescence imaging showed that the mixture in the squish region ignited first, and the reaction zone proceeded inward toward the center of the combustion chamber. The fuel tracer PLIF data shows that the combustion events proceed down gradients in n-heptane distribution. The chemical kinetic modelling showed that primary reference fuel (PRF) number stratification is a dominant factor controlling the ignition location and growth rate of the reaction zone [1.95]. Liu et al. [1.96] investigated the flame development progress of RCCI combustion. Results from this study show that RCCI has a shorter ignition delay than PPC due to fuel reactivity stratifications. The natural luminosity, formaldehyde, and OH PLIF images show the flame front propagation in the early stage of PPC while no distinct flame propagation is seen in RCCI combustion at 70% premixing ratio. It was also found that a high premixed ratio reduced the combustion rate in RCCI mode and flame propagation can be seen with flame speed like spark ignition combustion but lower than PPC [1.96].

1.5 Advantages and Challenges with Reactivity Charge Controlled Compression Ignition Engine

RCCI combustion has several advantages as compared to conventional diesel combustion and other low temperature combustion strategies such as HCCI and PCCI. Advantages with RCCI combustion are described below :

1.5.1 Advantages :

- High thermal efficiency is achieved with RCCI combustion over wide engine operating conditions with peak gross indicated efficiency of 56% at 9.3 bar IMEP operating point on heavy duty engine [1.97]. Operation over the load range from 2 bar IMEP to 14.6 bar IMEP low and medium loads) at 1300 rpm demonstrated in the previous studies [1.97].
- As compared to other LTC combustion techniques such as HCCI and PCCI, RCCI combustion provides improved combustion duration and combustion phasing control [1.97].
- RCCI is a fuel flexible technology therefore different types of low reactivity fuel and high reactivity fuel can be used.
- RCCI is a promising combustion strategy to meet current emission regulations such as Euro VI without relying on costly NOx and soot aftertreatment system [1.97].
- RCCI experiments on heavy duty engines demonstrated that nearly 60% efficiency is possible through optimized combustion management and thermodynamic conditions. Improved efficiency compared to conventional diesel combustion is due to reduced heat transfer losses [1.98]. These ultra-high efficiencies were reached by operating with higher compression ratio without piston cooling [1.98].
- Nearly three orders of magnitude of NOx, six times lower soot emissions are achieved RCCI combustion compared to conventional diesel combustion [1.97].

1.5.2 Challenges :

- Excessive pressure rise rate at higher loads and high-speed engine operating conditions.
- High cyclic variations at low loads
- Combustion phasing control
- Cold starting operation
- Higher CO and unburned HC emissions at low loads
- High particle number emissions (size < 23 nm)

1.6 Objectives of Research Work

The main goal of this research is to gain an in-depth understanding of nano-particles emission characteristics of RCCI engines vis-à-vis conventional diesel engines. Typically, RCCI engines have higher nucleation mode particles due to homogeneous nucleation. The RCCI combustion is a mainly premixed combustion, and operated at advanced diesel injection timings. Particle formation is primarily governed by soot precursors and pressure-temperature in the chambers. Thus, to understand the formation of soot precursors, particle number density and different PAH species in the cylinder, a preliminary numerical study was performed at advanced diesel injection timings. Later, an experimental investigation was conducted to study the particle emission characteristics and their relationship with the heat release rate of RCCI engine. Volatile and non-volatile nature of particles are investigated to further characterize the nucleation mode particles of the RCCI engine.

To achieve this goal, the specific objectives of this research work are as follows :

- Numerical investigation of the effect of advanced injection timing and injection pressure relevant to RCCI strategy on in-cylinder soot precursor formation and particle emission characteristics using a detailed soot model.
- To investigate the effect of low-temperature heat release and high-temperature heat release on particle number characteristics of RCCI engine and develop empirical correlations for estimation of particle emissions.
- To develop a thermodesorption system to characterize the volatile and non-volatile particles from RCCI engine.
- Investigate the effect of the different operating parameters on the volatility of particles using developed thermodesorption system.

1.7 Thesis Organization

The thesis is organized in following manner :

Upto this point in the chapter 1 the general background, motivations, and objectives of this research work is discussed. Combustion in conventional diesel engine and reactivity-controlled compression ignition is discussed. An introductory explanation of RCCI engine to relate RCCI engines to classic diesel engines, highlight the benefits, and examine the problems associated with them.

Chapter 2 provides a detailed literature review describing relevant literature relevant to the scope of the study. The chapter gives the background of the combustion and emission formation process in conventional diesel operation. Literature review describes the theory and mechanism of PM formation in diesel engines and RCCI engines. Optical and numerical studies investigating the formation of PM is discussed. Thorough examination of current literature relating to combustion and particulate emission characteristics of diesel and RCCI engine is discussed in detail which aids in defining the state of the art and illustrate how the technology has evolved up to this point. At last research gaps in the literature are identified.

Chapter 3 describes 3D CFD model which includes various physical and chemical sub models and model validation. Details about the engine set up, instrumentation, measurement techniques and experimental parameters are discussed along with design and development of thermodesorption system.

Chapter 4 presents the results and discussion of the research work. In this chapter effect of engine operating parameters on combustion and particle emission characteristics of diesel and RCCI engines are presented. This is followed by the development of empirical correlations for the estimation of particle emissions from RCCI engine. At last, characterization of solid particle emissions using developed thermodesorption is also discussed.

Chapter 5 provides the summary of the main conclusions from this thesis and suggestions for future work

Chapter 2

Literature Review

This chapter presents the reviewed literature of previous studies related to diesel engine and RCCI engine. In this chapter firstly combustion characteristics of diesel engine and RCCI engine is presented. Then particulate matter formation is discussed in diesel and RCCI engine. For diesel engines previous optical and computational studies are discussed which focus on particulate formation while for RCCI engines previous experimental studies are discussed. Then the studies investigating the effect of engine operating conditions on diesel and RCCI PM characteristics are discussed. Further particle measuring measurement program and design and development of thermodesorption system is discussed. At last effect of thermodesorption system on engine particle size distribution is discussed. Finally, research gaps are identified based on the literature survey.

2.1 Combustion Characteristics of Diesel Engines

2.1.1 Ignition Delay

Ignition delay is the period between the start of fuel injection into the combustion chamber and the start of combustion [2.1]. This delay period consists of physical delay wherein atomization, vaporization, and mixing of air-fuel occur and chemical delay attributed to precombustion reactions. The delay is preliminary dependent on ambient temperature [2.1], [2.2], [2.3], [2.4]. Correlations in the literature show that ignition delay exponential dependence on temperature as in the Arrhenius equation for the rate of reaction. Studies have shown a strong influence of injection parameters like hole size, injection pressure, and types of fuel and hence quality of fuel on measured ignition delay [2.2]. Studies have shown that the ignition delay period not only depends on the chemical characteristics of fuel, but also on the fluid mechanics of atomization, vaporization, and mixing. Aromatics and alcohols have chemical bonds that are difficult to break and result in long ignition delay. If these fuels are injected rapidly enough to mix completely with air before autoignition occurs, they will burn rapidly when ignition occurs in the premixed phase. On the other hand, the chemical bonds of some fuel, such as alkanes (straight-chain paraffins), are easily broken. Ignition delay is then short, and with a long injection, most of the fuel to be burned is injected after autoignition occurs. Relatively little fuel burns in the premixed combustion phase and most of the fuel burns at a rate limited by the rate of mixing with the cylinder air. As engine speed increases, the ignition delay period will need to be decreased to maintain a relatively constant combustion duration in crank angle degrees. In direct injection engines, the fuel-air mixing rate is increased using increased turbulence, swirl generated by the intake port geometry, and deeper piston bowls. In a diesel engine, it can be determined experimentally as the time interval between the start of injection and the start of combustion. Due to vaporization effects, the apparent heat release changes from negative to positive. The start of injection is defined as the crank angle at which the needle of the nozzle lift by 5%. The time difference between the start of injection and the start of combustion is called as ignition delay. The Arrhenius type equation to describe ignition delay is described by equation (2.1) [2.5], [2.6], [2.7], [2.8].

$$\tau_{id} = a\, \varphi^{-k}\, P^{-n}\, exp(\frac{E_a}{R_u\, T_{cyl}}) \tag{2.1}$$

Where τ_{id} is the ignition delay, φ is the equivalence ratio, E_a is the activation energy, T_{cyl} is the cylinder charge temperature, R_u is the gas constant, and a, k, n are empirical constants.

2.1.2 Incylinder Pressure and Rate of Heat Release

Cylinder pressure data analysis is the most effective tool to analyze engine combustion behavior because cylinder pressure history directly influences power output, combustion behavior, and engine out emissions. Understanding the rate and amount of energy transformed from chemical energy into heat produced by combustion is possible through heat release analysis. Based on the first rule of thermodynamics, the observed incylinder pressure calculates the rate of heat release. Studies found that maximum cylinder pressure increases with an increase in fuel injection quantity. Advancing SOI leads to longer ignition delay, which promotes premixed combustion higher maximum cylinder pressure, and high ROHR peak [2.9], [2.10], [2.11], [2.12] [2.13], [2.15]. When injection timing is retarded and it came close to TDC in the compression stroke, ignition delay was shorter, which led to a higher amount of fuel consuming in diffusion-controlled combustion thereby reducing maximum cylinder pressure. With an increase in fuel injection pressure peak cylinder gas pressure increases due to proper fuel-air mixing which leads to better oxidation of fuel and high HRR with rapid burning and shorter combustion duration [2.17], [2.18], [2.19], [2.20], [2.21].

2.2 Combustion Characteristics of RCCI Engine

RCCI is a dual-fuel engine combustion technology that uses at least two fuels of different reactivity to achieve incylinder blending and employs a multiple injection strategy and an appropriate EGR rate to control incylinder reactivity to optimize combustion phasing and magnitude, resulting in higher thermal efficiency and lower soot and NOx emissions. During the intake stroke, the LRF is injected via PFI and premixed with air in the cylinder. During the compression stroke, high-reactivity fuel is pumped into the cylinder via a DI injector using a single, double, or triple injection technique. The early injected HRF is aimed at the squish region, whereas the later injected HRF serves as an igniting source. Ingnaki et al. [2.22] investigated a strategy for control of PCCI combustion by means of varying fuel reactivity. Dual fuel PCCI was achieved through direct injection of diesel fuel around 40° bTDC and port fuel injection of isooctane [2.22]. They found that engine operating range can be extended by changing the ratio of n-heptane and isooctane. Diesel fuel ignited earlier in the cycle while isoctane was consumed later. The phasing of HTHR was observed to be dependent on the local equivalence ratio. The local equivalence ratio was found to be dependent on diesel injection timing. The HTHR was found to be advanced with retarded injection timing because of fuel-rich zones trapped in the squish region. By advancing diesel fuel injection timing the equivalence ratio was reduced due to enhanced premixing and HTHR retarded. It was also found low NOx and smoke emissions less than 10 ppm and 0.1 FSN with high thermal efficiency (> 50%). Diesel gasoline RCCI has been extensively studied in the literature over a wide range of operating conditions on light-duty and heavy-duty CI engines [2.23-2.27]. Studies investigated RCCI combustion concept both experimentally and numerically found reduction of the rate of pressure rise rate and increased combustion duration due to fuel reactivity stratification through early direct split injection of diesel [2.23], [2.24]. This combustion strategy also increased the engine operating range to higher loads while low NOx and soot emissions are maintained well below prescribed emission limits [2.23], [2.24]. Splitter et al. [2.25] found that 60% thermal efficiency can be achieved with RCCI with optimized combustion management and thermodynamic conditions [2.25]. The results from this study show that high thermal efficiency can be achieved by using high dilution and by optimizing incylinder fuel stratification with two fuels of large reactivity gradient [2.25]. RCCI combustion is capable of operating over a wide range of loads (4.6 – 14.6 bar) with near zero levels with near-zero levels of NOx and soot, acceptable peak pressure rise rates, and high indicated thermal efficiency. Kokjohn et al.[2.26] compared RCCI operation between light-duty and heavy-duty engines. They reported comparable low NOx and soot emissions but lower thermal efficiency on light-duty engine compared to heavy-duty engine [2.26]. Kokjohn et al. [2.27] investigated RCCI combustion in an optical engine to investigate the mechanism controlling RCCI energy release. Chemiluminescence imaging shows that RCCI features a reaction zone that appears to grow by the appearance of small autoignition pockets. The fuel tracer fluorescence imaging shows that the ignition location corresponds to the regions with the lowest PRF number and highest equivalence ratio. The rate of the reaction zone is then controlled by the level of stratification in equivalence ratio and PRF number. Kinetic modelling-based fuel tracer fluorescence imaging shows that the PRF number has the largest effect on the rate of reaction zone growth [2.27].

RCCI combustion is a fuel-flexible combustion strategy and hence different low-reactivity and high-reactivity fuels can be used. However, lower operating load range in comparison with conventional diesel combustion, higher pressure rise rate (PRR) at higher load, higher cyclic variations at lower load, higher carbon monoxide (CO), and unburnt hydrocarbon (HC) emissions are still major challenges for RCCI combustion. Compressed natural gas (CNG) has gained attention due to the advantage of low cost and its potential to reduce PM emissions emanating from engines. RCCI combustion with natural gas as LRF with an optimized injection strategy has shown promising results in extending the combustion duration and low peak PRR at high engine loads because of the large reactivity gradient between diesel and natural gas. Methane as LRF can extend the operating load limits of the RCCI engine [2.28]. The CNG–diesel RCCI engine can meet the Euro-VI limits of NOx and soot emissions between the engine speed of 1200-1500 rpm, but unburnt HC is significantly higher [2.29]. However, unburnt HC, CO, and NOx emissions can be reduced by using an optimal fuel injection strategy. The amount of HRF and SOI can be used to control the CA_{50}, and an increase in the amount of HRF results in decreased unburnt HC and CO emissions. For medium engine load (7 to 9 bar indicated mean effective pressure (IMEP)) operation, an increase in pilot injection fuel quantity by decreasing main injection is suggested in a numerical study [2.30]. For higher load operation, combustion can be controlled by decreasing the pilot fuel injection quantity and increasing the main injection. The use of exhaust gas recirculation (EGR) in CNG–diesel RCCI operation resulted in decreased NOx emissions whereas soot emissions increased [2.31]. The following subsection below describes the effect of engine operating parameters on the combustion characteristics of RCCI engine.

2.2.1 Effect of Single and Double Injection Strategy

Among many other aspects, the injection strategy plays a significant role in improving the performance of the RCCI engine. The timing of high-reactivity fuel (like diesel) injection might be referred to as the injection strategy. Utilizing a single, double, or triple injection method, high-reactivity fuel can be injected into the combustion chamber. Hanson et al. [2.32] investigated the effect of diesel fuel injection parameters on RCCI combustion and emissions. It was found that with double injection strategy, retarding first injection (SOI 1) and second injection (SOI 2) timing resulted in advanced combustion phasing (CA_{50}) and increased peak pressure rise rate (PRR). Splitter et al. [2.33] investigated the effect of injection timing with single and double injection strategy on the combustion characteristics of RCCI engine. It was found that later injection timings resulted in diesel-like combustion with a high pressure rise rate. Walker et al. [2.34] investigated the effect of diesel fuel injection pressure on RCCI combustion using gasoline direct injection (GDI) injector and found comparable performance and emission results with low injection pressure enabled GDI injector. Ma et al. [2.35] investigated the effect of diesel injection timings and injection strategies on gasoline diesel dual fuel combustion and emission characteristics. It was found that in the single injection strategy, too early or too late injection timings can retard the combustion phasing far away from TDC. In the double injection strategy advancing SOI 1 while SOI 2 fixed resulted in a decrease in peak cylinder pressure and peak heat release rate. It was also found that retarding SOI 2 with fixed SOI 1 resulted in decreased pressure rise rate [2.35].

2.2.2 Effect of Premixing Ratio

One of the factors that can impact the fuel-air mixture's reactivity in the cylinder is the premixing ratio. Most of the studies reported an increase in ignition delay and retarded combustion phasing (CA_{50}) with an increase in the premixing ratio [2.35-2.44]. Benjas et al. [2.36] found that as the diesel/gasoline incylinder blending ratio is reduced the ignition delay increases due to the global lowering of fuel reactivity and CA_{50}, peak pressure rise rate is lowered. Qian et al. [2.40] ethanol, butanol, and amyl alcohol as LRF in RCCI experiments and found similar combustion characteristics at a low premixing ratio, however at a higher premixing ratio combustion phasing was found to be retarded with ethanol with an increase in premixing ratio. Poorghasemi et al. [2.41] found that with an increase in natural gas premixing ratio from 55% to 85% the peak incylinder pressure and HRR reduced and CA$_{50}$ retarded. However, a further increase in the premixing ratio from 85% resulted in the rise in CA$_{50}$ due to the lower global reactivity of the charge. Li et al. [2.43] investigated the combustion and emission characteristics of a methanol/ diesel reactivity-controlled compression ignition engine (RCCI) using a multidimensional model coupled with chemical kinetics. The study reported that both methanol mass fraction and diesel injection timing have a significant impact on the cetane number distribution (fuel reactivity distribution) which decides the ignition delay and peak heat release rate (HRR).

2.3 Particulate Formation

Diesel PM is defined in terms of the mass collected on a filter paper from the exhaust which is diluted and cooled to 52° C or lower temperature [2.45], [2.46]. PM emitted from the engine is in the form of fine particles in the liquid or solid phase [2.46]. Solid particles are mainly carbonaceous matter (soot) and consist of a small fraction of inorganic substances. Various liquid phase substances and other materials may also either absorbed [2.46]. Figure 2.1 shows the illustration of diesel particulate matter which shows soot particles with adsorbed hydrocarbons (soot particle : black colour, Condensed HC/H$_2$SO$_4$: green colour, nucleation mode particles : yellow colour, embedded ash: blue colour). Typically, Chemical composition of diesel PM is a complex mixture of elemental carbon (EC) and organic carbon (OC), sulphur compounds metals and elements, inorganic ions, and other species [2.47], [2.48], [2.49]. The chemical composition of PM strongly depends on fuel properties and mode of combustion. The chemical composition of PM mass for the blend of diesel-biodiesel-ethanol for different fuelling modes i.e., neat diesel, blended, fumigation, and blend (F+B), and fumigation mode are illustrated in Figure 2.2.

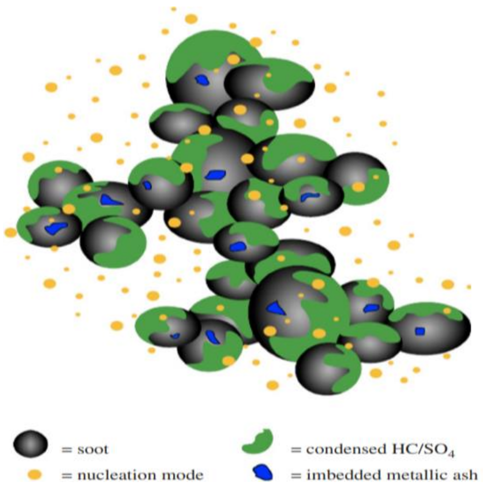

Figure 2.1 Illustration of diesel particulate matter (DPM) [2.49]

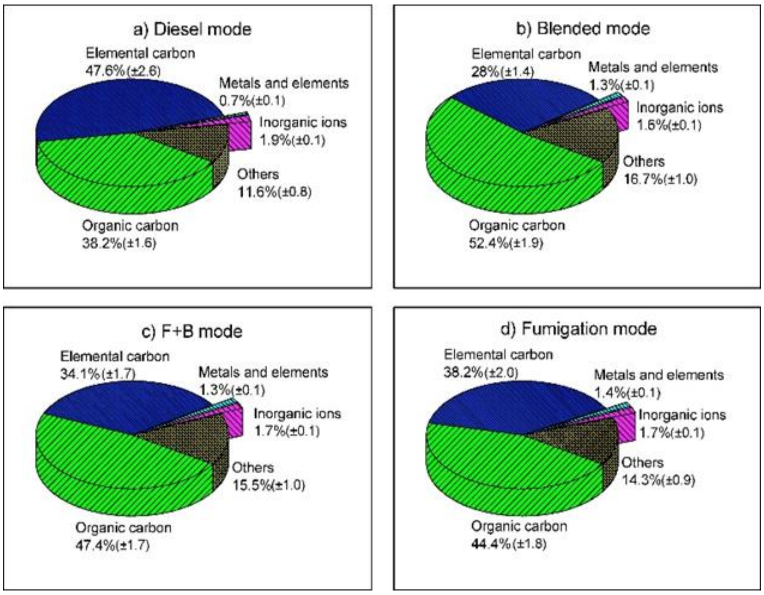

Figure 2.2. PM mass composition for the blend of D80B5E15 (% volume) for different fuelling modes [2.48]

The chemical composition and concentration of PM influence the oxidation of PM, which is one of the critical parameters in designing of diesel particulate filter (DPF) [2.50]. In the case of blended mode operation, lower inorganic ions and EC in PM, geometric mean diameter (GMD) of particle and total PN concentration, and higher OC in PM, positively influence the efficiency of DPF catalyst [2.50]. Reduced EC improves the soot oxidation reactivity, and reduces the soot ignition temperature [2.50], which could enhance the rate of regeneration of DPF. Additionally, reduced particle concentration with a smaller diameter can be easily oxidized during regeneration in DPF than a higher number of particles with a larger diameter [2.50]. Physical characterization ultrafine particles emitted from the CI-engine can be broadly categorized into soot, ash-bearing soot, and ash. Soot bears either as a single, nearly spherical primary particle or compact agglomerates [2.51]. The primary particles that compose the ultrafine agglomerate in size range between approximately 7nm and 20 nm [2.51]. The ash-bearing particles have an irregular shape and are in a size range between 4nm and 7nm, attached to soot, or enclosed into primary particles [2.51]. Later the ash nanoparticles serve as nucleation cores for soot growth [2.51]. Ultrafine ash consists of Ca, P, S, O (in the form of CaSO4 and/or CaO and/or CaPO4) and Si, Fe, and minor Zn (in form of oxides) (Originating from lubricating oil additive). The ash particles occur as distinct phases forming single particles or aggregates. Ash particle consists of Fe-O and some fraction of O, Al, and Ca-S ± P ± Fe ± Zn-O compounds [2.51].

2.3.1 Particulate Formation in Diesel Engines

Diesel engines offer high thermal efficiency and low fuel consumption and are most suitable for heavy duty applications compared to any other power plant used for road transportation. However strict emission regulations have been imposed on these engines owing to their harmful emissions of PM and NOx. To meet stringent emission regulations improved understanding of incylinder combustion and pollutant formation is essential for engine designers.

2.3.1.1 Optical Studies

Soot formation in flames from gas or liquid phase molecules comprises of the following sequence of events: generation of polycyclic aromatic hydrocarbons (PAH) due to fuel pyrolysis, particle inception due to collision of PAH, surface growth through hydrogen abstraction and carbon addition (HACA) mechanism, coagulation in which soot particle collide and form chain-like structure [2.52], [2.53]. Oxidation is another process in which soot particles react with available OH or O_2 molecules [2.54]. Incomplete combustion produces chemical species that lead to the development of PAH species, which are foundation molecules for engine particulates [2.55]. These particulates are consumed by OH radicals in the high-temperature diffusion flames around the circumference of the burning jet [2.56]. Optical diagnostics and physical probing techniques can be utilized to study soot formation and oxidation in diesel engines. Optical diagnostics techniques involve two colour method, techniques based on light scattering theory and laser-induced incandescence (LII). In this section diesel engine soot formation studies with two color method and laser induced incandescence will be discussed.

Miyamato et al. [2.57] investigated the effect of oxygenated additives on the combustion and emissions in direct injection diesel engine using a high speed camera for full field two color temperature and KL factors. Results from this study showed that the KL factor decreased during combustion while flame temperature distribution was not affected by the addition of oxygen additives. Kobayashi et al. [2.58] also measured full-field two color temperature and KL factors in a single-cylinder diesel engine with optical access in the piston. Experimental was done at a fixed engine speed of 1000 rpm with a high-pressure injection system. Results showed that high temperatures in the central portion of the combustion chamber. High KL factors were observed at the end of spray plumes and these regions contributed to exhaust emissions [2.58]. Choi et al. [2.59] conducted an optical analysis to study the effect of multiple injections on the combustion process of heavy-duty diesel engine. Optical engine experiments were conducted using an endoscope device and flame temperature, and soot density were calculated from combustion images. Based on combustion images, the combustion period can be divided into two sections. During the first half of the combustion period, flame propagation occurred and the soot formation rate was higher than the soot oxidation rate therefore increasing soot density. The high PM due to pilot injection is due to high soot density at the beginning of fuel combustion. The post-injection lowered the peak flame temperature and enhanced soot oxidation resulting in low NOx and PM emissions [2.59].

Flame lift-off length of the diesel jets strongly influences the soot formation rates in diesel engines. It is dependent on various factors such as ambient temperature, injection pressure, ambient density, oxygen concentration, fuel cetane number, and nozzle diameter [2.60]. Increasing the lift-off length reduces the equivalence ratio of the premixed vapor fuel and air mixture therefore reduce soot emissions [2.55], [2.56], [2.60]. After the lift-off length oxygen entrained into the jet is consumed by diffusion flame. Hence the engine design and operating parameters affect the soot formation and oxidation processes in diesel engines [2.60]. Soot particles, which are produced when burning diesel jets reach high temperatures in fuel-rich combustion areas, account for a sizeable portion of the particulates in CI-engines [2.55]. In CI-engine, mixing controlled combustion flame structure plays an important role in the formation of soot [2.56], [2.61]. The formation of soot particles in diesel engines takes place at a temperature in the range between 1000K – 2800 K and pressure in the range between 50 and 100 atm with adequate air required to burn fully all fuel [2.62]. The adiabatic flame temperature in air for typical diesel combustion traverses both soot and NOx formation regions [2.61], [2.62]. According to the conceptual model of diesel combustion according to Dec and co-workers based on LII measurements, the fuel and air first react in the rich mixture (~ ϕ=4), and then the combustion progresses and completes in stoichiometric diffusion flame (ϕ =1) Figure. 2.3 Initially, the fuel and air react in a fuel-rich charge, which leads to the formation of soot precursors, later on, this rich charge burns in high-temperature diffusion flame at the jet periphery, which leads to the formation of NOx emission (Figure 2.3) [2.61], [2.62]. Products of these fuel-rich reactions at the leading edge of the jet shown in Figure 2.3 are largely C_2H_2, C_2H_4, C_3H_3 fuel fragments, CO, and H_2O [2.63], [2.64], [2.65]. The highest particulate concentration is found in the core region of fuel spray, where the average equivalence ratio is very high. More details about the fundamentals of soot formation in flames are available in studies [2.52], [2.53],[2.66].

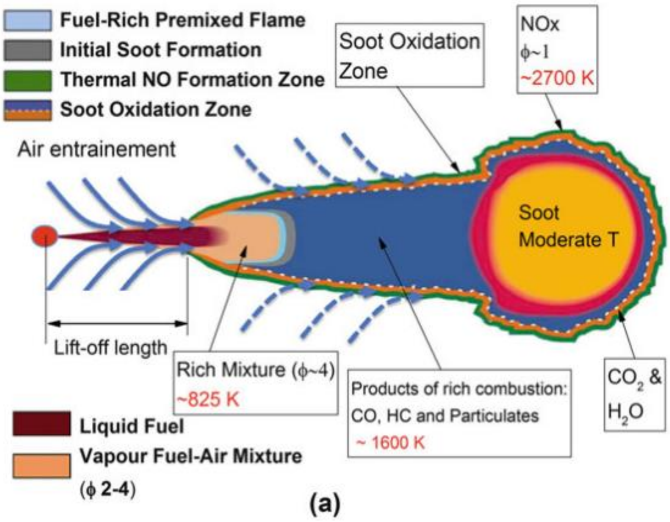

Figure 2.3. Soot Formation in Diesel Combustion [2.55]

Experimental measurement suggests PAH appearing in the fuel-rich premixed combustion region and a large number of soot particles detected in the head vortex. Nucleation is triggered during combustion when PAH molecules commence condensing into small clusters. Soot precursor distribution is throughout the interior of the combustion zone. Larger soot particles exist downstream in the rich “head vortex” zone [2.61], [2.63]. Combustion diagnostics study shows that the product of rich combustion produces the species that causes particulate formation in the interior of diffusion flames [2.65]. Flame lift-off length plays a vital role in the formation of soot in CI-engine [2.61], [2.67]. Most of the surrounding air entrainment into the jet is through flame lift-off length. It depends on ambient temperature (cylinder gas), density, injector orifice diameter, injection pressure, and oxygen concentration. Penetration of the liquid phase fuel is needed to promote fuel and air mixing; however, it may also lead to higher emissions if liquid fuel impinges and collects on the piston bowl wall [2.68]. During the initial soot formation, the precursors transform into solid-phase particles (because of carbonization). Consequently, the size of primary particles increases due to surface growth, and aggregation leads to the formation of larger aggregates having complex fractal structures. Few soot aggregates show a long-stretched chain-like structure, whereas some soot aggregates depict compact structures [2.69]. Matured primary soot particles have an onion-like structure in which the graphitic layers are oriented nearly parallel to the particle surface [2.70], [2.71]. Jiang et al. [2.72] investigated the soot morphology and nanostructure along the axial direction in diesel spray jet flames. The TEM images of soot particles sampled along the spray flame axis are shown in Figure. 2.4 (a). The distance of the sampling position from the nozzle is shown on the top left side Figure. 2.4 (a). The primary particle diameter distribution at distinct axial locations is shown in Fig. 4(b). Figure 2.4 (a) depicts that the upstream locations show small transparent and large "liquid-like" particles; therefore, the diameter distribution peak moves towards the large value side (Fig. 4(b)). Additionally, the averaged primary particle diameter (presented via discontinued line) declines from upstream to downstream (Figure 2.4 (b)). Their results indicate in the upstream zone; higher liquid-like particles are formed from the reactive coagulation of PAHs, which are generated during the pyrolysis of fuel [2.72]. Whereas in the case of the up-to-middle stream, several tiny-sized soot particles bloat on the liquid particle surface, and PAH depletes around these particles. This reduces the averaged primary particle size [2.72]. In the case of middle-to-downstream, due to higher ambient temperature, the soot particles oxidized; thus, the primary diameter of the soot particle still decreased [2.72]. The soot formation in diesel engines can be suppressed by achieving low combustion temperature combustion by utilizing a high amount of EGR. In the low-temperature range, the soot-forming reactions through PAH – PAH collisions are suppressed [2.73].

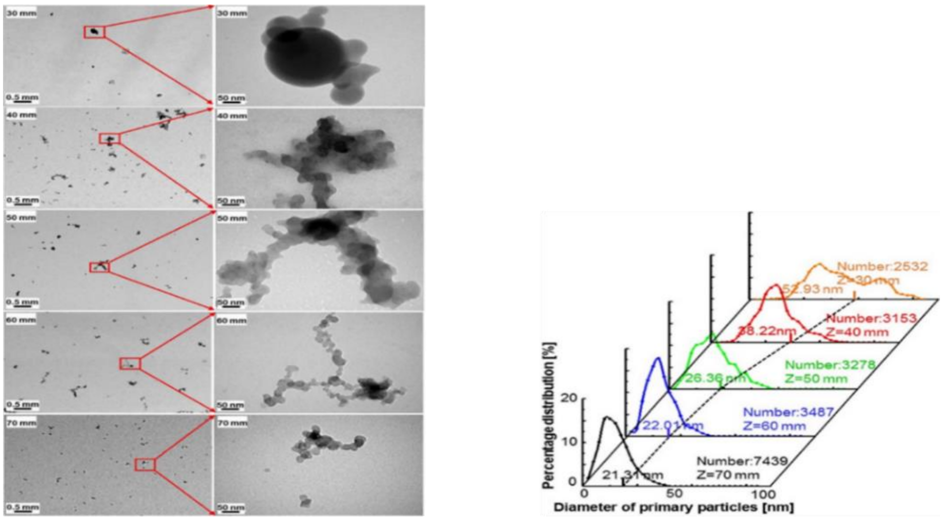

(a) (b)

Figure. 2.4 (a) TEM images of soot particles, (b) Primary particles diameter distribution at various axial locations [2.72]

Particle size distribution from diesel engine is shown in Figure 2.5 [2.74]. The benefit of plotting PSD with a normalized axis depicts the particle concentration of any diameter proportional to the area below the curve within that range [2.74]. The total area below the trace indicates the total PN concentration. The PSD follows the bimodal or trimodal lognormal distribution, in which the first, second, and third peaks depict the NMPs, AMPs, and coarse mode particles, respectively [2.74]. The lognormal distribution can be explained by assuming that fragmentation occurs in addition to coagulation [2.74], [2.75]. NMPs are mainly liquid particles, which are usually smaller than 50 nm diameter [2.74], [2.75]. These nanoparticles are mainly composed of water, sulfuric acid, and hydrocarbons [2.76], [2.77], [2.78]. Khalek et al. [2.79] used a dilution residence chamber to measure the growth of diesel nanoparticles and found that the growth rates were proportional to mainly hydrocarbon and sulphate condensation on primary nuclei [2.79]. When the exhaust gas is diluted and cooled supersaturation of semi volatile compounds leads to nucleation or condensation [2.79]. Shi et al. [2.80] found that the particle size distributions are sensitive to dilution conditions. They pointed out that conditions of high dilution ratio and high relative humidity favor the formation of nucleation mode particles of sizes less than 50 nm. Previous studies have shown that the formation of NMPs is related to high sulphur or high hydrocarbon content in exhaust gases during combustion [2.76], [2.77], [2.78]. The nanoparticle formation mechanism is the nucleation of sulfuric acid and water followed by particle growth by condensation of organic species. The formation of NMP relies on the rates of nucleation, condensation, and adsorption, which is a non-linear function of saturation ratio [2.74], [2.79]. Tobias et al. [2.76] used a thermal desorption particle beam spectroscopy to study nanoparticles chemical composition (mass median diameter 25-60 nm). Branched alkanes and alkyl-substituted cycloalkanes from unburned fuel and lubricating oil contribute to diesel nanoparticle mass. Sulfuric acid was also detected in this study as a few percent of the total nanoparticle mass [2.76]. The formation of NMPs can be described by two theories, i.e., ion-induced nucleation and homogeneous nucleation, most likely binary of sulfuric acid and water [2.81], [2.82]. In modern CI-engines, a smaller surface area is available for the adsorption of vapours making the formation of NMPs more likely. Around 85% of the number concentration and 0.1–10 % of the engine out particulate mass are found in NMPs [2.74]. AMPs range in size from roughly 50 nm to 500 nm. These particles comprise carbonaceous soot agglomerates with condensed volatile material on the core [2.74]. These particles are non-volatile and their measurement is independent of sampling conditions; therefore, the measurement is easy to reproduce [2.74]. Coarse mode particles consist of deposited particles that reenter in a full-flow dilution tunnel [2.74].

Particle size has a direct effect on the residence time of the particle in the environment. Larger diameter particles have lesser residence time, whereas smaller diameter particles are suspended for more time in the environment due to lesser particle mass. Additionally, particle size also affects the optical properties and surface area of the particles. Particle number and surface area have a direct impact on the human respiratory system. Correlation of particle surface area to inflammatory response has been found in the studies [2.83], [2.84], [2.85]. Xue et al. [2.85] investigated the correlation of two in vitro toxicological assays with PM mass and a number of real-time metrics based on PSD measurements. Their results indicate that assessing the mass or number of AMPs had better correlated metrics with in vitro toxicity. Additionally, they have reported that ultrafine particles are a poor indicator of the toxicity markers. Thus, the gravimetric PM mass and solid particle number metrics used in the United States and Europe appear to be well aligned with reducing the health impacts of vehicle-emitted PM. Hence it is important to study the particle size and number characteristics.

As discussed above, particle number concentration and PSD are measured using particle measuring equipment such as Scanning Mobility Particle Sizer (SMPS) and Electric Low-Pressure Impactor (ELPI), Differential Mobility Spectrometer (DMS), and the Engine Exhaust Particle Sizer (EEPS). Both DMS and SMPS measure particle size by charging the particles and then sizing by electric mobility but DMS detects particles electrically, while SMPS detects by condensation particle counter [2.86]. Particles emitted from the CI-engine consist of several volatile organic fractions and solid particles and distinguishing between volatile and solid particles in the aerosol is challenging during particle measurement. In the European Union (EU), the solid particle number emission having diameter > 23 nm has been regulated since 2011 (in Euro 5b) for light-duty diesel vehicles and gasoline direct injection (GDI) light-duty since 2014 (Euro 6). The measurement of solid particles requires dilution of exhaust gases in the dilution tunnel with constant volume sampling. In PMP (particle measurement protocol), the sample of exhaust gas is diluted with air to obtain stable measurements and then passed through a thermal conditioning device i.e., evaporation tube. To ensure repeatability in number counting, the removal of volatile organic fractions is required since these particles exhibit different characteristics under different sampling conditions [2.87].

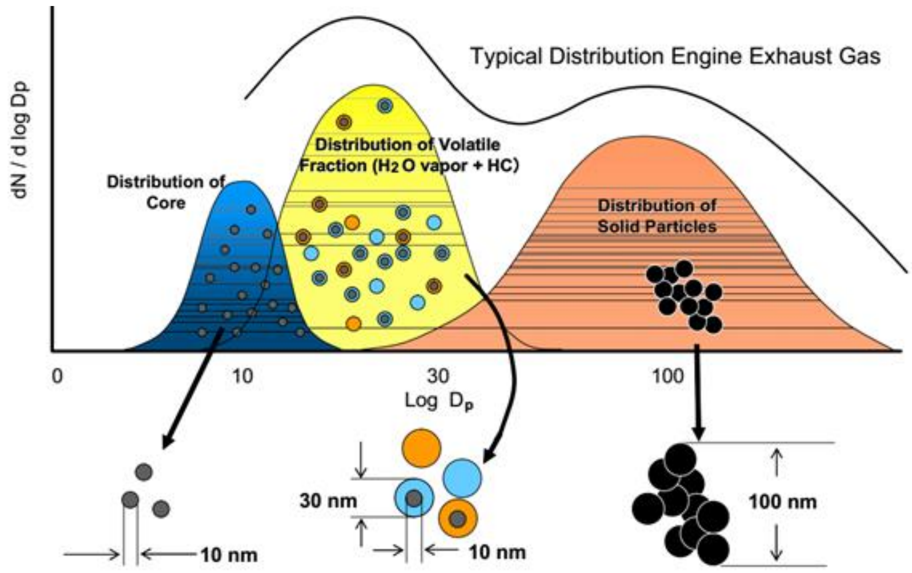

Figure 2.5 Hypothetical model for diesel nano-particles distribution [2.87]

2.3.1.2 Computational Studies

This section reviews the previous literature related to soot particle size modelling studies in diesel engine combustion. Because experimental study of soot in diesel engines is more expensive in terms of lead time, predictive capabilities through simulations offers a more profitable alternative. Simulation also provides a more in-depth understanding of the combustion process in terms of the spatial and temporal evolution of each chemical species, temperature, and velocities. Increasingly strict emission regulations necessitate a good modelling framework and the capacity to forecast incylinder combustion and emission characteristics. Aside from soot mass, the recent addition of legal constraints on soot particle number density necessitates accurate numerical models capable of forecasting particle dynamics.

Quantitative and qualitative prediction of soot formation and oxidation in diesel engines can be done through four type of modelling approaches: empirical models [2.88-2.89], semi-empirical models [2.90-2.91], phenomenological models [2.92], [2.93], [2.94] and, detailed soot models [2.95 -2.96]. The empirical soot models employ the correlation of experimental data for soot mass numerical calculations. Semi-empirical models calculate the functional relationship between in-cylinder soot and time based on physical processes and parameters such as soot particle number density, species mass fraction, and soot volume fractions [2.91]. The soot particle size classes are however neglected by these models. These models solve the rate equations for soot particle formation and oxidation [2.89 – 2.90]. These are used in engine CFD codes with changes in activation energy parameters [2.97-2.100]. The phenomenological soot models predict the intermediate species between the conversion of fuel to soot [2.101-2.104]. These models also include various particle formation processes such as soot particle nucleation or inception, particle coagulation, surface growth, and oxidation [2.101-2.104]. Additionally, they also include chemical reaction rates for intermediate chemical species formation and oxidation. Such models have been successfully employed in engine CFD codes [2.101-2.104]. In such multi-step phenomenological models, detailed chemical kinetic mechanisms are employed to predict intermediate soot precursor species such as acetylene and PAH. Physical and chemical phenomena for soot particle formation and oxidation were also included in these models. Soot parameters such as particle number density and mass can be calculated by solving the transport equations [2.104 – 2.105].

In detailed soot models complete description of particle size distribution function is provided. In these models, chemical kinetics is coupled with the soot particle dynamics. Therefore, these models provide more details about the soot parameters relevant to engine operating conditions. This requires an efficient particle dynamics model and detailed soot chemistry. They are of three types: (1) Stochastic method [2.105 -2.106] (2) Sectional method [2.107-2.108] and (3) Method of moments [2.109 – 2.110]. In the stochastic method growth molecules and particles are tracked using Monte Carlo methods [2.105 – 2.106]. In these three detailed soots models stochastic method is most accurate for predicting soot particle dynamics [2.105 – 2.106]. It assumes a certain number of stochastic particles and handles the particle dynamics with probability methods. These detailed soot models estimate the global soot quantities such as mass, number density, volume fraction, and surface area. In addition to these quantities, these models also reveal the soot's physical and chemical properties such as morphology and chemical composition [2.95]. However computational cost increases when this method is coupled with CFD codes. In the literature, this method is only used as a post-processing tool to investigate the distribution of soot particles in the direct injection engine exhaust [2.111]. Sectional method is another detailed soot modelling technique [2.107-2.108]. In this method, discretization of particle size distribution function is performed into number of sections and then the population balance equations are converted into coupled ordinary differential equation. The time evolution of particles is then calculated with these coupled ODE in each section to obtain the particle size distribution function. This method is simple to use in CFD codes but large number of sections are required to obtain the complete particle size distribution function which results in high computational time and hence not adaptable for computational fluid dynamic engine simulations [2.112-2.113].

A detailed soot model was developed by Frenklach and Wang which operated on method of moments [2.109-2.110]. Methods of moments is lucrative method for detailed soot modelling due to its high computational efficiency [2.114-2.115]. In method of moments the PBE is transformed into moment equations and only few moments describe the soot particle characteristics such as number density and mass [2.109-2.110]. By knowing the moments, the particle size distribution can be estimated [2.109- 2.110]. This method has been successfully implemented in engine CFD codes for the prediction of soot particle size, mass, and number [2.116- 2.121]. A study implemented a method of moments in KIVA CFD code to estimate the soot particle formation and soot particle transport process. This model employed skeletal chemistry for n-heptane combustion and connects acetylene chemistry to the soot particle inception process. The results for the soot mass predicted agreed with experimental results for varied injection timings and two EGR levels [2.116]. In another study soot and PAH modelling was done with the method of moments. The spatial distribution of PAH concentration and important chemical species relevant to soot formation were investigated by coupling a detailed chemical kinetic model with a three-dimensional fluid dynamic model [2.117].

2.3.2 Particulate Formation in RCCI Engine

Dempsey et al. [2.122] investigated the particle size distribution from RCCI combustion employing a single-stage micro dilution tunnel system along with PMP style two-stage dilution system. Large number of nucleation mode particles were observed from single-stage dilution tunnel operating at a temperature greater than 150℃. These particles were reduced with a second stage of dilution and heating confirming their volatile nature and organic carbon chemical composition [2.122]. Prikhodko et al. [2.123] compared the particulate matter characteristics of conventional diesel, RCCI, and PCCI combustion at fixed engine operating conditions. It was found that RCCI combustion mode generated lower particle emissions as compared to CDC and PCCI combustion mode and PSDs for RCCI showed a large fraction of nucleation mode particles. Figure. 2.6 shows the PSD characteristics of conventional diesel, PCCI, and RCCI combustion at fixed engine operating conditions. Filter collected sample showed evidence of the presence of volatile particles in RCCI exhaust (Figure. 2.7) [2.123]

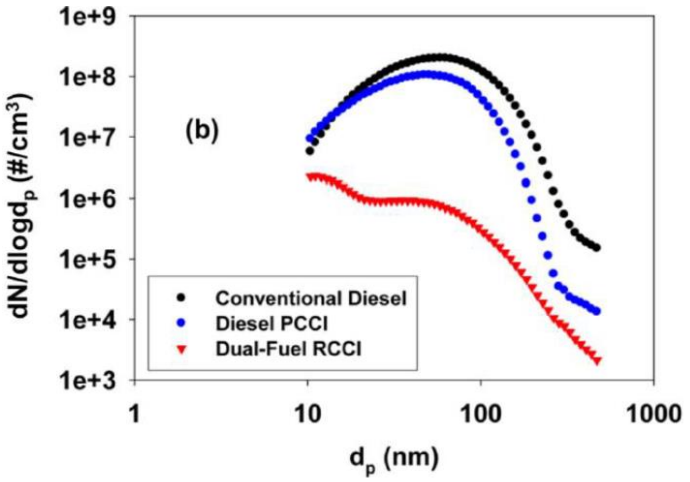

Figure. 2.6 PSD comparison between CDC, diesel PCCI, and RCCI at 2300 rpm and 4.2 bar IMEP [2.123]

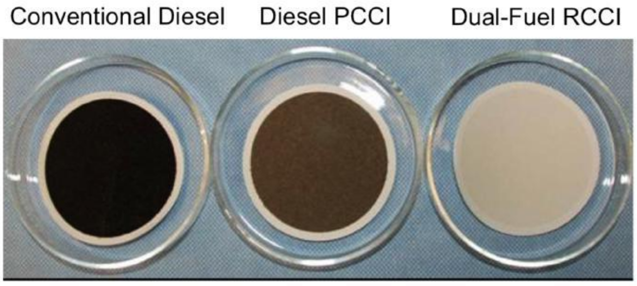

Figure. 2.7 Comparison of filter collected samples for conventional diesel, diesel PCCI, and dual fuel RCCI combustion [2.123]

Kolodziej et al. [2.124] conducted RCCI engine experiments with direct cylinder injection of both fuels. The results demonstrate a bimodal PSD for RCCI that is sensitive to both the gasoline/diesel ratio and the SOI of the gasoline. Additionally, it was shown that the particle concentration for RCCI was lower than for LTC combustion. It was found that the accumulation mode particle concentration increased significantly when gasoline injection timing was advanced from 340° bTDC to 360° bTDC, which may suggest that the large amount of accumulation mode particles seen was related to insufficient mixing or pool firing associated with direct injection of gasoline under low-pressure conditions [2.124]. Storey et al. [2.125] investigated PSD sensitivity to fuels with three combinations of fuel sets: diesel- gasoline, diesel- E 85 (85% ethanol + 15 % gasoline), and B20 (20% biodiesel + 80% diesel) – gasoline. It was found that RCCI PSD was insensitive to fuel properties [2.125]. Benajes et al. [126] investigated the dual mode dual fuel combustion concept that combines fully and highly premixed RCCI regime for low and medium engine loads and changes to dual fuel combustion at greater engine loads. The highly premixed reactivity-controlled compression ignition regime showed a transitional particle size distribution with peaks of mobility diameter around 20 nm and 80 nm. It was discovered that fully premixed RCCI combustion was dominated by small particles (less than 30 nm in diameter) and that the dual fuel dual mode displayed larger-sized particles similar to diesel soot particles, which are nearly 100 nm in mobility diameter [2.126]. Zhang et al. [2.127] used a thermodenuder to remove volatile organic components from engine exhaust a study used a thermodenuder. The peak of the particle size distribution migrated to the 10 nm particle size range in modern LTC combustion techniques like HCCI and RCCI, although particles with a size range of 20 nm to 50 nm can still be efficiently eliminated using a high dilution ratio and a thermodenuder. Contrary to these findings, the CDC particle size distribution held steady at both high and low dilution ratios with thermodenuder. In the HCCI and RCCI combustion techniques, nucleation mode particles made up a significant portion of the total particle number concentration [2.127].

Gracia et al. [2.128] investigated particulate emissions of a modified medium-duty engine working in dual mode dual fuel combustion concept to maintain ultra-low NOx and very low soot emission generation on RCCI combustion mode. The study found that premixed RCCI combustion generated particles between diameter 5nm and 40 nm. In a diffusion combustion regime, larger particles around 80 nm and 200 nm consisting of solid black carbon are generated due to fuel-rich incylinder charge and higher temperature that decreases the gas-to-particle conversion [2.128]. RCCI combustion mode generated a particle mass of around 4 mg/kWh due to premixed combustion while diffusive combustion mode generated a particle mass of around 50 mg/kWh [2.128]. Agarwal et al. [2.129] compared the particulate matter characteristics of CI, PCCI, and RCCI combustion strategies on a single-cylinder diesel engine. A significant result of this study was the relatively higher concentration of accumulation mode particles (AMP) compared to nucleation mode particles (NMP) in the exhaust of the RCCI combustion. In comparison to other combustion techniques, it was discovered that the RCCI combustion approach was dominant in the reduction of PM and NOx [2.129].

Fang et al. [2.130] investigated the PM emissions from a modified single-cylinder diesel engine operating in RCCI and conventional diesel combustion (CDC) modes under controlled dilution settings [2.130]. Low reactivity fuels 150-proof hydrous ethanol and gasoline were utilized to examine how the fumigated fuel affected the PM emissions. According to this research, PM from RCCI combustion is more susceptible to changes in dilution conditions than PM from traditional diesel combustion using a single fuel. Semi-volatile organic compounds made up the majority of RCCI PM, with solid carbonaceous particles making up a lesser portion. For RCCI combustion, the characteristics of the PM emissions were significantly influenced by the fumigated fuel. The RCCI PM powered by hydrous ethanol had a higher percentage of volatile compounds and was more sensitive to changes in dilution conditions [2.130]. Agarwal et al. [2.131] compared the particulate size, mass, and number characteristics of CI, PCCI, and RCCI combustion strategy [2.131]. This study found that the PCCI combustion strategy emitted higher particle concentration at low loads as compared to conventional CI combustion. A comparison of particle sizes of different ranges shows that the RCCI combustion strategy emitted larger particles and CI and PCCI strategies emitted significant amount of smaller-sized particles (NPs and NMPs). Among all combustion strategies, conventional CI combustion emitted the highest TPN concentration in which the concentration of AMPs was dominant. This study found that the PCCI combustion strategy emitted higher particle concentration at low loads as compared to conventional CI combustion. A comparison of particle sizes of different ranges shows that the RCCI combustion strategy emitted larger particles and CI and PCCI strategies emitted significant amount of smaller-sized particles (NPs and NMPs). Among all combustion strategies, conventional CI combustion emitted the highest TPN concentration in which the concentration of AMPs was dominant [2.131].

2.4 Particle Size and Number Characteristics of Diesel Engine

2.4.1 Effect of Engine Load and Speed

The particle size and number characteristics strongly depend on engine load, and particle GMD and total number concentration increase with an increase in the engine load according to previous studies [2.132 – 2.139]. The reason for this effect is due to more amount of fuel is injected inside the combustion chamber at a higher engine load, which increases the soot precursor concentration in rich premixed combustion and increases the formation of particles. High temperature accelerates the agglomeration process, which increases the particle GMD [2.132]. On the other hand, higher engine speed caused to decrease in the particle GMD and an increase in the total PN concentration [2.133], [2.139]. At higher engine speeds more particulate is generated and hence the total number concentration increases [2.133], [2.139]. GMD of the particulates decreases with an increase in engine speed as particles have less residence time in the combustion chamber and exhaust system to agglomerate and coagulate.

2.4.2 Effect of Injection Timing and Injection Pressure

The diesel injection events such as injection timing, fuel injection pressure, and the number of injections significantly influence the combustion characteristics which causes variation in particle formation in the CI engine. Advance or retard injection timing leads to changes in the cylinder pressure and temperature at the time of fuel injection, affecting the combustion parameters such as ignition, peak pressure, combustion phasing, etc., leading to the variation of combustion characteristics and particle formation in the combustion chamber. Advanced diesel injection timing leads to longer ignition delays, which increases the availability of timing for the mixing of fuel and air [2.140]. In the literature, no definite trend is found between injection timings and particle number emissions [2.140 – 2.149]. Xu et al. [2.142] found that retarded injection timing at low load results in decreased concentration of AMPs due to better-premixed combustion, while at higher load, number concentration of AMPs increases [2.142]. Li et al. [2.143] reported that the concentration of AMPs increases when the diesel injection timing is retarded from -23° aTDC to 0° aTDC. Too retard diesel injection (after TDC) leads to a decrease in the concentration of AMPs [2.143]. Zhu et al. [2.144] found that advanced injection timing from 20° to 23° bTDC results in decreased particle emissions. Further advanced injection timing leads to an increase in particle concentration [2.144]. Geng et al. [2.147] found that the number concentration of ultrafine particles first decreases and then increases when injection timing was advanced from 2° to 18° bTDC at low loads while ultrafine particle number concentration decreased at medium and high engine loads [2.147]. This phenomenon is due to an increase in cylinder temperature and large-scale production of OH radicals with advancing injection timing which supports particle oxidation and retard formation [2.149]. The count mean diameter of particulates decreases for advanced injection timing and increases for retarded injection timing [2.140].

Multiple fuel injection and post-fuel injection strategies are beneficial to reduce particle emissions [2.150, 2.151]. Li et al. [2.150] found that particle number concentration and mass increased when the pilot and main injection were used in multiple injection strategies, whereas particle number concentration decreased and reduced particle diameter was observed for pilot and post injections [2.150]. More intense diffusion combustion occurred for pilot and main injections, increasing the soot nuclei formation, and leading to higher particle mass and number concentration. The main and post-fuel injection strategy leads to increasing the in-cylinder temperature and enhancing the fuel-air mixing, which accelerates the rate of soot oxidation and results in decreased particle mass and number concentration [2.150].

Studies reported that increased injection pressure significantly reduces the AMP concentration and decreases the GMD of the particles [2.152 – 2.156]. This is due to an increase in lift-off length which increases air entrainment into the premixed reaction zone forming lean equivalence ratio zones inside the cylinder as a result decreasing soot precursors formation and enhancing soot oxidation [2.152]. Studies also reported that increasing fuel injection pressure at certain engine operating conditions resulted in an increased number of NMPs [2.154], [2.155]. The increase in NMPs is due to less surface area of carbonaceous fraction available for the adsorption of hydrocarbons, increasing the probability of a homogeneous nucleation process [2.157]. It is summarized that with an increase in engine load, the GMD and total PN concentration increases. No definite trend was observed between the injection timing and particle size and number characteristics. In some cases, with advanced injection timing, the concentration of AMPs decreases. With the increase in injection pressure, the GMD, total mass concentration, and AMPs decrease while the NMP concentration increases.

2.4.3 Effect of Exhaust Gas Recirculation

The use of exhaust gas recirculation leads to an increase in the GMD, particle mass concentration, and AMP concentration while the concentration of NMP decreases. This is due to the dilution effect of the EGR, which reduces the oxygen concentration inside the cylinder and increases the locally fuel-rich zones, which increases the rate of soot formation and reduces the rate of soot oxidation. The decrease in NMPs is due to an increase in AMPs which favours the condensation process.

2.5 Particle size and number characteristics of RCCI engine

2.5.1 Effect of engine load and speed

Previous studies also investigated the effect of fuel premixing ratio, engine load, diesel injection timing, and injection pressure on RCCI PM characteristics. With an increase in engine load, the accumulation mode particles (AMPs) and CMD of particles increase while engine speed has a negligible effect on particle size and number [2.158], [2.159], [2.160], [2.161]. An increase in AMPs with engine load is due to an increase in the mass of fuel injected at higher engine load, leading to fuel-rich regions in the combustion chamber and higher combustion. At higher engine load, the mass of fuel injected in the combustion chamber increases which increases the combustion temperature and high equivalence ratio zones inside the combustion chamber [2.158]. With the increase in engine speed, the concentration of nucleation mode particles increased in RCCI combustion mode.

2.5.2 Effect of Single and Double Injection Strategy

According to previous studies, total particle number concentration increased with advanced diesel injection timing in both single and double injection strategy [2.162-2.165]. Saxena et al. [163] investigated the effect of diesel injection timing for gasoline diesel RCCI combustion and found that accumulation mode particles contributed to particle mass. Diesel injection timing has no significant effect on the particle mass having diameter less than 20 nm. However, the mass of particles in the size range 20-300 nm significantly increases with advanced injection timing. Also, it was observed that particle mass increases with double injection strategy. With methanol diesel RCCI operation the total number of particle concentration decreased in comparison to diesel gasoline RCCI due to higher oxygen content of methanol [2.162-2.165]. A Study by the same authors also investigated the effect of direct injection timing and gasoline on nanoparticle emissions from diesel gasoline RCCI. It was found that advanced injection timing and increase in port injected gasoline mass produced high particle emissions. Also, a good correlation was found between premixing ratio, start of injection of diesel and novel parameter defined as premixed fraction of total heat release and particle emissions characteristics [2.163].

2.5.3 Effect of Premixing Ratio

According to most of the studies increase in the premixing ratio the total particle number concentration increases [2.166- 2.168]. Some studies reported a decrease in the concentration of nucleation mode, accumulation mode particle concentration, and total PN with an increase in the premixing ratio [2.159]. The number concentration of NMPs depends on the quantity of diesel fuel injected. Diesel fuel contains high boiling point hydrocarbons, which can escape the combustion and nucleate to form NMPs. On the contrary, some studies had reported an increase in NMPs and a decrease in particle size with an increase in the premixing ratio. It could be due to a reduction in combustion temperature and higher unburnt hydrocarbon emissions. These hydrocarbons form NMPs through homogeneous nucleation mechanism.

2.6 Particle Measurement Programme

The particle number regulation has been implemented since 2011 in European union. PN measurement procedure defined in ECE regulation No 83 requires detecting only solid particles by eliminating volatile particles, the concentration of which are highly influenced by dilution conditions, using a volatile particle remover. Particulate matter particle size distribution of engine exhaust is influenced by a number of factors:

engine condition, fuel and lube oil composition, exhaust system configuration, sampling system, and sampling condition. The measurement of nuclei mode particles which make up 90% of the particle number is difficult to replicate. The volatile material can condense on the soot particles and coagulation leads to a reduction number concentration but an increase in particle size. To obtain a repeatable and reproducible measurement of PN concentration, a regulation is adopted by UNECE GRPE (working party on pollution and environment) 2011 to measure only nonvolatile particles according to particle measurement protocol (PMP) [2.169]. This protocol regulates only nonvolatile soot particles of diameter greater than 23 nm. According to this protocol, a volatile particle remover is used for the measurement of solid particles. In volatile particle remover devices, aerosol emitted from the engine is diluted in a primary hot dilution system at a temperature of 150℃ followed by an evaporative tube maintained at a temperature between 300 – 400 °C to remove semi-volatile fraction followed by cold dilution. In this thermo-dilution process, heating brings the volatile species into the gaseous phase, and dilution decreases the vapor pressure below the critical required for saturation, thus, reducing the probability of renucleation. The conditioned aerosol containing solid particles is detected with a condensation particle counter (CPC) with a 50 % detection limit at 23 nm [2.169]. Figure 2.8 depicts the volatile particle removal processes in an evaporation tube (ET) according to the particle measurement program (PMP) protocol.

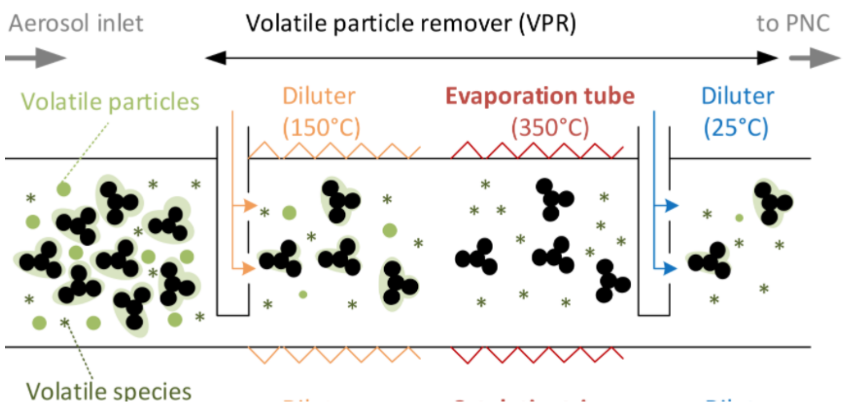

Figure 2.8 Schematic of volatile particle removal processes in evaporation tube (ET) according to particle measurement program (PMP) protocol [2.169]

Currently widely used VPRs include the evaporation tube (ET), thermodenuder (TD) and catalytic stripper (CS). In this study, thermodesorption system (TDS) is employed as VPR hence its design and development of thermodenuder (TD) is discussed in detail. TD works on the principle of thermo-desorption. The device consists of two sections, i.e., the desorber section (heating section) and the adsorber section (cooling section) [2.170], [2.171]. In the desorber section, engine exhaust aerosol is heated to evaporate all volatile components adsorbed on soot particles and volatile particles. The adsorber section consists of activated carbon, which removes the volatile components by diffusion. The TD operating temperature is fixed at 250 ℃, which is enough for the elimination of volatile particles. Solid soot particles have a lower diffusion velocity than the volatile species, which permits the desorber section to eliminate volatile species [2.170]. The schematic of volatile particle removal process by thermodesorption system is shown in Figure 2.9 [2.172]. TD performance depends on the temperature profile in the heating section, particle losses, and gas adsorption efficiency of activated carbon [2.170], [2.171]. The dimensions and internal construction (especially the surface of the adsorption part) are required to be selected carefully. Sharp temperature gradients should be avoided to reduce thermophoresis losses [2.171]. Adsorption rates depend on the operating temperature, pressure conditions, adsorbent material properties such as active surface area, and adsorbate gases [2.171], [2.173]. TD can effectively remove large volatile triacontane particles ($C_{30}H_{62}$) and their evaluation has shown that their performance can be repeatable [2.174]. A study found that thermodesorption system have high volatile removal efficiency for monodisperse 30 nm tetracontane (C40) hydrocarbons [2.175]. However, the efficiency of thermo-denuder may decrease with time due to the limited lifetime of activated charcoal. It was also found that thermo-denuder may introduce artifacts due to pyrolysis reactions [2.173, 2.174, 2.175]. Swanson et al. [2.176] reported tetracosane particles downstream of the TD with an estimated aerosol volume concentration range from 14 to 380μm^3. TD can be beneficial compared to PMP-ET as TD offers increased measurement sensitivity because it requires low dilution ratios for its operation.

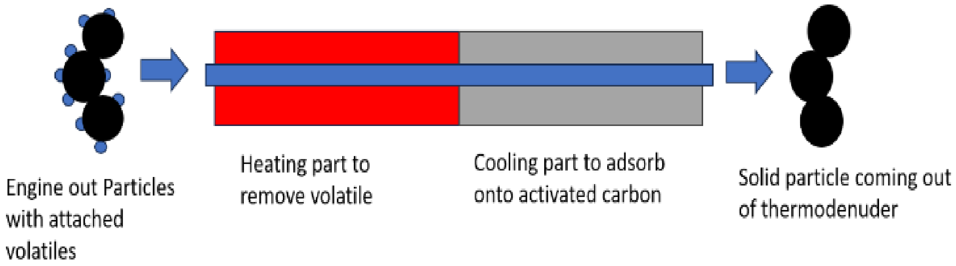

Figure 2.9. Removal of volatiles from particles after passing through thermodenuder [2.172].

2.7 Design and development of thermodenuder

This section presents the design and development aspects of thermodenuder (TD) briefly. Commercial TDS by Dekati consists of a heating section followed by an adsorption section containing activated carbon, which is either actively or passively cooled. Dekati TD operates on high sample flow rates and utilizes activated charcoal fiber for adsorbing volatile compounds. The length and width of this instrument were 95 cm and 22 cm, respectively. The cooling medium in the adsorber section was air or water. The main challenges with the current design are rapid temperature drop at the intersection of the heating and cooling sections. The Dekati TD is designed to be used in conjunction with an electric low-pressure impactor (ELPI) with a flow rate of 10–20 L/min. The recommended operating temperature for this device is 275°C [2.177]. It generally takes a longer time to reach operating temperature. Figure 2.10 shows the actual commercial Dekati TD consisting of the desorber section and adsorber section. The red curved part is the heater (Figure 2.10), called the desorber section and the steel tube contains charcoal paper for adsorption of volatile species that can be replaced very easily. This thermodenuder has been employed in steady-state engine experiments for diesel nanoparticle studies in laboratories. TSI low-flow thermodenuder is another commercial thermodenuder. This is a low-flow thermodenuder optimized for a flow rate of 0.2 lpm to 2 lpm and uses activated charcoal as an adsorbent. The temperature can be controlled in steps to achieve 400℃. Construction material is glass, ceramic, and stainless steel [2.178]. Fierz et al. evaluated the performance of commercial thermodesorbers and a hot dilution system [2.178]. The devices tested were TSI TDS, Dekati TD, Fraunhofer TD, and a hot dilution system. Penetration efficiency of these devices was measured using aerosol particles generated with a flame generator with a mean diameter of 50 nm. The laboratory test shows that all systems tested efficiently remove volatile material. Thermodesorbers fail at a very high concentration of volatile material; no such results have been observed for the hot dilution system. The losses in the thermodesorbers are significant at low flow rates. No reproducible results for losses could be obtained with the TSI thermodesorber. The hot dilution system tested showed high losses for 20 nm particles. The chassis dynamometer test at an operating point with an extremely high volatile fraction shows an efficient operation of dekati TD and hot dilution system. The efficiency of Fraunhofer TDS in removing the volatile material decreased after some measurement which was not observed in the laboratory tests. The drawbacks of commercially available TD are high particle losses inside the instrument and low residence time in the desorber section, leading to incomplete removal of volatile particles [2.170].

Figure. 2.10 Commercial Dekati TD [2.177] (Courtesy: Dekati)

The Burthser TD was designed to improve commercial TD and was used primarily for combustion engine experiments [2.170]. Burthser et al. [2.170] designed a thermo-desorption device with the heated section separated from the cooled section containing activated charcoal for adsorption of the volatile fraction. In their study, the operating parameters were determined theoretically and experimentally before studying exhaust particle size distributions. The desorber section or the heated section was made of stainless steel of length 50 cm and diameter 2 cm and was heated using a coaxial heating element, which increased the temperatures in steps up to 400°C. The adsorbent section consisted of a stainless-steel mesh housed in a cylindrical metal casing containing activated charcoal. The optimum flow rate in the device was 3 lpm. Optimization of the temperature profile in the heating section was not performed in this design. Park et al. designed and characterized thermo-denuder both experimentally and numerically [2.179]. Sodium chloride particles, toluene gas, and carbon black particles were used for evaluating the performance of the TDS. The temperature profile, penetration efficiency, and gas adsorption efficiency were used to evaluate the performance of the TDS.

Fiertz et al. developed a low-flow TD having three independent heaters at a flow rate of 0.315 L/min to improve the penetration of solid particles [2.180]. They incorporated a heated adsorption section as compared to the cooled adsorption section in the previous designs. The advantage of this design was the better temperature stability of the instrument and efficiently removed volatile fractions from solid particles in the entire adsorption section. With this device, the measurement of nonvolatile core particles of size 3 nm is possible due to low thermophoretic losses because of the heated adsorption section. The thermo-denuder developed by Huffmann et al. consisted of a heated tube (2.5 cm inner diameter, 55 cm long) kept at a constant temperature by a 3-zone controller, followed by a cooling zone with a diffusion tube lined with activated charcoal for adsorption of evaporated gases [2.181]. The main difference with this design was additional temperature control and reduced thermal mass for temperature stepping. An et al. [2.182] utilized the general designs of Burtscher et al. [2.170] and Wehner et al. [2.183]. They further developed a new thermo-denuder design that exhibits high-temperature stability, but low temperature-ramping speed due to its placement in a tube furnace. They investigated the role of residence time on particle evaporation. It was concluded that the thermodenuder could under-predict particle volatility by not allowing adequate time for mass transfer kinetics to act and approach equilibrium. At a flow rate of 1L/min, the aerosol residence time in the furnace is 15.8 sec, which is significantly longer than commercial instruments. The heating tube is fabricated from stainless steel with an inner diameter of 3.5 cm and a total length of 83 cm, but the actual heating length is only 55 cm. The adsorption/cooling section comprises two concentric stainless-steel cylinder with a length of 55 cm and an inner and outer diameter of 6 and 10 cm. Adsorption rate in the instrument is governed by operating temperature, pressure, the property of adsorbent material such as porosity, and active surface area. Ronko et al. [2.184] designed a TD with low solid nanoparticle losses. The flow range for this design was between 0-10 slpm to produce low residence time (0.51 sec in the heating section and 2.15 sec in the adsorbing section). High penetration of nonvolatile particles larger than 3 nm is achieved while maintaining high volatile particle removal efficiency for automotive exhaust applications. This TDs comprises of an evaporation tube (Inner Diameter of the tube = 8mm and length of the tube = 600 mm where sample flow was heated to 265°C followed by adsorbing section (Inner diameter of the mesh tube: 36 mm, Length of the mesh tube: 500 mm). Solid particle penetration was reported in the range 33 -68% for particle size in range of 3 - 10 nm. Thermophoresis is the main loss mechanism for particle sizes above 30 nm. Thermophoresis losses were observed independent of particle size in this design. Major design parameters such as instrument geometry, particle losses, operating temperature, and flow rate of laboratory-based thermodenuder are discussed in next subsections.

2.7.1 Temperature profile characterization

This section presents the temperature profile characterization of thermodenuder. Temperature profile characterization is required as the temperature profile inside the desorber section governs the residence time inside the thermodenuder and volatile particle removal efficiency. Uniform temperature profile inside the desorber section and optimum residence time inside the adsorber section is needed for the complete evaporation of volatile particles. Characterization of the temperature profile is also required to calculate thermophoretic losses inside the instrument. Thermophoretic losses govern the overall performance of the thermo-denuder. Thus, the calculation of these losses is significant from the design point of view. Stevanoic et al. [2.185] characterized the commercially available thermo-denuder and a diffusion drier. This device operated efficiently in a very confined flow rate range of 1L/min. Outside this flow range resulted in inhomogeneous temperature profiles. The reason for this inhomogeneous temperature profile is the: glass metal interface between the desorber section and adsorber section, different thickness of the heating section, and loosely packed heating tape. Increasing flow rate resulted in a distorted temperature profile. This was due to the low residence time of aerosol inside the heating section at high flow rates. Fierz et al. [2.178] evaluated the temperature profile inside the commercial TD (Dekati TD, TSI TD, and Matter hot dilution system. The results show that a temperature drop takes place at the start of the adsorber section as shown in Figure 2.11. This temperature drop can induce renucleation of volatile particles. As compared to commercial thermodenuders, a higher exit temperature at the end of the desorber section was obtained in the design of a laboratory-based thermodenuder. Figure 2.12 depicts that the exit temperature is much higher as compared to commercial thermodenuder and a comparison of temperature profiles obtained in different design concepts [2.170], [2.179], [2.183]. Wehner et al. performed the optimization of the temperature profile in the heating section [2.183]. The exit temperature with this design was higher than the previous design by [2.158], which prevents the renucleation of volatile species as shown in Figure 2.12. The improved insulation composed of the fine sand and the ceramic plates reduced thermal diffusion from the heating section resulting in a uniform temperature profile.

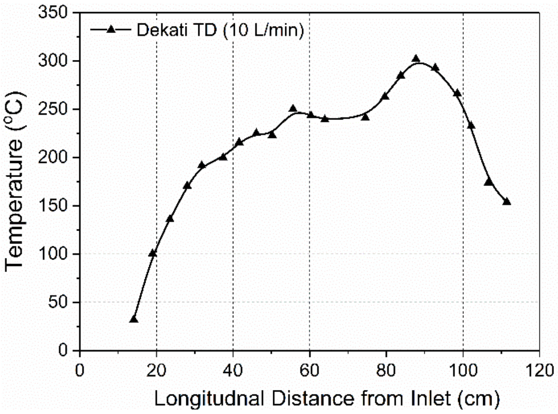

Figure 2.11 Temperature profile inside heating section of commercial Dekati thermodenuder (adapted from [2.178]).

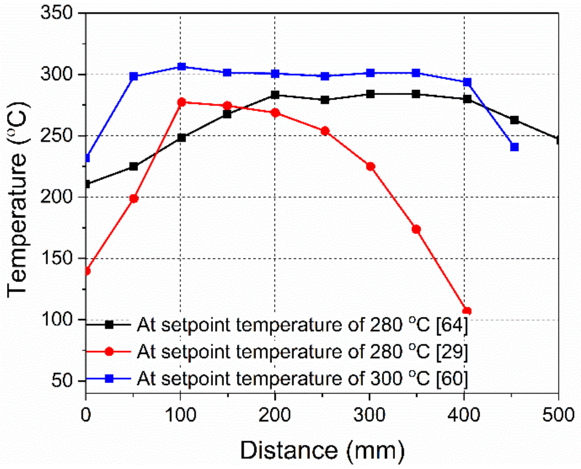

Figure 2.12 Comparison of temperature profiles inside the heating section of different designs of thermodenuders (adapted from [2.170], [2.179], [2.183].

2.7.2 Performance parameters

Performance parameters used to characterize the design of thermo-denuder and catalytic stripper are penetration efficiency and volatile removing efficiency. Particle losses inside the thermo-denuder are generally due to thermophoresis and diffusion, which decreases the transportation efficiency of particles. Moreover, the calculation of these losses is required for the determination of particle concentration reduction factors (PCRF). In this section, the performance parameters of the volatile particle remover are discussed. The genesis of particle losses in the conditioning devices and empirical equation from the previous literature used for the theoretical determination of these losses are discussed.

2.7.2.1 Solid particle penetration efficiency

Solid particle penetration efficiency measurements are performed with aerosol particles generated with a flame soot generator (CAST). The CAST particles resemble the engine exhaust particles [2.186]. The particle losses in the conditioning devices can be due to sampling and transport processes. Losses due to sampling include an iso-axial and isokinetic exhaust gas sample extraction at the sampling point in the measurement systems. Losses due to transport include losses due to internal processes like (agglomeration) and external processes (like diffusion and thermophoresis). The effect of each loss process is defined in terms of particle penetration efficiency [2.186]. Particle penetration efficiency (P), is defined as the ratio of particle concentration (downstream) at the outlet of the conditioning device to the upstream concentration at the inlet of the conditioning device measured with a particle number counter [2.186]. Particle penetration fraction in the conditioning devices can be determined both theoretically and experimentally. The total penetration efficiency through the sampling system is the product of the penetration fractions for each deposition mechanism (thermophoresis and diffusion) [2.186]. Penetration fraction can be calculated by given Eq. (2.2) [2.186].

$$Penetration\ (P) = \frac{N_{downstream\ (d_p)}}{N_{upstream}(d_p)} \tag{2.2}$$

Where $N_{downstream}$ is the particle number concentration downstream of the conditioning device (VPR) measured with particle number counter (PNC), $N_{upstream}$ is the number concentration upstream of the conditioning device (VPR) measured with particle number counter and d_p denotes the particle diameter. The diffusion losses are size-dependent, while thermophoretic losses are temperature dependent. Losses in the devices are given by Eq. (2.3) [2.186].

$$L_{di} = 1 - P \tag{2.3}$$

Where L_{di} denotes the particle losses and P is the particle penetration fraction. The theory and empirical equation required for the calculation of these losses are discussed below.

(a) Diffusion Losses

Thermophoresis and diffusion are dominant mechanisms for ultrafine particle losses in thermodenuder and catalytic stripper. Inertial deposition losses also occur in flow constrictions and bends in tubes. However, these losses are very small and therefore not significant for small particles. Hence only the theory of these losses is discussed. Figure 2.13 shows the mechanism of particle losses occurring during exhaust aerosol transport in the transport tube to the measuring instrument.

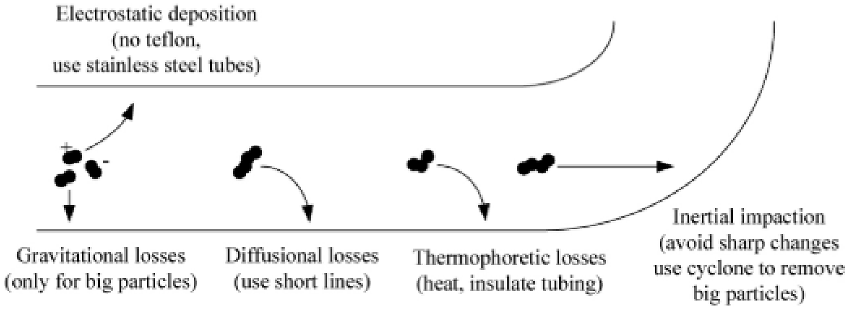

Figure 2.13. Mechanism of particle losses occurring during the sampling of ultrafine particles from diesel engines [2.186].

Ultrafine particles suspended in the fluid motion perform Brownian motion, which results in fluctuating forces exerted on them from surrounding gas molecules [2.187]. This caused the net movement of the particles from high concentration to low concentration called diffusion. Brownian motion or diffusion can bring particles suspended in gas to tube walls. Smaller particles diffuse faster than larger particles hence these losses are significant for particles smaller than about 50 nm in diameter [2.188]. To minimize particle losses due to diffusion and inertial deposition laminar aerosol sampling is recommended [2.188]. Diffusion losses depend only on the flow rate and length of the tube. These losses are independent of tube diameter for laminar flow conditions. Taking into account diffusion losses inside the tube, particle penetration efficiency denoted by P_{diff} for diffusion losses through the straight tube is given by Eq. (2.4) and Eq. (2.5) [2.188].

$$P_{diff} = 1.256\,\varepsilon^{\frac{2}{3}} + 1.2\,\varepsilon + 0.177\,\varepsilon^{\frac{4}{3}} \tag{2.4}$$

for $\varepsilon < 0.02$ and

$$P_{diff} = 0.189\,exp(-3.657\varepsilon) + 0.097\,exp(-22.3\,\varepsilon) + 0.032\,exp\,(-57\varepsilon) \tag{2.5}$$

for $\varepsilon > 0.02$

Where ε = ΠDL/Q is a dimensionless deposition parameter; 'D' is the diffusion coefficient of the particles, 'L' is the length of the tube in meters, and 'Q' is the volumetric flow rate (m^3/sec). To increase transport efficiency, 'ε' should be kept small by keeping the transport and distance 'L' smaller or by increasing the flow rate 'Q' [2.188].

Diffusion coefficients of the particles can be calculated from Eq. (2.6) [2.188]

$$D = \frac{K_B \times T_{gas} \times C_c}{3 \times \pi \times d_p \times \mu} \tag{2.6}$$

Where 'K_B' is the Botlzmann constant, 'T_{gas}' is the exhaust gas temperature, 'C_c' is the Cunningham slip correction factor, 'd_p' is the particle diameter in nm, and 'μ' is the viscosity of surrounding gas. To incorporate this effect of slip boundary condition, the Cunningham slip correction factor is incorporated in equation (2.6). Cunningham slip correction factor can be calculated using equation (2.7). As the typical particle size distribution of diesel engine exhaust has peaks between 40 and 70 nm, sizes are almost comparable to or even smaller than the mean free path of gas molecules in the ambient. Larger particles will collide with the gas molecules, while smaller particles will slip through gas molecules. Particles < 100 nm fall in the slip regime, and a corresponding C_c in Eq. (2.7) must be used.

$$C_c = 1 + 2.52\,\frac{\lambda}{d_p} \tag{2.7}$$

Where 'λ' is the mean free path of gas molecules, d_p is the particle diameter in nm.

Thermodenuders suffer diffusional losses due to the additional length of the desorber section containing activated charcoal. In optimized designs, these losses are minimized by reducing the length of the desorber section [2.186].

(b) Thermophoresis losses

Thermophoresis is a physical phenomenon in which aerosol particles move toward the direction of decreasing temperature when subjected to a thermal gradient [2.188]. Figure 2.14 shows the thermophoresis deposition mechanism for soot particles [2.189]. In the thermo-denuder heating section, the thermophoretic force will favor the focusing of the particles in the center of the tube, since the tube wall is hotter than the aerosol flow. Once the flow equals the temperature of the tube wall the thermophoretic force ceases to exist. At the exit of the heating section, the tube walls cool down faster than the gas, creating a temperature differential that enhances particle deposition. The thermophoresis force can be significant for sub-micron sized particles such as soot particles emitted from diesel engines, where the temperature gradient exceeds 10 K/cm. Lin et al. [2.190] developed a semi-empirical equation for penetration efficiency for thermophoresis losses denoted by P_{therm} for laminar gas flow inside a tube given by Eq. (2.8).

$$P_{therm} = 0.783 \left(\frac{Pr\,K_{th}}{\theta^*}\right)^{0.94} \tag{2.8}$$

Where 'Pr' = Prandtl number, 'K_{th}' = Thermophoretic coefficient, 'θ^*' = $\left(\frac{T_e - T_w}{T_e}\right)$, '$T_e$' = Temperature of exhaust gas and 'T_w' = tube wall temperature. Tablot et al. [2.191] developed an expression for K_{th} given by Eq. (2.9) below

$$K_{th} = \frac{\frac{2\,C_s C}{1+3\,C_m\left(\frac{2\lambda}{d_p}\right)} \times \left(\frac{K_g}{k_p}\right) + C_t\,(\frac{2\lambda}{d_p})}{1+2\left(\frac{K_g}{K_p}\right)+2C_t\left(\frac{2\lambda}{d_p}\right)} \tag{2.9}$$

Where 'k_g' is the thermal conductivity of the gas and 'k_p' is the particle's thermal conductivity, C is the slip correction factor, C_m momentum exchange coefficient, C_s is the thermal slip coefficient, and Ct is the temperature jump coefficient.

In thermodenuder, thermophoretic losses generally occur when rapid cooling of hot gases occurs at the intersection of the desorber section and the adsorber section. These losses are typically between 20 -25% [2.186]. Optimized design with a heated adsorption section can reduce these losses [2.186]. For heated tubes, the losses are in the range of 5-25% for exhaust gas temperature of the order of 100 – 600°C [2.186]. Losses of nonvolatile particles of the order of 10 -20% have been measured experimentally for exhaust gas temperature of 300 °C through a 1-meter unheated tube [2.186]

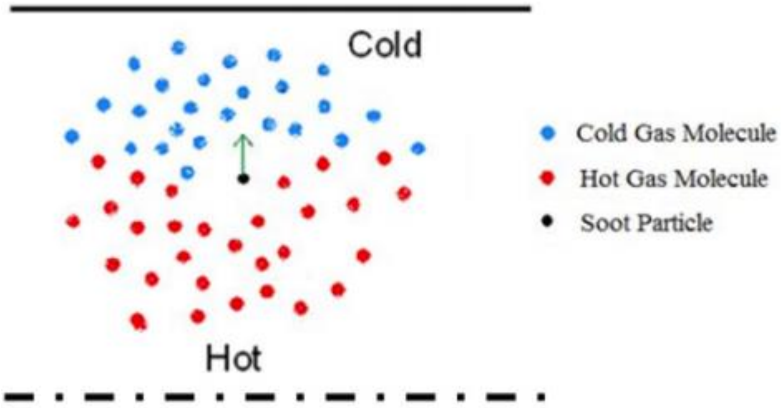

Figure 2.14 Thermophoresis mechanism impacting soot particles [2.188]

2.7.2.2 Volatile particle removal efficiency

Evaluation of volatile particle removal efficiency of VPR is performed with tetracontane (C40 alkanes) hydrocarbons according to PMP requirements. The volatile particle removal efficiency is measured by challenging VPR with a high concentration (> $10^4/cm^3$) of 30 nm tetracontane particles measured with particle number counter and measuring particle concentration downstream of VPR with a particle number counter [2.192]. The volatile particle removal efficiency can be calculated by Eq. (2.10) [2.192].

$$Volatile\ Particle\ Removal\ Efficiency = 1 - \frac{N_{downstream}}{N_{upstream}} \tag{2.10}$$

Where $N_{downstream}$ is the particle number concentration downstream of the conditioning device (VPR) measured with particle number counter (PNC) and $N_{upstream}$ is the number concentration upstream of the conditioning device (VPR) measured with particle number counter.

The volatile removal efficiency of studies can also be done with hydrocarbons (tetracosane C24, Octacosane C28, and emery oils). These hydrocarbons are applied in these studies because they roughly simulate diesel nanoparticles [2.192]. It is important to minimize the penetration of volatile species inside the conditioning devices. Tetracosane / sulfuric acid particles are chosen because they roughly simulate the composition of semi-volatile found in exhaust. Giechaskiel et al. [2.192] characterized various sample preconditioning systems, which included a dekati commercial thermodenuder. The volatile particle removal efficiency results of the thermodenuder showed that at a concentration of 10^6 / cm^3 (or higher) a small peak at 15 nm in PSD was detected. Kittelson et al. [2.193] challenged TD with tetracosane and tetracosane/ sulfuric acid aerosol. Particle size distribution was measured downstream of CS and TD + CS. CS and CS+ TD configuration removed all challenges aerosols. A nucleation mode was found downstream of TD when challenged with tetracosane/sulfuric acid particles of 33 $\mu m^3/cm^3$ [2.193]. In another study by Giechaskiel et al. [2.194] volatile artifacts < 10 nm were observed for catalytic stripper while thermodenuder showed volatile artifact < 23 nm. DPF vehicles equipped in this study showed a very low percentage of solid sub 23 nm particles.

2.8 Effect of thermodenuder on PSD

In this section, the previous studies related to solid particle measurement with thermodesorption system are presented. Fierz et al. [2.178] evaluated the evaporation of volatiles from three commercial thermodenuders (Dekati TDS, matter hot dilution system) at the engine operating point generating the maximum number of volatiles. When the measurement was done with these devices peak at 10 nm particles was observed in particle size distribution curves. This peak is due to the removal of volatile material from the solid core. Burthsher et al. [2.158] characterized nanoparticles from diesel engines with laboratory designed thermodenuder. Measurement was done on single cylinder 4 stroke 4 KW nominal power engine. From the results, it can be inferred that at low engine load conditions the particle size significantly decreases whereas it fairly remains constant at higher power. This indicates a decrease in volatile fraction with increasing engine load. Amanatidis et al. [2.195] assessed the performance of a thermodenuder and a catalytic stripper marine exhaust aerosol produced by a medium speed marine engine using high sulfur fuels. Sampling with CS and TD results in substantial reductions in the mass of organic and sulfate species in the range of 94% - 97% and 80% - 84%, respectively, while black carbon mass remains unaffected. The different sulfur content of fuels was used in this study. Formation of artifact formation downstream the TD and CS was performed with the nano – SMPS. With no treatment, the particle size distribution appears mono-modal. With the CS, the size distribution becomes bimodal with a new mode forming in the 5–30 nm size range. When the TD is used, the size distribution appears tri-modal, when the fuel with high sulfur content is used. The thermodenuder developed by Ronko et al. [2.184] has been employed in diesel exhaust nanoparticle volatility studies. The results reported that the developed thermodenuder was efficient in removing volatile nucleation mode particles and volatiles condensed on soot mode and core mode [2.196], [2.197].

Zhang et al. [2.198] investigated the nonvolatile PSD using thermodenuder to remove semi-volatile at different engine loads and constant speed. They observed an increase in nonvolatile particle number concentration with an increase in engine load with the application of thermodenuder. At lower engine load, both volatile and nonvolatile particles are present and PSD is bimodal. The distinctive nucleation mode at diameters of 8- 10 nm and accumulation mode with the peak diameters of 45–52 nm. At higher engine load, unimodal PSD was observed. PSD remained bimodal at low engine load even after thermal conditioning. This is possible because of the presence of nonvolatile nucleation mode core particles, which may not evaporate at a thermodenuder operating temperature of 250℃. To study the nature of these nonvolatile nucleation mode particles, further experiments at high temperature thermodenuder operation are required [2.198]. Heikkila et al. [2.199] investigated the nonvolatile particles emitted from diesel engines fueled with three different fuels (rapeseed methyl ester, diesel fuel, and synthetic gas to liquid fuel (GTL) using a thermodenuder. They have found that the concentration and GMD of nonvolatile nucleation mode cores were higher with rapeseed methyl esters. This is possibly due to the presence of viscous molecules such as triglycerides and glycerol with a high boiling point. Triglycerides and glycerol can survive when passed through the thermodenuder. Ajitai et al. [200] studied the thermal evolution of diluted diesel exhaust using thermodenuder. The peak position in the particle size distribution curves was shifted to a small size region at high temperature of 250℃. Monomodal to bimodal transitions were observed in particle size distribution curves at high temperature. The particulates at high temperature represent soot with graphitic nature devoid of volatile adsorbed species. This could be explained by the rearrangement in size distribution due to the evaporation of condensable compounds, which are previously adsorbed on the surface of soot particles.

Zhang et al. [2.127] compared particle size distribution for conventional diesel, HCCI, and RCCI combustion strategies using a thermodenuder (TD). The influence of low dilution ratio (LDR) and high dilution ratio (HDR) with and without TD on PSD for conventional diesel combustion is shown in Figure 2.15 The LDR operating condition without TDS depicts a bimodal size distribution with large nucleation mode particles. This is because, at LDR, the concentration of hydrocarbons is higher, which increases the nucleation rate as observed in the previous investigation. HDR reduces the size of nucleation mode particles due to the low concentration of hydrocarbons. A large portion of nuclei mode particles with mobility diameters between 20 nm and 50 nm are removed using HDR and use of TDS for RCCI and HCCI cases. This is because these volatiles particles are removed by thermodenuder, changing the shape of PSD. PSD curve for conventional diesel remains unaffected with HDR and thermo-denuder. This happens due presence of a large number nonvolatile soot particles in CDC mode which are not affected by thermal conditioning and dilution. PN of LDR TD smaller than 10 nm is higher than that of LDR < 10 nm. This trend is due to the fact that with TD volatiles condensed on nonvolatile nucleation mode particles are removed by heating. Hence, the number of particles smaller than 10 nm at the outlet of the thermodenuder is higher than the inlet. Graves et al. [201] investigated the volatility of particulate matter (PM) emitted from a single-cylinder compression-ignition, natural-gas engine fitted with a high-pressure direct-injection (HPDI) system using a thermodenuder at varying loads and EGR conditions. Sampling particles through thermodenuder changed the GMD and particle number concentration. The change in GMD is related to the amount of internal mixing between semi-volatile liquids and solid fractal-like carbonaceous particles. Internal mixing implies both species are present on the single-particle (a solid elemental carbon coated with liquid volatile material. As the particles are heated in a thermodenuder the liquid volatile material evaporates from the surface of soot particles changing the GMD and PSD.

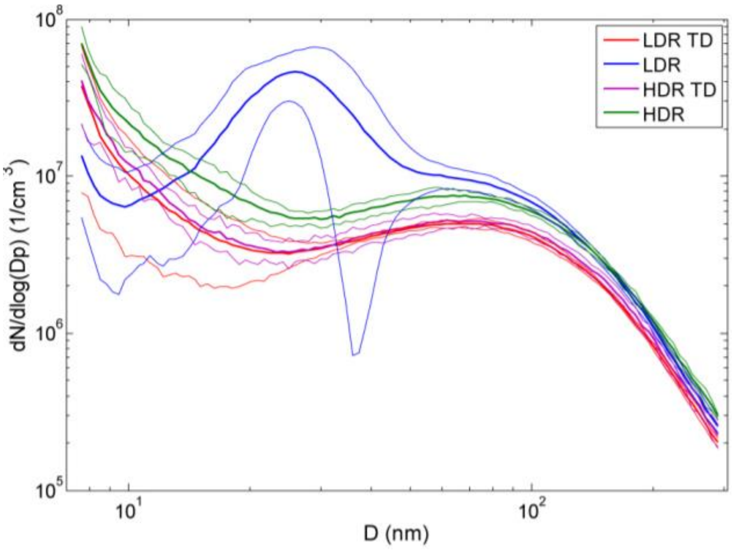

Figure 2.15 Effect of LDR and HDR with and without TD on CDC PSD [2.127]

2.9 Research Gaps in Literature

The literature review summarizes that considerable research has been done in combustion and particle emission characteristics of diesel and RCCI engines. However, there are still areas that need to be further investigated for making diesel and RCCI engines more efficient and cleaner. The following research gaps have been identified based on the literature review and further research questions need be answered

- Formation of soot particles in diesel engines is dependent on the formation of soot precursors such as acetylene, pyrene, acenapthalene. The experimental incylinder measurement of these soot precursors is not possible in metal engine at different engine operating conditions. Therefore, it is necessary to conduct numerical investigation to quantify these soot precursors at various engine operating conditions. Therefore, it is necessary to conduct a numerical study which investigates the effect of engine operating parameters on incylinder formation of soot precursor and soot particle size and number characteristics of diesel engine.

- In RCCI combustion heat release using different fuels a small peak of LTHR before main HTHR is observed. The amount of low temperature heat release (LTHR) has a significant effect on phasing and amount of high temperature heat release (HTHR). The formation of particle emission in RCCI operation depends on phasing on HTHR. Therefore, there must be relationship between LTHR, HTHR and particle emissions. Therefore, effect of LTHR and HTHR on particle emissions from RCCI engine is investigated. Further empirical models are developed for prediction of particle emission at different engine operating conditions and combustion parameters.

- The characteristics of PM from RCCI engines are different from those from diesel engines. RCCI combustion produces lower particle concentration compared to conventional diesel and PCCI combustion and PSDs for RCCI engine display high concentration of nucleation mode particles. To study the characteristics of nucleation mode particles a thermodesorption system is developed and tested in the laboratory and the effect of thermodesorption on particle emission from RCCI engine at different engine operating parameters is investigated.

Chapter 3

Methodology

This chapter describes the numerical models, experimental setup, and methodology used in the thesis. In this work, ANSYS FORTE CFD software is used to conduct a preliminary numerical study on automotive single cylinder diesel engine. CFD study is conducted to predict the in-cylinder distribution and mass fraction of particulate matter (PM) precursors (PAHs, olefins, aromatics), radicals and PM number density. It is not possible to characterize these quantities in metal engines. The numerical study is conducted to analyze the different pathways through which PM formation takes place. In the present study, the effect of advanced injection timing (relevant to RCCI) is explored in the CFD simulations aimed at predicting the PAHs, olefins, radicals, and PM number density. For the experimental study of RCCI engine PM characteristics, suitable hardware and instrumentation were done on existing automotive single-cylinder diesel engine to operate the engine in RCCI mode. In the first part of this chapter numerical methodology is discussed which includes the discussion on governing equation, physical and chemical submodels, computation domain, chemical reaction mechanism, detailed soot model, simulation test matrix, and numerical model validation. In the second part of this chapter experimental methodology is described in which engine setup, instrumentation, incylinder pressure measurement, and particle emission measurement are discussed. Furthermore, the working principle of particle measuring instrument with their specifications is also discussed. Then details about the methodology used for calculating the combustion and particle emissions parameters and experimental test matrix and procedures are discussed. A description of design and development of thermodesorption system is also provided in the chapter.

3.1 Numerical Methodology

In this section numerical methodology is discussed. The numerical methodology ANSYS FORTE CFD code with improved sub-models for turbulence, spray formation, chemical kinetics and detailed soot model using method of moments. The following subsections provide a brief about the governing equations and models implemented in ANSYS FORTE CFD code.

3.1.1 Overview of 3D CFD Model

Numerical study is conducted using ANSYS FORTE CFD code. This CFD code is an advanced CFD simulation package for realistic simulation of CI engine performance and emissions which incorporates ANSYS Chemkin Pro solver technology [3.1]. This software allows multicomponent fuel models to be combined with comprehensive spray dynamics without sacrificing simulation time to solution. The sub-models implemented in ANSYS FORTE have been well validated against experimental data over a broad range of conditions. ANSYS FORTE takes advantage of well-established theoretical representation of 3D fluid flow, spray dynamics, and combustion behavior. In internal combustion engines, the fuel-air mixture before combustion and the burned gases after the combustion are working fluids. The fluid considered is turbulent, multiphase, and reactive. ANSYS FORTE applies a turbulent reacting flow representation, which basic fluid dynamics is governed Navier stokes equation. Turbulent flow is characterized by a wide range of flow length scales as significant and irregular variations in the flow field. In the present study, the Reynolds average Navier Stokes (RANS) approach is used for turbulence modelling, which aims to capture the ensemble of the flow field. The RANS approach removes the necessity of resolving small-scale structures and fluctuations seen in individual flow realizations while retaining the main effects of turbulence on average flow and combustion characteristics. The governing equations in ANSYS FORTE are formulated to solve the ensemble-averaged flow field in the RANS approach. [3.1]. The gas phase working fluids in the combustion engines are modeled as a mixture of individual gas components, or species and this composition changes during the engine cycle due to flow convection, molecular diffusion, turbulent transport, interaction with fuel sprays, and combustion. The conservation equation for the mass of species k is described by Eq. (3.1) [3.1].

$$\frac{\partial \bar{\rho}_k}{\partial t} + \nabla.(\bar{\rho}_k \, \tilde{u}) = \nabla.[\, \bar{\rho}\, D \nabla \bar{y}_k] + \nabla.\Phi + \dot{\bar{\rho}}_k{}^{c} + \dot{\bar{\rho}}_k{}^{s} \; (k = 1 \ldots \ldots.., K \tag{3.1}$$

Where ρ is the density, subscript k is the species index, K is the total number of species, u is the flow velocity and $y_k = \frac{\rho_k}{\rho}$ is the mass fraction of species k. Application of ficks law of diffusion results in mixture–averaged molecular diffusion, the mixture mean diffusion coefficient D is obtained. The term Φ denotes the equation $\Phi = \overline{\rho_k}\, \tilde{u} - \overline{\rho_k u}$ that needs to be modelled by group averaging or filtering of the convection terms due to chemical reactions and spray evaporation in other words evaporated liquid fuel represents the fuel mass that passes into the gas phase. The summation of Eq. (3.1) over all species gives the continuity equation Eq. (3.2) [3.1] for the total gas phase fluid

$$\frac{\partial \bar{\rho}}{\partial t} + \nabla.(\bar{\rho}\, \tilde{u}) = \dot{\bar{\rho}}^{s} \tag{3.2}$$

The fluid momentum equation takes into account the effect of convection, pressure force, viscous stress and turbulent convection, as well as effects from liquid sprays and body force. The momentum equation is given by equation 3.3 [3.1] :

$$\frac{\partial \bar{\rho}}{\partial t} + \nabla.(\bar{\rho}\;\; \tilde{u}\, \tilde{u}) = - \nabla\, \bar{P} - \nabla.\bar{\sigma} - \nabla.\Gamma + \bar{F}^{S} + \overline{\rho g} \tag{3.3}$$

Where P represents the pressure force, $\bar{F}^S$ the rate of momentum gain per unit volume due to spray, g is the specific mass force, and $\bar{\sigma}$ the viscous shear stress is given by Eq. (3.4) [3.1]

$$\bar{\sigma} = \bar{\rho}\, v\, [\nabla\tilde{u} + (\nabla\tilde{u})^t - \frac{2}{3}\,(\nabla.\tilde{u})I \tag{3.4}$$

In equation v represents for laminar kinematic viscosity, I for similarity tensor, and superscript t for transpose of tensor. Stress Γ represents the effect of ensemble averaging or filtering of non-linear convection term, that is $\Gamma = \bar{\rho}\,(\overline{uu} - \tilde{u}\,\tilde{u})$. In RANS approach this is called reynolds stresses which are modelled through adoption of appropriate turbulence models. Based on first law of thermodynamics, the change in the internal energy must be balanced by pressure work and heat transfer. For the flow problems relevant to internal combustion engines. For the flow problems in internal combustion engines, the effect of convection, turbulent transport, turbulent dissipation, sprays, chemical reactions, and enthalpy diffusion of multicomponent flow should be considered. The internal energy transport equation energy Eq. (3.5) [3.1] reads as :

$$\frac{\partial\bar{\rho}}{\partial t} + \nabla.(\bar{\rho}\tilde{u}\,\tilde{I}) = -\bar{p}\,\nabla.\tilde{u} - \nabla.\bar{J} - \nabla.H + \bar{\rho}\,\bar{\varepsilon} + \dot{\vec{Q}}_C + \dot{\vec{Q}}_S \tag{3.5}$$

Where I is the specific internal energy, J is the heat flux vector accounting for contributions due to heat conduction and enthalpy diffusion described by Eq. (3.6) [3.1].

$$\bar{J} = -\lambda\nabla\bar{T} - \bar{\rho}\,D\sum_K \tilde{h}_k\,\nabla y_k \tag{3.6}$$

Where λ is the thermal conductivity which is related to thermal diffusivity α and heat capacity c_p by $\rho c_p \alpha$, T is the fluid temperature, and h_k is the specific enthalpy of species k. $\bar{\varepsilon}$ is the dissipation rate of turbulent kinetic energy which is defined in turbulence models. $\dot{\vec{Q}}_C$ and $\dot{\vec{Q}}_S$ are the source terms due to chemical heat release and spray interactions. The H accounts for ensemble averaging or filtering of convection terms that $H = \bar{\rho}\,(u\tilde{i} - \tilde{u}\tilde{I})$ which is modelled using the turbulence approach. The chemical reactions that occur in combustion simulations can be described by chemical kinetic mechanism that define the reaction pathways and associated reaction rates leading to change in species concentration. In detailed mechanism, the reversible (or irreversible reactions) involving species K can be represented in general form by Eq. (3.7) [3.1].

$$\sum_{k=1}^{K} v'_{ki}X_k \leftrightarrow \sum_{k=1}^{K} v''_{ki}\,X_k \tag{3.7}$$

The production rate of the k_{th} species in the i_{th} reaction can be described by Eq. (3.8) [3.1]

$$\dot{\omega}_{ki} = (v'_{ki} - v''_{ki})\, q_i \tag{3.8}$$

Where q_i is the rate of progress of reaction

Correspondingly chemical heat release in the energy equation is given Eq. (3.9) [3.1]

$$\dot{Q}_c = \sum_{i=1}^{I} \sum_{k=1}^{K} (v'_{ki} - v''_{ki})\, (\Delta h_f^0)_k \tag{3.9}$$

Where Q_i heat of reaction i at absolute zero and $(\Delta h_f^0)_k$ is the heat of formation of species k at absolute zero.

The governing equations are discretized with respect to spatial coordinates of the system, on a computational grid based on finite volume approach. Further, in order to provide time accurate solution, the equations are further discretized with respect to time following the operator splitting method. ANSYS FORTE uses an implicit method in solving the algebraic finite volume equations that results from differencing. It uses a modified version of the SIMPLE method which is two step iterative procedure used to solve flow field variables. Velocities at each time step in the numerical simulation need to be computed from time advanced pressure gradients. This requires an iterative solution procedure, because the time advanced pressure depend on the acceleration and velocities computed from pressures. The SIMPLE method extrapolates the pressure, iteratively solves for velocities, then temperature and finally pressure.

3.1.2 CFD sub-models and Computational Domain

Various physical and chemical sub-models available in ANSYS FORTE CFD code are used in this study. The spray atomization and drop breakup are modelled using the Kelvin-Helmholtz (KH-RT) hybrid model, which works on the theory of linear stability of liquid jets [3.2]. The Kelvin Helmholtz model is based on linear stability analysis of liquid jets and is used to model the jet's primary breakup region. Beyond break up length from the nozzle exit, the Rayleigh Taylor (RT) model is used together with the KH model to predict the secondary breakup of spray droplets. The KH model is employed within the breakup length from the nozzle exit. The breakup length KH model is employed concurrently with the RT model to model the secondary breakup of droplets [3.2]. Air entrainment is modelled using the gas jet model, which works on the unsteady gas jet theory [3.3], [3.4]. Mesh dependency in coupling from the gas phase to the liquid phase is mainly from gas velocity in the droplet momentum equation. In ANSYS FORTE, an unsteady gas jet model is used to remove this mesh dependency for liquid droplet ambient gas coupling. The gas jet model is based on unsteady gas jet theory in which the axial droplet gas relative velocity is modelled without the use of discretization on the CFD mesh. An adaptive collision mesh model is used for modelling the fuel droplet collision [3.5]. The adaptive Collison mesh model uses a pseudo collision mesh to partition parcels into collision partners but is more flexible in that collision mesh adaptively encloses the evolving spray structure during the simulation. This method produces a collision mesh that is independent of gas phase mesh and adaptively refined according to local parcel number density. For the evaporation of fuel droplets, a discrete multi-component fuel vaporization model is employed [3.6]. In this model, fuel droplets are followed during evaporation and permit incorporation with the reaction kinetics of individual fuel molecules [3.6]. Similar distribution of the liquid droplets and fuel mass fractions are predicted by this multi-component fuel vaporization model for gasoline and diesel sprays as compared to the comparable single-component fuel model. However, local vapor fuel composition, which is not resolved by a single component model, varies significantly depending on mixture location and time after fuel injection [3.6]. Wall heat transfer is modelled using the temperature wall function model developed in the study [3.7]. The in-cylinder turbulence is modelled using an advanced version of the k-ε model, which is derived from the Renormalization group (RNG) theory proposed by Yakhot and Orszag [3.8 – 3.9]. This is the advanced version of a k-ε model derived from the Re- Normalization group theory, as proposed by Yakhot and Orszag. The K equation in the RNG version of the model is the same as the standard version, but the ε equation is derived from rigorous mathematical derivation rather than empirically derived constants. A study found that the modified RNG k-ε model simulated engine compressing and expanding flows agreed well with experimental data, and the large-scale flow structures, which are affected by spray and squish flows, were consistent with endoscopic combustion images [3.9]. A study also reported a good quantitative agreement between measured and predicted NOx and soot emission data obtained with the use of the modified RNG k-ε model [3.10]. Since then, this RNG k-ε model has been widely adopted into many CFD codes and applications to various simulations and therefore, this model is used in this work.

Diesel injector possessed six equally spaced holes therefore a 60° degree sector mesh is employed for the simulation study. FORTE sector mesh generator is used to generate 60° sector mesh as shown Figure 3.10. Meshing of the sector mesh geometry is done in ANSYS forte sector mesh by taking appropriate number of cells in radial, axial, and azimuthal direction. After the meshing compression ratio was checked by running simulation in no hydro mode (mesh movement only). This process was repeated until required compression (18:1) is obtained. Simulation is performed to validate the experimental in-cylinder pressure published the previous study [3.11]. These simulations are performed from inlet valve closing to exhaust valve opening to reduce the computation time. The average cell size is approximately about 1mm. Constant wall temperature of 435 K, 480 K and 440 K corresponding to the cylinder liner, cylinder head and piston face respectively. A periodic boundary condition is selected in azimuthal direction.

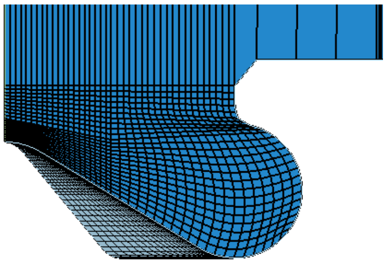

Figure 3.1 45° sector mesh employed for simulation

3.1.3 Chemical Reaction Mechanism

The simulation study is performed with a chemical reaction mechanism which was developed for use with 66.8/33.2% weight percent of n-decane-alpha methyl naphthalene (AMN) diesel surrogate. This mechanism consists of 189 species and 1392 reactions [3.1]. It contains reaction pathways to predict soot precursors required for soot surface mechanism. The mechanism considers soot nucleation from pyrene, acenapthalene, naphthalene, benzene, and acetylene. Soot surface growth occurs through HACA (hydrogen abstraction and carbon addition) and PAH condensation routes. Soot oxidation occurs through the attack of oxygen molecules and hydroxyl radicals. The mechanism contains active and inactive sites on the soot surface [3.1]. This accurate soot chemistry is directly employed with the particle tracking method.

3.1.4 Simulation Test Matrix and Initial Conditions

The numerical study is performed for a single cylinder four stroke diesel engine at a constant speed and load of 1500 rpm and 1.5 bar BMEP. Technical specifications of the engine are presented in Table 3.1. Simulation initial parameters are presented in Table 3.2. The temperature and pressure of the mixture at inlet valve closing (IVC) was taken 320 K and 1.2 bar respectively. The initial turbulent kinetic energy and turbulent length scale were initialized to 10000 cm^2 /sec and 1.0 cm. The initial swirl ratio and swirl factor was set to 1.1 and 3.11 respectively.

Table 3.1. Specification of test engine

Engine Characteristics	**Specification**
Displaced Volume	625 cc
Stroke	93 mm
Bore	92.5 mm
Connecting Rod	156 mm
Compression Ratio	18: 1
Number of Valves	2
Maximum Torque	38 Nm @ 1100- 2000 rpm
Maximum Power	11 BHP @ 3000 rpm
IVO Timing	1° after suction TDC @ 0.1mm Lift
IVC Timing	239° after suction TDC @ 0.1mm Lift
EVO Timing	139° after compression TDC @ 0.1mm Lift
EVC Timing	16° after suction TDC @ 0.1mm Lift

Table 3.2 Simulation initial parameters

Pressure (IVC)	1.2 bar
Temperature (IVC)	320 K
Charge Composition (mass fraction)	N_2 = 0.78, O_2 = 0.22, $C_{10}H_{22}$ = 1
EGR (%)	0

3.1.5 Detailed Soot Model

The method of moment in ANSYS FORTE CFD code have been utilized to model soot particle mass and number density. The application of method of moments to soot particle modelling was first investigated by frencklach and coworkers [3.1]. The method of moment tracks the evolution of aerosol system by its moment of particle size distribution function. This method finds the average properties of particle population. The loss of details of particle size distribution function due to the use of the method of moments is compensated by the computational speed which reduces the demand for computing resources. Method of moments can provide overall properties of a particle system such as number density, total particle volume fraction, total particle surface area and average particle size. The dynamics of particle coagulation can be described by following set of Eq. (3.10-3.12) [3.1].

$$\frac{dM_0}{dt} = R_0 - W_0 \tag{3.10}$$

$$\frac{dM_1}{dt} = R_1 + W_1 \tag{3.11}$$

$$\frac{dM_2}{dt} = R_2 + G_2 + W_2 \tag{3.12}$$

Where R, G, and W are the nucleation, coagulation, and surface growth terms.

In this method system of differential equations describing the time evolution of individual size classes is studied. In a spatially homogeneous aerosol with a discrete size distribution, the smallest particle having volume v1 and the particle of size (it) having volume (iv1) is considered. Assuming as usual the particle collision is coalescent; the coagulation terms are given by Eq. (3.13) and Eq. (3.14) [3.1].

$$\frac{dN_1}{dt} = -N_1 \sum_{J=1}^{n_{max}} \beta_{1,j} N_J \tag{3.13}$$

$$\frac{dN_i}{dt} = \frac{1}{2} \sum_{j=1}^{i-1} \beta_{j,i-j} N_J \; N_{i-j} - N_i \sum_{j=1}^{n_{max}} \beta_{i,j} N_J, \tag{3.14}$$

$i = 2\ldots\ldots n_{max}$. Where t is the reaction time, N_i is the number density of particles of size class i and n_{max} is chosen to be large enough to ensure the first two moments of the size distribution can calculated accurately.

The particle size distribution function n (j) where $0 \leq j < \infty$ represent a measure of particle size i.e., measure of particle mass or particle diameter, the r_{th} moment of this particle size distribution is defined in Eq. (3.15) [3.1].

$$M_r = \int_0^\infty j^r \times n(j) \times dj \tag{3.15}$$

3.1.6 Grid Independence Test

The grid size has great impact on simulation accuracy, so grid sensitivity analysis is needed before the model validation. Three different cell numbers are considered in this numerical study as shown in Figure 3.2. As seen in Figure 3.2 the difference between the peak pressure with medium (73964 cells) and fine mesh (163650 cells) is negligible. Simulations were performed with medium mesh (73964 cells) due to low computational cost and good accuracy. The numerical results derived from medium mesh displayed a high degree of similarity with experimental data without increasing computational cost.

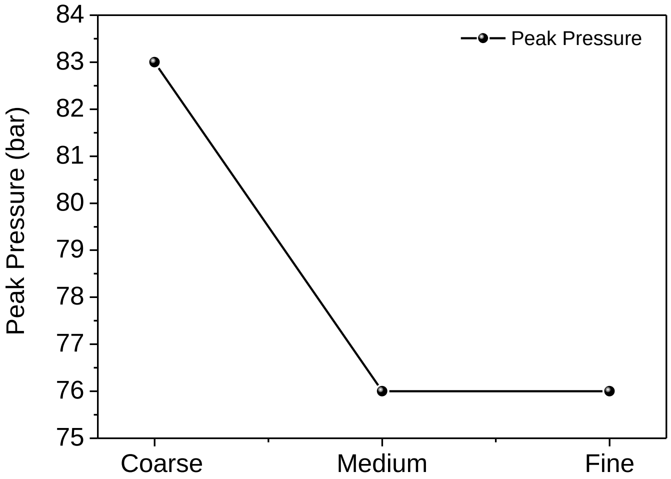

Figure 3.2 Mesh independency based on the peak pressure

3.2 Experimental Methodology

3.2.1 Engine Test Set Up

Experiments in this work are conducted on a single-cylinder, water-cooled, 625 cc four stroke naturally aspirated automotive engine with technical specifications listed in Table 3.1. The schematic and actual image of experimental set up is shown in Figure 3.3 and Figure 3.4. This engine is coupled with eddy current dynamometer (Manufacturer: TECHNOMEC, Model: TMEC 20) for power absorbing. For the measurement of rotational torque, a strain gauge load cell is used (Manufacturer: Load master: Model: DB 100). In order to achieve RCCI operating mode the intake manifold is modified to accommodate a port fuel injector that is operated independently by a low-pressure fuel pump. Modified intake manifold is depicted in Figure 3.5. The port fuel injector is assembled in such a way that fuel is injected close to intake valve. The major components of the port fuel injection system are (1) fuel filter (2) fuel pump (3) fuel line (4) fuel injector and (5) fuel tank. A 12 V battery was employed for the power supply to the fuel pump and injector. The amount of injected fuel quantity and timing is varied by a developmental ECU. Using port fuel injector, Low reactivity fuels like methanol and gasoline are supplied into the intake manifold during the suction stroke of engine cycle. A centrally mounted common rail injector is located in the cylinder head and is used to deliver direct injected (DI) fuel. Diesel is injected into the cylinder using a common rail direct injection (CRDI) system with adjustable fuel rail pressure in range 200 - 1800 bar, injection timings and injection duration. Developmental ECU controls the amount of diesel injected, the timing of the injections, and the quantity of injections. In engine test set up, various sensors are used for measuring air and fuel flow rate. The differential transmitter is used for measuring air flow rate. The fuel transmitter (Manufacturer Wica Model SL1) is used for measuring fuel flow rate. The actual picture of the differential pressure transmitter is shown in Figure 3.7. In the engine setup, the engine demand and fuel injection events are controlled and decided using a development engine ECU (Manufacturer: NIRA, Sweden, Model Nira i7r). The ECU processes the data after reading the signals from various sensors and sending the output signal (command to the actuators). The ECU reads signals from a variety of sensors, including the manifold absolute pressure sensor, the manifold air temperature sensor, the crankshaft position sensor, the accelerator pedal position sensor, the cam position sensor, the engine coolant sensor, the fuel temperature sensor, the fuel pressure sensor, and the oil pressure sensor. Development ECU manages actuators such fuel injectors, EGR valve, fuel pressure control, fuel pump relay, and main relay by processing input signals from input sensors and controlling output signals.

Figure 3.3. Modified intake manifold of the engine for conducting RCCI experiments

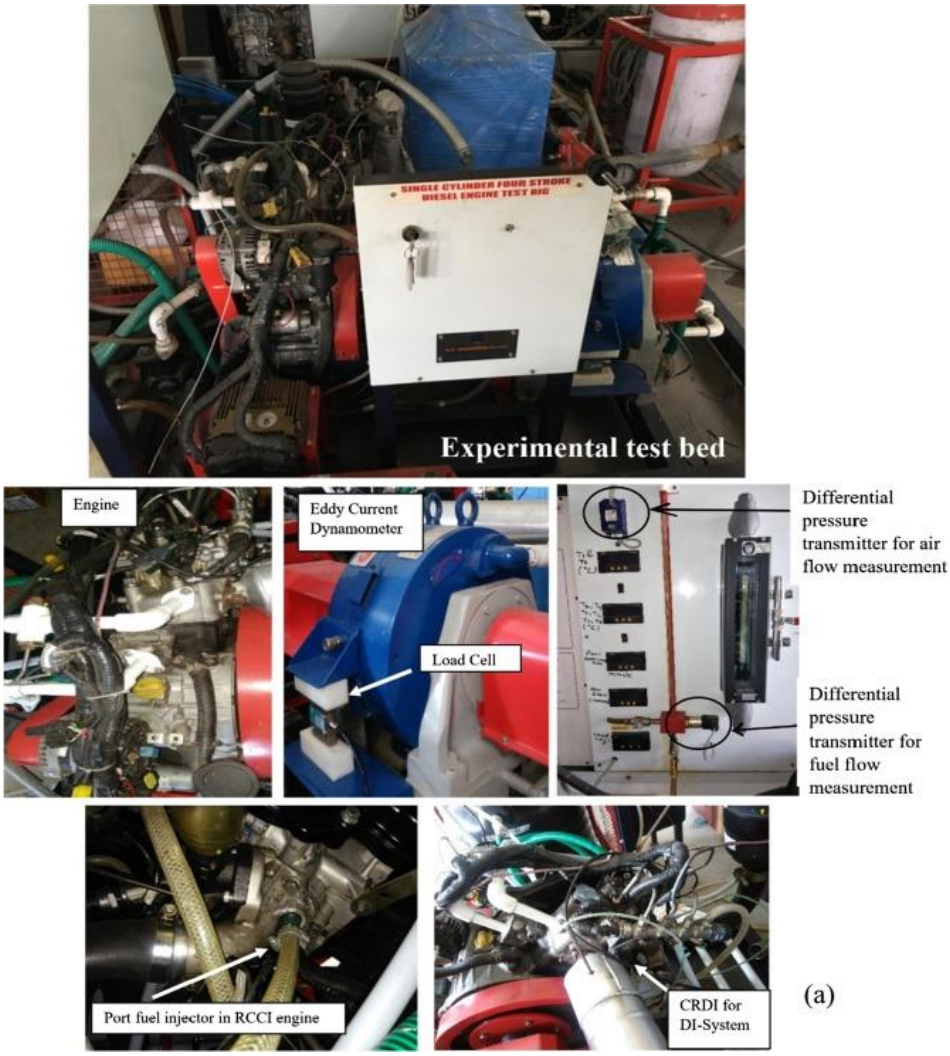

Figure 3.4. Actual pictures of the experimental set up

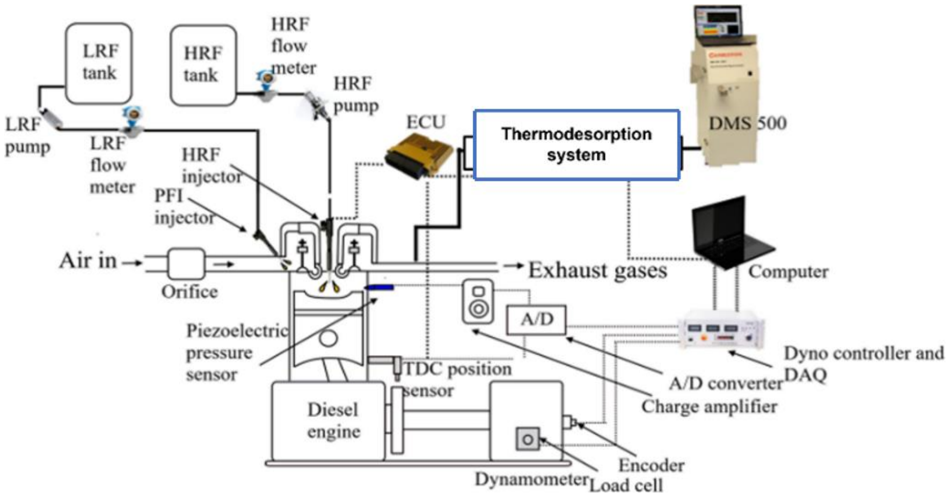

Figure 3.5 Schematic of experimental set up

3.2.2 Incylinder Pressure Measurement

For the purpose of measuring combustion pressure, a piezoelectric pressure transducer (Manufacturer: KISTLER; Model: 211B2) is mounted on the cylinder head. For measuring crank shaft position, a crank angle encoder with a resolution of 0.1 CAD is installed on the crankshaft. The pressure transducer converts the combustion pressure into an electric charge, which is proportional to force acting on the piezoelectric crystal of pressure transducer. This electric charge is converted into corresponding voltage using charge amplifier (Manufacturer: Kistler model; Model: Type 5018). In order to measure representative cylinder pressure versus volume for combustion analysis, it is imperative to determine the engine crank angle that corresponds to the measured pressure data. This is accomplished using an optical incremental encoder. The pressure relative to this voltage is logged into computer by using high speed data acquisition hardware and LabVIEW based program. Four step pressure signal processing consisting of absolute pressure correction, phasing w.r.t to crank angle, filtering high frequency noise, and cycle averaging (for obtaining mean cylinder pressure and heat release rate) is used in this study. Digital butterworth filter is used for filtering high frequency noise from incylinder pressure signal. In this work, CDAQ (Manufacturer: National Instruments; Model: NI C DAQ-9718) was utilized to acquire analog (cylinder pressure) and digital (angle encoder) signals using two separate NI modules (NI – 9222 and NI 9411). The averaged incylinder pressure data, which is used to calculate combustion parameters, is obtained by averaging the results of multiple successive engine cycles, which are recorded and examined to prevent change in the combustion. For engine testing and combustion analysis of RCCI engine, the crank angle encoder of 0.1 degree resolution (Manufacturer : Kubler - Germany) was employed in the research work. In one rotation of crankshaft. In one rotation of the crankshaft, encoder gives 3600 electrical pulses. A separate 5 to 24 VDC power supply was employed for the operation of encoder.

3.2.3 Particle Emission Measurement

Engine exhaust particle size and number distribution is measured by differential mobility spectrometer (Manufacturer: Cambustion, UK, Model: DMS 500) [3.12]. Measurement of PM emissions was done using a differential mobility spectrometer (Manufacturer: Cambustion, UK, Model: DMS 500) after sample preconditioning through a thermodesorption system (as shown in Figure 3.5) [3.12]. The actual image of the particle sizer (DMS 500) is shown in schematic diagram of experimental set up (Figure 3.5). For measurement of PM emission exhaust line of the engine was modified and separate probes were fabricated for exhaust sampling Particles of 38 different sizes in the range of 5 nm to 1000 nm can be measured by the instrument. It is real-time instrument and measures particle size and number characteristics based on electrical mobility diameter. Exhaust gas sample from the engine exhaust tail pipe. The DMS500 uses electrical mobility measurements to produce particle size distributions between 5 nanometres and 2.5 microns [3.12]. Since the classification of particles according to their differing electrical mobility takes place in parallel (rather than in series as in a scanning instrument) the DMS can offer the fastest measurement of its type. The user interface processes the size distribution data in real-time to output particle mass, surface area and number. A DMS 500 system for engine sampling incorporates two stage dilution system. The 1st dilution stage uses metered compressed air to provide low dilution factor up to 5: 1. The second dilution stage uses a rotating disc to provide a high dilution factor which may be varied to maintain good signal to noise ratio. The DMS uses a classifier column operating at 0.25 bar absolute with an external vacuum pump. A cyclone separator removes particles above measurement range to reduce need for cleaning. Two optional stages of software-controlled dilution is applied before the sample gas passes through a corona charger and into classifier column. The charged particles flow within a particle free sheath which is uniform cylindrical laminar column designed to carry charged particles in a predictable manner. The particles are then deflected toward ground electrometers rings by repulsion from high central voltage electrode. When high voltage is applied to the central electrode, the charged particles are deflected toward electrometer rings. Particles with a higher charge/ lower drag will be deflected more, and will land on electrometer ring closer to sample inlet. Their landing position is uniform function of their charge and their aerodynamic drag. The particles yield their charge to the electrometer amplifier and the resulting current are translated by user interface into particle size and number data. The working principle of DMS 500 is depicted in Figure 3.6.

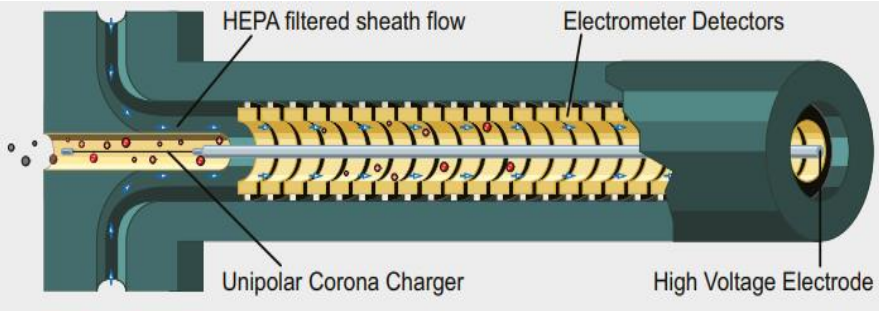

Figure 3.6 Working principle of DMS 500 [3.12]

3.2.4 Design and Testing of Thermodesorption System

A thermodesorption system is designed and developed in this work to investigate the correct number of solid particle emissions. The thermodesorption system operates by first vaporizing volatile compounds in an aerosol heater, which heats the exhaust sample to 250 °C. After heating, the sample enters the absorber section, where the vaporized compounds are adsorbed by activated charcoal pellets. The details of fabrication and design of instrument are discussed in the following sections. Ideally, transmission of the volatile material should be zero and penetration of solid particle should be 100. However, there are losses due to particle diffusion and thermophoretic effects in the sampling tubes. Final instrument dimensions were chosen based on design calculations for the temperature, residence time calculation, and aerosol losses calculations. To prevent particulate build-up during both stages, all components of the TD were manufactured of stainless-steel tube with a seamless inner surface. Different parts of thermodesorption system are described in more detail in the following subsections.

3.2.4.1 Design Calculations

(a) Temperature and Residence Time Calculations

Theoretical calculations done to arrive at final design of the thermodesorption system are described below. Prior to construction, the estimation of total losses for a given design is done using aerosol loss calculations. According to particle loss calculations, it is found that heating section longer than 0.5 m contributes to increased particle losses among smallest particle size range. On the other hand, a shorter heater section doesnot give the sampled particle load enough time to thoroughly heated up. Thus, with the help of particle loss calculations required length and diameter of desorber pipe are decided. Residence time of particles in heated section is calculated by Eq. (3.16) [3.13].

$$t_{heater} = \frac{d_h^2 \times \pi \times L_h \times 60 \times 10^3}{4 \times Q_{gas}} \tag{3.16}$$

Where $t_{residence}$ is the residence time in seconds, d_h is the diameter of the pipe in meters, Q_{gas} is the flow rate of exhaust gas in L/min, and L_h is the length of the desorber section in meters.

Temperature calculations were done with an assumed inlet exhaust gas temperature of 180℃. The average nusselt number is calculated using the assumed bulk temperature for fluid properties. The Reynolds number is calculated using Eq. (3.17) [3.13]

$$Re = \frac{V_m \times D_h}{\nu} \tag{3.17}$$

Where V_{gas} is the velocity of exhaust gas in m/sec, D_h is the diameter of the pipe in meters and ν is the kinematic viscosity of exhaust gas.

The calculated Reynolds number is used to determine the average nusselt number given by Eq. (3.18) [3.13]

$$Nu = 3.66 + \frac{0.065 \times \left(\frac{d}{L}\right) \times Re \times Pr}{1 + 0.04[\left(\frac{D}{L}\right) \times Re \times Pr]^{\frac{2}{3}}} \tag{3.18}$$

Where Re is the Reynolds number, Pr is the Prandtl number, D_h is the pipe diameter in meters, L_h is the length of the pipe in meters.

Where Nu is the nusselt number used to calculate the heat transfer coefficient using Eq. (3.19) [3.13]

$$h = \frac{k}{D} Nu \tag{3.19}$$

Where h is the convective heat transfer coefficient, D_h is the diameter of the pipe in meters and k_{gas} is the thermal conductivity of exhaust gas in W/mk.

Then we determine the exit exhaust gas temperature from Eq. (3.20) [3.13]

$$T_e = T_s - (T_s - T_i) \exp\left(\frac{-hA_s}{\dot{m}\, C_p}\right) \tag{3.20}$$

Where T_e is the exit exhaust gas temperature at the exit of the desorber section of the thermodesorption system in K, T_s is the pipe surface temperature, T_i is the inlet exhaust gas temperature at the inlet of the desorber section of the thermodesorption system, h is the heat transfer coefficient, $\dot{m}$ is the mass flow rate of exhaust gas in L/min, C_p is the specific heat of exhaust gas, A_s is the surface area of the pipe in m^2.

(b) Aerosol Loss Calculations

Losses that occur in the thermodesorption system are Brownian diffusion losses and thermophoretic losses. Calculations of losses are described below :

(i) Diffusion Losses

Brownian diffusion plays a major mechanism for losses in transport tubes. It is the movement of particles due to the concentration gradient. Diffusion of particles to walls is independent of tube diameter for a given flow rate. The fraction of particles entering the tube that will exit the tube is called penetration fraction P given by equation. To reduce the diffusion losses during the experiments, a high sample flow rate (around 8 L/min) and shorter length of the sampling tube (2 m) are used. To reduce the thermophoresis losses, thermodesorption system heating unit is insulated with glass wool insulation.

The diffusion losses are calculated in terms of penetration fraction (P_{diff}) which is the ratio of particle concentration upstream and downstream of the thermodesorption system calculated by using the Eq. (3.21) [3.14].

$$P_{diff} = \frac{N_{out}}{N_{in}} = \exp(-\xi\,\mathrm{Sh}) \tag{3.21}$$

Where $\xi = \frac{\pi DL}{Q}$ is a dimensionless parameter; Sh is the Sherwood number; 'D' is the diffusion coefficient, 'L' is the length of the pipe, 'Q' is the volume flow rate (m^3/sec). Diffusion coefficients of the particles can be calculated from Eq. (3.22) [3.14]

$$D = \frac{K_B \times T_{gas} \times C_c}{3 \times \pi \times d_p \times \eta} \tag{3.22}$$

Where 'K_B' depicts Boltzmann constant, 'T_{gas}' depicts exhaust gas temperature, 'C_c' depicts the Cunningham slip correction factor, 'd_p' depicts particle diameter in nm, and 'η' depicts the viscosity of exhaust gas.

(ii) Thermophoretic Losses

Thermophoretic losses are calculated in terms of penetration fraction (P_{therm}) using the Eq. (3.23) [3.14]

$$P_{therm} = \left(\frac{T_w}{T_{gas}}\right)^{\mathrm{Pr}\,K_{th}} \tag{3.23}$$

Where T_w is the wall temperature of the sampling line, T_{gas} is the exhaust gas temperature, Pr is the Prandtl number and K_{th} is the thermophoretic coefficient. The value of factor 'PrK_{th}' is used as 0.55 [3.14]. Using the above equations, the thermophoresis and diffusion losses are calculated for different particle diameters and presented in Table 3.3. In this study, particle losses are calculated for particle diameters of 10 nm, 30 nm, 50 nm, and 100 nm. It is found that the diffusion losses are 4.7%, 2%, 1%, and 0.2% for 10 nm, 30 nm, 50 nm, and 100 nm diameter particles, respectively. The thermophoresis losses are 7.6% for 10 nm, 30 nm, 50 nm, and 100 nm diameter particles.

The penetration efficiency (η_p) is the product of penetration fraction due to each deposition mechanism (diffusion and thermophoresis) given by Eq. (3.24)

$$\eta_p = P_{diff} \times P_{therm} \tag{3.24}$$

The losses in the thermodesorption system are calculated using Eq. (3.25)

$$Losses = 1 - P \tag{3.25}$$

Where P is the penetration fraction due to diffusion and thermophoresis deposition mechanism inside the tubes of thermodesorption system

Penetration efficiency was found between 0.8 and 0.9 for 10 nm, 30 nm, 50 nm and 100 nm diameter particles according to equation 3.24. Penetration fraction due to thermophoresis and diffusion is calculated using Eq. (3.21) and Eq. (3.22). Particle losses due to diffusion and thermophoresis are calculated using equation 3.25. To validate computational results, testing of thermodesorption system was done on single cylinder diesel operated in diesel and RCCI mode. Results of experimentally calculated penetration efficiency are presented in Table 3.4. Error between computational and experimental results is 3.75%. Volatile particle removal efficiency was calculated experimentally as 97.4% for diesel mode presented in Table 3.5 which is close to the value of 99% as recommended by particle measurement programme.

Table 3.3 Calculation of diffusion and thermophoresis losses based on empirical equations.

Particle diameter (d_p)	Diffusion losses	Thermophoresis losses
15 nm	4.7 %	7.6%
30 nm	2%	7.6%
50 nm	1%	7.6%
100 nm	0.2 %	7.6%

3.2.4.2 Design of Thermodesorption System

(a) Desorber Section

The desorber section is fabricated with 1 inch OD and 50 cm length SS (stainless steel) tube with an insulated heating tape wrapped around it with equal number of turns over the whole pipe. The insulated heating tape can heat up to 500℃ with a fast thermal response and is heavily insulated to withstand high temperature. The heating tape was controlled by PID temperature controller with input from J-type thermocouple at the end of the heated section. In order to have real-time temperature data during the measurement process to explain any deviation in the particle sizing data. For this purpose, J type thermocouple was fixed on the middle point of the heated section, registering the core aerosol temperature. A thermocouple was also added at the end of the desorber section to measure the TD exit temperature.

(b) Adsorber Section

The adsorber section is made up of two concentric tubes. The middle tube 2.5 cm in diameter and 50 cm in length can slide in and out easily in aerosol pathway tube. For charging and discharging the activated carbon a port was fabricated and welded to the outer casing. The aerosol pathway has holding rings in it to accommodate stainless steel wire mesh tube. The fabricated aerosol pathway fitted into holding tube. The schematic diagram and actual picture of fabricated instrument is depicted in Figure 3.7 and Figure 3.8. When aerosol enters the adsorber section the volatiles are adsorbed on activated charcoal. Fraction of molecules that will pass the adsorber section is given by Eq. (3.26) [3.19]

$$\frac{n_{out}}{n_{in}} = e^{\frac{-h_x A}{Q}} \tag{3.26}$$

Where h_x is the mass transfer coefficient, A is the active surface area of the channel and Q is the volumetric flow rate through the channel.

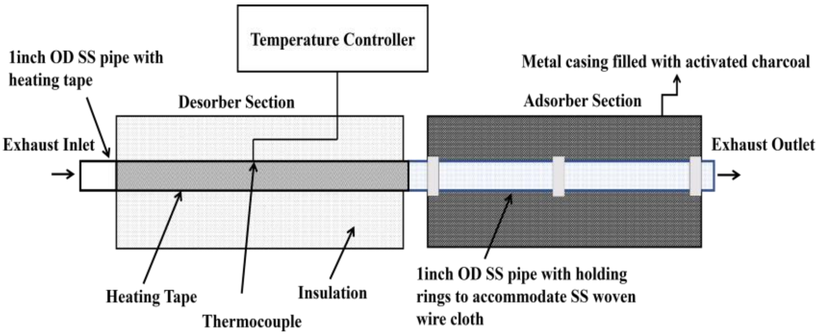

Figure 3.7 Final assembly of the fabricated instrument for particulate sampling

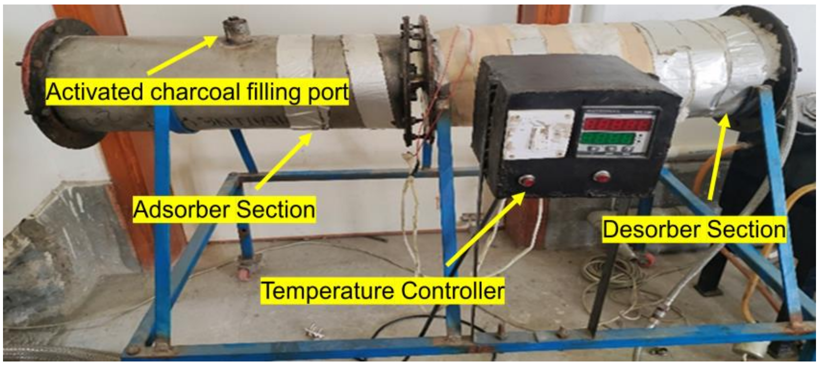

Figure 3.8 Actual photo of final assembly of the fabricated instrument for particulate sampling

3.2.4.3 Thermodesorption System Testing

The penetration efficiency of solid particles is an important parameter of thermodesorption system. It is important to measure the penetration efficiency of solid particles (30 nm, 50 nm and 100 nm) according to particle measurement program. For the calculation of penetration efficiency experimentally, thermodesorption system is tested for neat diesel at idle speed of 1000 rpm with no load condition and for 45% GD r_p in RCCI combustion at 1500 rpm with 1.5 bar BMEP. The experimental penetration efficiency (P) is calculated using the Eq. (3.27) [3.15].

$$Penetration\ efficiency\ (\eta_p) = \frac{N_{with\ thermo-desorption\ (d_p)}}{N_{without\ thermo-desorption}(d_p)} \tag{3.27}$$

Where $N_{with\ thermo-desorption\ (d_p)}$ is the PN concentration at particular particle diameter with the developed thermo-desorption system, $N_{without\ thermo-desorption\ (d_p)}$ is the PN concentration at particular particle diameter without the developed thermo-desorption system. The losses in the thermo-desorption system are calculated using the Eq. (3.28) [3.1]. In this study penetration efficiency is calculated by measuring the number concentration of AMPs which are typically solid particles with and without thermodesorption system.

$$Losses\ =\ 1 - \eta_p \tag{3.28}$$

Where η_p is the particle penetration efficiency.

Another important parameter which governs the performance of thermodesorption system is volatile particle removal efficiency. Tetracontane (C40 alkanes) hydrocarbons are used to test the effectiveness of removing volatile particles in accordance with the procedure for particle measurement [3.15, 3.16]. The volatile particle removal efficiency is measured with a high concentration (> $10^4/\text{cm}^3$) of 30 nm tetracontane particles [3.15]. The characteristics of nano-particle of tetracontane is similar to the diesel nano-particles [3.15]. In this study, the volatile particle efficiency is calculated by measuring the number concentration of nucleation mode particles which are typically volatile in nature using Eq. (3.29) [3.15].

$$Volatile\ particle\ removal\ efficiency\ (\eta_v) = 1 - \frac{N_{with\ thermo-desorption\ (d_p)}}{N_{without\ thermo-desorption\ (d_p)}} \tag{3.29}$$

For calculating the volatile particle removal efficiency, thermo-desorption system is tested for neat diesel at idle condition of 1000 rpm with no load condition and for GD and CNG diesel RCCI combustion at 1500 rpm with 1.5 bar BMEP for 45% r_p. Figure 3.9 depicts the particle size distribution with and without thermodesorption system (TDS) in diesel and GD RCCI operation. It can be seen peak of nucleation mode particles is reduced by order of magnitude with thermodesorption system in both diesel and GD RCCI operation. However, accumulation mode particle peak is less affected. The calculated η_p and η_v for neat diesel, GD-RCCI combustion is presented in Table 3.4 and Table 3.5 respectively.

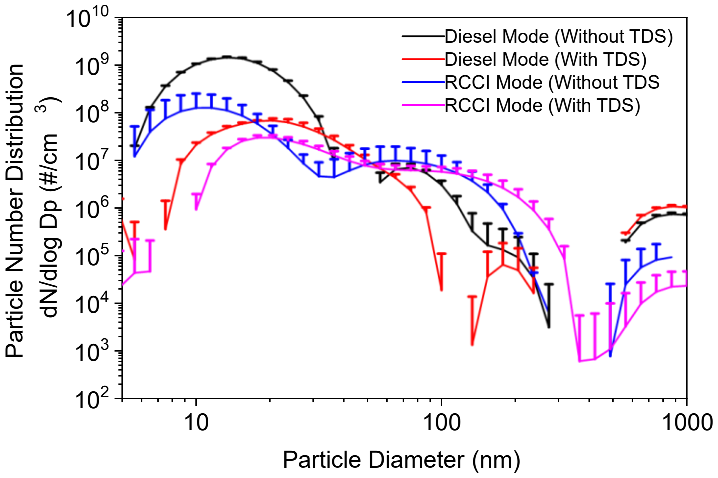

Figure 3.9 Testing of thermodesorption system (TDS) in diesel and RCCI mode

Table 3.4 Penetration efficiency (η_p) of Diesel and RCCI AMPs

Particle diameter (d_p)	η_p for Diesel	η_p for GD RCCI at 45% r_p	η_p for CNG RCCI at 45% r_p
50 nm	0.65	0.83	0.63

Table 3.5 Volatile particle removal efficiency (η_v) of RCCI NMPs

Operating Mode	Without Thermodesorption (particles/cm^3)	With Thermodesorption (particles/cm^3)	η_v
Diesel mode	1.32×10^9	3.53×10^7	97.4%
CNG Diesel RCCI at 45% r_p	3.77×10^7	1.03×10^7	67.55%
GD-RCCI at 45% r_p	1.02×10^8	1.30×10^7	87.25%

3.2.5 Experimental Procedure and Test Matrix

In this work, experiments are performed at steady state conditions which means exhaust and coolant temperature becomes constant, after around 15 mins of operation depending on the operating condition. RCCI combustion mode is tested for 1.5 bar (lower load) and 3 bar BMEP (medium load) at fixed 1500 rpm. For GD and MD RCCI operation engine experiments are performed at different diesel (HRF) SOI with single and double injection strategies with constant LRF mass injected in the intake manifold. The LRF and HRF injection strategy is shown in Figure 3.10 and engine test conditions are shown in Table 3.6. LRF is injected at 350° bTDC (during intake stroke) and diesel injection timing is varied for single and double injection strategy (Figure 3.10). For GD RCCI operation with single injection strategy, the engine is tested for 10°, 40° and 50° bTDC diesel SOIs, whereas for double injection strategy, pilot diesel SOI is kept fixed at 55° bTDC and the engine is tested for 10°, 40° and 50° bTDC main diesel SOI timings. For MD RCCI operation with single injection strategy, the engine was tested for 10° and 40° bTDC diesel SOIs, whereas for double injection strategy, pilot diesel injection timing is kept fixed AT 30° bTDC and the engine is tested for 10° and 25° main diesel SOI timings.

CNG diesel RCCI combustion mode is tested for two diesel SOIs, i.e., 40^o bTDC and 50^o bTDC, with single and double injection strategies and different port-injected CNG masses (m_c). In the double injection strategy, two cases are considered. In the first case, diesel mass is split in the ratio of 50:50% between the first and second injection, whereas in the second case, diesel mass is divided into 70:30% proportion. Fuel injection strategy for CNG diesel RCCI operation is shown in Figure 3.11 and engine operating conditions are presented in Table 3.6. For GD RCCI and CNG diesel RCCI operation engine is also tested at different premixing ratios (r_p) at constant engine speed of 1500 rpm and l.5 bar BMEP engine load with and without thermodesorption system for characterization of solid particle measurement. Engine operating conditions are presented in Table 3.6. Eq. (3.30) is used to compute the premixing ratio, which is determined as the proportion of port-injected fuel (gasoline/CNG) energy to total fuel energy. In this equation, port-injected fuel and direct-injected fuel are indicated by the subscript's "P" and "D," respectively. The abbreviations "m_P" and "LHV_P" stand for port injected fuel mass, LHV_P stands for lower heating value of port injected fuel. "m_D" stands for the mass of fuel that is direct-injected (diesel), and "LHV_D" stands for the lower heating value of direct-injected fuel.

$$Premixing\ Ratio\ (r_p) = \frac{m_P \times LHV_P}{m_P \times LHV_P + m_D \times LHV_D} \tag{3.30}$$

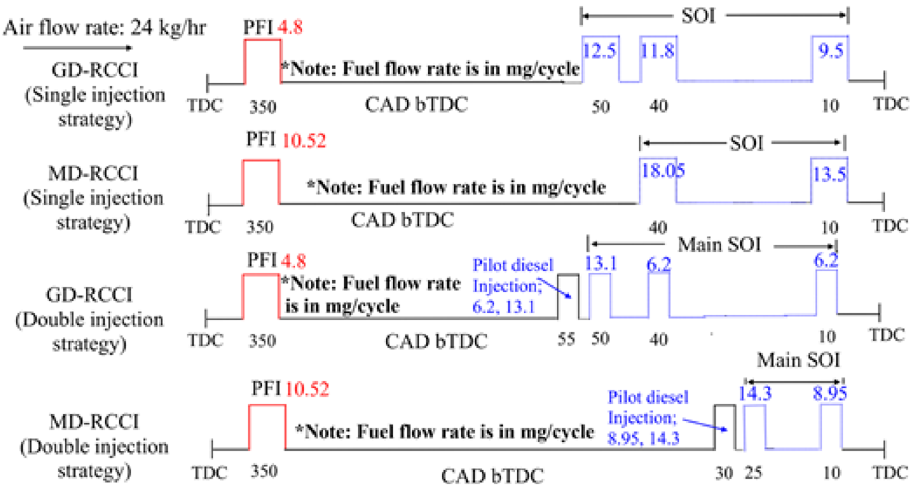

Figure 3.10 Fuel injection strategy for GD RCCI and MD RCCI operation

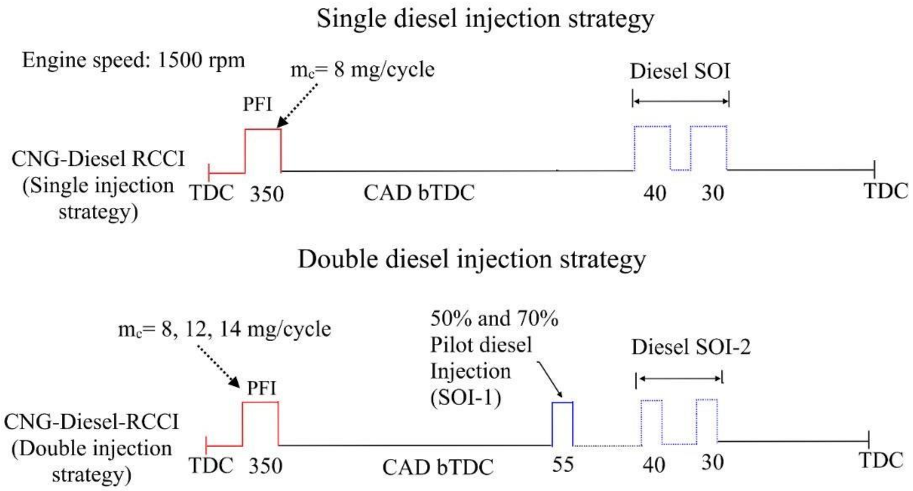

Figure 3.11 Fuel injection strategy for CNG diesel RCCI operation

Table 3.6 Engine operating condition

Engine operating parameters	GD RCCI	MD RCCI	CNG RCCI
Engine speed (rpm)	1500 rpm	1500 rpm	1500 rpm
Engine Load (BMEP)	1.5 bar	1.5 bar	1.5 bar
PFI Timing	350°bTDC	350°bTDC	350°bTDC
Diesel SOI (Single injection strategy)	10°bTDC,40°bTDC, 50°bTDC	10°bTDC, 30°bTDC	30°bTDC, 40°bTDC
Pilot diesel injection (Double injection strategy)	55°bTDC	30° bTDC	55°bTDC
Port Fuel Injected Mass (mg/ cycle)	4.8	10.52	8, 12, 14
Premixing Ratio (%)	45, 50 55	-	40, 45, 50
Diesel injection pressure (bar)	500	500	500

Online incylinder pressure data was recorded for 1000 consecutive cycles. The combustion characteristics are analyzed based on incylinder pressure data recorded for 1000 consecutive cycle using equations below. The heat release rate as function of crank angle is calculated from Eq. (3.31) [3.17]

$$\frac{dQ}{d\theta} = \frac{\gamma}{\gamma - 1} \cdot P \frac{dv}{d\theta} + \frac{1}{\gamma - 1} \cdot V \cdot \frac{dP}{d\theta} + \frac{dQ_{wall}}{d\theta} \tag{3.31}$$

Where, P and V are incylinder combustion pressure and volume as function of crankshaft position Q_{net} is the energy released, γ is the instantaneous ratio of specific heat of the system of gases, P is the cylinder pressure and V is the cylinder volume as a function of crankshaft position (θ) respectively. $\frac{dQ}{d\theta}, \gamma, and \ \frac{dQ_{wall}}{d\theta}$ are the heat release rate (HRR), the ratio of specific heat, and heat transfer loss from the cylinder wall, respectively. The ratio of specific heat (γ) is calculated using Eq. (3.32) [3.18].

$$\gamma = \gamma_0 - \frac{k}{100} \frac{T}{1000} \tag{3.32}$$

To calculate gross heat release, the heat transfer is modeled as convection heat transfer from gas to solid surface and the heat flux is expressed as Eq.(3.33) [3.19].

$$\frac{dQ}{dt} = h_c(T_g - T_w) \tag{3.33}$$

Where h_c is the heat transfer coefficient, T_g is the instantaneous cylinder gas temperature which can be estimated from ideal gas, and T_w is the cylinder wall temperature. The heat transfer coefficient model proposed by honberg was used for calculation in this thesis work. The heat transfer coefficient according to the honberg model according to Eq. (3.34) [3.19].

$$h = \alpha_s V^{-0.06} P^{0.8} T^{-0.4} (S_p + 1.4)^{0.8} \tag{3.34}$$

Where P, V, T, α_s, and S_p are the pressure, volume, combustion chamber temperature, scaling factor and mean piston speed. The CA_{10} and CA_{50} (combustion phasing) are calculated by determining the crank angle position corresponding to 10% and 50% heat release of the total heat release.

The LTHR and HTHR are not exactly separated in the rate of heat release (ROHR) trace. The LTHR and HTHR are extracted from the ROHR trace, which is calculated from Equation (3.29). The LTHR is typically obtained as a small peak prior to the main heat release (HTHR) due to “cool-flame” oxidation reactions in the temperature range around 760–880 K (during compression) attaining the main HTHR. HTHR obtains in two stages/parts, i.e., the premixed phase of combustion and diffusion phase of combustion depending on diesel

SOI. Figure 3.12 shows the different events of the combustion process in conventional dual-fuel (diesel SOI 10 deg bTDC) and RCCI regime, i.e., the start of combustion, LTHR duration, HTHR duration, premixed phase of combustion and mixing controlled (diffusion) combustion phase. The start of combustion is considered as a point where the heat release rate (HRR) turns positive after diesel injection. The LTHR duration is defined as the duration between the start of combustion and the end of LTHR. After attaining the peak, the low-temperature heat release rate (LTHRR) starts decreasing because the cool-flame oxidation reaction starts falling with increasing temperature. The end of LTHR is defined as a point after which the HRR starts rising after attaining the peak which means it is the change in the slope between LTHR and HTHR. The HTHR duration is defined as the duration between the point where the main HRR starts increasing and the point where the main high-temperature heat release rate (HTHRR) turns negative. This study calculates the amount of LTHR and HTHR by determining the absolute area under the LTHRR and HTHRR curve.

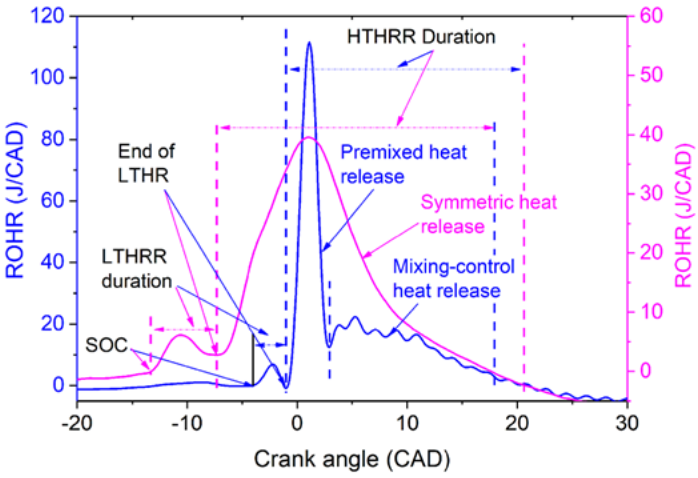

Figure 3.12 Schematic diagram of ROHR identifying the LTHR and HTHR

In each test particle emissions were recorded together with cylinder pressure data with and without thermodesorption system. For online measurement of particle number concentration and distribution, differential mobility spectrometer was employed. Particle data was recorded at thermally stable and steady state condition of the engine at each test point. The sampling of particle size data was done for 1 min at 1 HZ sampling frequency. Average of 60 acquired data points of particle size number concentration is presented in this work. To ensure the repeatability of trends in particle size distribution, the measurement was repeated twice at every test point. In general, particle having a size lower than 50 nm are considered as nucleation mode particles and particles having size between 50 nm and 1000 nm are considered as accumulation mode particles. In this study, nucleation and accumulation mode particles are calculated by fitting a lognormal curve. Total particle number and mass of the particles was calculated using Eq. (3.33) and Eq. (3.34) [3.12]

$$Total\ PN = \frac{1}{16}\sum_{d_{p1}}^{dp2}\frac{dn}{d\,log(d_p)} \tag{3.33}$$

$$Mass_{agg} = 1.72 \times n_{agg} \times {d_p}^{2.65} \times 10^{-24} \tag{3.34}$$

Where d_p is the aggregated diameter, n_{agg} is the concentration of aggregated particles at diameter d_p. Particle sampling is performed with and without thermodesorption system at operating temperature of 250°C. Firstly, measurement were performed without thermodesorption and particle size and number data is recorded. Then thermodesorption system was employed in the measurement and data was recorded. Several processs may lead to particle losses in the sampling line. To calculate the losses from sampling line and thermodesorption system, we assumed that losses came from brownian diffusion, thermophoresis and sedimentation. To study the effect of thermodesorption on particle losses an empty thermodesorption system was prepared by removing the charcoal filter, then the exhaust was sampled through empty TD and measurements were performed with particle sizer. The results of particle measurement with empty thermodesorption system and without thermodesorption system were compared to study the effect of thermodesorption on the losses of solid particles.

3.2.6 Uncertainty Analysis

Uncertainty analysis is important to quantifying the uncertainty in the measured data to built more confidence in experimental results [3.20-3.22]. Conducting uncertainty analysis for engine experiments displays distinctive challenges due to the multiple and varied parameters measured, the signal conditioning performed, and the large amount of data collected [3.20]. In this study, uncertainties due to both systematic and random errors in engine measurement are calculated. This section is divided into two subsections presenting uncertainty analysis of combustion parameters (incylinder pressure, heat release rate, CA_{10} and CA_{50}), and particle emissions.

3.2.6.1 Uncertainty Analysis of Combustion Parameters

In-cylinder pressure is a critical parameter that plays a crucial role in determining combustion parameters. Furthermore, these parameters demonstrate the combustion behavior, quality, and performance of the engines. [3.21]. Therefore recording the undistorted and unbiased cylinder pressure from the pressure transducer is critical. The primary sources of uncertainty in measuring in-cylinder pressure are linearity (systematic error) and cyclic temperature drift (systematic error) during most of the cycle. However, near the point of maximum pressure, random fluctuations (random error) become the predominant source of uncertainty [3.21]. We can derive the combined overall uncertainty of the incylinder pressure ($P_{cylinder}$) by using the root mean square method as [3.21]:

$$u_c^2\left(P_{cylinder}\right) = u^2(linearity) + u^2(cylic\ temperature\ drift) + \\ u^2(charge\ amplifer\ accuracy) + u^2(quantization) + u^2(random\ fluctuations) \tag{3.35}$$

Uncertainties for the systematic errors (linearity, cyclic temperature drift, charge amplifier accuracy) in incylinder pressure measurement was obtained from manufacturers data sheets. The main source of error due to quantization introduced by the analog to digital convertor is quantization error, which is computed as half of the resolution and is calculated using Eq. (3.36) [3.21].

$$Quantization\ error\ =\ 0.5 \times Resolution = 0.5\ \times (\frac{V_D}{V_S.2^{(n-B)}}\ \times E) \tag{3.36}$$

Where V_D is the full scale output range of the convertor, V_s is the full scale output range of the signal, E is the full scale ouptut of transducer, n is the bit resolution of the converted signal and B is the polarity factor (B=1 if the range is bipolar, = 0 if unipolar). The used module for acquiring analog in-cylinder signal in the present study is NI 9222, which is a 16 bit module with ± 10 V range. Linearity and temperature drift uncertainties account for more than 90% of the overall uncertainty. Experimental fluctuation becomes predominant near the top dead center and combustion event. The random component of the uncertainty for mesaurement of the incylinder pressure is estimated by calculating the standard deviation of peak pressure among 100 cycles at a stable engine operating point.

The heat release is usually integrated from net heat release rate expression given by as :

$$\frac{dQ}{d\theta} = \frac{\gamma}{\gamma-1}\ P\ \frac{dV}{d\theta} + \frac{1}{\gamma-1}\ V\ \frac{dP}{d\theta} \tag{3.37}$$

Uncertainty in Eq. (3.37) is mostly due to uncertainty in the $\frac{dP}{d\theta}$ estimates. The intervals chosen for the calculation of derivatives have to be carefully chosen since it has a significant impact on the estimation of uncertainty of value. Assuming linearity, the uncertainty for $\frac{dP}{d\theta}$ can be written as a function of the interval (j-i) :

$$\frac{dP}{d\theta} = \frac{P_j - P_i}{\theta_j - \theta_i} \tag{3.38}$$

Where i and j refer to i_{th} and j_{th} row of experimental data (here: pressure) recorded every 0.1 crank angle degrees with j-i > 0. P_j, P_i, θ_j, and θ_i each having an associated uncertainty.

Therfore, $U(\theta_i) = U(\theta_j)$:

$$U\left(\frac{dP}{d\theta}\right) = \frac{\sqrt{U^2(P_i) + U^2(P_j) + 2\left(\frac{P_j - P_i}{0.1(j-i)}\right) U^2(\theta_i)}}{0.1\,(j-i)} \tag{3.39}$$

The uncertainty in pressure, volume, and ratio of specific heat plays an insignificant role and hence not considered in the analysis for the uncertainty of equation 3.39 [3.21]. Uncertainties of combustion parameters and technical details of all measured parameters are presented in Table 3.7 and Table 3.8. In Table 3.7, it can be seen that, the uncertainty for pressure measurement comes out to be 5%. Also, uncertainty in $\left(\frac{dP}{d\theta}\right)$ comes out to be 5%. The uncertainty in heat release rate is directly related to uncertainty in $\left(\frac{dP}{d\theta}\right)$.

Table 3.7 Uncertainties of Combustion Parameters

Combustion Parameter	**Uncertainty (%)**
Incylinder Pressure	5 %
$U\left(\frac{dP}{d\theta}\right)$ *(j-i = 20)*	5%

Table 3.8 Technical details of measured parameters

Variable measured	**Instruments**	**Range**	**Accuracy**	**Linearity**	**Hysteresis**	**Resolution**
Incylinder pressure	Piezoelectric sensor	5000 psi	± 1.2 bar	± 1%	1%	0.05 psi (rms)
Crank angle	Optical encoder	-----	± 0.1 CAD	------	------	0.1 CAD

3.2.6.2 Uncertainty Analysis of Particle Emission Measurements

Uncertainties in particle emission measurement can arise from the accuracy of the particle measurement instrument and random errors [3.23-3.27]. For particle emission measurement tests were carried out steady state engine operating conditions. Particle emissions were measured close to the engine exhaust valve, and the data have been collected for sampling frequency of 1HZ. For every engine operating condition, the data is logged at steady state and thermally stable condition. The mean of data of 60 sec is utilized for analyzing particle size and number distribution. Combined standard uncertainty u_N at 95% confidence level for total particle number concentration, nucleation mode particle concentration, and accumulation mode particle concentration was calculated using the root sum square method assuming normal distribution of errors [3.23].

$$u_N = \sqrt{u_r^2 + u_s^2} \tag{3.40}$$

Where u_s represents the uncertainty due to systematic error and u_r represent uncertainty due to random error. The random error was calculated by taking the standard deviation of 64 measurements. Uncertainity (%) of particle emissions parameters is presented in Table 3.9. The accuracy of the particle sizer is presented in Table 3.10.

Table 3.8 Uncertainties of Particle Emissions Parameters

Particle emission parameter	**Uncertainty (%)**
Total Particle number	1.3
Nucleation mode particle number	1.5
Accumulation mode particle number	1

Table 3.9 Accuracy of particle sizer

Particle diameter (nm)	Accuracy (95% CI)
Upto 300 nm diameter	± 5% Standard deviation
Over 300 nm	±10% Standard deviation

Chapter 4

Results and Discussions

This chapter presents the main results of this research work. In this chapter, the observations regarding the combustion and particulate matter (PM) emissions characteristics of diesel and RCCI engines are presented. Combustion and in cylinder PM characteristics of diesel engine is investigated by conducting a numerical study on a single cylinder automotive diesel engine using detailed soot model based on method of moments available in ANSYS FORTE CFD software. Combustion and PM emission characteristics of RCCI engines is investigated by conducting experimental study on modified single cylinder automotive diesel engine. This chapter is divided into three sections. The first section presents the combustion analysis of diesel and RCCI engines. In the second section results related to particulate emission characteristics of diesel and RCCI engines are discussed. In the last section results related to the characterization of solid particle emissions from RCCI engine using developed thermodesorption system are presented.

4.1 Numerical Model

Experimental in-cylinder combustion pressure and heat release rate published in the article authored by Saxena and Maurya [4.1] is used to validate the simulated in-cylinder pressure and heat release rate at engine speed of 1500 rpm, load of 1.5 bar BMEP, diesel injection timing of 12 °bTDC and diesel injection pressure of 500 bar. Additionally, simulated in-cylinder pressure and rate of heat release (ROHR) are also validated with experimental results for diesel injection pressures of 800 bar and 1000 bar. The initial swirl ratio and swirl factor were assumed to be 1.1 and 3.11 respectively. Figure 4.1 - 4.3 shows the comparison between experimental and numerical in-cylinder pressure and heat release rate at different injection pressures. These figures indicate that numerically simulated in-cylinder pressure and heat release rate are matched with experimental in-cylinder pressure and heat release rate with good accuracy. Minor difference in the peak of cylinder pressure is possibly due to the chemical mechanism employed for the numerical investigation as the combustion processes. Experimental and numerical in-cylinder combustion pressure matched decently; therefore, the detailed combustion mechanism can be used for combustion and PM analysis for this engine. Slight variation in combustion phasing between experimental and numerical results can be due to the initialization of initial temperature and pressure at inlet valve closing. Figure 4.4 shows the validation of simulated soot particle number density with experimental results. It also indicates that the numerically investigated soot particle number density at fixed operating condition is decently matched with the experimental results. Slight variation in combustion phasing between experimental and numerical results can be due to initialization of initial temperature and pressure at inlet valve closing.

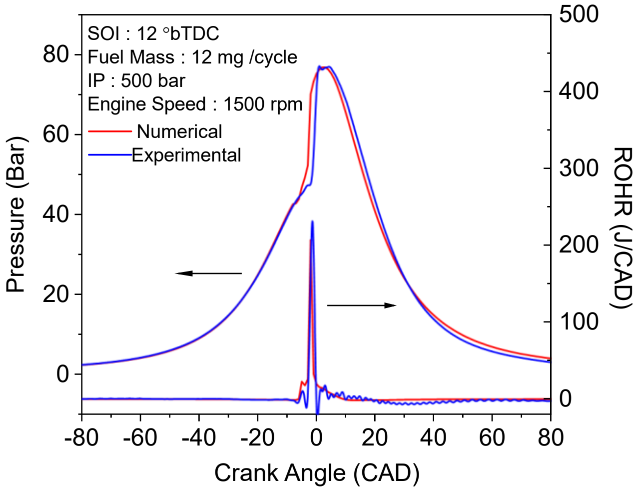

Figure 4.1 Comparison of experimental and numerical in-cylinder combustion pressure at 500 bar injection pressure (IP).

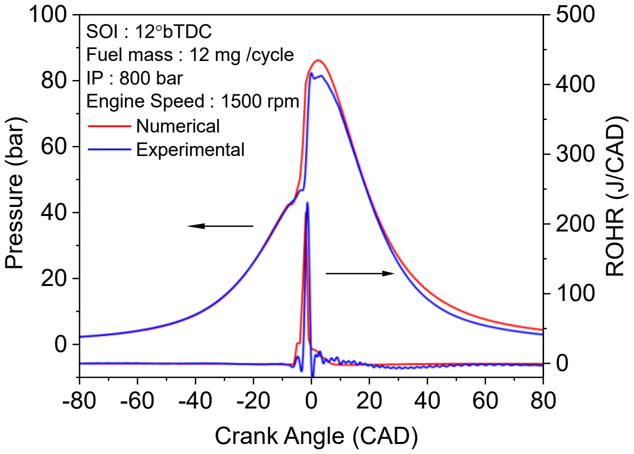

Figure 4.2 Comparison of experimental and numerical apparent heat release rate at 800 bar injection pressure (IP)

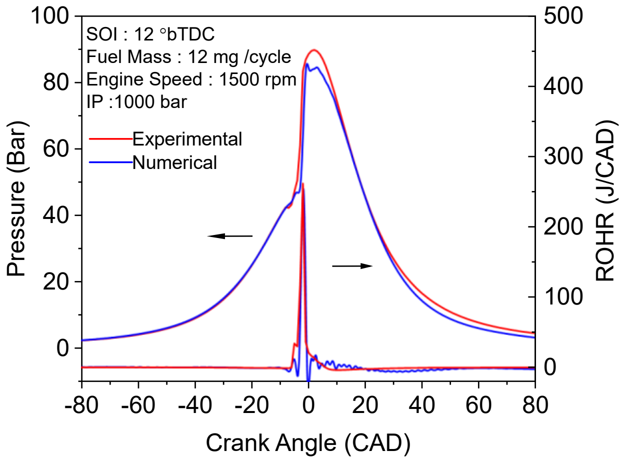

Figure 4.3 Comparison of experimental and numerical in-cylinder combustion pressure at 1000 bar injection pressure

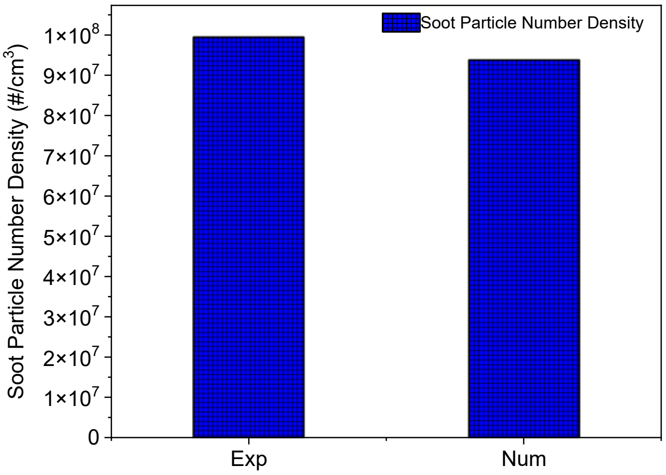

Figure 4.4 Comparison of experimental and numerical results of soot particle number density at engine speed of 1500 rpm , Load : 1.5 bar BMEP, Injection timing : 12°bTDC and 500 bar injection pressure.

4.2 Combustion Analysis

This section presents the combustion characteristics of diesel and RCCI engine. This section is divided into two subsections in which first subsection present the combustion analysis of diesel engine and the second subsection presents the combustion analysis of RCCI engine. In each subsection effect of engine operating parameters has been analyzed and discussed.

4.2.1 Combustion analysis of diesel engine

Figure. 4.5 (a) depicts the effect of injection timings on in-cylinder pressure and apparent heat release rate (AHRR). It can be observed that the even though the in-cylinder pressure increased with advanced diesel injection, but the AHRR decreases when diesel injection timing was advanced from 6° bTDC to 15° bTDC. The decreased AHRR is because of the less amount of premixed fuel auto-ignites primarily. In this range of injection timing, charge burn in both premixed and diffusion-controlled combustion due to short ignition delay. For earlier diesel injection, comparatively more time is available for the mixing of diesel with air which decreases the charge reactivity, thus it does not auto-ignite immediately. For 18° bTDC, the time available for mixing is significantly higher and nearly whole charge is premixed and burnt during the end stage of compression stroke, which leads to steep rise in the peak AHRR and peak pressure. Figure 4.5 (b) shows the effect of injection timing on in-cylinder mean gas temperature. It can be seen that gas mean temperature increases when injection timing is advanced from 6° bTDC to 18°bTDC. This is due to the high in cylinder pressure generated during advanced injection timings due to combustion taking place in the compression stroke of the engine cycle [4.2]. Figure 4.6 (a-b) shows the effect of fuel injection pressure on combustion characteristics. It can be observed that with an increase in fuel injection pressure, the peak in-cylinder pressure and heat release increases. This is due to improved fuel air mixing at high injection pressure because of smaller droplet size and increased turbulence. Improved fuel air mixing increases the premixed and diffusion combustion rate which increases the peak cylinder pressure and heat release rate. Figure 4.6 (b) shows the effect of fuel injection pressure on mean gas temperature. It can be observed that with an increase in injection pressure, the mean gas temperature increases due high peak in-cylinder pressure due to high combustion rate.

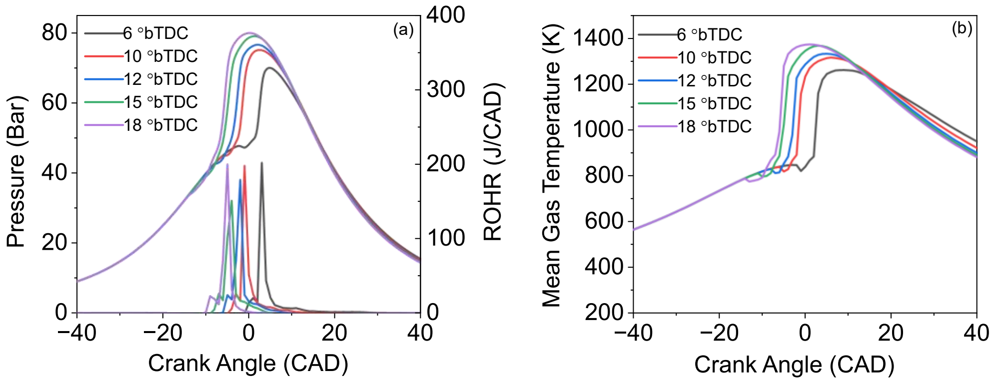

Figure 4.5 Effect of fuel injection timing on (a) in-cylinder Pressure and heat release rate (b) Mean gas temperature.

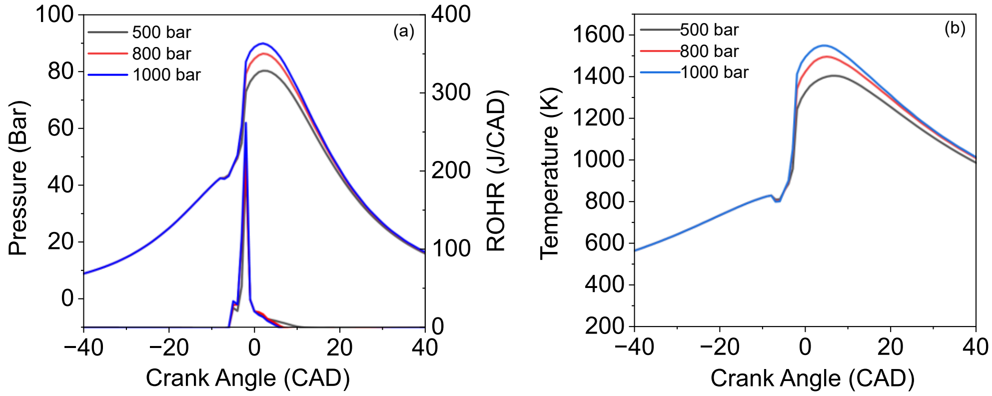

Figure 4.6 Effect of fuel injection pressure on (a) in-cylinder Pressure and heat release rate (b) Mean gas temperature.

4.2.2 Combustion analysis of RCCI engine

4.2.2.1 Incylinder Pressure and Heat Release Analysis

This section presents the combustion characteristics of the gasoline diesel, methanol diesel and CNG diesel dual-fuel RCCI operation. The comparison of in-cylinder pressure and HRR for gasoline diesel and methanol diesel dual-fuel RCCI operation is shown in Figure 4.7 (a-b). HRR curve for 10° bTDC diesel SOI shows the two distinct phases of combustion like conventional dual-fuel operation, i.e., premixed and mixing controlled combustion phase. For advanced 40° bTDC diesel SOI, only a premixed combustion phase is observed (symmetric HRR trace). Similar trend is observed for both the fuel operations. For the RCCI operation (i.e., 40° bTDC), the peak HRR and in-cylinder pressure are lower than conventional dual-fuel operation. In RCCI operation, diesel has adequate time to mix with the premixed mixture of LRF (i.e., gasoline/methanol) and air, which creates the fuel reactivity stratification inside the cylinder. This causes to decrease in the local equivalence ratio of charge and reactivity gradient of the charge. A lower local equivalence ratio leads to a reduction in the rate of autoignition reactions. Therefore, initiation of combustion is delayed, and the combustion initiates from the location where autoignition condition is reached in the most reactive zone of the combustion chamber. The delayed start of combustion, correspondingly, CA_{10} and CA_{50} (combustion phasing), is also retarded and increases the combustion duration. Figure 4.7 (a) indicates that for 10° bTDC diesel SOI (i.e., conventional dual-fuel operation), the peak HRR is lower and advanced with a double injection strategy compared to a single injection strategy, whereas for 40° bTDC diesel SOI (i.e., RCCI operation), the peak HRR is higher and advanced with a double injection strategy compared to a single injection strategy. For 10° bTDC diesel SOI with double injection strategy, the decreased HRR is attributed to less fraction of diesel auto-ignite during premixed heat release (in the premixed phase of combustion) because a lower amount of diesel injected during the main injection in comparison of single injection strategy. The diesel fraction injected during pilot injection mixes with the premixed gasoline and air mixture and creates a comparatively higher reactivity charge but does not auto-ignite immediately. The auto-ignition starts from the most reactive zone after the main injection. For 40° bTDC diesel SOI (RCCI operation), the higher peak of HRR with double injection strategy is due to combustion of more fraction of premixed charge since the overall reactivity of the charge is relatively higher due to the pilot injection of diesel, which leads to an advanced and higher peak of HRR. Additionally, for conventional dual-fuel and RCCI operations, the peak HRR is lower for MD operation than GD operation for the same diesel SOI (except for 10° bTDC with single injection) (Figure 4.7(b)). Methanol has lower reactivity and LHV in comparison to gasoline. For maintaining the same energy of port injected fuel, more fraction of methanol needs to be injected. This leads to a decrease in the overall reactivity of the charge. Additionally, higher heat of vaporization of methanol leads to a decrease in the temperature of the charge during the compression. Both these factors contribute to retard the ignition timing; thus, the combustion phasing is also delayed. This leads to more fraction of fuel + air mixture burns when the piston moves toward BDC, resulting in decreased HRR. The peak of HRR is higher for MD operation at 10° bTDC diesel SOI with a single injection strategy. As discussed in dual-fuel operation, the combustion starts from the most reactive zone inside the combustion chamber. Overall charge reactivity is reduced due to the lower reactivity of methanol. Diesel is injected on a comparatively lower reactivity charge (methanol + air), leading to an increase in the ignition delay. Therefore, more fraction of the diesel burns in the premixed combustion phase. Additionally, inbound oxygen molecules of methanol also contribute to enhancing the premixed combustion. Both these factors lead to an increase in the peak of HRR. The effect of single and double injection strategy on cylinder pressure and ROHR of CNG diesel RCCI operation is shown in figure 4.8 (a-b). Figure 4.8 (a) indicates that advanced diesel SOI results in decreased peak cylinder pressure and ROHR in the case of a single injection strategy. Additionally, the peak ROHR is retarded. The peak ROHR is retarded and slightly increased with advanced diesel SOI for double injection strategy (Figure 4.8 (b)). The reasons for these observations are same as explained for gasoline and methanol fuels.

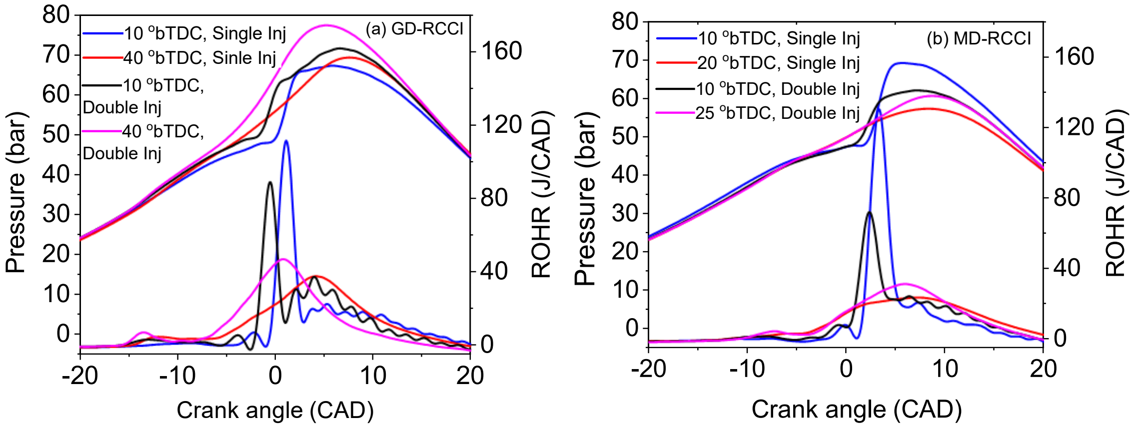

Figure 4.7 Cylinder pressure and HRR for GD and MD for conventional dual fuel and RCCI combustion for Single injection and double injection strategy.

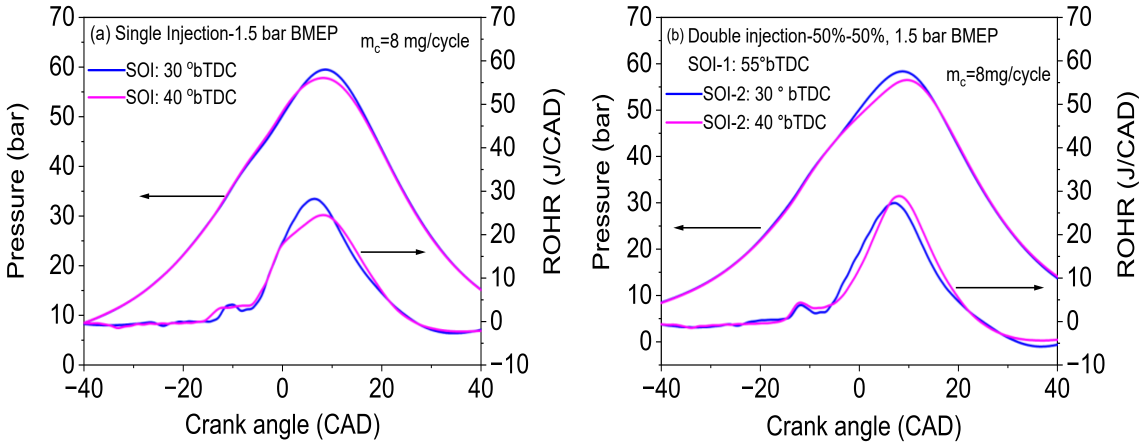

Figure 4.8. In-cylinder pressure and ROHR for (a) single (b) double injection strategy at 1.5 bar BMEP for CNG diesel RCCI operation.

4.2.2.2 LTHRR and HTHRR Analysis

(a) Effect of Single and Double Injection Strategy

This section discusses the effect of single and double injection on LTHRR and HTHRR of GD RCCI, MD RCCI and CNG diesel RCCI operation. It is observed that in dual-fuel operation (i.e., 10° bTDC), a small peak of LTHRR is obtained near about 4° bTDC, whereas for the case of RCCI operation, the LTHRR is too advanced and observed near about 12° bTDC. This finding is similar to both the injection strategies in conventional dual-fuel and RCCI operation with gasoline, methanol and CNG fuels. In conventional dual-fuel and RCCI combustion mode, the combustion process initiates with the spontaneous auto-ignition of the premixed charge during the compression stroke (because of an increase in in-cylinder pressure and temperature). The radical species such as HO_2, H_2O_2, OH, and H play a vital role in the auto-ignition process. The LTHR is mainly allied with the HO_2 and H_2O_2. The other crucial components to low-temperature branching in kinetics are the ketohydroperoxide radical and hydroxyl radicals (to a lesser extent). These radicals gradually increase with the engine cycle and reach a maximum point near the primary combustion [4.3], [4.4]. Additionally, the figure indicates that MD-RCCI operation has a lower peak of LTHRR than GD-RCCI operation for the same diesel SOI (Figure 4.9 (b)). Methanol is short-chain alcohol having a lower reactivity than gasoline and acts as a reaction inhibitor. The intermediate species such as CH_3O, HCO, CH_2O, and CH_2OH are mainly associated with methanol combustion [4.3], [4.4]. The decomposition of methanol during the combustion is mainly initiated with the abstraction of hydrogen by H, HO_2, and OH radicals. The abstraction of hydrogen by OH radical is favorable for the formation of CH_2OH and CH_3O. These intermediate radicals cause formaldehyde formation and help in controlling the charge (fuel–air mixture) reactivity. The abstraction of hydrogen from the formaldehyde produces the formyl radical and then oxidizes to form CO and CO_2. Methanol produces formaldehyde when the combustion temperature exceeds 800 K and then oxidizes to form CO and CO_2 [4.3], [4.4], [4.5]. However, in the RCCI regime, the charge reactivity depends on diesel injecting into the engine cycle.

The amount of LTHRR and its phasing play a vital role in the dual-fuel RCCI engine combustion characteristics. For better characterizing the LTHRR and HTHRR, separate LTHRR and HTHRR are extracted from the HRR traces. The methodology used for extracting the LTHRR and HTHRR discusses in the chapter 3. The amount of LTHRR and HTHRR is typically indicating the absolute area under the respective trace. The variation of LTHRR and HTHRR with diesel SOI for single and double injection strategy in GD operation is shown in figure 4.9. Figure 4.9 (a) indicates that in GD operation with a single injection strategy, the advanced diesel SOI leads to decrease the peak of LTHRR, and the phasing of LTHRR is also advanced. Generally, HRFs depict the two-staged HRR when the cool flame oxidation reactions (LTHR) occur prior to ignition in the temperature range of 760-880 K [4.3], [4.6]. The cool flame reaction starts earlier in the engine cycle when diesel SOI is advanced, resulting in advanced LTHRR. Additionally, with advanced diesel SOI, the amount of LTHRR increased, which is mainly because of increased LTHRR duration. The duration of LTHRR is higher with advanced diesel SOI because the cool-flame reactions take place with a slower oxidation rate at lower in-cylinder temperature conditions. The slower oxidation rate is due to the in-cylinder mixture lower temperature (because of the higher heat of vaporization of LRF). Advanced diesel SOI has a slightly higher in-cylinder mean gas temperature in GD operation in single and double injection strategy, mainly because of the advanced LTHRR. Additionally, the double injection strategy has a slightly higher in-cylinder mean gas temperature than the single injection strategy in GD operation due to the pilot injection of diesel, which will also contribute to low-temperature oxidation reactions. In the case of MD operation at 10° bTDC diesel SOI with a single injection strategy, the peak of in-cylinder mean gas temperature is higher due to the increased peak of LTHRR . The higher peak is attributed to more fraction of charge burns during low-temperature oxidation reactions. In the case of MD operation at 40° bTDC diesel SOI with a single injection strategy, diesel has adequate time to mix with the premixed charge of methanol and air. This leads to a decrease in the local equivalence ratio of the charge. Therefore, a small peak of LTHRR is observed during low-temperature reactions and results in decreased in-cylinder mean gas temperature.

For 10° bTDC diesel SOI, the conventional dual-fuel combustion is observed (Figure. 4.9 (b)). In contrast, for 40° and 50° bTDC diesel SOI timings, only a premixed combustion phase is present. When the diesel SOI is advanced from 40° bTDC to 50° bTDC, the peak of HTHRR decreases and is slightly retarded. For advanced diesel SOI, sufficient time is available to mix diesel with a premixed air and gasoline mixture. Availability of a long time for mixing caused to decrease in the local equivalence ratio of the charge. The peak of the HTHRR depends on its phasing, which relies on the local equivalence ratio of the charge. The local equivalence ratio of the charge changes with diesel SOI [4.7]. Thus, the retarded HTHRR with advanced diesel SOI is attributed to a decreased local equivalence ratio of the charge, which causes to slow down the high-temperature auto-ignition reactions. In conventional dual fuel injection timings, the advanced HTHRR is attributed to the combustion of locally rich charge [4.7], [4.8].

In GD operation, the LTHRR for 10° bTDC diesel SOI is lower and slightly advanced in double injection than a single injection strategy (Figure 4.9 (c)). The advanced LTHRR is because of the occurrence of cool-flame oxidation reactions earlier in the engine cycle since half of the total diesel is injected during the pilot injection. Additionally, the peak of LTHRR is higher and slightly advanced for 40° bTDC and decreases when further advanced to 50° bTDC. For RCCI operation, the peak and duration of LTHRR are higher and slightly advanced in the double injection strategy than a single injection strategy. This may be because of the overall higher reactivity of charge due to the pilot injection of diesel. Figure 4.9 (d) shows that the HTHRR is also decreased and delayed with advanced diesel SOI in the double injection strategy. For 10° bTDC diesel SOI, the peak of LTHRR is lower and advanced in double injection strategy than single injection strategy; correspondingly, the peak of HTHRR is also lower and advanced. As discussed earlier, the peak of HRR depends on CA_{50}. Local equivalence ratio and reactivity stratification play a vital role in the phasing of HRR.

Local charge and reactivity stratification vary with the amount of LRF inducted into the cycle, diesel SOI and number of injections. For 10° bTDC SOI with double injection strategy, a lower fraction of diesel is injected in the main injection. Since in conventional dual-fuel, the combustion starts from the most reactive zone in the combustion chamber, the combustion initiates earlier in the cycle. It is due to the relatively high overall reactivity of the charge because of the pilot injection of diesel and the lower fraction of diesel burns during the cool-flame low-temperature reaction. Thus, it results in decreased and advanced LTHR. The advanced LTHR and relatively higher charge reactivity than the single injection strategy (due to pilot injection) lead to an increase in the in-cylinder mean gas temperature. This causes to increase in the high-temperature oxidation reactions rate and results in advanced HTHRR. On the other hand, the peak of LTHRR is higher and advanced (especially for 40° bTDC) in double injection strategy; correspondingly, the HTHRR is also higher and advanced for the same injection timing (Figure. 4.9 (c) and 4.9 (d)). For RCCI operation, the higher peak of HTHRR with double injection strategy is attributed to an increase in the overall mixture reactivity, which leads to prior ignition. Thus, the phasing is advanced and results in higher HTHRR. This observation confirms that the amount of LTHR and its phasing play a key role in the phasing of RCCI combustion. Interestingly, the amount of HTHR increases with advanced diesel SOI (except for 50° bTDC with a single injection strategy) due to an increase in high-temperature oxidation reactions duration. In this study, the amount of HTHR is considered as the area under the curve. When diesel SOI is advanced, the CA_{10} and CA_{50} position in RCCI combustion is retarded due to the slower rate of high-temperature oxidation reaction (because of a decrease in the local equivalence ratio of the charge) and resulted in a longer high-temperature combustion duration. For a longer high-temperature combustion duration, the area under the trace is higher; therefore, HTHR will be higher.

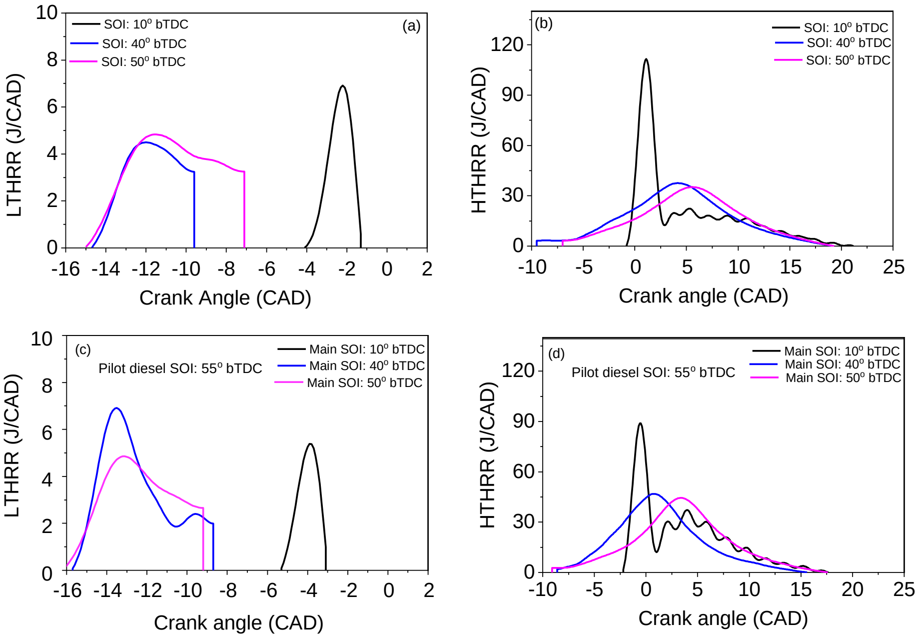

Figure 4.9 LTHRR and HTHRR rate at different diesel SOI with single and double injection strategy for GD operation

The LTHRR and HTHRR for different diesel SOI with single and double injection strategies for MD operation are shown in Figure 4.10. The typical trend of HTHRR for MD operation is the same as that for GD operation; i.e., for 10° bTDC diesel SOI, HTHRR trace depicts premixed and mixing control combustion phase as well, whereas, for advanced diesel SOI, symmetric premixed heat release is observed. Additionally, RCCI operation shows advanced and reduced LTHRR compared to conventional dual-fuel operation, same as GD operation. The possible reason for this observation is the same as discussed in Figure 4.9. For 10° bTDC diesel SOI, the MD operation has retarded and a higher peak of LTHRR (close to TDC position). In contrast, the peak of LTHRR is comparatively retarded and lower in RCCI operation (40° bTDC with single injection) compared to GD operation for both the fuel injection strategies.

Methanol is an ignition suppression and reaction inhibitor additive, which causes to slows down the autoignition reactions and results in a longer ignition delay. A study investigated the sensitivity analysis of ignition delay measured in a rapid compression machine for methanol/O_2/Ar mixture (on the operating condition of 30 bar, 905 K, under stoichiometric conditions) [4.9]. The study found that the reactions that mainly promote the ignition delay are $CH_3OH + HO_2 \leftrightarrow CH_2OH + H_2O_2$ and $H_2O_2(+M) \leftrightarrow OH + OH\ (+M)$. Initially H_2O_2 is formed, which decomposes to reactive OH radical [4.9]. However, the combining of HO_2 radical restrict the autoignition of methanol ($HO_2 + HO_2 \leftrightarrow H_2O_2 + O_2$) [4.3]. As discussed, in conventional dual-fuel operation, the combustion initiates with the autoignition of diesel fuel from the most reactive core in the combustion chamber. Since methanol has a higher autoignition temperature and lower reactivity than gasoline, it causes to relativity longer ignition delay. Additionally, methanol has a higher heat of vaporization than gasoline, which will reduce the in-cylinder mixture temperature during the compression stroke, contributing to a longer igniting delay period. In conventional dual-fuel operation (10° bTDC), combustion of relatively more mixture during low-temperature oxidation reactions (due to higher oxygen content of methanol) leads to increases in the peak LTHRR and amount of LTHR than the GD operation. The higher peak of LTHRR causes a further increase in the in-cylinder mean gas temperature, resulting in an advanced peak of HTHRR. On the other hand, methanol has lower reactivity and higher heat of vaporization, which will cause to retard the ignition timing, and correspondingly the CA_{50} of HRR will be retarded. With the advanced diesel SOI, the HTHRR also decreases and retarded also in MD-RCCI operation (Figure. 4.10 (c) and 4.10 (d)). The reason for this observation is the same as discussed in the case of the GD-RCCI operation. The phasing of HTHRR is more retarded for MD operation in comparison with GD operation. This is mainly attributed to the lower overall reactivity of the MD operation charge compared to the GD operation.

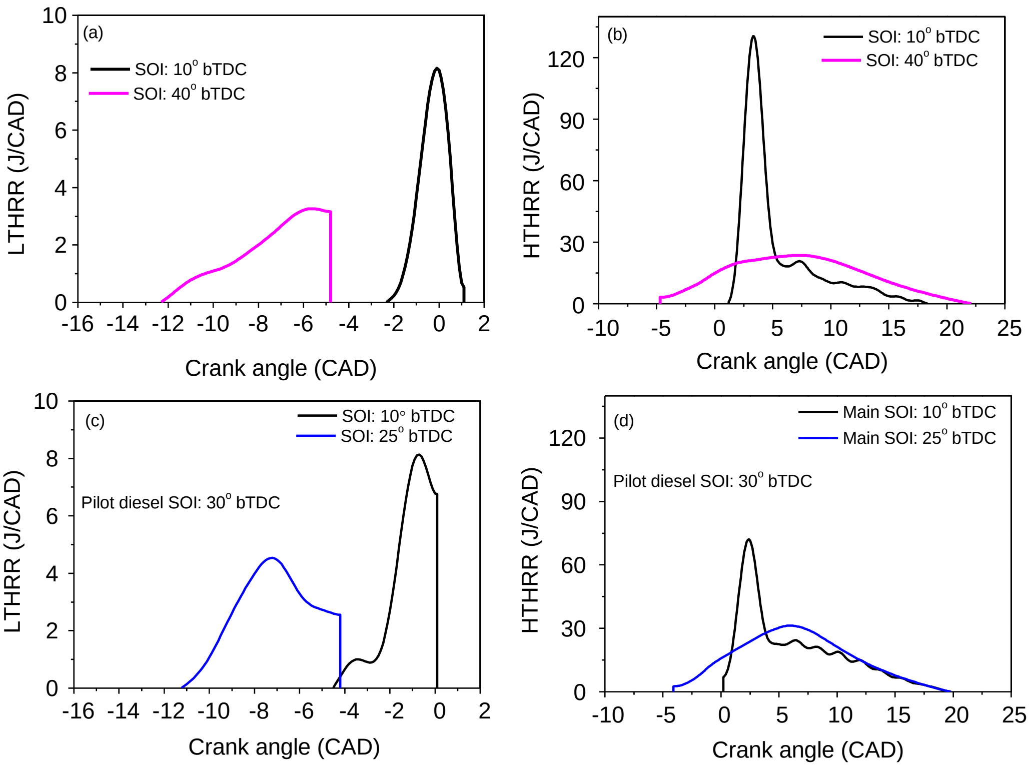

Figure 4.10. LTHRR and HTHRR at different diesel SOI in MD operation

Figure 4.11 (a-d) shows the effect of diesel SOI on LTHRR and HTHRR with single and double injection strategy for CNG diesel RCCI operation. In the single injection strategy, the advanced diesel SOI leads to a slightly advanced and reduced peak LTHR; correspondingly, the peak HTHR is also reduced and delayed (figure 4.11 (a-b)). Additionally, the duration of LTHR increased with advanced diesel SOI (figure 4.11 (a)). With advanced diesel SOI, low-temperature oxidation reactions start with a slower auto- ignition rate earlier in the engine cycle. The formation of active radicals starts earlier due to a leaner charge and its distribution. It causes an earlier start of combustion. A study found that in case of single injection strategy, CH_4 pathways were found more dominant in LTHR [4.10]. Lower local in-cylinder temperature and equivalence ratio leads to a decrease in the progression rate of combustion during low-temperature cool flame reactions, leading to an increase in the duration of LTHR. Availability of HO_2, OH, H_2O_2, O, and H radical also affects the amount and phasing of HTHR. HCO, CH_2O, and CO play a vital role at higher temperatures through HO_2, OH, H_2O_2, O, and H active radicals in the formation of HCO, which further reacts with O_2/O and forms CO and CO2 [4.10]. A decrease in local charge equivalence ratio with advanced diesel SOI also causes to decrease in the progression rate of high-temperature oxidation reactions. For 40° bTDC diesel SOI, comparatively leaner charge burns during the high-temperature oxidation reactions. More fraction of premixed leaner charge burns when piston moving towards the bottom dead centre (BDC) (during expansion volume expansion rate is higher), resulting in decreased and delayed HTHR. Similar to the single injection strategy, in the case of the double injection strategy, C_7H_{16} split up into C_7H_{15}-1, C_7H_{15}-2, and other lighter hydrocarbons by CH_3 and OH radicals during cool flame oxidation reactions. C_7H_{15}-1 and C_7H_{15}-2 react with O_2 and produce $C_7H_{15}O_2$. Later, ketone species of C_7KET_{21} are formed and split up in CH_2O, CO, and other hydrocarbons [4.10]. Additionally, CH_4 reacts with O/H/OH radicals and split into CH_3. CH_3 further reacts with HO_2, O_2, (+M), and O and splits into CH_3O, CH_2O, and C_2H_6 [4.9]. Figure 4.10 (c-d) shows that the peak LTHR increases with earlier SOI; correspondingly, the peak HTHR also slightly increases. Additionally, the duration of LTHR is reduced with advanced diesel SOI in a double injection strategy. The increased peak LTHR with reduced duration depicts an enhanced rate of cool-flame oxidation reactions. For advanced SOI (i.e., 40° bTDC), excessive diesel accumulated due to pilot and main injections with insufficient time for mixing with premixed CNG + air charge, which may lead to the comparatively locally fuel-rich region inside the combustion chamber [4.11]. It causes slightly delayed ignition timing and a comparatively more fraction of locally rich charge burns during cool flame oxidation reactions, resulting in an increased peak of LTHR. The shorter duration of LTHR is due to the progressive combustion rate of locally rich charges. In the case of the double injection strategy, the reactivity of the charge is relatively higher than the single injection strategy, which will cause an advanced ignition timing. However, the start of ignition will also depend on the local equivalence ratio and its distribution. 50% of the total amount of diesel is injected during the pilot diesel injection (55° bTDC), which will increase the reactivity of the charge in the double injection strategy, but the local equivalence ratio will be relatively decreased in the case of 30° bTDC diesel SOI (because pilot injected diesel has adequate time for blending). Auto-ignition of charge with a lower local equivalence ratio leads to a decrease in the rate of low-temperature reactions and increase in duration of LTHR in case of 30° bTDC diesel SOI. Local temperature condition also affects the ignition delay. Availability of O_2 (in the air) at the start of combustion affects the LTHR. A study found the formation of O, HO_2, and O_2 species in higher concentration leads to delayed LTHR [4.11].

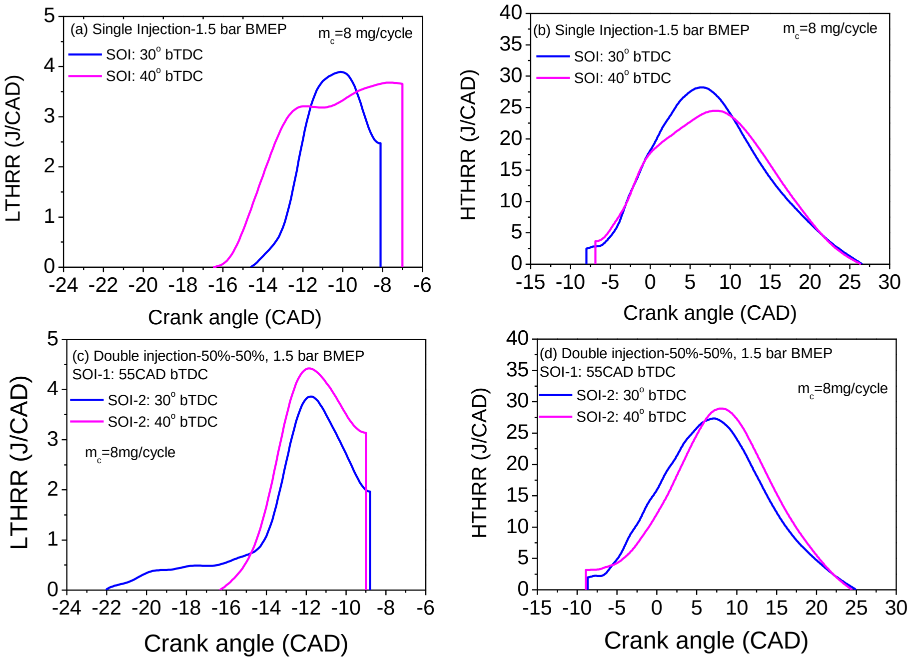

Figure 4.11 LTHRR and HTHRR for single and double injection strategy for CNG diesel RCCI operation at 1.5 bar BMEP (lower load)

The effect of the diesel mass split injection strategy on LTHR and HTHR at medium load is shown in Fiure 4.12 (a-d) for CNG diesel RCCI operation. For the 50%-50% diesel split injection strategy, when diesel SOI is advanced from 30° to 40° bTDC, the peak LTHR decreases and slightly advances. It is significant to note here that the ignition starts almost from the same location for both the diesel SOI. Up to a certain crank angle degree (16° bTDC in 50-50% diesel mass split injection strategy), no significant variation in LTHR trajectory (slope) is observed with diesel SOI. However, after 16° bTDC the rate of oxidation reactions starts increasing. For advanced diesel SOI (40° bTDC), the rate of the low-temperature oxidation reaction is relatively higher than 30° bTDC diesel SOI due to the formation of locally rich charge and possibly distributed non-uniformly inside the combustion chamber. The auto-ignition of relatively rich charge results in advanced LTHR. The lower peak of LTHR is due to less fraction of premixed diesel autoignites during the initial phase of LTHR. After attaining the certain low-temperature oxidation reactions, further reactions occur with a slower progression rate in the low-temperature region, leading to an increase in the LTHR duration due to the lower local equivalence ratio and its distribution. A similar inclination of LTHR with SOI is observed for 70%-30% diesel split injection strategy (Figure 4.12 (c)). Additionally, the start of ignition is slightly advanced for the 70-30% diesel mass split injection strategy than 50-50% injection strategy. It is due to comparatively higher charge reactivity because 70% of the total diesel is injected during the pilot injection. In the case of 50-50% diesel mass injection strategy, the earlier SOI leads to retard the HTHR (Figure 4.12 (b)). For advanced diesel SOI, initially, the progression rate of high-temperature oxidation reactions are slower, and premixed charge auto-ignites when the piston moves towards BDC. It results in a delayed peak of HTHR. For 30^{0} bTDC diesel SOI, the peak HTHR is lower and retarded for 70 – 30% diesel mass split injection strategy (Figure 4.12 (d)) than for 50-50% diesel mass split injection strategy. A higher peak HTHR for 40° bTDC diesel SOI than 30° bTDC is attributed to a greater fraction of premixed combustion during high- temperature oxidation reactions. Additionally, the HTHR is more retarded for a 70-30% diesel mass split injection strategy than the 50-50% diesel mass split.

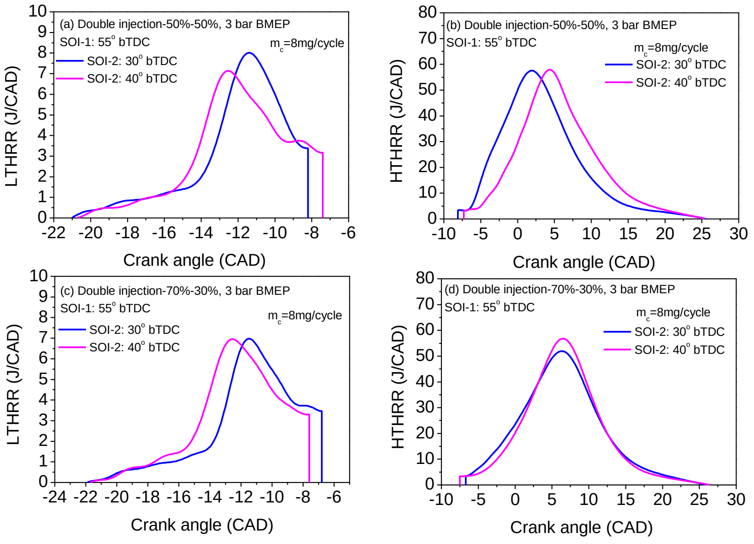

Figure 4.12. Influence of diesel mass split regime on LTHRR and HTHRR for CNG diesel RCCI operation at 3 bar BMEP (medium load)

(b) Effect of CNG Mass

The variation of LTHRR and HTHRR with m_c is shown in Figure 4.13 (a-d). The figure indicates an increase in m_c resulting in reduced and retarded LTHRR and HTHRR. CNG has lower reactivity. An increase in the CNG mass causes a decrease in the overall charge reactivity, leading to a longer ignition delay. As discussed, the availability of O_2 (in the air) at the start of combustion affects the LTHR. An increase in m_c relatively displaces more amount of air inducted into the cylinder during the intake stroke. Availability of less fraction of O_2 at the time of auto-ignition reactions may also contribute to longer ignition delay. Since the engine is tested at constant engine speed and load condition, the amount of diesel injected in the cycle decreases with an increase in the m_c. Thus, less diesel auto-ignites during the cool flame oxidation reactions resulted in reduced and delayed LTHR. For the same diesel SOI, the duration of LTHR decreased with an increase in m_c due to the lower fraction of diesel auto- ignite during low-temperature auto-ignition reactions [4.12- 4.14]. Decrease in charge reactivity with mc leads to reduce the progression rate of high-temperature oxidation reactions and more percentage of charge burns during expansion which results in decreased and retarded HTHR. Additionally, the peak HTHR is lower and retarded in the 70 -30% diesel mass split injection strategy for the same m_c. In 70-30% diesel mass split injection strategy, 70% mass of the total mass is injected during the pilot injection; thus, more percentage of diesel is premixed, leading to a reduction in the local charge equivalence ratio resulting in decreased and retarded HTHR. Retarded HTHR can also be seen for this injection strategy in Figure 4.12.

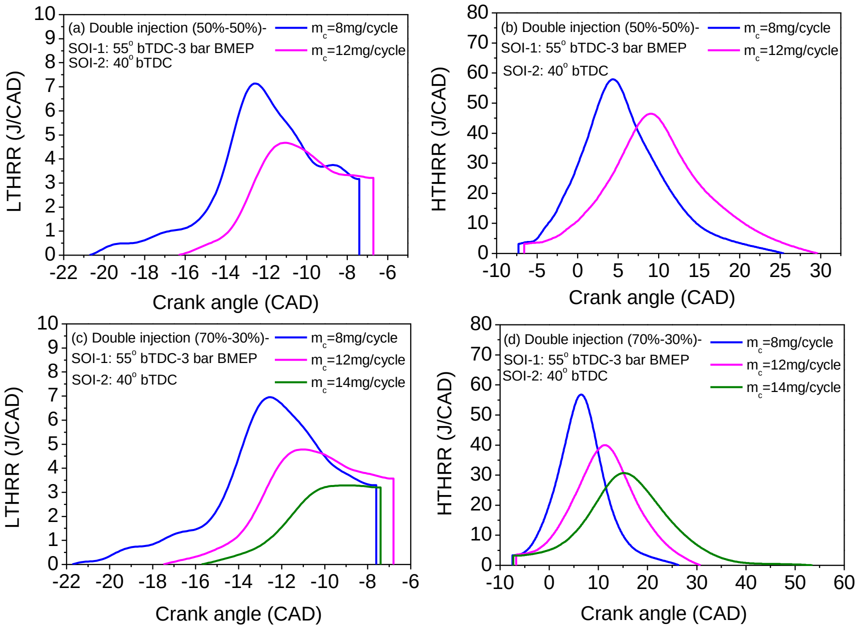

Figure 4.13 Variation of LTHR and HTHR with CNG mass

4.2.2.3 CA_{10} and CA_{50} Analysis

Figure 4.14 shows the variation of peak LTHRR and combustion phasing (CA_{50}) with diesel SOI for GD RCCI and MD RCCI operation. The values mentioned inside the figure depict the diesel SOI. For a higher amount of LTHR, the CA_{50} position is advanced. For conventional dual-fuel operation (10° bTDC), the peak LTHRR is higher, and CA_{50} is comparatively more advanced than RCCI operation (Figure 4.14). The peak and amount of LTHR depend on the location and duration of LTHRR, in-cylinder mean gas temperature during low-temperature oxidation reactions, amount of fuel burnt during low-temperature reactions, and local equivalence ratio of the charge. Some factors are dominating under certain conditions. In conventional dual-fuel operation, the diesel is injected on a relatively more compressed premixed mixture of LRF and air. The delayed diesel SOI (10° bTDC) leads to form a stratified charge. The higher LTHRR peak is due to auto-ignition of more fraction of stratified charge during low-temperature cool-flame reactions because of relatively higher in-cylinder local temperature during the start of combustion. The low-temperature reactions initiate with a locally rich charge (since the combustion begins from the most reactive core). The higher peak of LTHRR may lead to the advanced CA_{50} position due to the initiation of high-temperature oxidation reactions earlier in the cycle. Figure 4.14 indicates that in the case of a single injection strategy when diesel SOI is advanced from 10° bTDC to 40° bTDC (RCCI operation), the peak of LTHRR decreases, and correspondingly, the CA_{50} position is retarded. The cool-flame oxidation reaction starts earlier in the engine cycle when the diesel SOI is advanced, resulting in advanced and decreased LTHRR. The reduced peak of LTHRR is because of the slower rate of low-temperature oxidation reactions due to lower local equivalence ratio and distribution, which causes to increase in the duration of LTHR. Even though the duration of LTHR is higher (Figure 4.9 (a)), the lower local equivalence ratio of the charge leads to retard the CA_{50} position due to a slower rate of high-temperature oxidation reactions. Further, an advanced diesel SOI from 40° to 50° bTDC leads to a slight increase in the peak of LTHRR; however, the CA_{50} is retarded. This is because of the comparatively lower local equivalence ratio for 50° bTDC diesel SOI than 40° bTDC diesel SOI.

In the double injection strategy, the CA_{50} is advanced for all the diesel SOI timings, irrespective of peak LTHRR (Figure 4.14). The advanced CA_{50} position in the double injection strategy is attributed to increased reactivity of the charge due to the pilot injection diesel in the double injection strategy. In the double injection strategy, when diesel SOI is advanced from 10° to 40° bTDC, the peak of LTHRR is increased; correspondingly the CA_{50} position is also advanced. Further advanced diesel SOI from 40° to 50° bTDC results in a decreased peak of LTHRR and retarded CA_{50}. The slower rate of cool-flame oxidation reactions and lower local equivalence ratio of the charge is responsible for the reduced peak of LTHRR and delayed CA_{50}. A similar trend is observed in the case of MD operation; i.e., with advanced diesel SOI, the peak of LTHRR decreases, and correspondingly the CA_{50} is retarded (Figure 4.14). For conventional dual-fuel operation (10° bTDC), the CA_{50} is retarded in MD operation, whereas the peak of LTHRR is higher than that of GD operation for both the fuel injection strategies. Methanol fuel has inbound oxygen molecules that are possibly improving the cool-flame oxidation reactions since the more stratified charge is prepared for this injection timing. Thus, more fraction of charge burns during the Low-temperature reactions and results in increased peak and amount of LTHR. On the other hand, lower reactivity, and higher heat of vaporization lead to a slowdown high-temperature oxidation reactions responsible for the retard CA_{50} position. In general, it is observed that for RCCI operation, the retarded CA_{50} is observed where peak LTHRR is lower in most cases. As discussed earlier, local equivalence ratio and charge reactivity stratification play a vital role in the CA_{50} position. Local charge and reactivity stratification vary with the amount of LRF inducted into the cycle, diesel SOI, and number of injections. For RCCI diesel SOIs, diesel has adequate time to mix with the premixed charge of LRF and air, leading to a decrease in the charge's local equivalence ratio. This causes a reduction in the rate of low-temperature oxidation reactions and results in a decreased peak of LTHRR. The reduced peak of LTHRR causes to lower high-temperature oxidation reactions rate due to a lower local equivalence ratio. It results in a delayed CA_{50} position.

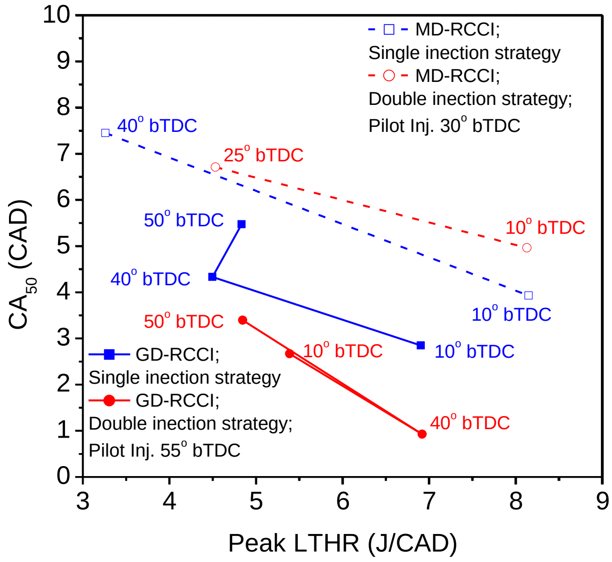

Figure. 4.14 Variation of peak LTHRR and combustion phasing (CA_{50}) with diesel injection timing for GD RCCI and MD RCCI operation

The variation of CA_{10} and CA_{50} with diesel SOI for CNG diesel RCCI operation is shown in Figure 4.15 (a-b). The values shown corresponding to CA_{10} are the amount of LTHR, whereas the values corresponding to CA_{50} are the amount of HTHR for respective diesel SOI. The amount of LTHR and HTHR depicts the absolute area under the curve. In a single injection strategy, advanced/earlier diesel SOI leads to retard the CA50 even though the CA10 is slightly advanced (Figure 4.15(a)). The slightly advanced CA_{10} is due to the early start of low-temperature oxidation reactions for 40° bTDC diesel SOI. The delayed CA_{50} indicates the slower rate of high-temperature oxidation reactions due to a lower local equivalence ratio. For the double injection strategy, CA_{10} and CA_{50} positions are retarded with earlier SOI. Advanced diesel SOI enhanced the blending of diesel with the premixed charge of CNG and air (due to the availability of a relatively higher time for premixing), leading to a decrease in the local equivalence ratio of the charge. Therefore, the rate of reactions during low and high temperature is reduced and results in delayed CA_{10} and CA_{50} positions. It is observed that the amount of LTHR increased with advanced diesel SOI. An increase in the amount of LTHR is mainly due to the slower rate of low-temperature cool flame oxidation reactions, which increases the duration of LTHR. The figure indicates that for the single injection strategy, advanced diesel SOI resulted in a decreased amount of HTHR. The decrease in the amount of HTHR is mainly due to a reduced and retarded peak HTHR. However, in the double injection strategy, the amount of HTHR increased with earlier SOI. The increase in the amount of HTHR is due to an increased peak HTHR.

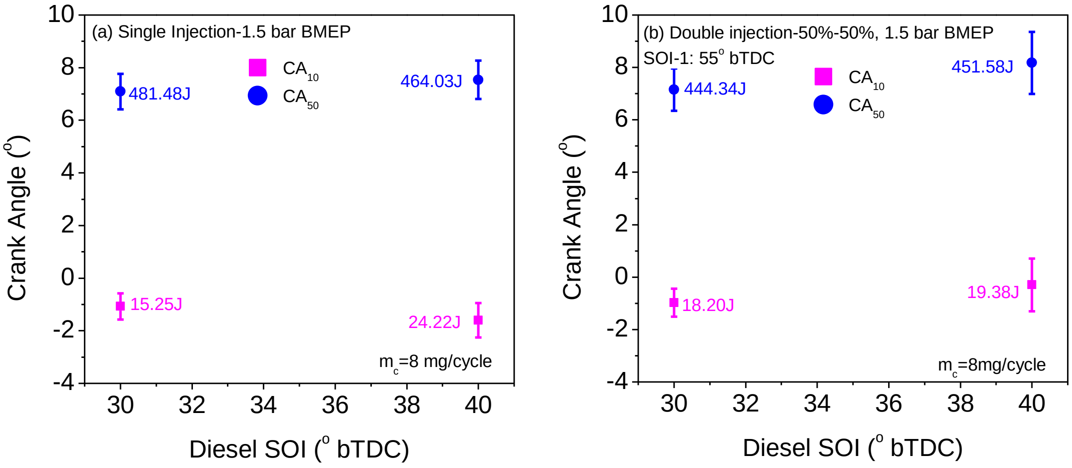

Figure 4.15 Influence of single and double injection regime on CA$_{10}$ and CA$_{50}$ at 1.5 bar BMEP for CNG diesel RCCI operation

Figure 4.16 (a-b) shows the effect of the diesel mass split injection strategy on CA$_{10}$ and CA$_{50}$. Advanced diesel SOI led to delayed CA$_{10}$ and CA$_{50}$. The reason for the delayed CA$_{10}$ and CA$_{50}$ with diesel SOI is the same as discussed in Figure 4.11. The figure indicates that the CA$_{10}$ and CA$_{50}$ are more delayed in the 70-30% diesel mass split injection strategy even though the combustion starts earlier Figure 4.12. The earlier start of combustion is because of the relatively higher reactivity of the charge. The delayed CA$_{10}$ and CA$_{50}$ indicate a slower combustion rate in the case of 70-30% diesel mass split injection strategy. The slower combustion rate is because of the lower local equivalence ratio since more percentage of diesel is injected during the pilot injection, and more time is available for blending of diesel (injected during pilot injection) with a premixed charge of air and CNG. With advanced diesel SOI, the amount of LTHR increases, whereas the amount of HTHR decreases (figure 4.12). The increase in the amount of LTHR is due to the combustion of more fraction of charge during cool flame oxidation with a slower rate, leading to an increase in the duration of LTHR. The slight decrease in the amount of HTHR with advanced diesel SOI is attributed to a lower fraction of charge burns during high-temperature oxidation reactions with retarded CA$_{50}$. It can be understood that even though the CA$_{50}$ is delayed with advanced diesel SOI, the HTHR ends almost from the same position. Additionally, 70-30% diesel mass split injection strategy has a higher amount of LTHR for the same diesel SOI, whereas the amount of HTHR is lower. The higher amount of LTHR is due to the prolonged duration of LTHR. The decreased amount of HTHR is due to auto-ignites of leaner charge during high- temperature reactions when piston moving towards BDC and resulting in delayed CA$_{50}$.

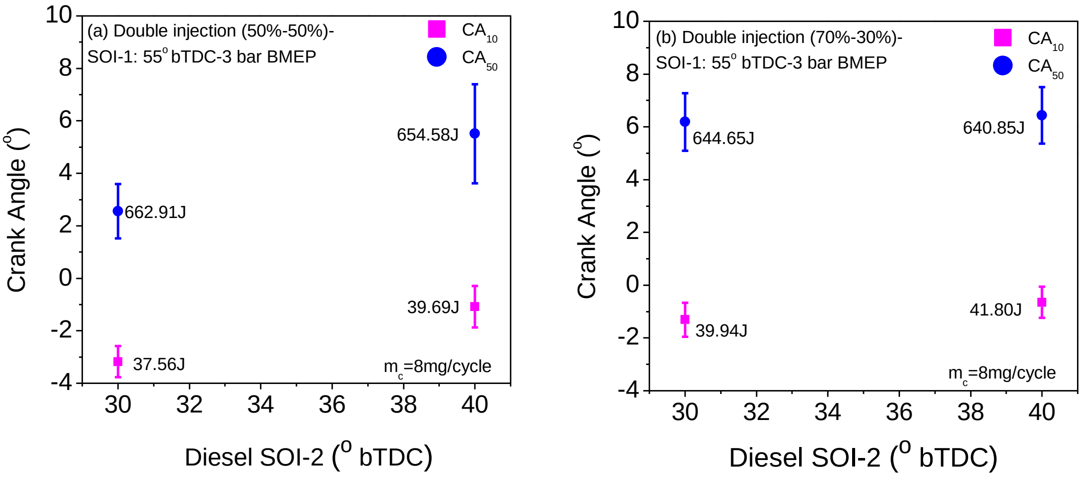

Figure 4.16 Effect of diesel mass split injection strategy on CA_{10} and CA_{50} at 3 bar BMEP for CNG diesel RCCI operation

The variation of CA_{10} and CA_{50} with CNG mass is shown in Figure 4.17. The values shown corresponding to CA_{10} are the amount of LTHR, whereas the values corresponding to CA_{50} are the amount of HTHR at particular diesel SOI. With an increase in m_c, the CA_{10} and CA_{50} is retarded for both the injection strategies. It is attributed to a lower rate of autoignition reactions since CNG has lower reactivity. Additionally, for 70-30% diesel mass split injection strategy, the CA_{10} and CA_{50} is more retarded than the 50-50% diesel mass split injection strategy. It is due to the lower local equivalence ratio of the charge. Figure 4.17 also indicates that the amount of LTHR and HTHR decreases with an increase in m_c. This trend is the same for both injection strategies. With an increase in m_c, less fraction of diesel injected in the cycle. The lower amount of LTHR and HTHR is due to decreased, delayed and shorter duration of low and higher temperature oxidation reactions. A slower combustion rate (due to lower reactivity of CNG) leads to retard the LTHR and HTHR; thus, more charge burns during expansion, resulting in a decreased amount of HTHR.

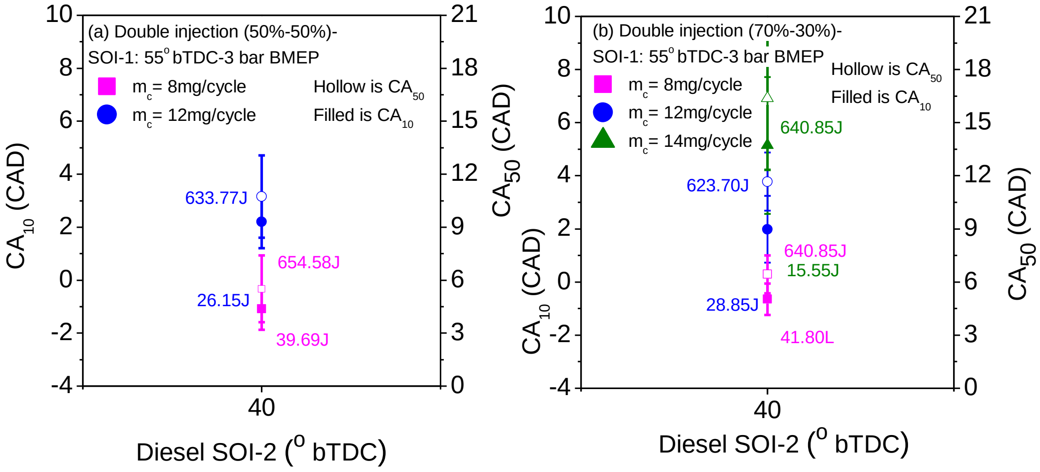

Figure. 4.17 Influence of m_c on CA_{10} and CA_{50}

4.3 Particulate Emission Analysis

This section presents the particulate emission analysis from diesel and RCCI engine. This section is divided into two subsections. First subsection presents the effect of injection timing and pressure on incylinder soot precursor concentration and PM characteristics of diesel engine which includes particle number density, particle volume fraction and mean PM average diameter. Second subsection presents the effect of injection strategy, CNG mass and engine load on PM characteristics of RCCI engine which includes particle number and mass distribution, total particle number concentration (TPN), nucleation mode particle, accumulation mode particle.

4.3.1 Particulate Emission Analysis of Diesel Engine

Figure 4.18 (a-d) presents the computed mass fraction of soot precursor species such pyrene (A_4), phenanthrene (A_3), acetylene, and OH at different start of injection timings at constant speed and load as function of crank angle. Soot formation in diesel engine includes nucleation, surface growth, coagulation, and agglomeration. In the conceptual model of Dec, species such as PAH were detected after the rich premixed burn. These PAH grow to form soot inside the diffusion flame envelope [4.15]. In a study it was found that phenanthrene (A3) and pyrene (A_4) contribute to 68 % of the total PAH emissions [4.16]. These PAH can be formed from fuel itself or combustion generated from the fuel pyrolysis [4.16]. During the fuel rich combustion, fuel molecules break down to form PAH through cyclization reactions in which some PAH have identity similar to PAH present in parent fuel while some PAH are different in molecular structure [4.17- 4.18]. Figure 4.14 (a-d) shows the PAH (Acetylene (C_2H_2), pyrene (A_4) and phenanthrene (A_3)) and OH mass fractions with respect to crank angle at different injection timings. Acetylene (C_2H_2), pyrene (A_4), and phenanthrene (A_3) are produced instantly after the start of combustion and the mass fraction decreases in the expansion stroke due to soot inception which is creation of soot nuclei through the collision of two PAH [4.19]. When the injection timing is retarded, the concentration of soot precursor curve shifts to right. With advanced injection timing, the concentration of soot precursor species decreases during the combustion. This is due to increased ignition delay with advanced injection timing which promotes premixed combustion with low equivalence ratio. The concentration of soot precursor increased with retarded injection timings. This results from diffusion-controlled combustion due to reduced ignition delay. Fuel rich diffusion combustion at high temperature and pressure are ideal conditions for production of soot precursors [4.19 - 4.21]. Figure 4.18 (d) shows the effect of injection timings on OH fraction at constant speed and load condition. It can be observed that when the OH radicals appear the soot precursors start to recede. A study also used the OH radicals as oxidants in their soot model and found its importance in soot oxidation kinetics [4.21]. As the injection timing is advanced the peak OH mass fractions increase [4.22], [4.23]. The increase in OH fraction is due to formation of charge with high concentration of O_2 molecules at high mean gas temperature at advanced injection timings. These OH radicals play important role in soot particle oxidation as reported in previous study [4.20].

It is observed in the previous studies that the RCCI PM mass collected over filter paper mostly consist of high boiling range of diesel hydrocarbons [4.24 - 4.27]. This shows that direct injection of diesel is mostly responsible for particle formation in RCCI engine. Thus, CFD simulations were also done at injection timings employed in RCCI operation. Figure 4.19 shows the effect of injection timing used in RCCI experiments on acetylene mass fraction. It can be observed that acetylene mass fraction starts rising after the start of combustion and then decreases and remain constant at injection timings employed in RCCI experiments in this study. This is due to low incylinder temperature during RCCI combustion which inhibits the consumption of acetylene in soot particle formation and surface growth. This is opposite to the trend observed in diesel engine combustion in which acetylene mass fraction drops to zero after attaining the peak value after the start of combustion (Figure 4.18). This is due to consumption of acetylene in soot particle formation and surface growth in high temperature diesel combustion. Also, it was observed that for very advanced injection timings (30° bTDC to 50° bTDC) incylinder particle number density and mass fraction of PAH (pyrene, napthalene) was negligible. This shows that particle formation mechanism in RCCI engines is different from that in diesel engines. It can be concluded from these observations that particle formation in RCCI engines occurs due to condensation of products of incomplete combustion of diesel such as acetylene in the exhaust plume.

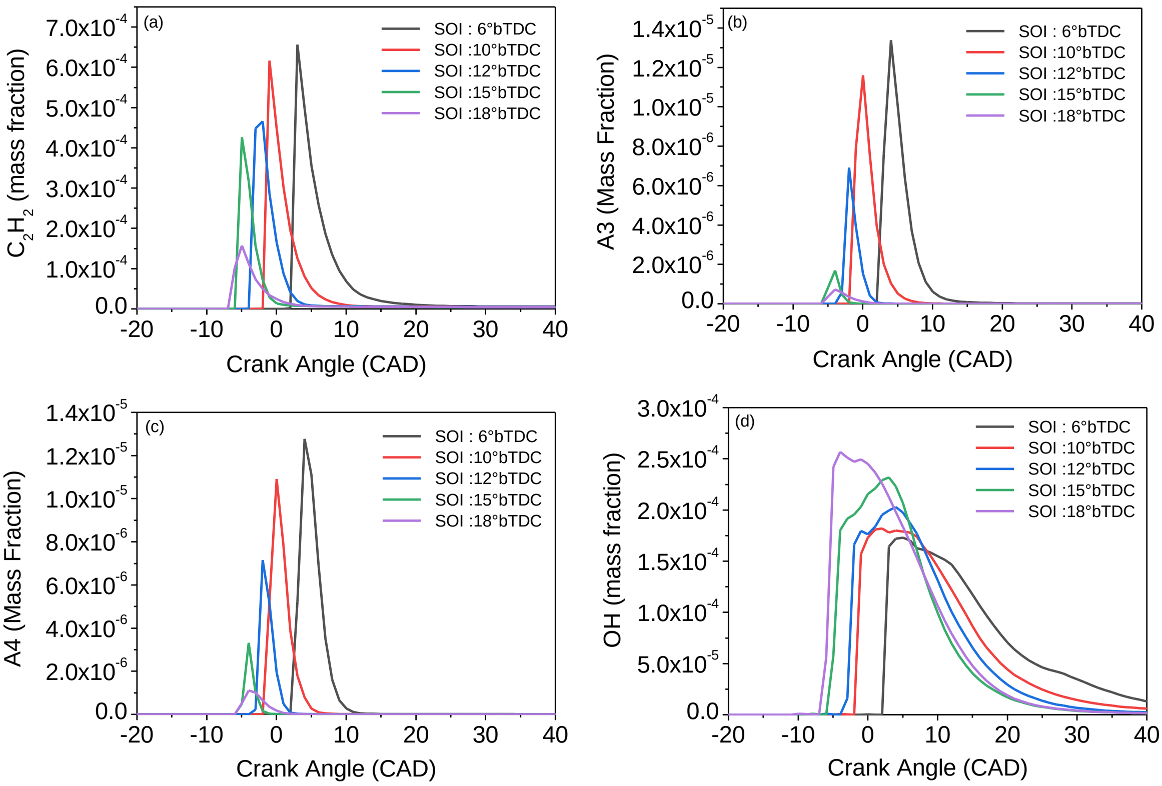

Figure 4.18 Effect of fuel injection timing on soot precursors and OH mass fraction.

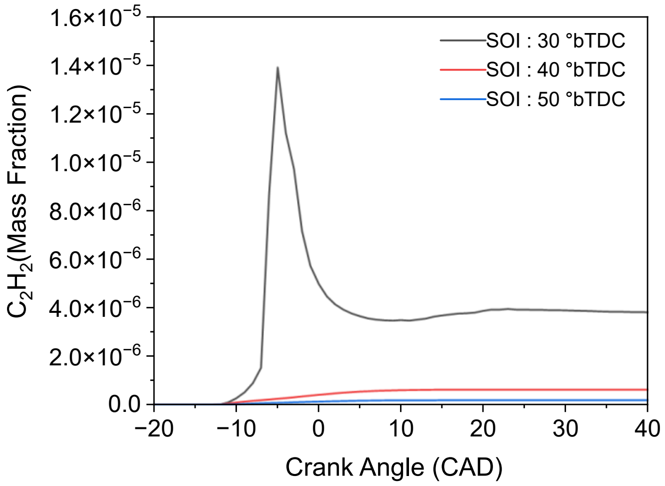

Figure 4.19 Effect of fuel injection timing on acetylene mass fraction for advanced injection timing.

Figure 4.20 (a-d) indicates that with increase in fuel injection pressure the peak concentration of soot precursors such as acetylene, pyrene, and phenanthrene decreases. The concentration of precursors increases immediately after the start of combustion and the concentration decreases with an increase in injection pressure. This is due to an increase in the lift-off length with increases with increase in fuel injection pressure. Increased lift-off length increases the air entrainment into the burning jet which decreases the equivalence ratio and lowers the soot precursor formation rate. Figure 4.20 (d) shows the effect of fuel injection pressure on OH mass fraction. It can be observed that with an increase in fuel injection pressure the OH mass fraction increases. With an increase in fuel injection pressure the combustion rate increases which increases the in-cylinder temperature and OH radical mass fraction.

In current emission legislation, particle number emissions are also regulated in addition to gaseous emissions. Particle number density is obtained from the integration of particle size distribution functions $n(D_p)$ and can be defined as number of particles per unit volume of exhaust gas. Smaller sized particles govern the particle number density. Another important parameter which governs the toxicity and health effect of particulate is mean PM average diameter, which is defined as the geometric mean of lognormal size distribution. PM volume fraction is dimensionless parameter and is defined as particle volume per unit volume of gas. Figure 4.21 (a-c) depicts the crank angle basis evolution of particle number density, mean PM average diameter and PM volume fraction with change in injection timings. It can be observed in Figure 4.21 (a) that maximum peak of particle number density as a function of crank angle is observed for retarded injection timing. Also, particle number density is highest for retarded injection timing of 6° bTDC. This due to high mass fraction of pyrene is observed after the start of combustion in retarded injection timing. As the ignition takes place pyrene molecules are formed and they collide to incept soot particles. Later in the expansion stroke, the particle number density decreases due to particle coagulation and pyrene molecule condensation on the surface of soot particles. A study has also observed increase in soot emissions with retarded injection timings [4.21].

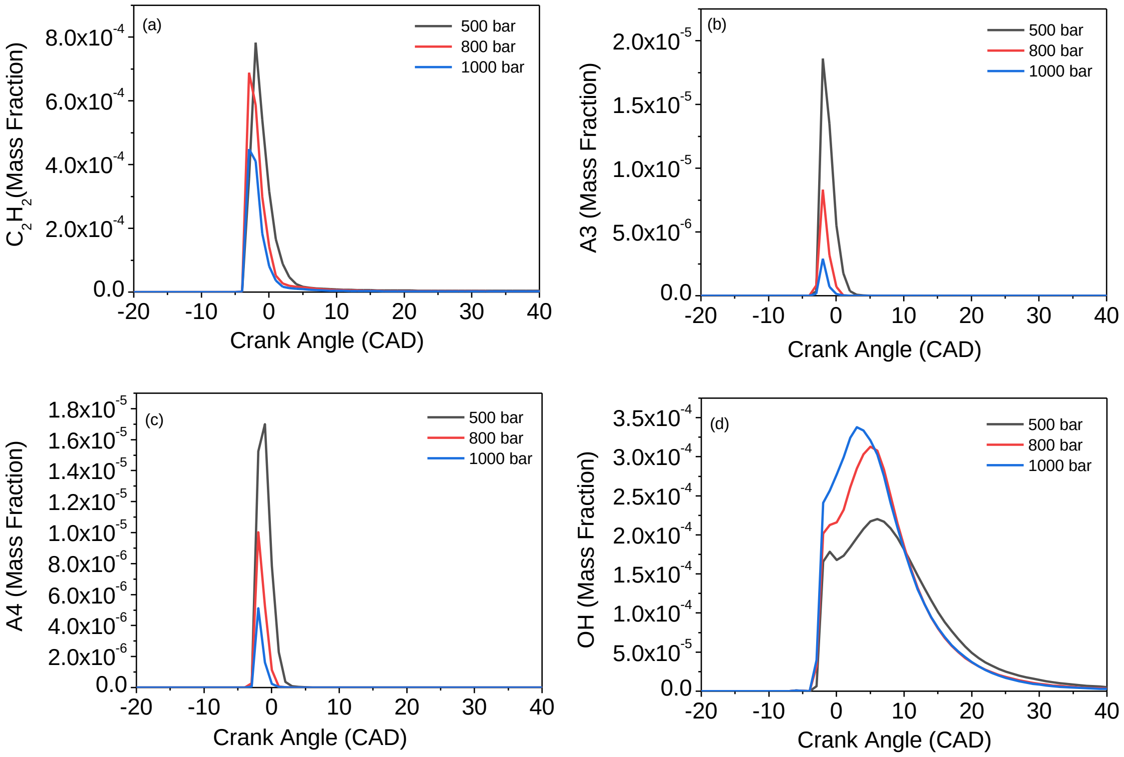

Figure 4.20 Effect of fuel injection pressure on (a) Pyrene (A4) (b) Acetylene (c) Phenanthrene (A3) (d) OH mass fraction.

This due to high mass fraction of pyrene is observed after the start of combustion in retarded injection timing. As the ignition takes place pyrene molecules are formed and they collide to incept soot particles. Later in the expansion stroke, the particle number density decreases due to particle coagulation and pyrene molecule condensation on the surface of soot particles. A study has also observed increase in soot emissions with retarded injection timings [4.21].

Mean PM average diameter as function crank angle is presented in Figure 4.21 (b). The trends show that with retarded injection timings, mean PM average diameter increases. This is due to conducive environment of soot surface growth in presence of high concentration of acetylene with retarded injection timing due diffusion-controlled combustion. Acetylene is an important chemical species for soot surface growth reactions thorough HACA mechanism in which carbon is added and hydrogen is removed [4.17]. Additionally, soot oxidation reactions are retarded due to low concentration OH radicals at retarded injection timing. This is due to decrease in maximum cylinder gas temperature with retarded injection timing. According to a study based on kinetic theory of gases, soot oxidation reaction is dominated by OH radicals in fuel rich premixed and diffusion flames at temperature ranging from 1530 K to 1890 K [4.20]. It can also be seen that at retarded injection timings, large size particles emit at EVO compared to advanced injection timings. This is also due to high in-cylinder gas temperature with advanced injection timings which accelerates the soot oxidation rates. The concentration of OH radicals increase during combustion with advanced injection timings which increase the oxidation rates.

Effect of injection timing on PM volume fraction is presented in Figure 4.21 (c). It can be observed that PM volume fraction decreases with advanced injection timings. With advanced injection timing, the soot oxidation reactions enhanced due to high concentration of OH which decreases the soot particle size and volume. Additionally, the concentration of acetylene is low in case of advanced injection timings, which is responsible for soot surface growth reaction. Soot surface growth reaction determines the mass of the PM therefore governs the PM volume fraction. With retarded injection timings the soot surface growth increases, and oxidation decreases due to the longer duration of diffusion-controlled combustion which is ideal for the formation of large sized particles therefore the PM volume fraction increases. The condensation and coagulation processes lead to soot particle growth thereby increasing the particle diameter. There is an exception of PM volume fraction decrease with injection timing at TDC. For this injection timing, most of the charge burns during expansion stroke under low pressure and temperature conditions due to an increase in in-cylinder volume. In these conditions of low temperature and pressure, the soot formation is decreased thus, the PM volume fraction decreases.

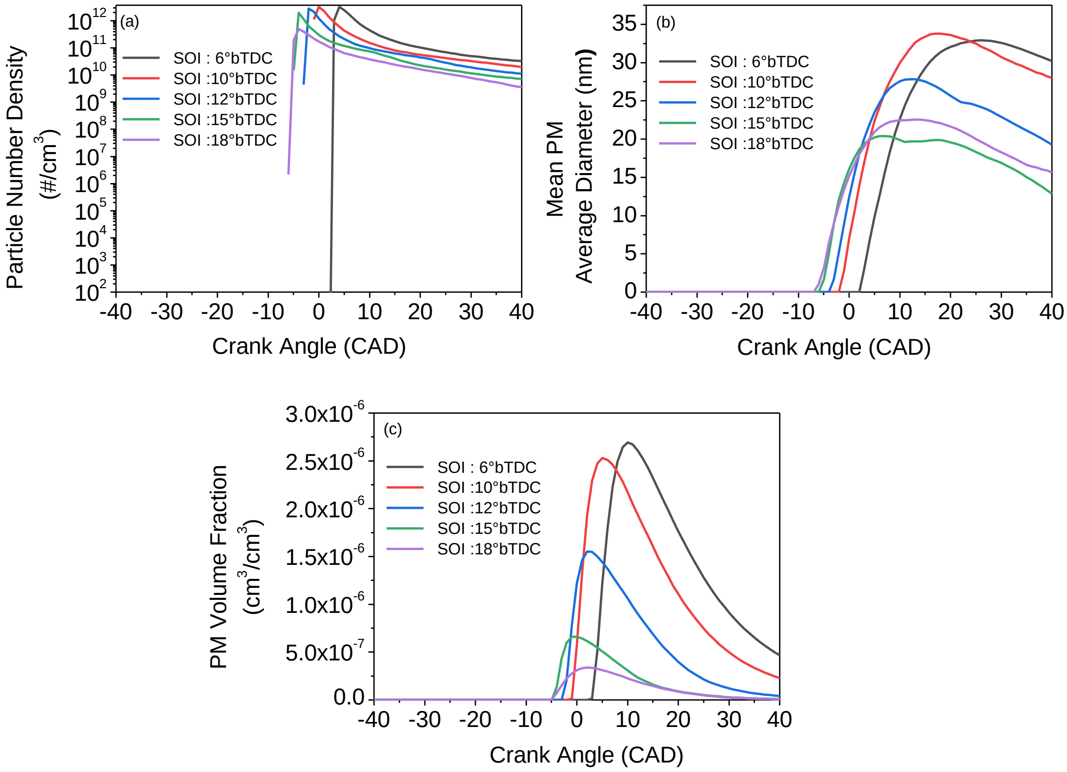

Figure 4.21 Effect of Injection Timing on PM characteristics

Figure 4.22 (a-c) shows the effect of injection pressure on PM characteristics. It can be observed that particle number density is decreased with an increase in injection pressure. This is due to reduced formation rate of soot precursors at high injection pressure (because of better in-cylinder fuel air mixing). Additionally, the OH radical mass fraction increases with an increase in injection pressure due to high in-cylinder mean gas temperature which increases the oxidation rate. After the start of combustion, no significant difference in particle number density is observed for all the fuel injection pressure. As the combustion progresses, the soot particles are oxidized due to better fuel-air mixing and less fuel-rich regions at high injection pressure. Similar trends can be observed for mean PM average diameter. With an increase in injection pressure, the mean PM average diameter decreases. This is due to retarded soot surface growth reaction because of less availability of surface growth species such as acetylene at high injection pressure. Additionally, the soot oxidation reaction kinetics improves due to high temperature and large amount of OH radicals. PM volume fraction also decreases with increase in injection pressure due to lower soot particles per unit volume (figure 4.22 (c).

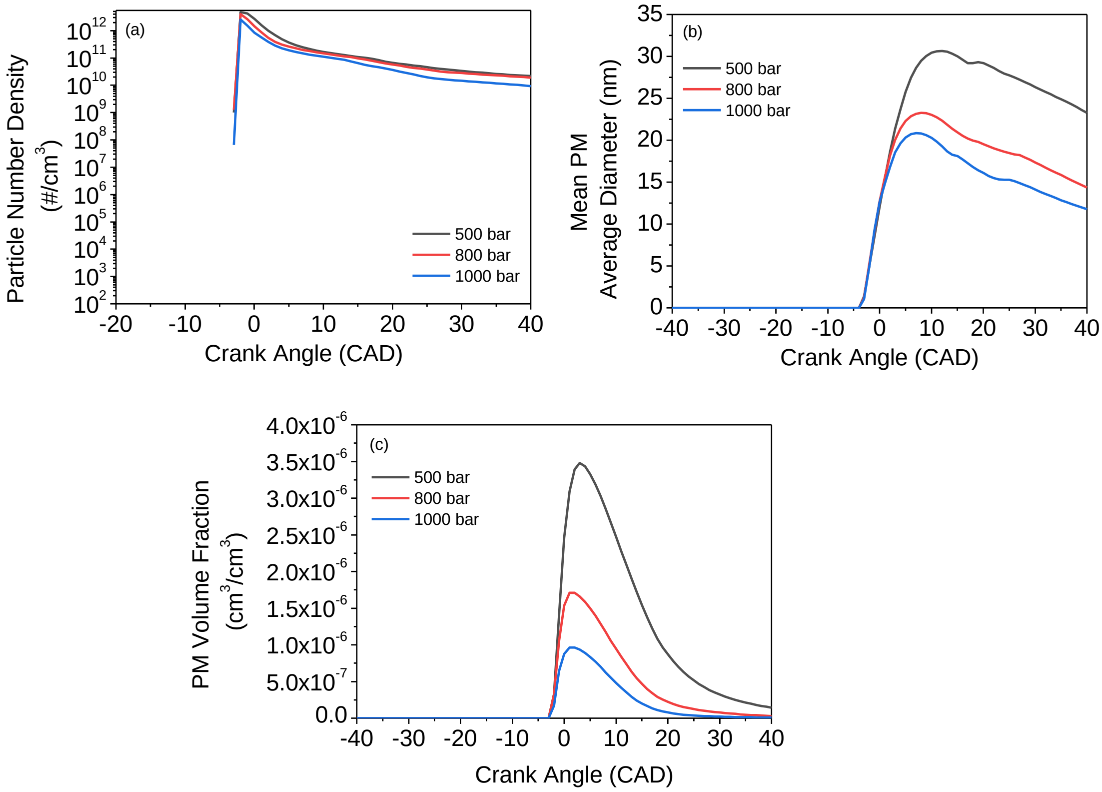

Figure 4.22 Effect of injection pressure on incylinder PM characteristics of diesel engine

4.3.2 Particulate Emission Analysis of RCCI Engine

This section presents the particle number characteristics of conventional dual-fuel and RCCI operations. This section presents the influence of the diesel injection strategy on the particle emissions from the RCCI engine.

4.3.2.1 Effect of Single and Double Injection Strategy

In RCCI combustion, mainly premixed charge burns in the combustion chamber. During premixed combustion, NMPs as well as AMPs form, which depends on the local charge reactivity and stratification. The particle of diameter less than 50 nm are considered as NMPs while particles of diameter more than 50 nm are considered as

AMPs. The particle size distribution (PSD) for conventional diesel engine typically displays bimodal lognormal characteristics i.e., two peaks in which first and second peak depicts NMPs and AMPs [4.28], [4.29]. Particles are usually divided into three categories based on their mobility diameter, i.e., nucleation, accumulation, and coagulation modes [4.28]. Nucleation mode particles (NMPs) have a diameter in the range of 5-50 nm. They comprise volatile organic and sulfur compounds that form during cooling and dilution of engine exhaust and might also include solid carbon and metal compounds. The nuclei mode particles typically contain 1- 20% of the particle mass and more than 90% of the particle number. These particles are formed during exhaust dilution and cooling; thus, they are susceptible to measuring methods, measuring conditions such as ambient temperature, humidity, and dilution ratio [4.29], [4.30]. The particle mass mainly exists in accumulation mode particles (AMPs) with a mobility diameter ranging from 100-300 nm. The accumulation mode particles are solid soot particles that are carbonaceous in nature. These particles formed from incomplete combustion of charge in fuel-rich zones, which leads to the formation of fractals-like carbonaceous aggregates that are typically 30 - 300 nm in mobility diameter [4.28]. Smaller solid particles are in the form of a single sphere [4.31], [4.32]. The measurement of these particles is repeatable and independent of sampling conditions. The coarse mode particles contain 5-20% of the total particle mass. Coarse mode particles consist of accumulation mode particles deposited in the cylinder surface and exhaust system and later re-entrained.

PSD is plotted with an error bar for conventional dual-fuel and RCCI operation at different diesel SOI (Figure 4.23). PSD indicates the bimodal lognormal distribution for dual-fuel and RCCI operations as well. The first peak indicates the NMP whereas the second indicates the AMP. The figure shows that conventional dual-fuel operation has a lower peak of NMP and AMP. The peak of NMP and AMP increased in RCCI operation. For RCCI operation, the availability of time for the mixing of LRF and air is relatively higher. Advanced diesel SOI causes to decrease in the in-cylinder temperature, which may result in larger size fuel droplets [4.33]. In RCCI operation, the ignition delay is longer, which causes to increase in the LRF+ HRF+ air premixing. The formation of NMPs is higher when a more percentage of premixed charge burns in the combustion chamber, possibly because of a slower agglomeration rate [4.33]. Moreover, for RCCI operation, more percentage of the charge burns when the piston moves towards BDC because of retarded CA_{50} position. This may cause a decrease in the in-cylinder mean gas temperature, which will also cause the formation of NMPs. Additionally, in conventional dual-fuel mode, the peak of NMP in MD operation is significantly lower. Figure 4.24 shows the PSD for GD and MD operation for double injection strategy. The typical trend for MD operation in double injection strategy is also same as GD operation (Figure 4.23). No significant variations have been found in the peak of NMP with diesel SOI for double injection strategy in GD operation (Figure 4.24).

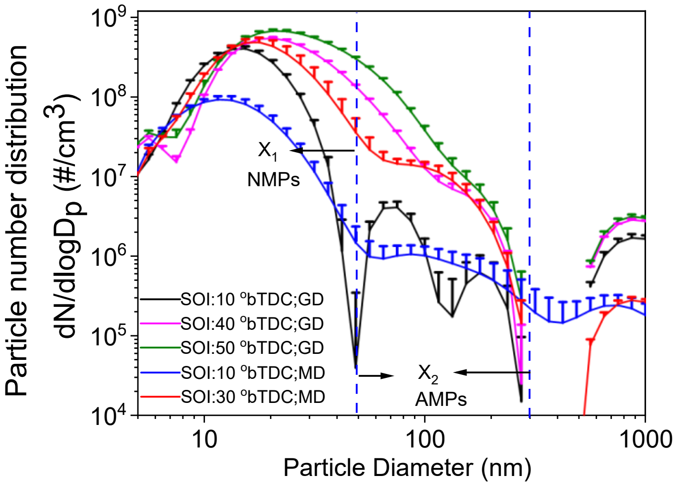

Figure. 4.23. PSD for GD and MD operation for different diesel injection timing for single injection strategy

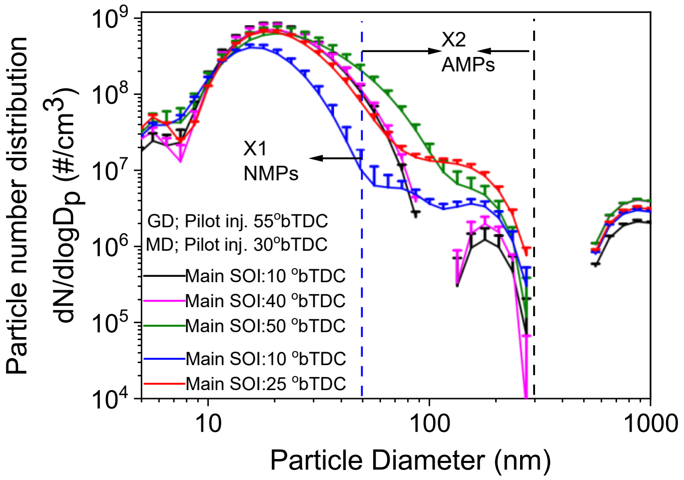

Figure. 4.24. PSD for GD and MD operation for different diesel injection timing for double injection strategy

The PSD at 1.5 bar BMEP (lower load) is presented in Figure 4.25 (a-b) for CNG diesel RCCI operation. PSD depicts a bimodal lognormal distribution trajectory. In PSD first and the second peak indicates the NMPs and AMPs, respectively. The figure indicates that the peak of NMPs is significantly higher than AMPs. Higher concentrations of NMPs than AMPs were also observed with other low-reactivity fuels i.e., gasoline/methanol in the previous study by the authors [4.33]. The formation of NMPs in higher concentrations is attributed to the combustion of a relatively more homogeneous charge in the premixed phase of combustion during the expansion stroke [4.33]. Additionally, higher HC emissions in RCCI combustion mode increase the formation of NMPs due to homogeneous nucleation of unburned HC. The PSD depicts a higher peak for particles having a diameter less than 20 nm for 30° bTDC diesel SOI with a single injection strategy. Whereas no significant variation in the PSD peak for particles having a diameter less than 20 nm is observed in the double injection strategy. As per the

European Union (EU) norms, particles with a diameter above 23 nm are only considered solid particles. The particles having a diameter less than 23 nm are volatile organic fractions. The repeatability of these particles is challenging since they exhibit different characteristics under different sampling conditions [4.34]. For advanced diesel SOI (i.e., 40° bTDC), the PSD peak is higher for particles in the size range between 30 to 300 nm for both injection strategies.

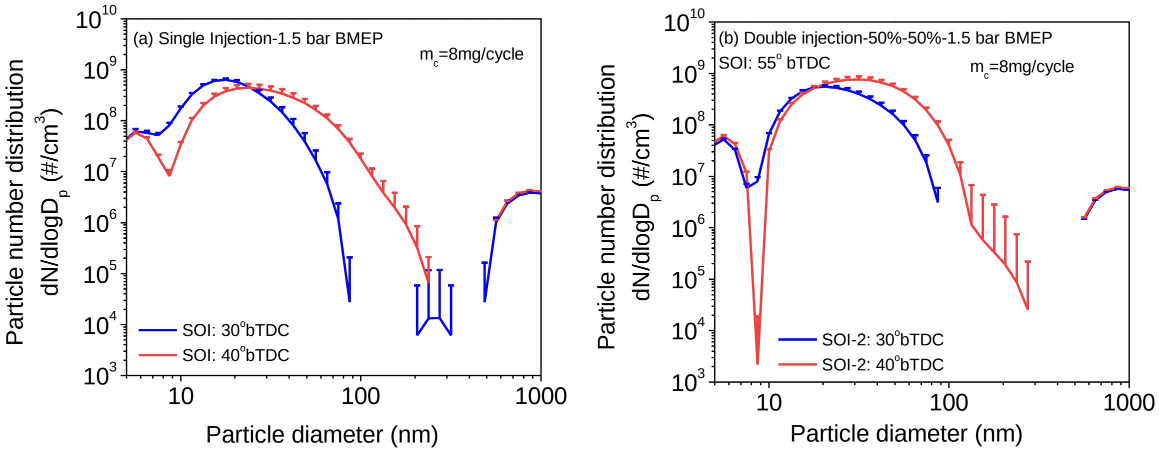

Figure 4.25 Influence of diesel SOI on PSD at 1.5 bar BMEP for CNG diesel RCCI operation

The influence of the diesel mass split injection strategy on the PSD at 3 bar BMEP (medium load) is shown in Figure 4.26 (a-b) for CNG diesel RCCI operation. Figure 4.21 (a) indicates that the PSD peak is lower for particles having a diameter less than 30 nm when diesel SOI is advanced from 30° to 40° bTDC. For earlier SOI (i.e. 40° bTDC), the PSD peak is higher for particles in the size range between 40 to 300 nm (figure 4.26 (a)). For advanced SOI (i.e., 40° bTDC), excessive diesel accumulated due to pilot and main injections with not adequate time for mixing with premixed CNG + air charge leads to the locally fuel-rich region inside the combustion chamber [4.10], [4.11]. It will cause the formation of larger-sized particles. The enhanced premixing of diesel for 30° bTDC diesel SOI (in comparison to 40° bTDC diesel SOI), injected during both the injections with the premixed charge, led to a reduction in the local charge equivalence ratio. The particles less than 30 nm are slightly higher for 30° bTDC SOI is due to combustion of lean charge. However, no significant variations have been found in the peak of NMPs and AMPs with diesel SOI for 70-30% diesel mass split injection strategy. It is due to more percentage of diesel (70% injected during the pilot injection) is blended with the premixed charge of CNG and air, which compensates for reduced mixing time between the two injections. The peak of NMPs and AMPs is slightly higher for 70-30% diesel mass split injection strategy than 50-50% diesel mass split regime.

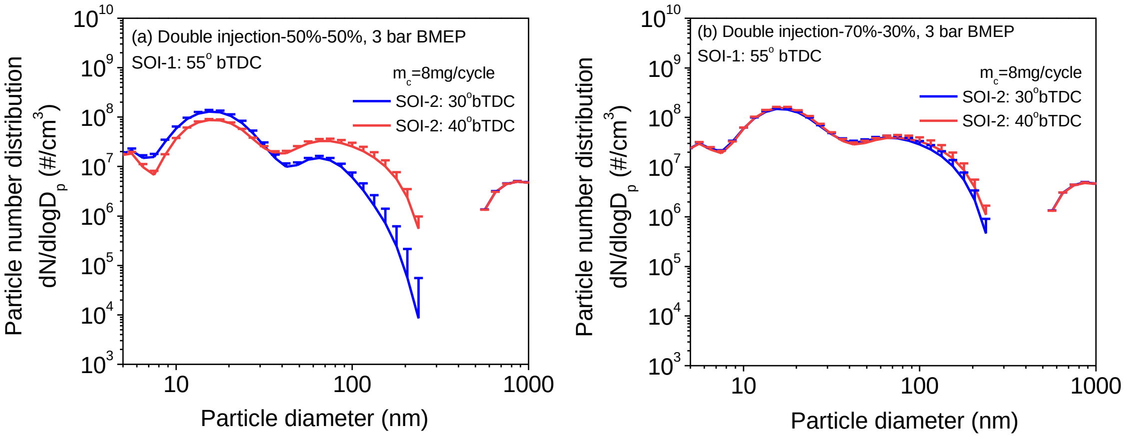

Figure 4.26 Influence of diesel mass split regime on PSD at 3 bar BMEP

4.3.2.2 Effect of CNG Mass (m_c) and Engine Load

Figure 4.27 (a-b) depicts the influence of CNG mass (m_c) on PSD for constant injection of 30° bTDC and 1.5 bar BMEP. It can be observed from Figure 4.27 (a) that the particle having a diameter of less than 30 nm has no significant variation with an increase in m_c. However, particles having diameters between 30 and 100 nm are comparatively lower for higher m_c. This figure also confirms that the NMPs are mainly contributing to total PN emissions (figure 4.27(b)). However, the total PN slightly increased with m_c, which is due to a slight increase in the concentration of larger size particles. Figure 4.28 (a-b) shows the effect of CNG mass on the PSD at different loads and for the diesel mass split injection strategy. The figure indicates that at 1.5 bar BMEP, the peak of NMPs is significantly higher than 3 bar BMEP. More diesel burns during higher engine load leads to increased incylinder combustion temperature, which enhances the rate of oxidation and results in reduced NMPs. It can also be observed that as the engine load increases, the peak of NMPs decreases while the peak of AMPs increases. This is due to high combustion temperature and the presence of fuel-rich regions in the combustion chamber (because of the higher amount of injected diesel). For lower engine load with 50-50% diesel mass split injection strategy, the peak of NMPs decreased with an increase in m_c, whereas no significant variation in PSD is found for particles having a diameter of less than 20 nm. For the rest of the cases, the NMPs peak increased with an increase in m_c, while the AMPs peak decreased. This trend is due to the fact that the increasing the m_c caused to decrease in the in-cylinder reactivity, which retards the combustion phasing resulting in a lower in-cylinder combustion temperature. At lower in-cylinder combustion temperatures, the formation of NMPs is higher due to the slower rate of agglomeration. Additionally, HC emissions increase with an increase in m_c, which forms NMPs as exhaust gas cools through homogeneous nucleation. It is significant to note that the PSD traces changed from bimodal distribution to unimodal distribution with an increase in m_c. This indicates that an increase in CNG fraction leads to forming comparatively smaller-sized particles.

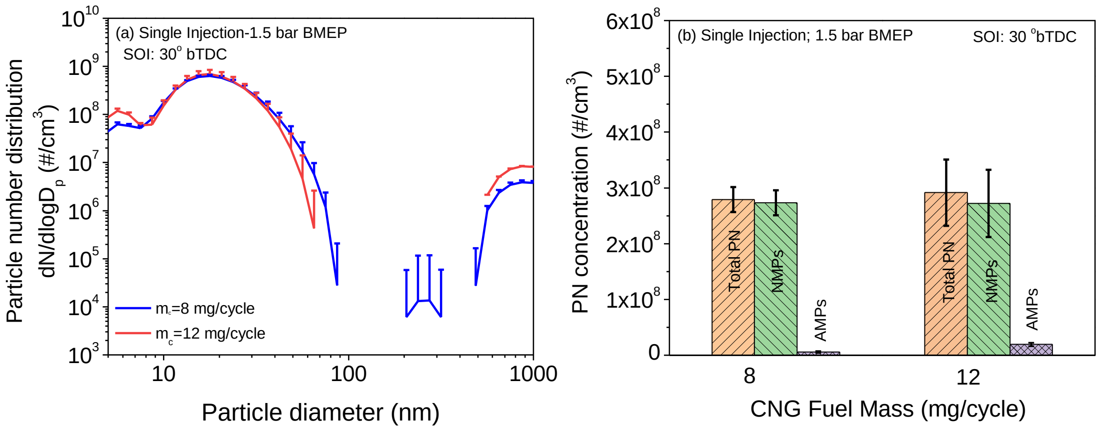

Figure. 4.27 Effect of CNG mass on PSD and number concentration at 1.5 bar BMEP (lower load)

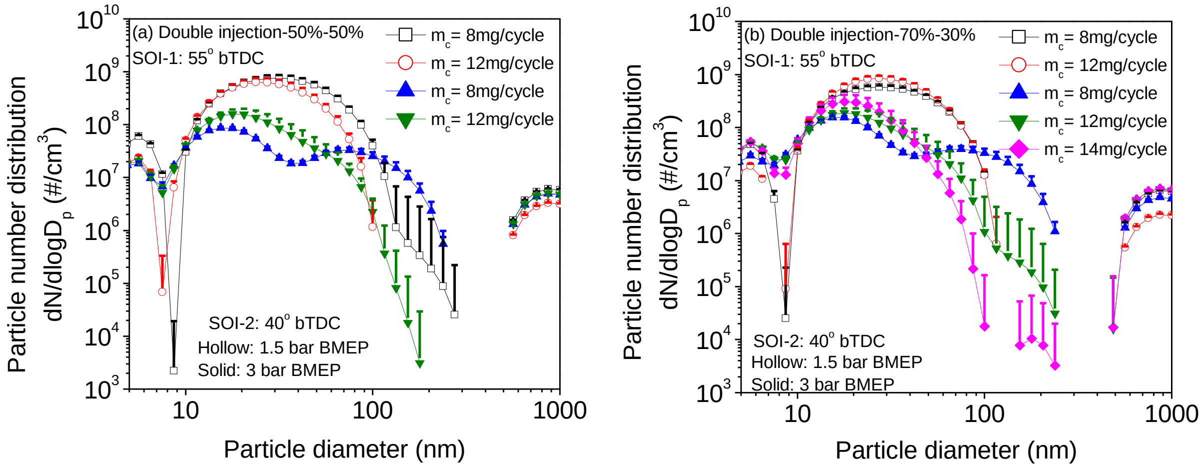

Figure 4.28. Effect of CNG mass on PSD at different load and diesel mass split injection strategy

4.3.2.3 Effect of LTHRR and HTHRR

To determine the effect of the amount of LTHR on the particle emissions, total PNs, NMPs, and AMPs concentration is plotted with the amount of LTHR for various diesel SOIs (Figure 4.29 (a-c)). The amount of LTHR provides the local temperature and pressure conditions required for the high-temperature oxidation reactions. The phasing of HTHR also depends on the peak, amount, and location of LTHR, which vary with diesel SOI. For reducing particle formation within the combustion chamber, LTHR can play a key role. The total PN, NMPs, and AMPs concentration increases with advanced diesel SOI with a single injection strategy in GD operation (Figure 4.29). Along with total PN concentration, the amount of LTHR is also increasing (Figure. 4.29 (a)). An increase in the amount of LTHR is attributed to the increased duration of low-temperature oxidation reactions. A higher amount of LTHR leads to enhanced premixed combustion. The NMPs formed significantly higher during premixed combustion (higher NMP number can be seen in (Figure. 4.29 (b)). The higher concentration of NMPs contributes more to total PN concentration. In conventional dual-fuel operation (10° bTDC), the total PN concentration is significantly lower than RCCI operation. For 10° bTDC diesel SOI with single injection strategy, the peak of LTHRR is higher (except for GD double injection strategy); correspondingly, the peak of HTHRR is advanced and higher, which results in advanced CA_{50} (compared to RCCI operation). Additionally, in conventional dual-fuel operation, the mixture burns in the premixed and diffusion phase of combustion. Thus, the formation of NMPs is lower in comparison to RCCI operation (since only premixed combustion is observed in RCCI combustion). No significant variations have been found in total PN and NMPs concentration with diesel SOI in double injection strategy for GD operation even though the amount of LTHR increased significantly. However, AMP's concentration significantly increased with diesel SOI in the double injection strategy for GD operation. Interestingly, for GD operation, the double injection strategy has a significantly higher total PN concentration for conventional dual-fuel and RCCI operation at 40° bTDC compared to the single injection strategy. The higher total PN concentration is because of the combustion of a relatively more premixed charge in RCCI operation, which causes a higher concentration of NMPs (Figure 4.29 (b)). These nanoparticles contribute more to total PNs. Figure 4.29 (c) also shows that in the case of GD operation, the AMPs are significantly lower in concentration for the double injection strategy than single injection strategy when the engine is operated in RCCI combustion mode. Additionally, in the case of GD operation for 40° bTDC diesel SOI, the reduction in AMPs concentration is significantly higher in comparison to 50° bTDC diesel SOI in the double injection strategy. The trend for total PN, NMPs, and AMPs with diesel SOI for both the injection strategies is the same in MD operation as that for GD operation (Figure 4.29 (b)). For conventional dual-fuel operation, the total PN concentration is lower in MD operation than in GD operation. Lower total PN concentration in MD operation in conventional dual-fuel mode is attributed to the formation of lower concentration of NMPs (Figure 4.29 (b)). A higher concentration of NMPs in GD conventional dual-fuel operation is possible because of the nucleation, condensation, and coagulation of unburnt species (such as hydrocarbons). Methanol has inbound oxygen molecules, leading to an improved combustion process and reduced particle emissions.

Figure 4.30 (a-d) shows the variation of PN concentration with LTHR and diesel injection strategy at lower load for CNG diesel RCCI operation. For 30 °bTDC diesel SOI, no significant variation in total PN is found for both the injection strategy even though the amount of LTHR is higher for the double injection strategy (figure 4.30 (a)). However, for advanced diesel SOI (40° bTDC), the total PN emissions are significantly higher for the double injection strategy, and the amount of LTHR is lower than the single injection strategy (figure 4.30 (a)). It is significant to note that for 30° bTDC diesel SOI, NMPs are significantly higher than AMPs for both the injection strategies, which are mainly contributing to total PN emissions (figure 4.30 (b-c)). For 30° bTDC diesel SOI with a single injection strategy, the charge is relatively leaner because diesel has adequate time to mix with the premixed charge (CNG-air).

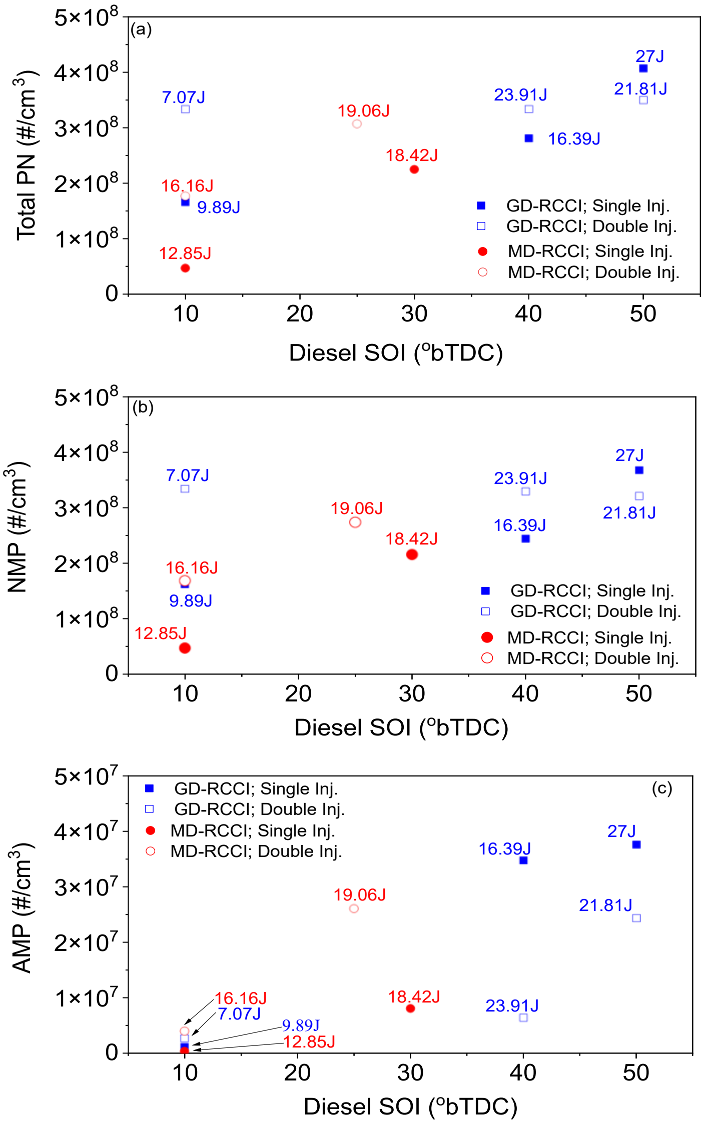

Figure 4.29 Variation of total PN, NMPs, and AMPs with diesel SOI and amount of LTHRR for GD and MD RCCI operation

Combustion of lean premixed charge cause to lower amount of LTHR and further retard the high-temperature oxidation reactions. Therefore, the premixed charge mainly burns during the expansion stroke, which promotes the formation of small particles. For 40° bTDC diesel SOI with a single injection strategy, the amount of LTHR increased due to the slower rate of low-temperature oxidation reactions. Slower reaction rate during low-temperature oxidation reactions further retards the high-temperature oxidation reactions and results in a decreased amount of HTHR. The decreased HTHR leads to a slight decrease in the formation of NMPs (figure 4.30 (b)). For 30° bTDC diesel SOI with a double injection strategy, the NMPs are lower in comparison to the single injection strategy, whereas the amount of LTHR is higher. The relatively higher amount of LTHR is due to the more reactive charge burn during low-temperature oxidation reactions with a slower rate. Because of the slower rate of oxidation reactions, the combustion phasing is retarded, and a decrease in the amount of HTHR in comparison to single injection strategy is obtained, this results in a lower concentration of NMPs. For 40° bTDC diesel SOI with a double injection strategy, the NMPs are lower in comparison to 30° bTDC diesel SOI.

For 40° bTDC diesel SOI, AMPs are contributing more in total PN concentration (more significant in double injection strategy) (figure 4.30 (b-c)). In the double injection strategy for 40° bTDC diesel SOI, an increase in total PN concentration with a large contribution of AMPs is observed with the lower amount of LTHR. In RCCI, diesel injection timing, number of injections, and amount of LRF control the charge reactivity and stratification. For advanced SOI, excessive diesel accumulated due to pilot and main injections with insufficient time for mixing with premixed CNG + air charge leads to a locally fuel-rich region inside the combustion chamber and increases the reactivity of the charge. The locally rich region inside the combustion chamber promotes the formation of larger size particles.

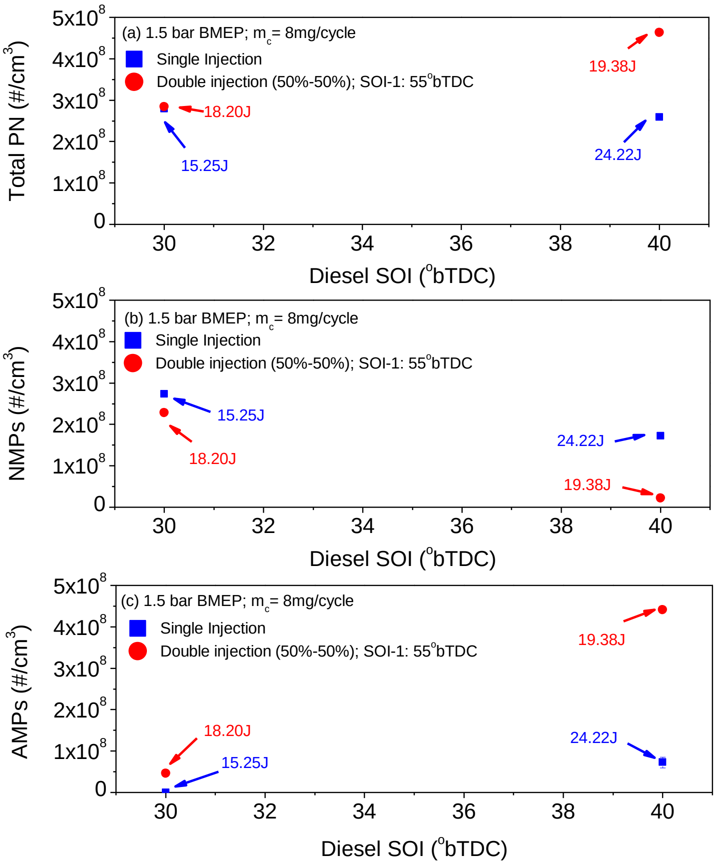

Figure 4.30. Variation of PN concentration with LTHR and diesel injection strategy at 1.5 bar BMEP (lower load)

Figure 4.31 (a-c) shows the variation of particle concentration with LTHR and diesel mass split regime at 3 bar BMEP (medium load) for CNG diesel RCCI operation. Diesel SOI is not much significantly influencing the total PN emissions for this load. The total PN emissions are slightly higher with a 70% - 30% diesel mass split regime. Additionally, for both the diesel SOI, the amount of LTHR is also higher for the 70% - 30% diesel mass split regime. The amount of LTHR increased due to a slower low temperature oxidation rate, which further retards the higher temperature oxidation rate reactions and results in delayed CA$_{50}$. Therefore, a relatively higher percentage of premixed charge burn during LTHR and during expansion in HTHR leads to the formation of small size particles in higher concentration, which mainly contribute to total PN emissions.

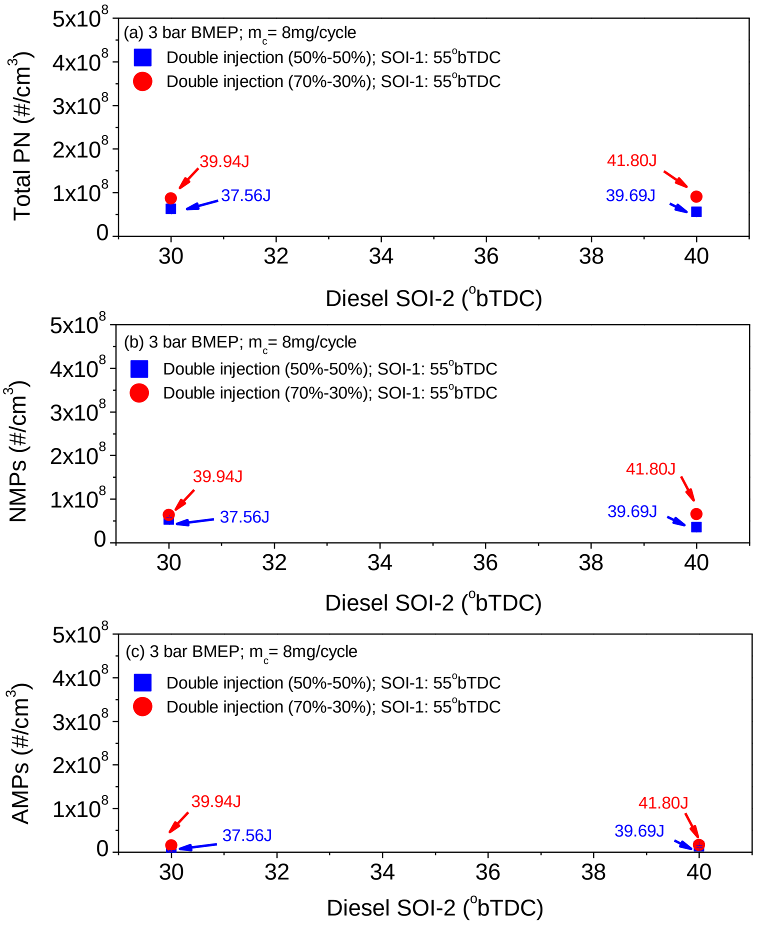

Figure 4.31 Variation of particle concentration with LTHR and diesel mass split regime at 3 bar BMEP (medium load)

Figure 4.32 (a-b) shows the variation of PN concentration with LTHR and CNG mass. The figure indicates that an increase in m_c results in a higher concentration of total PN emissions. Additionally, the higher concentration of NMPs mainly contributes to total PNs. This observation is true for both the injection strategies. The figure also shows a decrease in the amount of LTHR, resulting in an increased concentration of PN concentration. The decrease in LTHR with an increase in m_c caused a reduction in the in-cylinder mean gas temperature leading to incomplete combustion of charge with retarded CA_{50}. It causes to increase in the formation of NMPs in higher concentrations. The figure also shows that with an increase in CNG fuel mass (m_c), the AMPs decrease. The reduction in AMPs is due to a decrease in injected diesel fuel mass with an increase in m_c to maintain the constant load and speed. The number of soot precursors reduces with reduced diesel mass due to less diesel fuel being pyrolyzed.

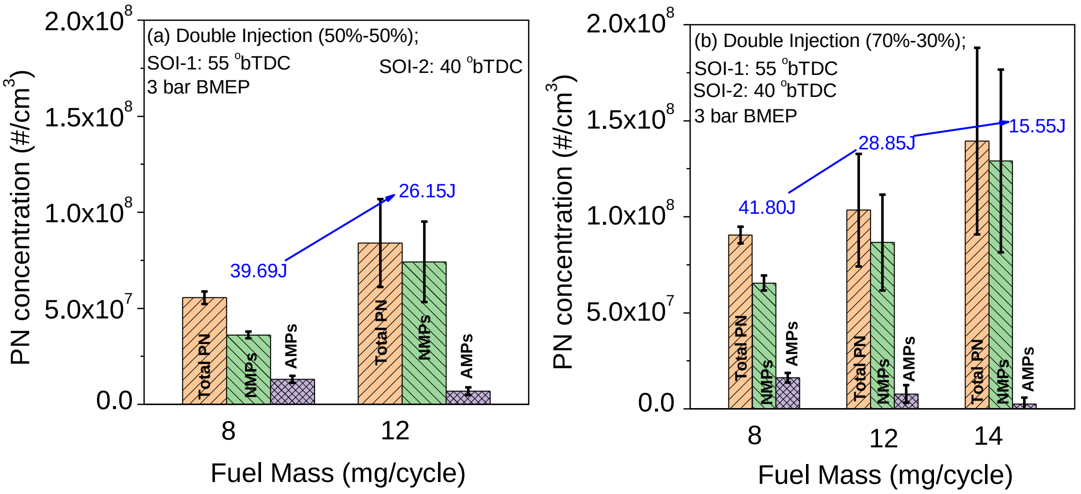

Figure. 4.32 Variation of PN concentration with LTHR and CNG mass

4.3.2.4 Estimation of Particle Emissions from Empirical Correlation

This section presents the developed empirical correlation for the assessment of PN emissions. It is found in the analysis that diesel SOI plays a vital role in the amount of LTHRR and HTHRR, and their location varies with diesel SOI. In this analysis, an empirical correlation is developed using diesel SOI and the ratio of the amount of HTHRR to the amount of LTHRRR. The multi-variable technique is used for developing the correlations. The correlations are developed using experimental data of single and double injection strategy in GD and MD operations. The methodology used for estimating the amount of LTHRR and HTHRR is already discussed in the 'Test setup and Methodology' section. The correlations for the assessment of PN concentration are given below.

$$Total\ PN\ concentration\ \left(\frac{\#}{cc}\right) = a + b\alpha - c\beta + d\beta^2 \tag{4.1}$$

$$NMP\ concentration\ \left(\frac{\#}{cc}\right) = a + b\alpha - c\beta + d\beta^2 \tag{4.2}$$

$$AMP\ concentration\ \left(\frac{\#}{cc}\right) = -a + b\alpha + e\gamma \tag{4.3}$$

Where 'a', 'b', 'c', and 'd' are the constants. 'α', 'β', and 'γ' are the diesel SOI, the ratio of HTHRR to the LTHRR and combustion phasing. The values of constants are given in Table 4.1. Table 4.1 depicts that total PN and NMP concentration are better correlated with diesel SOI and 'β'. The correlation coefficient for total PN and NMP with diesel SOI and 'β'is above 90%. However, no significant correlation coefficient has been found for AMP with diesel SOI and 'β.' For AMP, a comparatively better correlation coefficient is found with diesel SOI and CA_{50}; even though the result is still not satisfactory. Diesel SOI and 'β' could be used to estimate the total PN emission characteristics.

Table 4.1 Empirical correlation constant values

Particle concentration	Regression constants					Correlation coefficients (R^2)
	a	b	c	d	e	
Total PN	542587682	4048889	-27776961	407429	-	90.16%
NMP	550321779	3392884	-28280751	416182	-	91.81%
AMP	-17545809	655439	-	-	3417530	77.09%

For validating the empirical models, the total PN, NMPs, and AMPs concentration was estimated from developed empirical correlations and compared with the experimental results. The validation is performed for 30 deg bTDC diesel SOI with a single injection strategy and 20° bTDC diesel SOI with a double injection strategy for MD operation. These conditions were not used for developing the correlations. The comparison of estimated particle number concentration and experimentally measured particles is shown in Figure. 4.33. The validation results depict the developed correlation estimate particle concentration with satisfactory accuracy (within the variation of experimental results) at some operating conditions (Figure 4.33). Empirical model is also validated with experimental data for CNG diesel RCCI operation (Figure 4.34). However, further investigation is required in this direction for developing the model for particulate emissions. These parameters can be considered in the future for developing the empirical model for particle estimation.

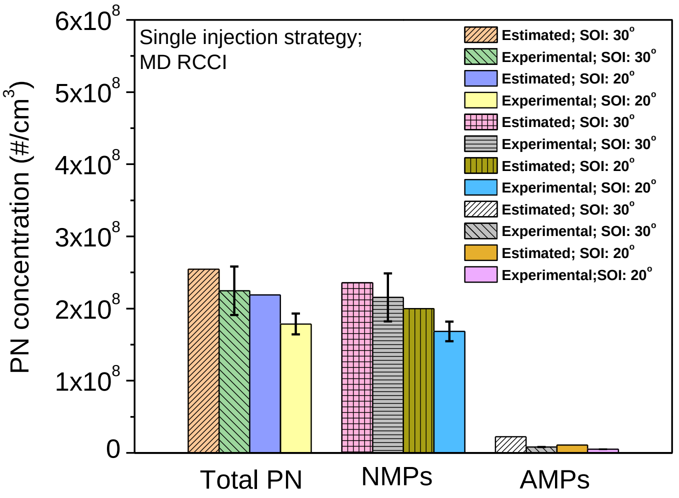

Figure 4.33 Comparison of estimated particle emissions with experimental data for methanol diesel RCCI

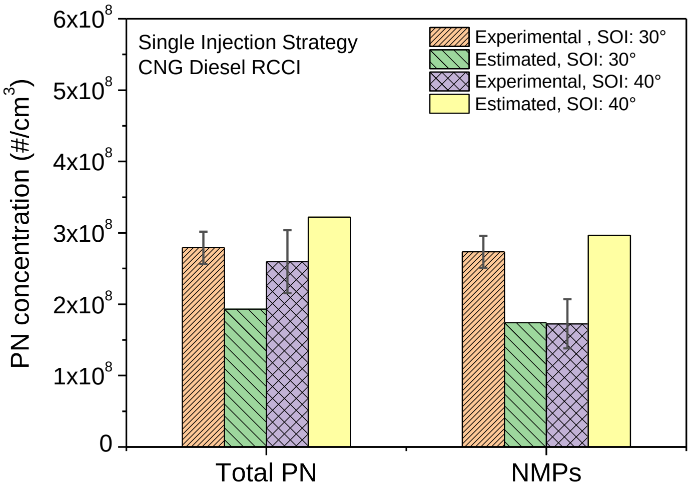

Figure 4.34 Comparison of estimated particle emissions with experimental data for CNG diesel RCCI

4.4 Characterization of Solid Particle Emissions

Characterization of solid particle emissions from GD and CNG – diesel RCCI engine is presented in this section. Nano-particle emission characteristics includes the particle-size distribution (PSD), particle mass distribution (PMD), and total particle number concentration along with NMPs and AMPs concentration. For the analysis of solid PNs, the sampling of nanoparticles is performed through the developed thermo-desorption system at a temperature of 250°C.

Effect of thermo-desorption on the particle size distribution (PSD) for GD and CNG-diesel RCCI engine is presented in Figure 4.35 (a-b). Error bars in the figure indicate the standard deviation from the mean experimental data. It can be observed that the peak of the NMPs in the size range of 10-30 nm is reduced by an entire order of magnitude when sampling is performed with the developed thermo-desorption system. This suggest that NMPs are primarily volatile organic aerosols which are removed due to the sampling of nano-particle with the developed thermo-desorption system. This observation is same for both the fuel operations. In the thermo-desorption system, the highly volatile organic carbon (OC) stemming from unburned hydrocarbons is removed between 30℃ and 175℃, and low volatility OC stemming from lubricant oil is removed between 175℃ and 300℃ [4.34]. Additionally, one can notice a modest increase in the peak of PSD between the particles in the size range 50-60 nm when sampling is performed with thermo-desorption system. These observations can be due soot particle restructuring, and fragmentation due to removal of volatile organic compounds when exhaust is passed through thermodesorption system [4.35- 4.38].

Figure 4.35 (a-b) shows that the peak of AMPs also decreased when particles are sampling with the developed thermo-desorption system. This implies that some of these larger-sized particles with elemental carbon core have some organic carbon content condensed on their surface and are volatile. It is interesting to notice that the bimodal shape of PSD curve is changed to unimodal when sampling performed with the developed thermo-desorption system. This trend is same for both the fuel operations (GD RCCI and CNG diesel RCCI) and the effect of r_p is insignificant when sampling is performed with the developed thermodesorption system. With the use of thermodesorption system, a decrease in the peak of AMPs is significantly less in comparison to a reduction in the peak of NMPs in CNG diesel RCCI operation. This can be due to fact that use of CNG in diesel engine affect the particle morphology, chemical composition, and reactivity [4.39]. AMPs are less affected by thermodesorption system because of less molecular speed due to their higher molecular weight. The less molecular speed solid and liquid particles pass through adsorber stage without adsorbing on activated charcoal pellets. Figure 4.35 (a-b) also shows that uncertainty in particle measurement is reduced when sampling was performed with thermodesorption system. This is due to fact that nucleation mode particles cause large variability in particle measurement. When particle measurement was performed with thermodesorption system, concentration of nucleation mode particles reduced and less variations in particle size and number distribution was observed for both GD and CNG diesel RCCI mode. Also, condensed hydrocarbons on soot particle surface were effectively removed with thermodesorption system which decreased the uncertainty in particle measurement. This shows that particulate sampling conditions are very important factor for achieving repeatable particle measurement results. The current emission norms (such as BS VI and Euro VI) also include particulate emissions emitted from engine based on mass along with PN concentration [4.40]. In PM sampling, a sample of the engine's exhaust gas is taken, diluted with air, and then filtered via sampling filters. The PM mass is obtained by weighing these collected filters on weight balance [4.40]. Other methods involve calculating mass based on the particle density and mobility diameter [4.40]. In this study, particle mass distribution (PMD) is calculated from particle density and mobility diameter.

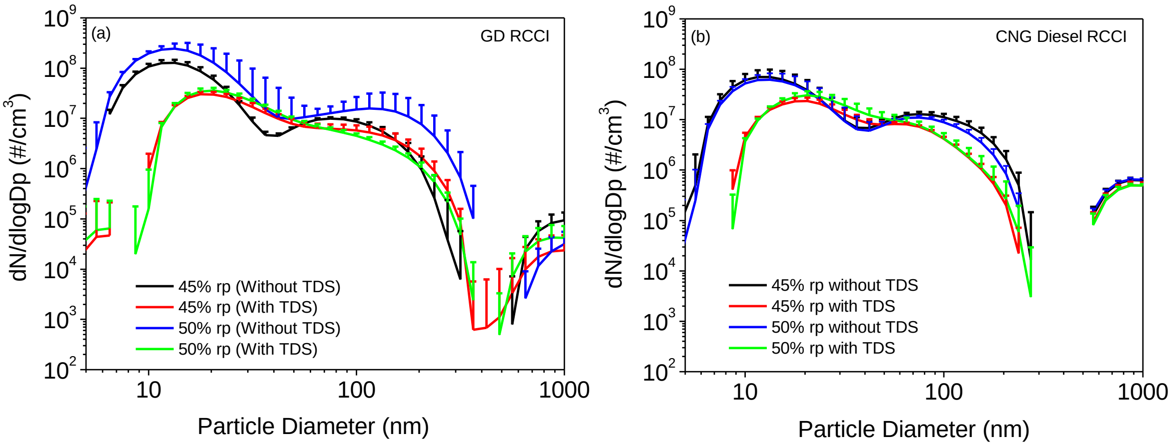

Figure 4.35 Effect of thermo-desorption system (TDS) on particle size distribution (PSD) for GD and CNG-diesel RCCI engine

Figure 4.36 (a-b) shows the effect of GD and CNG-diesel r_p on PMD with and without the developed thermo-desorption system. Figure 4.36 (a-b) shows that for both fuel operation, the largest peak arises in the particle size range of 50 to 400 nm. It indicates that large size AMPs mainly contributing in the total particulate mass in RCCI combustion. The peak of PMD rises as GD r_p increases from 45% to 50%, as seen in Figure. 4.36 (a). The overall reactivity of the charge decreases with increase in GD r_p which causes retarded combustion phasing and formation of high concentration of unburned hydrocarbons. These large AMPs are likely to be formed by condensation and coagulation of unburned hydrocarbons during exhaust cooling. These AMPs have large mobility diameter and high density therefore contributing more to particulate mass. In CNG-diesel RCCI combustion, the peak of PMD is significantly lower as compared to GD-RCCI combustion. This suggests that the combustion of CNG-diesel RCCI reduces the generation of solid soot particles. Additionally, as r_p increases, the peak of PMD declines as a result of less diesel fuel being fed into cylinder, which reduces the creation of soot particle precursors in the cylinder [4.41]. This reason for this observation can be due chemical structure of methane (the main component of CNG) which is devoid of C-C bonds, therefore particle precursor formation rate decreases for increased r_p. Furthermore, an increment in ignition delay with r_p tend to form low equivalence ratio regions in the engine cylinder. Combustion of lean fuel-air mixture resulted in low in-cylinder mean gas temperature. The rate of agglomeration is lower due to low combustion temperature, which prevents the creation of larger-sized particles. Figure 4.35 (a) indicates that when particle sampling is performed with thermodesorption system, the peak of PMD decreases drastically for all the tested GD 50% r_p. However, for 45% r_p the peak of PMD shifts towards large-size particles with thermodesorption system. This is due to an increase in the number concentration of particles with size > 120 nm with thermodesorption system at 45% r_p for GD RCCI. These observations can be due to soot particle restructuring, and fragmentation due to the removal of volatile organic compounds when the exhaust is passed through thermodesorption system. At 45% r_p, the amount of diesel injected is more as compared to 50%. More direct injection of diesel can lead to the formation of large-size solid soot agglomerates. During the thermodesorption process, coated soot particles are passed through a heated section of the thermodesorption system, typically at ~200–300 °C to evaporate the volatile coating material. Previous studies have shown that the soot particles can restructure during the evaporation of the coating material, depending on their surface tension [4.42-4.44].

Figure 4.36 (b) shows the PMD for CNG-diesel RCCI combustion. It can be observed that particle mass is substantially smaller for CNG-diesel RCCI combustion than for GD RCCI combustion. This is due to a reduction in the formation of accumulation mode particles with an increase in CNG mass with an increase in premixing ratio. The reduction in AMPs is due to a decrease in injected diesel fuel mass with an increase in CNG mass to maintain the constant load and speed. The number of soot precursors reduces with reduced diesel mass due to less diesel fuel being pyrolyzed. Also, CNG has a smaller number of C-C bonds and is gaseous, which decreases the particle precursors. Accumulation mode particles mainly contribute to particle mass, and therefore, the peak of PMD decreases. The peak of PMD also decreases with the thermodesorption system at all premixing ratios. This indicates that some AMPs are volatile and are formed from condensation and coagulation of unburned hydrocarbons. This shows that volatile organic compounds, which are decreased through the heating and desorption processes in the thermo-desorption system, make up the majority of the particles generated during the combustion in the RCCI. Therefore, these high boiling organic compounds with high molecular mass may contribute to particle mass at higher r_p [4.45-4.49]. Similar results are also observed for CNG-diesel RCCI combustion; however, the particle mass is substantially smaller for CNG-diesel RCCI combustion than for GD RCCI combustion.

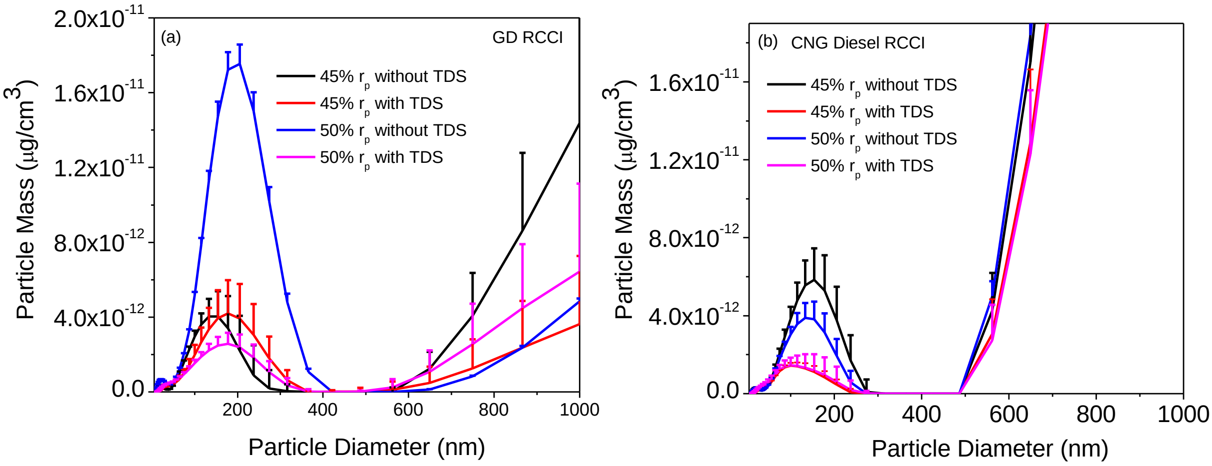

Figure 4.36. Effect of r_p on particle mass distribution with and without the developed thermo-desorption system (TDS) for GD and CNG-diesel RCCI engine

For GD RCCI combustion, Figure 4.37 (a-c) illustrates the impact of r_p on the total PN, NMPs, and AMPs with and without the thermo-desorption system. Figure 4.37 (a-c) indicates that with an increase in the GD r_p from 45% to 50%, the total PN, NMPs and AMPs concentration increased. Further increase in the GD r_p from 50% to 55%, the total PN, NMPs and AMPs concentration decreased. Figure 4.37 (a-c) indicates that NMPs are mainly contributing in the total PN concentration. NMPs mainly comprise liquid particles without solid core and formed from volatile organic compound and sulphur compounds during exhaust dilution and cooling [4.49]. As previously mentioned, the onset of ignition is delayed as the fuel r_p rises, and as a result, CA_{10} and CA_{50} are delayed. When the GD r_p is increased from 45% to 50%, the CA_{50} is delayed and most of the fuel air mixture burns in premixed combustion phase during the expansion stroke, as a results high concentration of NMPs are formed. On the other side, during the delayed CA_{50} the in-cylinder combustion temperature later in the engine cycle will be comparatively higher which may tend to the formation of AMPs in the later stage of the combustion due to the higher rate of agglomeration. When GD r_p is further increased from 50% to 55%, the CA_{50} is further retarded and more amount of the charge emits directly without combustion and is visualized as less formation of total PN, NMPs and AMPs concentration for 55% GD r_p. Figure 4.37 (a-c) also shows that when the particles are sampled with the thermo-desorption system, the total PN, NMPs and AMPs concentration is significantly decreased. The volatile particle removal efficiency (η_v) was found to be 77.5% when sampling with thermodesorption system for 45% GD r_p. It indicates that particles in GD-RCCI combustion form through the homogeneous nucleation of low volatility organic compounds and growth of these particles takes place through condensation of semi-volatile unburned hydrocarbons [4.49]. This demonstrates how premixed combustion decreases high equivalence ratio areas inside the engine cylinder in RCCI mode, which decreases the generation of elemental carbon-based soot.

A previous study found that in the premixed combustion mode, the organic carbon to total carbon ratio was high [4.49]. TEM analysis of the particles at lower load also showed the presence of condensed HC droplets [4.49]. This indicates the volatile nature of these particles. For 50% and 55 % GD r_p, the volatile particle removal efficiency (η_v) was found 87.29% and 77.83% respectively when particles are sampled with thermo-desorption system. These results suggest that majority of particles formed in RCCI combustion mode are volatile in nature and removed by thermodesorption system upon heating and adsorption of volatile compounds on activated charcoal. It is also observed that uncertainty in particle measurement is reduced when sampling was performed with thermodesorption system. This shows effectiveness of volatile particle removal by developed thermodesorption system.

Figure 4.37 (a-c) also shows that when the particles are sampled with the thermo-desorption system, the total PN, NMPs and AMPs concentration is significantly decreased. The volatile particle removal efficiency (η_v) was found to be 77.5% when sampling with thermodesorption system for 45% GD r_p. It indicates that particles in GD-RCCI combustion form through the homogeneous nucleation of low volatility organic compounds and growth of these particles takes place through condensation of semi-volatile unburned hydrocarbons [4.49]. This demonstrates how premixed combustion decreases high equivalence ratio areas inside the engine cylinder in RCCI mode, which decreases the generation of elemental carbon-based soot. A previous study found that in the premixed combustion mode, the organic carbon to total carbon ratio was high [4.33]. TEM analysis of the particles at lower load also showed the presence of condensed HC droplets [4.49]. This indicates the volatile nature of these particles. For 50% and 55 % GD r_p, the volatile particle removal efficiency (η_v) was found 87.29% and 77.83% respectively when particles are sampled with thermo-desorption system. These results suggest that majority of particles formed in RCCI combustion mode are volatile in nature and removed by thermodesorption system upon heating and adsorption of volatile compounds on activated charcoal. It is also observed that uncertainty in particle measurement is reduced when sampling was performed with thermodesorption system. This shows the effectiveness of volatile particle removal by developed thermodesorption system.

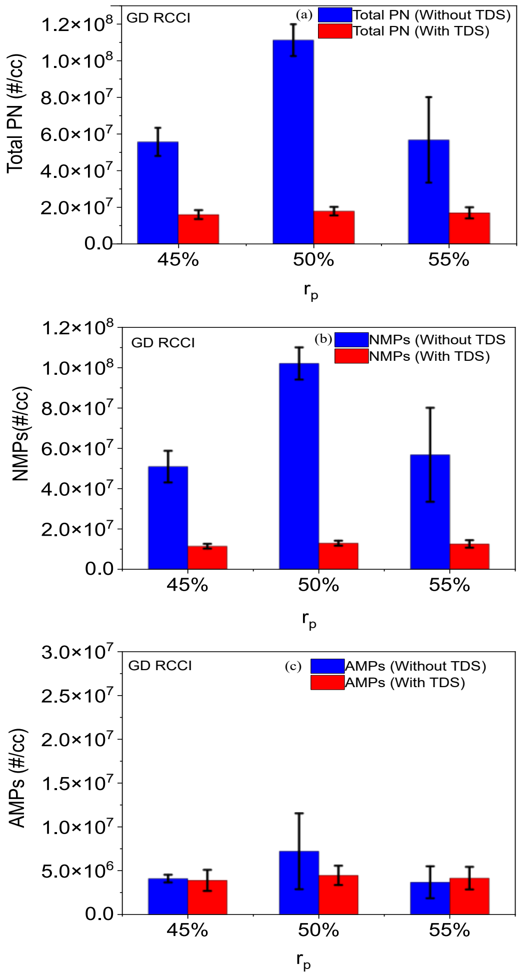

Figure 4.37 Effect of r_p on total PN, NMPs and AMPs emissions with and without thermo-desorption system (TDS) from GD-RCCI combustion

For CNG-diesel RCCI combustion, Figure 4.38 (a-c) illustrates the impact of r_p on the total PN, NMPs, and AMPs with and without the thermo-desorption system. Figure 4.38 (a-c) indicates that with an increase in the CNG-diesel r_p from 40% to 45% in CNG-diesel RCCI, the total PN and NMPs concentration increased, whereas AMPs decreased. The NMPs are mainly contributing in the total PNs. With an increase in the CNG-diesel r_p from 40% to 45%, the ignition delay will be longer; correspondingly CA_{10} and CA_{50} are also delayed. The formation of NMPs is higher when more amount of fuel air mixture burns in premixed combustion phase during the delayed CA_{50}. Another explanation is that hydrocarbons from diesel fuel may have undergone incomplete combustion reactions and condensed or nucleated to contribute to the formation of nucleation mode particles. CNG mainly contains methane and possess very less C-C bonds, which lowering the probability of forming benzene ring and other aromatic hydrocarbons during the combustion [4.50], [4.51]. The size of soot particle depends on rate of surface growth and particle agglomeration. Fewer precursors generated during combustion leads to less frequent collisions among particles. Additionally, as the CNG-diesel r_p rises, less diesel fuel is injected, which reduces the production of soot precursors such PAH and aliphatic chemical compounds, which are primarily contributors to AMPs formation. Further increase in CNG-diesel r_p from 45%

to 50%, the total PN and NMPs concentration decreased. When CNG-diesel r_p is further increased to 50%, the CA_{50} is retarded and most of the incylinder charge emits directly without the combustion and is visualized as less formation of total PN, NMPs, and AMPs concentration for 50% CNG-diesel r_p. One can be noticed from Figures 4.37 (a-c) and 4.38 (a-c) that the total PN emissions in CNG-diesel RCCI combustion is less as compared to GD-RCCI combustion for the same r_p. Figure 4.38 (a-c) indicates that when the particles are sampled with the thermo-desorption system, the total PN, NMPs, and AMPs concentration is significantly decreased in CNG-diesel RCCI combustion. For 40% CNG-diesel r_p, volatile particle removal efficiency (η_v) was determined at 51.76% when particles are sampled with thermo-desorption system. For 45% and 50% CNG-diesel r_p, the volatile particle removal efficiency (η_v) is determined at 67.55% and 52% respectively when particles are sampled with thermodesorption system. This suggests that volatile particles, which are eliminated by a thermodesorption device, also dominate CNG-diesel RCCI combustion. Thermo-desorption system also reduces the AMPs for all the r_p. It suggests that particle formation is through homogeneous nucleation of unburned hydrocarbons upon cooling and surface growth through surface condensation reactions leads to the formation of large-size volatile particles.

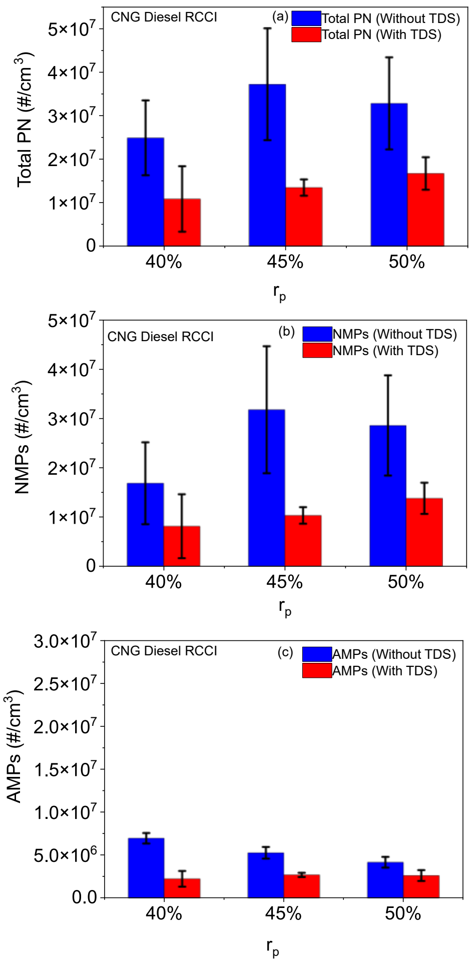

Figure 4.37 Effect of r_p on total PN, NMPs and AMPs emissions with and without thermo-desorption system (TDS) from CNG-diesel RCCI combustion

A qualitative association between the number and mass distribution of particles released during RCCI combustion mode at various premixing ratios, both with and without a thermodesorption device, is shown in Figure 4.39 (a-b) for both GD and CNG diesel RCCIs. In this figure, particle number is represented along X -axis, and Particle mass is represented along Y- axis. Each particle size's associated particle number and mass were joined by a lobe. Size and shape reflect the association between particle number and particle mass. Larger lobe indicates higher particle number and mass emissions. Inclination of lobe toward X axis indicates relative dominance of Particle number and inclination of lobe towards X axis indicates the dominance of particle mass. In GD RCCI operation at 45% premixing ratio peak of the lobe is small and it is more inclined toward particle mass. When the premixing ratio is increased from 45% to 50% the lobe is inclined both to particle mass and particle number. This is due to increase in concentration of both nucleation mode and accumulation mode particles. With a further increase in premixing ratio from 50% to 55% the peak of the lobe decreased and it inclined more toward particle mass. This is due to a decrease in concentration of both nucleation mode and accumulation mode particles. The apex of the lobe in the CNG diesel RCCI lowers as the premixing ratio rises, but the inclination towards particle mass and number does not change. This is due to a decrease in the number of accumulation mode particles with rise in premixing ratio which contributes more towards particle mass. With use of thermodesorption system there was a decrease in the peak of the lobe and it was more inclined toward particle mass. This indicates that thermodesorption system removed the small number of volatile nanoparticles while large particle consisting of high molecular weight hydrocarbons were less affected with use of thermodesorption system due to their high boiling points. These high molecular weight hydrocarbons are formed due to incomplete oxidation reactions of diesel and CNG as CA_{50} is retarded with rise in premixing ratio. These form larger particles upon homogeneous nucleation, condensation, and surface growth reactions.

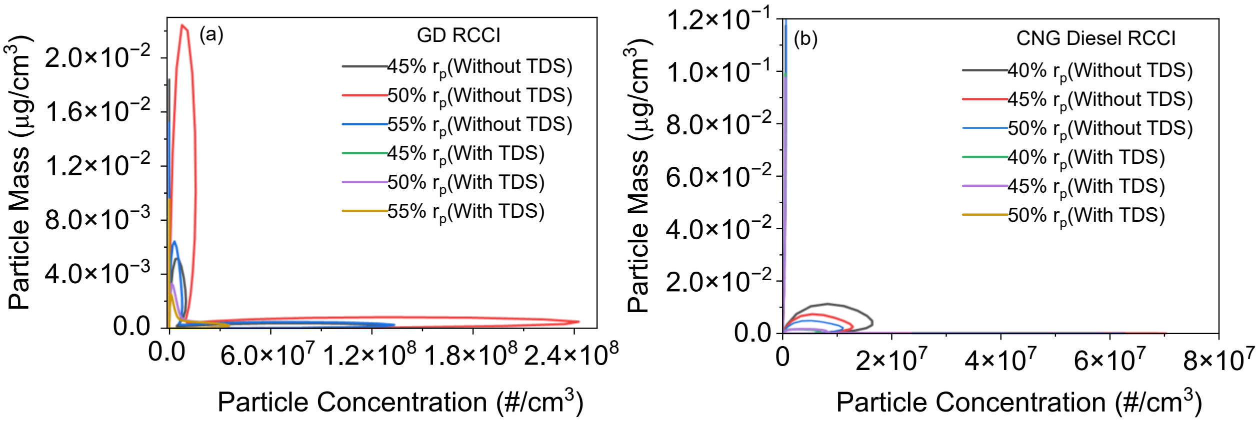

Figure 4.39 Influence of r_p on correlation between particle mass and particle number emission from GD RCCI and CNG diesel RCCI

Chapter 5

Conclusions and Future Scope

This chapter summarizes work included in the thesis. Combustion and incylinder PM emission characteristics of diesel engine is investigated by conducting a numerical study on a single cylinder diesel engine using A detailed soot model based on method of moments available in ANSYS FORTE CFD software. Combustion and PM emission characteristics of RCCI engine is investigated by conducting experimental study on modified single cylinder diesel engine. Main results and findings are summarized and recommendation for future work is discussed.

5.1 Summary and Conclusions

This section presents main results of combustion and PM analysis of diesel and RCCI engines. This section is divided into three subsections. First two subsection summarized the results of combustion and PM analysis of diesel and RCCI engines. Third subsection presents the main outcome and potential impact of the thesis work.

5.1.1 Combustion and PM emission characteristics of Diesel Engine

In this work, a parametric numerical study is conducted to investigate the effect of engine operating parameters on combustion and incylinder PM characteristics (PAH species mass fraction, number density, size, and volume fraction) of single cylinder automotive diesel engine using a detailed soot model based on method of moments available in ANSYS FORTE CFD software. Numerical model was validated with experimental results at different engine operating condition at different engine operating conditions. A good agreement was found between the experiment and numerical soot particle number density. Combustion analysis of diesel engine shows that peak combustion pressure and mean gas temperature increase with advanced injection timing and an increase in injection pressure. Numerical investigations on diesel engine shows that PAH species mass fraction decreased when injection timing was advanced from 6° bTDC to 18° bTDC and injection pressure increased. Particle number density, mean PM average diameter and PM volume fraction decreased with advanced injection timings and increase in fuel injection pressure. CFD simulations were also done at injection timings employed in RCCI operation. It was observed that acetylene mass fraction is not fully consumed during RCCI combustion in soot formation due to low incylinder temperature during combustion. This is opposite to the trend observed in diesel engine combustion in which acetylene mass fraction drops to zero after attaining the peak value after the start of combustion. Also, it was observed that for very advanced injection timings (30° bTDC to 50° bTDC) incylinder particle number density was negligible. This shows that particle formation mechanism in RCCI engines is different from that in diesel engines. It can be concluded from these observations that particle formation in RCCI engines occurs due to condensation of products of incomplete combustion of diesel such as acetylene in the exhaust plume.

5.1.2 Combustion and PM emission characteristics of RCCI engine

Combustion and particulate matter emission characteristics of RCCI engine is investigated by conducting an experimental study on modified single cylinder diesel engine. Combustion analysis of RCCI operations reveals that peak of LTHRR decreased and phasing of LTHRR is advanced with advanced diesel SOI for single injection strategy. On the other hand, peak HTHRR decreases and is slightly retarded with advance in diesel SOI. With double injection strategy it was observed that peak of LTHRR and HTHRR is lower and advanced as compared to single injection strategy. Analysis of diesel mass split regime on LTHRR and HTHRR shows that HTHRR is more retarded for 70 -30% diesel mass split injection strategy as compared to 50-50% diesel mass split regime. It was found that increase in CNG mass results in reduced and retarded LTHRR and HTHRR for 50-50% and 70-30% diesel mass split regime.

Particle number analysis for gasoline diesel and methanol diesel RCCI operation shows that total PN, NMPs, AMPs increased with advanced diesel SOI with an increase in amount of LTHR with single injection strategy. While for the double injection strategy, no significant variation was observed in total PNs and NMPs concentration with diesel SOI for gasoline diesel and methanol diesel RCCI operation even though LTHR is increasing. Interestingly, higher particle emissions were observed for gasoline diesel RCCI operation compared to single injection strategy RCCI operation. It was found that conventional dual fuel operation has a lower peak of NMPs and AMPs compared to RCCI operation. Additionally in conventional dual fuel mode, the peak of NMP in methanol diesel RCCI operation is significantly lower compared to gasoline diesel RCCI operation. For CNG diesel RCCI operation total PN emissions were significantly higher with the double injection strategy when SOI was advanced and the amount of LTHR was lower than the single injection strategy. Analysis of diesel mass split regime on PSD for CNG diesel RCCI operation shows that PSD peak is lower for particles having a diameter less than 30 nm when diesel SOI is advanced from 30° to 40° bTDC for 50-50% diesel mass split injection strategy. For 40° bTDC the PSD peak is higher for particles in the size range between 40 nm and 300 nm for 50% - 50% diesel mass split injection strategy. However, no significant variation has been found in the peak of NMPs and AMPs with diesel SOI for 70 – 30% diesel mass split injection strategy. Analysis of the effect of the diesel mass split regime on particle concentration and LTHR shows that the amount of LTHR and total PN concentration is slightly higher with 70 – 30% diesel mass split regime. With an increase in engine load from 1.5 bar BMEP to 3 bar BMEP peak of NMPs decreases and the peak of AMPs increase for CNG diesel RCCI operation for both diesel mass split regime. With an increase in CNG mass total PN, NMPs increased while AMPs decreased with a decrease in the amount of LTHR for CNG diesel RCCI operation. With thermodesorption system peak of NMPs in PSD curves is reduced by an order of magnitude for both gasoline diesel and CNG diesel RCCI operation. Peak of PMD also reduced drastically with thermodesorption system at all premixing ratios for gasoline diesel and CNG diesel RCCI operation. Thermodesorption system displayed high volatile particle removal efficiency for gasoline diesel RCCI operation at all premixing ratios while for CNG diesel RCCI operation the volatile particle removal efficiency was comparatively low. It was also found that uncertainty in measurement is reduced when sampling was performed with thermodesorption system. This is due to fact that nucleation mode particles cause large variability in particle measurement. When particle measurement was performed with thermodesorption system, concentration of nucleation mode particles reduced and less variations in particle size and number distribution was observed for both GD and CNG diesel RCCI mode. Also, condensed hydrocarbons on soot particle surface were effectively removed with thermodesorption system which decreased the uncertainty in particle measurement. This shows that particulate sampling is very important factor for achieving repeatable particle measurement results.

5.1.3 Main Outcome and Potential Impact

The present study investigated particle emission characteristics of RCCI engine employing Gasoline, Methanol, and CNG using single and double diesel direct injection strategy. The RCCI combustion is mainly premixed combustion and operated at advanced diesel injection timings. Typically, Gasoline-Diesel RCCI has higher particle number emissions as compared to Methanol and CNG. The study found that total PN, NMPs, and AMPs increased with advanced diesel SOI with an increase in the amount of LTHR with single injection strategy. For the double injection strategy, no significant variation was observed in total PNs and NMPs concentration with diesel SOI for gasoline diesel and methanol diesel RCCI operation even though LTHR is increasing. Additionally, the double diesel injection strategy has relatively higher particle numbers than the single injection strategy for CNG diesel RCCI operation.

This study also found the correlation between low temperature heat release with particle formation and developed the empirical correlation for the prediction of particle numbers with a good correlation coefficient based on heat release characteristics and engine operating conditions. Volatile and non-volatile nature of particles is further characterized using thermodesorption system developed as a part of present work. It was found that the peak of NMPs in PSD curves is reduced by an order of magnitude for both gasoline diesel and CNG diesel RCCI operation with thermodesorption system. This observation clearly suggests that a significant amount of particles are volatile and are liquid particles. Present emission legislations regulate solid particle number concentration from engine exhaust. The results of this study will help meet the regulatory norms during the commercial implementation of RCCI engines. The results of this work can assist in the development of a dedicated after-treatment system for RCCI engines.

5.2 Scope for future work

The current study focussed on the investigation of number and size data for PM emissions. Empirical correlation can be improved in future studies for predicting AMPs with the inclusion of direct injection parameters such as injection pressure. Chemical Analysis and TEM morphology analysis would be helpful to understand the detailed chemical composition and structure of soot particles. Comparison between two-stage dilution system, catalytic stripper, and thermodesorption system in terms of volatile particle removal efficiency can be made in future studies. Although it has been demonstrated that soot emissions are incredibly minimal, RCCI combustion mode has been found to produce a lot of volatile particles. To better understand the effects of the RCCI PM emissions on human health and the environment, it would be of significant study interest to investigate the chemical compositions of these emissions in the future.

References

[1.1] Kalghatgi, G. T. (2015). Developments in internal combustion engines and implications for combustion science and future transport fuels. Proceedings of the Combustion Institute, 35(1), 101-115.

[1.2] Kalghatgi, G. (2018). Is it really the end of internal combustion engines and petroleum in transport? Applied energy, 225, 965-974.

[1.3] Kalghatgi, G. (2013). Fuel/engine interactions. SAE international.

[1.4] Schiffer, H. W., Kober, T., & Panos, E. (2018). World energy council's global energy scenarios to 2060. Zeitschrift für Energiewirtschaft, 42(2), 91-102.

[1.5] Frei, C., & General, S. (2011). Global transport scenarios 2050. World Energy Council: London, UK.

[1.6] Kober, T., Schiffer, H. W., Densing, M., & Panos, E. (2020). Global energy perspectives to 2060–WEC's World Energy Scenarios 2019. Energy Strategy Reviews, 31, 100523.

[1.7] Reitz, R. D., Ogawa, H., Payri, R., Fansler, T., Kokjohn, S., Moriyoshi, Y., … & Zhao, H. (2020). IJER editorial: The future of the internal combustion engine. International Journal of Engine Research, 21(1), 3-10

[1.8] Agarwal, A. K., Singh, A. P., García, A., & Monsalve-Serrano, J. (2022). Challenges and Opportunities for Application of Reactivity-Controlled Compression Ignition Combustion in Commercially Viable Transport Engines. Progress in Energy and Combustion Science, 93, 101028

[1.9] Paykani, A., Garcia, A., Shahbakhti, M., Rahnama, P., & Reitz, R. D. (2021). Reactivity controlled compression ignition engine: Pathways towards commercial viability. Applied Energy, 282, 116174.

[1.10] Nimesh, V., Sharma, D., Reddy, V. M., & Goswami, A. K. (2020). Implication viability assessment of shift to electric vehicles for present power generation scenario of India. Energy, 195, 116976.

[1.11] Sharma, I., & Chandel, M. K. (2020). Will electric vehicles (Evs) be less polluting than conventional automobiles under Indian city conditions? Case Studies on Transport Policy, 8(4), 1489-1503

[1.12] Senecal, P. K., & Leach, F. (2019). Diversity in transportation: Why a mix of propulsion technologies is the way forward for the future fleet. Results in Engineering, 4, 100060

[1.13] Reitz, R. D. (2013). Directions in internal combustion engine research. Combustion and Flame, 160(1), 1-8.

[1.14] Pundir, B. P. (2017). Engine emissions: fundamentals and advances in control (No. 8278). Alpha Science International.

[1.15] Lakshminarayanan, P. A., Aghav, Y. V., & Shi, Y. (2010). Modelling diesel combustion (Vol. 53, p. 287). New York: Springer.

[1.16] Rana, S., Saxena, M. R., & Maurya, R. K. (2022). A review on morphology, nanostructure, chemical composition, and number concentration of diesel particulate emissions. Environmental Science and Pollution Research, 1-58.

[1.17] Ristovski, Z. D., Miljevic, B., Surawski, N. C., Morawska, L., Fong, K. M., Goh, F., & Yang, I. A. (2012). Respiratory health effects of diesel particulate matter. Respirology, 17(2), 201-212.

[1.18] Bhatia, R., Lopipero, P., & Smith, A. H. (1998). Diesel exhaust exposure and lung cancer. Epidemiology, 84-91.

[1.19] Shindell, D., Faluvegi, G., Walsh, M., Anenberg, S. C., Van Dingenen, R., Muller, N. Z., … & Milly, G. (2011). Climate, health, agricultural and economic impacts of tighter vehicle-emission standards. Nature Climate Change, 1(1), 59-66

[1.20] Singh, S., Kulshrestha, M. J., Rani, N., Kumar, K., Sharma, C., & Aswal, D. K. (2023). An overview of vehicular emission standards. Mapan, 38(1), 241-263.

[1.21] Knecht, W. (2008). Diesel engine development in view of reduced emission standards. Energy, 33(2), 264-271.

[1.22] Bansal, G., & Bandivadekar, A. (2013). Overview of India’s vehicle emissions control program. ICCT, Beijing, Berlin, Brussels, San Francisco, Washington.

[1.23] Heywood, J. B. (2018). Internal combustion engine fundamentals. McGraw-Hill Education.

[1.24] Pundir, B. P. (2010). IC engines: Combustion and emissions.

[1.25] Maurya, R. K. (2019). Reciprocating engine combustion diagnostics: In-Cylinder pressure measurement and analysis. Springer.

[1.26] Rana, S., Saxena, M. R., & Maurya, R. K. (2021). Development and characterization of aerosol conditioning devices for solid ultrafine particle measurement from diesel engines: A review. SAE Technical Paper, 01-0615.

[1.27] Dec, J. E. (1997). A conceptual model of DI diesel combustion based on laser-sheet imaging. SAE transactions, 1319-1348.

[1.28] Yin, Z., Liu, S., Tan, D., Zhang, Z., Wang, Z., & Wang, B. (2023). A review of the development and application of soot modelling for modern diesel engines and the soot modelling for different fuels. Process

[1.29] Zhao, F., Yang, W., & Yu, W. (2020). A progress review of practical soot modelling development in diesel engine combustion. Journal of Traffic and Transportation Engineering (English Edition), 7(3), 269-281.

[1.30] Lee, Y., Lee, Y., Moon, S., Lee, S., Roh, Y., & Min, K. (2022). Development of semi-empirical soot emission model for a CI engine. Science of The Total Environment, 820, 153327.

[1.31] Mosbach, S., Celnik, M. S., Raj, A., Kraft, M., Zhang, H. R., Kubo, S., & Kim, K. O. (2009). Towards a detailed soot model for internal combustion engines. Combustion and Flame, 156(6), 1156-1165.

[1.31] Lee, Y., Lee, Y., Moon, S., Lee, S., Roh, Y., & Min, K. (2022). Development of semi-empirical soot emission model for a CI engine. Science of The Total Environment, 820, 153327

[1.32] Fontanesi, S., Del Pecchia, M., Pessina, V., Sparacino, S., & Di Iorio, S. (2022). Quantitative investigation on the impact of injection timing on soot formation in a GDI engine with a customized sectional method. International Journal of Engine Research, 23(4), 624-637.

[1.33] Del Pecchia, M., Sparacino, S., Pessina, V., Fontanesi, S., Breda, S., Irimescu, A., & Di Iorio, S. (2020). Development of a Sectional Soot Model Based Methodology for the Prediction of Soot Engine-Out Emissions in GDI Units (No. 2020-01-0239). SAE Technical Paper.

[1.34] Fraioli, V., Beatrice, C., & Lazzaro, M. (2011). Soot particle size modelling in 3D simulations of diesel engine combustion. Combustion Theory and Modelling, 15(6), 863-892.

[1.35] Frenklach, M. (1985). Computer modeling of infinite reaction sequences: a chemical lumping. Chemical engineering science, 40(10), 1843-1849.

[1.36] Hong, S., Wooldridge, M. S., Im, H. G., Assanis, D. N., & Pitsch, H. (2005). Development and application of a comprehensive soot model for 3D CFD reacting flow studies in a diesel engine. Combustion and Flame, 143(1-2), 11-26.

[1.37] Zhong, B. J., Dang, S., Song, Y. N., & Gong, J. S. (2012). 3-D simulation of soot formation in a direct-injection diesel engine based on a comprehensive chemical mechanism and method of moments. Combustion Theory and Modelling, 16(1), 143-171.

[1.38] Zhao, F., Yang, W., Zhou, D., Yu, W., Li, J., & Tay, K. L. (2017). Numerical modelling of soot formation and oxidation using phenomenological soot modelling approach in a dual-fueled compression ignition engine. Fuel, 188, 382-389.

[1.39] Duvvuri, P. P., Sukumaran, S., Shrivastava, R. K., & Sreedhara, S. (2019). Modeling soot particle size distribution in diesel engines. Fuel, 243, 70-78.

[1.40] Arad, A., Sher, E., & Enden, G. (2020). Phenomenological soot modeling with solution mapping optimization of biodiesel-diesel blends in diesel engines. Thermal Science and Engineering Progress, 18, 100544.

[1.41] Dong, X., Duan, H., Jia, M., Wu, S., & Chang, Y. (2023). Development of a practical soot model for diesel surrogate fuels and oxygenated fuels with specific soot precursor tracking and uniform model structure. Fuel, 340, 127531.

[1.42] Puduppakkam, K. V., Naik, C. V., & Meeks, E. (2021). Validation Studies of a Detailed Soot Chemistry for Gasoline and Diesel Engines (No. 2021-01-0618). SAE Technical Paper.

[1.43] Pan, K., & Wallace, J. (2022). Soot and combustion models for direct-injection natural gas engines. International Journal of Engine Research, 23(1), 150-166.

[1.44] Wu, S., Zhou, D., & Yang, W. (2019). Implementation of an efficient method of moments for treatment of soot formation and oxidation processes in three-dimensional engine simulations. Applied Energy, 254, 113661.

[1.45] Zhou, H., Li, X., & Liu, F. (2019). Soot formation and oxidation mechanisms in a diesel engine separated swirl combustion system. Fuel, 257, 115955.

[1.46] Duvvuri, P. P., Shrivastava, R. K., & Sreedhara, S. (2021). In-Cylinder Validation of a Method of Moments-Based Soot Model for Diesel Engines. SAE International Journal of Advances and Current Practices in Mobility, 4(2021-26-0414), 742-752.

[1.47] Development of a phenomenological soot model integrated with a reduced TRF-PAH mechanism for diesel engine application. Fuel, 283, 118810.

[1.48] Zhao, F., Yang, W., Yu, W., Li, H., Sim, Y. Y., Liu, T., & Tay, K. L. (2018). Numerical study of soot particles from low temperature combustion of engine fueled with diesel fuel and unsaturation biodiesel fuels. Applied Energy, 211, 187-193.

[1.49] Martos, F. J., Doustdar, O., Zeraati-Rezaei, S., Herreros, J. M., & Tsolakis, A. (2023). Impact of alcohol–diesel fuel blends on soot primary particle size in a compression ignition engine. Fuel, 333, 126346.

[1.50] Li, J., Gong, S., Liang, Y., Wu, S., Liu, R., & Yang, W. (2024). Analysis of soot formation and oxidation processes in the diesel engine fueled by n-octanol/biodiesel blends based on a detailed soot population balance model. Fuel, 358, 130376.

[1.51] Ciatti, S. A. (2015). Compression ignition engines–revolutionary technology that has civilized frontiers all over the globe from the industrial revolution into the twenty-first century. Frontiers in Mechanical Engineering, 1, 5.

[1.52] Yao, M., Zheng, Z., & Liu, H. (2009). Progress and recent trends in homogeneous charge compression ignition (HCCI) engines. Progress in energy and combustion science, 35(5), 398-437.

[1.53] Keeler, B., & Shayler, P. J. (2008). Constraints on fuel injection and EGR strategies for diesel PCCI-type combustion (No. 2008-01-1327). SAE Technical Paper.

[1.54] Kiplimo, R., Tomita, E., Kawahara, N., & Yokobe, S. (2012). Effects of spray impingement, injection parameters, and EGR on the combustion and emission characteristics of a PCCI diesel engine. Applied Thermal Engineering, 37, 165-175.

[1.55] Hildingsson, L., Johansson, B., Kalghatgi, G. T., & Harrison, A. J. (2010). Some effects of fuel autoignition quality and volatility in premixed compression ignition engines. SAE International Journal of Engines, 3(1), 440-460.

[1.56] Inagaki, K., Fuyuto, T., Nishikawa, K., Nakakita, K., & Sakata, I. (2006). Dual-fuel PCI combustion controlled by in-cylinder stratification of ignitability (No. 2006-01-0028). SAE Technical Paper.

[1.57] Kokjohn, S. L., Hanson, R. M., Splitter, D. A., & Reitz, R. D. (2010). Experiments and modelling of dual-fuel HCCI and PCCI combustion using in-cylinder fuel blending. SAE International Journal of Engines, 2(2), 24-39.

[1.58] Saxena, M. R., Rana, S., & Maurya, R. K. (2023). Experimental investigation on the effect of in-cylinder heat release features on particle emissions characteristics of CNG–diesel RCCI engine. International Journal of Environmental Science and Technology, 1-20.

[1.59] Hanson, R. M., Kokjohn, S. L., Splitter, D. A., & Reitz, R. D. (2010). An experimental investigation of fuel reactivity controlled PCCI combustion in a heavy-duty engine. SAE international journal of engines, 3(1), 700-716.

[1.60] Kokjohn, S. L., Hanson, R. M., Splitter, D. A., & Reitz, R. D. (2011). Fuel reactivity controlled compression ignition (RCCI): a pathway to controlled high-efficiency clean combustion. International Journal of Engine Research, 12(3), 209-226

[1.61] Hanson, R., Kokjohn, S., Splitter, D., & Reitz, R. (2011). Fuel effects on reactivity controlled compression ignition (RCCI) combustion at low load. SAE International Journal of Engines, 4(1), 394-411.

[1.62] Splitter, D., Hanson, R., Kokjohn, S., Wissink, M., & Reitz, R. D. (2011). Injection effects in low load RCCI dual-fuel combustion (No. 2011-24-0047). SAE Technical Paper

[1.63] Li, Y., Jia, M., Liu, Y., & Xie, M. (2013). Numerical study on the combustion and emission characteristics of a methanol/diesel reactivity controlled compression ignition (RCCI) engine. Applied energy, 106, 184-197.

[1.64] Ma, S., Zheng, Z., Liu, H., Zhang, Q., & Yao, M. (2013). Experimental investigation of the effects of diesel injection strategy on gasoline/diesel dual-fuel combustion. Applied energy, 109, 202-212.

[1.65] Molina, S., García, A., Pastor, J. M., Belarte, E., & Balloul, I. (2015). Operating range extension of RCCI combustion concept from low to full load in a heavy-duty engine. Applied Energy, 143, 211-227.

[1.66] Mikulski, M., Balakrishnan, P. R., Doosje, E., & Bekdemir, C. (2018). Variable valve actuation strategies for better efficiency load range and thermal management in an RCCI engine (No. 2018-01-0254). SAE Technical Paper.

[1.67] Doosje, E., Willems, F., & Baert, R. (2014). Experimental demonstration of RCCI in heavy-duty engines using diesel and natural gas (No. 2014-01-1318). SAE Technical Paper.

[1.68] Mikulski, M., & Bekdemir, C. (2017). Understanding the role of low reactivity fuel stratification in a dual fuel RCCI engine–A simulation study. Applied energy, 191, 689-708.

[1.69] Jia, Z., & Denbratt, I. (2015). Experimental investigation of natural gas-diesel dual-fuel RCCI in a heavy-duty engine. SAE International Journal of Engines, 8(2), 797-807.

[1.70] Dahodwala, M., Joshi, S., Koehler, E., Franke, M., & Tomazic, D. (2015). Experimental and computational analysis of diesel-natural gas RCCI combustion in heavy-duty engines (No. 2015-01-0849). SAE Technical Paper.

[1.71] Poorghasemi, K., Saray, R. K., Ansari, E., Irdmousa, B. K., Shahbakhti, M., & Naber, J. D. (2017). Effect of diesel injection strategies on natural gas/diesel RCCI combustion characteristics in a light duty diesel engine. Applied energy, 199, 430-446.

[1.72] Gharehghani, A., Salahi, M. M., Andwari, A. M., Mikulski, M., & Könnö, J. (2023). Reactivity enhancement of natural gas/diesel RCCI engine by adding ozone species. Energy, 274, 127341.

[1.73] Ganesan, N., Viswanathan, K., Karthic, S. V., Ekambaram, P., Wu, W., & Vo, D. V. N. (2022). Split injection strategies based RCCI combustion analysis with waste cooking oil biofuel and methanol in an open ECU assisted CRDI engine. Fuel, 319, 123710.

[1.74] Panda, K., & Ramesh, A. (2022). Parametric investigations to establish the potential of methanol based RCCI engine and comparison with the conventional dual fuel mode. Fuel, 308, 122025.

[1.75] Thomas, J. J., Nagarajan, G., Sabu, V. R., Manojkumar, C. V., & Sharma, V. (2022). Performance and emissions of hexanol-biodiesel fuelled RCCI engine with double injection strategies. Energy, 253, 124069.

[1.76] Duan, H., Jia, M., Xu, Z., Li, Y., & Xia, G. (2023). Comprehensive analysis of combustion behaviors of hydrogen (H2)/diesel reactivity-controlled compression ignition (RCCI) in a light-duty diesel engine. Fuel, 353, 129237.

[1.77] Wang, L., Liang, W., Ma, H., Ji, Q., Sun, P., & Liu, J. (2023). Simulation study on effects of EGR ratio and compression ratio on combustion and emission characteristics of PODE/methanol RCCI engine. Fuel, 334, 126593.

[1.78] Liu, X., Jiang, P., Zhong, W., He, Z., & Wang, Q. (2023). Optical diagnostics of premixed energy ratio effects on RCCI combustion and soot formation characteristics under low load conditions. Thermal Science and Engineering Progress, 46, 102164.

[1.79] Sun, W., Zeng, W., Guo, L., Zhang, H., Yan, Y., Lin, S., … & Sun, Y. (2022). Experimental investigation into the effects of pilot fuel and intake condition on combustion and emission characteristics of RCCI engine. Fuel, 325, 124912.

[1.80] Benajes, J., García, A., Monsalve-Serrano, J., & Boronat, V. (2017). An investigation on the particulate number and size distributions over the whole engine map from an optimized combustion strategy combining RCCI and dual-fuel diesel-gasoline. Energy Conversion and Management, 140, 98-108.

[1.81] Garcia, A., Monsalve-Serrano, J., Villalta, D., & Fogué-Robles, Á. (2022). Detailed analysis of particulate emissions of a multi-cylinder dual-mode dual-fuel engine operating with diesel and gasoline. Fuel, 330, 125578.

[1.82] Agarwal, A. K., Singh, A. P., & Kumar, V. (2021). Particulate characteristics of low-temperature combustion (PCCI and RCCI) strategies in single cylinder research engine for developing sustainable and cleaner transportation solution. Environmental pollution, 284, 117375.

[1.83] Geng, P., Yao, C., Wei, L., Liu, J., Wang, Q., Pan, W., & Wang, J. (2014). Reduction of PM emissions from a heavy-duty diesel engine with diesel/methanol dual fuel. Fuel, 123, 1-11.

[1.84] Wu, T., Yao, A., Yao, C., Pan, W., Wei, H., Chen, C., & Gao, J. (2018). Effect of diesel late-injection on combustion and emissions characteristics of diesel/methanol dual fuel engine. Fuel, 233, 317-327.

[1.85] Lee, J., Lee, S., & Lee, S. (2018). Experimental investigation on the performance and emissions characteristics of ethanol/diesel dual-fuel combustion. Fuel, 220, 72-79.

[1.86] Di Iorio, S., Magno, A., Mancaruso, E., & Vaglieco, B. M. (2016). Characterization of particle number and mass size distributions from a small compression ignition engine operating in diesel/methane dual fuel mode. Fuel, 180, 613-623.

[1.87] Qian, Y., Zhang, Y., Wang, X., & Lu, X. (2017). Particulate matter emission characteristics of a reactivity controlled compression ignition engine fueled with biogas/diesel dual fuel. Journal of Aerosol Science, 113, 166-177.

[1.88] Han, W., Lu, Y., Jin, C., Tian, X., Peng, Y., Pan, S., ... & Zhong, Y. (2020). Study on influencing factors of particle emissions from a RCCI engine with variation of premixing ratio and total cycle energy. Energy, 202, 117707.

[1.89] Saxena, M. R., & Maurya, R. K. (2020). Influence of direct injection timing and mass of port injected gasoline on unregulated and nano-particle emissions from RCCI engine. Fuel, 282, 118815.

[1.90] Pan, S., Liu, X., Cai, K., Li, X., Han, W., & Li, B. (2020). Experimental study on combustion and emission characteristics of iso-butanol/diesel and gasoline/diesel RCCI in a heavy-duty engine under low loads. Fuel, 261, 116434.

[1.91] Mikulski, M., Ramesh, S., & Bekdemir, C. (2019). Reactivity Controlled Compression Ignition for clean and efficient ship propulsion. Energy, 182, 1173-1192.

[1.92] Valladolid, P. G., Tunestål, P., Monsalve-Serrano, J., García, A., & Hyvönen, J. (2017). Impact of diesel pilot distribution on the ignition process of a dual fuel medium speed marine engine. Energy Conversion and Management, 149, 192-205.

[1.93] Taghavifar, H. (2023). The influence of different fuels and injection methods of RCCI and DCI in hybrid ICE-Battery vehicle performance. Fuel, 340, 127467.

[1.94] Kokjohn, S., Reitz, R., Splitter, D., & Musculus, M. (2012). Investigation of fuel reactivity stratification for controlling PCI heat-release rates using high-speed chemiluminescence imaging and fuel tracer fluorescence. SAE International Journal of Engines, 5(2), 248-269.

[1.95] Kokjohn, S. L., Musculus, M. P., & Reitz, R. D. (2015). Evaluating temperature and fuel stratification for heat-release rate control in a reactivity-controlled compression-ignition engine using optical diagnostics and chemical kinetics modelling. Combustion and Flame, 162(6), 2729-2742.

[1.96] Liu, H., Tang, Q., Yang, Z., Ran, X., Geng, C., Chen, B., ... & Yao, M. (2019). A comparative study on partially premixed combustion (PPC) and reactivity controlled compression ignition (RCCI) in an optical engine. Proceedings of the Combustion institute, 37(4), 4759-4766.

[1.97] Reitz, R. D., & Duraisamy, G. (2015). Review of high efficiency and clean reactivity controlled compression ignition (RCCI) combustion in internal combustion engines. Progress in Energy and Combustion Science, 46, 12-71.

[1.98] Splitter, D., Wissink, M., DelVescovo, D., & Reitz, R. D. (2013). RCCI engine operation towards 60% thermal efficiency (No. 2013-01-0279). SAE Technical Paper

[2.1] Aldhaidhawi, M., Chiriac, R., & Badescu, V. (2017). Ignition delay, combustion and emission characteristics of Diesel engine fueled with rapeseed biodiesel–A literature review. Renewable and Sustainable Energy Reviews, 73, 178-186.

[2.2] Lakshminarayanan, P. A., Aghav, Y. V., & Shi, Y. (2010). Modelling diesel combustion (Vol. 53, p. 287). New York: Springer.

[2.3] Ferguson, C. R., & Kirkpatrick, A. T. (2015). Internal combustion engines: applied thermosciences. John Wiley & Sons.

[2.4] Köten, H., & Parlakyiğit, A. S. (2018). Effects of the diesel engine parameters on the ignition delay. Fuel, 216, 23-28.

[2.5] Rodríguez, R. P., Sierens, R., & Verhelst, S. (2011). Ignition delay in a palm oil and rapeseed oil biodiesel fuelled engine and predictive correlations for the ignition delay period. Fuel, 90(2), 766-772.

[2.6] Wolfer, H. H. (1938). Ignition lag in diesel engines. VDI-Forschungsheft, 392, 621-436.

[2.7] Kamimoto, T., & Kobayashi, H. (1991). Combustion processes in diesel engines. Progress in Energy and Combustion Science, 17(2), 163-189.

[2.8] Lakshminarayanan, P. A., Nayak, N., Dingare, S. V., & Dani, A. D. (2002). Predicting hydrocarbon emissions from direct injection diesel engines. J. Eng. Gas Turbines Power, 124(3), 708-716.

[2.9] Agarwal, A. K., Srivastava, D. K., Dhar, A., Maurya, R. K., Shukla, P. C., & Singh, A. P. (2013). Effect of fuel injection timing and pressure on combustion, emissions and performance characteristics of a single cylinder diesel engine. Fuel, 111, 374-383.

[2.10] Panneerselvam, N., Murugesan, A., Vijayakumar, C., Kumaravel, A., Subramaniam, D., & Avinash, A. (2015). Effects of injection timing on bio-diesel fuelled engine characteristics—An overview. Renewable and Sustainable Energy Reviews, 50, 17-31.

[2.11] Kook, S., Bae, C., Miles, P. C., Choi, D., & Pickett, L. M. (2005). The influence of charge dilution and injection timing on low-temperature diesel combustion and emissions. SAE transactions, 1575-1595.

[2.12] Kook, S., Park, S., & Bae, C. (2008). Influence of early fuel injection timings on premixing and combustion in a diesel engine. Energy & Fuels, 22(1), 331-337.

[2.13] Sharma, A., & Murugan, S. (2015). Combustion, performance and emission characteristics of a DI diesel engine fuelled with non-petroleum fuel: a study on the role of fuel injection timing. Journal of the Energy Institute, 88(4), 364-375.

[2.14] Sazhina, E. M., Sazhin, S. S., Heikal, M. R., Babushok, V. I., & Johns, R. J. R. (2000). A detailed modelling of the spray ignition process in diesel engines. Combustion Science and Technology, 160(1), 317-344.

[2.15] Saxena, M. R., & Maurya, R. K. (2017). Effect of premixing ratio, injection timing and compression ratio on nano particle emissions from dual fuel non-road compression ignition engine fueled with gasoline/methanol (port injection) and diesel (direct injection). Fuel, 203, 894-914.

[2.16] Canakci, M., Sayin, C., Ozsezen, A. N., & Turkcan, A. (2009). Effect of injection pressure on the combustion, performance, and emission characteristics of a diesel engine fueled with methanol-blended diesel fuel. Energy & Fuels, 23(6), 2908-2920.

[2.17] Cao, D. N., Hoang, A. T., Luu, H. Q., Bui, V. G., & Tran, T. T. H. (2020). Effects of injection pressure on the NOx and PM emission control of diesel engine: A review under the aspect of PCCI combustion condition. Energy Sources, Part A: Recovery, Utilization, and Environmental Effects, 1-18.

[2.18] Dodge, L. G., Simescu, S., Neely, G. D., Maymar, M. J., Dickey, D. W., & Savonen, C. L. (2002). Effect of small holes and high injection pressures on diesel engine combustion (No. 2002-01-0494). SAE Technical Paper.

[2.19] Roy, M. M. (2009). Effect of fuel injection timing and injection pressure on combustion and odorous emissions in DI diesel engines. Journal of Energy Resources Technology, 131(3).

[2.20] Agarwal, A. K., Dhar, A., Gupta, J. G., Kim, W. I., Choi, K., Lee, C. S., & Park, S. (2015). Effect of fuel injection pressure and injection timing of Karanja biodiesel blends on fuel spray, engine performance, emissions and combustion characteristics. Energy Conversion and Management, 91, 302-314.

[2.21] Payri, R., Salvador, F. J., Gimeno, J., & De la Morena, J. (2009). Effects of nozzle geometry on direct injection diesel engine combustion process. Applied thermal engineering, 29(10), 2051-2060.

[2.22] Inagaki, K., Fuyuto, T., Nishikawa, K., Nakakita, K., & Sakata, I. (2006). Dual-fuel PCI combustion controlled by in-cylinder stratification of ignitability (No. 2006-01-0028). SAE Technical Paper.

[2.23] Kokjohn, S. L., Hanson, R. M., Splitter, D. A., & Reitz, R. D. (2010). Experiments and modeling of dual-fuel HCCI and PCCI combustion using in-cylinder fuel blending. SAE International Journal of Engines, 2(2), 24-39

[2.24] Splitter, D., Kokjohn, S., Rein, K., Hanson, R., Sanders, S., & Reitz, R. (2010). An optical investigation of ignition processes in fuel reactivity controlled PCCI combustion. SAE International Journal of Engines, 3(1), 142-162.

[2.25] Splitter, D., Wissink, M., DelVescovo, D., & Reitz, R. (2013). RCCI engine operation towards 60% thermal efficiency (pp. 01-0279). Warrendale, PE, USA: SAE International

[2.26] Kokjohn, S., Hanson, R., Splitter, D., Kaddatz, J., & Reitz, R. (2011). Fuel reactivity controlled compression ignition (RCCI) combustion in light-and heavy-duty engines. SAE International Journal of Engines, 4(1), 360-374.

[2.27] Kokjohn, S., Reitz, R., Splitter, D., & Musculus, M. (2012). Investigation of fuel reactivity stratification for controlling PCI heat-release rates using high-speed chemiluminescence imaging and fuel tracer fluorescence. SAE International Journal of Engines, 5(2), 248-269

[2.28] Ryan Walker, N., Wissink, M. L., DelVescovo, D. A., & Reitz, R. D. (2015). Natural gas for high load dual-fuel reactivity-controlled compression ignition in heavy-duty engines. Journal of Energy Resources Technology, 137(4).

[2.29] Doosje, E., Willems, F., & Baert, R. (2014). Experimental demonstration of RCCI in heavy-duty engines using diesel and natural gas (No. 2014-01-1318). SAE Technical Paper.

[2.30] Ansari, E., Poorghasemi, K., Irdmousa, B. K., Shahbakhti, M., & Naber, J. (2016). Efficiency and emissions mapping of a light duty diesel-natural gas engine operating in conventional diesel and RCCI modes (No. 2016-01-2309). SAE Technical Paper.

[2.31] Ansari, E., Shahbakhti, M., & Naber, J. (2018). Optimization of performance and operational cost for a dual mode diesel-natural gas RCCI and diesel combustion engine. Applied energy, 231, 549-561.

[2.32] Hanson, R. M., Kokjohn, S. L., Splitter, D. A., & Reitz, R. D. (2010). An experimental investigation of fuel reactivity controlled PCCI combustion in a heavy-duty engine. SAE international journal of engines, 3(1), 700-716.

[2.33] Splitter, D., Hanson, R., Kokjohn, S., Wissink, M., & Reitz, R. D. (2011). Injection effects in low load RCCI dual-fuel combustion (No. 2011-24-0047). SAE Technical Paper.

[2.34] Walker, N. R., Dempsey, A. B., Andrie, M. J., & Reitz, R. D. (2013). Use of low-pressure direct-injection for reactivity controlled compression ignition (RCCI) light-duty engine operation. SAE International Journal of Engines, 6(2), 1222-1237.

[2.35] Ma, S., Zheng, Z., Liu, H., Zhang, Q., & Yao, M. (2013). Experimental investigation of the effects of diesel injection strategy on gasoline/diesel dual-fuel combustion. Applied energy, 109, 202-212.

[2.36] Benajes, J., Molina, S., García, A., Belarte, E., & Vanvolsem, M. (2014). An investigation on RCCI combustion in a heavy duty diesel engine using in-cylinder blending of diesel and gasoline fuels. Applied Thermal Engineering, 63(1), 66-76.

[2.37] Liu, J., Liu, Y., Ji, Q., Sun, P., Zhang, X., Wang, X., & Ma, H. (2023). Effects of split injection strategy on combustion stability and GHG emissions characteristics of natural gas/diesel RCCI engine under high load. Energy, 266, 126542.

[2.38] Yıldız, M., & Çeper, B. A. (2022). A comparative study on gasoline/diesel-fueled RCCI combustion at different premixed ratios and high-EGR diesel CI combustion in an IC engine under low load conditions. Fuel, 324, 124596.

[2.40] Qian, Y., Ouyang, L., Wang, X., Zhu, L., & Lu, X. (2015). Experimental studies on combustion and emissions of RCCI fueled with n-heptane/alcohols fuels. Fuel, 162, 239-250

[2.41] Poorghasemi, K., Saray, R. K., Ansari, E., Irdmousa, B. K., Shahbakhti, M., & Naber, J. D. (2017). Effect of diesel injection strategies on natural gas/diesel RCCI combustion characteristics in a light duty diesel engine. Applied Energy, 199, 430-446

[2.42] Agarwal, A. K., Singh, A. P., & Kumar, V. (2022). Reactivity controlled compression ignition engine fueled with mineral diesel and butanol at varying premixed ratios and loads. Journal of Energy Resources Technology

[2.43] Li, Y., Jia, M., Liu, Y., & Xie, M. (2013). Numerical study on the combustion and emission characteristics of a methanol/diesel reactivity controlled compression ignition (RCCI) engine. Applied energy, 106, 184-197

[2.44] Agarwal, A., Singh, A. P., Kumar, V., Sharma, N., & Satsangi, D. P. (2021). Alcohol-fueled reactivity-controlled compression ignition combustion for partial replacement of mineral diesel in internal combustion engines. SAE International Journal of Engines, 14(6), 785.

[2.45] Johnson, T. V. (2010). Review of diesel emissions and control. SAE International Journal of Fuels and Lubricants, 3(1), 16-29.

[2.46] Eastwood, P. (2008). Particulate emissions from vehicles. John Wiley & Sons.

[2.47] Wu, B., Shen, X., Cao, X., Yao, Z., & Wu, Y. (2016). Characterization of the chemical composition of PM2. 5 emitted from on-road China III and China IV diesel trucks in Beijing, China. Science of the Total Environment, 551, 579-589.

[2.48] Ghadikolaei, M. A., Cheung, C. S., & Yung, K. F. (2019). Study of combustion, performance and emissions of a diesel engine fueled with ternary fuel in blended and fumigation modes. Fuel, 235, 288-300.

[2.49] Maricq, M. M. (2007). Chemical characterization of particulate emissions from diesel engines: A review. Journal of Aerosol Science, 38(11), 1079-1118.

[2.50] Wei, J., Fan, C., Qiu, L., Qian, Y., Wang, C., Teng, Q., & Pan, M. (2020). Impact of methanol alternative fuel on oxidation reactivity of soot emissions from a modern CI engine. Fuel, 268, 117352

[2.51] Liati, A., Schreiber, D., Dasilva, Y. A. R., & Eggenschwiler, P. D. (2018). Ultrafine particle emissions from modern Gasoline and Diesel vehicles: An electron microscopic perspective. Environmental pollution, 239, 661-669.

[2.52] Bockhorn, H. (Ed.). (2013). Soot formation in combustion: mechanisms and models (Vol. 59). Springer Science & Business Media.

[2.53] Glassman, I. (1989, January). Soot formation in combustion processes. In Symposium (international) on combustion (Vol. 22, No. 1, pp. 295-311). Elsevier.

[2.54] Frenklach, M. (2002). Reaction mechanism of soot formation in flames. Physical chemistry chemical Physics, 4(11), 2028-2037.

[2.55] Tree, D. R., & Svensson, K. I. (2007). Soot processes in compression ignition engines. Progress in energy and combustion science, 33(3), 272-309.

[2.56] Pickett, L. M., & Siebers, D. L. (2004). Soot in diesel fuel jets: effects of ambient temperature, ambient density, and injection pressure. Combustion and Flame, 138(1-2), 114-135.

[2.57] Miyamoto, N., Ogawa, H., Arima, T., & Miyakawa, K. (1996). Improvement of diesel combustion and emissions with addition of various oxygenated agents to diesel fuels (No. 962115). SAE Technical Paper.

[2.58] Kobayashi, S., Sakai, T., Nakahira, T., Komori, M., & Tsujimura, K. (1992). Measurement of flame temperature distribution in DI diesel engine with high pressure fuel injection. SAE transactions, 1436-1445.

[2.59] Choi, M., & Park, S. (2022). Optimization of multiple-stage fuel injection and optical analysis of the combustion process in a heavy-duty diesel engine. Fuel Processing Technology, 228, 107137.

[2.60] Maurya RK (2017) Characteristics and control of low temperature combustion engines: Employing gasoline, ethanol, and methanol. Springer

[2.61] Dec, J. E. (2009). Advanced compression-ignition engines—understanding the in-cylinder processes. Proceedings of the combustion institute, 32(2), 2727-2742.

[2.62] Dec, J. E. (1997). A conceptual model of DI diesel combustion based on laser-sheet imaging. SAE transactions, 1319-1348.

[2.63] Tao, F., Foster, D. E., & Reitz, R. D. (2006). Soot structure in a conventional non-premixed diesel flame. SAE Transactions, 24-40.

[2.64] Dec, J. E., & Kelly-Zion, P. L. (2000). The effects of injection timing and diluent addition on late-combustion soot burnout in a DI diesel engine based on simultaneous 2-D imaging of OH and soot (No. 2000-01-0238). SAE Technical Paper.

[2.65] Flynn, P. F., Durrett, R. P., Hunter, G. L., zur Loye, A. O., Akinyemi, O. C., Dec, J. E., & Westbrook, C. K. (1999). Diesel combustion: an integrated view combining laser diagnostics, chemical kinetics, and empirical validation. SAE transactions, 587-600.

[2.66] Smith, O. I. (1981). Fundamentals of soot formation in flames with application to diesel engine particulate emissions. Prog. Energy Combust. Sci.;(United Kingdom), 7(4).

[2.67] Chomiak, J., & Karlsson, A. (1996, January). Flame liftoff in diesel sprays. In Symposium (International) on Combustion (Vol. 26, No. 2, pp. 2557-2564). Elsevier.

[2.68] Kiplimo, R., Tomita, E., Kawahara, N., & Yokobe, S. (2012). Effects of spray impingement, injection parameters, and EGR on the combustion and emission characteristics of a PCCI diesel engine. Applied Thermal Engineering, 37, 165-175.

[2.69] Reilly, P. T. A., Gieray, R. A., Whitten, W. B., & Ramsey, J. M. (2000). Direct observation of the evolution of the soot carbonization process in an acetylene diffusion flame via real-time aerosol mass spectrometry. Combustion and flame, 122(1-2), 90-104.

[2.70] Ishiguro, T., Takatori, Y., & Akihama, K. (1997). Microstructure of diesel soot particles probed by electron microscopy: first observation of inner core and outer shell. Combustion and flame, 108(1-2).

[2.71] Cadrazco, M., Santamaría, A., & Agudelo, J. R. (2019). Chemical and nanostructural characteristics of the particulate matter produced by renewable diesel fuel in an automotive diesel engine. Combustion and Flame, 203, 130-142.

[2.72] Jiang, H., Li, T., Wang, Y., He, P., & Wang, B. (2019). The evolution of soot morphology and nanostructure along axial direction in diesel spray jet flames. Combustion and Flame, 199, 204-212.

[2.73] Akihama, K., Takatori, Y., Inagaki, K., Sasaki, S., & Dean, A. M. (2001). Mechanism of the smokeless rich diesel combustion by reducing temperature. SAE Transactions, 648-662.

[2.74] Kittelson, D. B. (1998). Engines and nanoparticles: a review. Journal of aerosol science, 29(5-6), 575-588.

[2.75] Harris, S. J., & Maricq, M. M. (2001). Signature size distributions for diesel and gasoline engine exhaust particulate matter. Journal of Aerosol Science, 32(6), 749-764

[2.76] Tobias, H. J., Beving, D. E., Ziemann, P. J., Sakurai, H., Zuk, M., McMurry, P. H., ... & Kittelson, D. B. (2001). Chemical analysis of diesel engine nanoparticles using a nano-DMA/thermal desorption particle beam mass spectrometer. Environmental Science & Technology, 35(11), 2233-2243.

[2.77] Scheer, V., Kirchner, U., Casati, R., Vogt, R., Wehner, B., Philippin, S., ... & Borrmann, S. (2005). Composition of semi-volatile particles from diesel exhaust (No. 2005-01-0197). SAE Technical Paper.

[2.78] Schneider, J., Hock, N., Weimer, S., Borrmann, S., Kirchner, U., Vogt, R., & Scheer, V. (2005). Nucleation particles in diesel exhaust: Composition inferred from in situ mass spectrometric analysis. Environmental science & technology, 39(16), 6153-6161.

[2.79] Khalek, I. A., Kittelson, D. B., & Brear, F. (2000). Nanoparticle growth during dilution and cooling of diesel exhaust: Experimental investigation and theoretical assessment. SAE Technical Papers.

[2.80] Shi, J. P., Mark, D., & Harrison, R. M. (2000). Characterization of particles from a current technology heavy-duty diesel engine. Environmental Science & Technology, 34(5), 748-755.

[2.81] Yu, F. (2001). Chemiions and nanoparticle formation in diesel engine exhaust. Geophysical Research Letters, 28(22), 4191-4194.

[2.82] Sakurai, H., Tobias, H. J., Park, K., Zarling, D., Docherty, K. S., Kittelson, D. B., ... & Ziemann, P. J. (2003). On-line measurements of diesel nanoparticle composition and volatility. Atmospheric Environment, 37(9-10), 1199-1210.

[2.83] Giechaskiel, B., Maricq, M., Ntziachristos, L., Dardiotis, C., Wang, X., Axmann, H., ... & Schindler, W. (2014). Review of motor vehicle particulate emissions sampling and measurement: From smoke and filter mass to particle number. Journal of Aerosol Science, 67, 48-86.

[2.84] Wierzbicka, A., Nilsson, P. T., Rissler, J., Sallsten, G., Xu, Y., Pagels, J. H., ... & Gudmundsson, A. (2014). Detailed diesel exhaust characteristics including particle surface area and lung deposited dose for better understanding of health effects in human chamber exposure studies. Atmospheric Environment, 86, 212-219.

[2.85] Xue, J., Hu, S., Quiros, D., Ayala, A., & Jung, H. S. (2019). How do particle number, surface area, and mass correlate with toxicity of diesel particle emissions as measured in chemical and cellular assays?. Chemosphere, 229, 559-569.

[2.86] Rubino, L., Phillips, P. R., & Twigg, M. V. (2005). Measurements of ultrafine particle number emissions from a light-duty diesel engine using SMPS, DMS, ELPI and EEPS (No. 2005-24-015). SAE Technical Paper.

[2.87] Montajir, R. M., Kawai, T., Goto, Y., & Odaka, M. (2005). Thermal conditioning of exhaust gas: potential for stabilizing diesel nano-particles (No. 2005-01-0187). SAE Technical Paper.

[2.88] Hiroyasu, H., & Kadota, T. (1976). Models for combustion and formation of nitric oxide and soot in direct injection diesel engines. SAE transactions, 513-526.

[2.89] Hiroyasu, H., Kadota, T., & Arai, M. (1983). Development and use of a spray combustion modeling to predict diesel engine efficiency and pollutant emissions: Part 1 combustion modeling. Bulletin of JSME, 26(214), 569-575.

[2.90] Tesner, P. A., Smegiriova, T. D., & Knorre, V. G. (1971). Kinetics of dispersed carbon formation. Combustion and flame, 17(2), 253-260.

[2.91] Khan, I. M., & Greeves, G. (1974). A method for calculating the formation and combustion of soot in diesel engines. Heat transfer in flames, 25.

[2.92] Kazakov, A., & Foster, D. E. (1998). Modeling of soot formation during DI diesel combustion using a multi-step phenomenological model. SAE transactions, 1016-1028.

[2.93] Tao, F., Golovitchev, V. I., & Chomiak, J. (2004). A phenomenological model for the prediction of soot formation in diesel spray combustion. Combustion and Flame, 136(3), 270-282.

[2.94] Tao, F., Foster, D. E., & Reitz, R. D. (2007). Characterization of soot particle distribution in conventional, non-premixed DI diesel flame using a multi-step phenomenological soot model. Proceedings of the Combustion Institute, 31(2), 2991-2998.

[2.95] Mosbach, S., Celnik, M. S., Raj, A., Kraft, M., Zhang, H. R., Kubo, S., & Kim, K. O. (2009). Towards a detailed soot model for internal combustion engines. Combustion and Flame, 156(6), 1156-1165.

[2.96] Fraioli, V., Beatrice, C., & Lazzaro, M. (2011). Soot particle size modelling in 3D simulations of diesel engine combustion. Combustion Theory and Modelling, 15(6), 863-892.

[2.97] Patterson, M. A., Kong, S. C., Hampson, G. J., & Reitz, R. D. (1994). Modeling the effects of fuel injection characteristics on diesel engine soot and NOx emissions. SAE transactions, 836-852.

[2.98] Micklow, G. J., & Gong, W. (2002). A multistage combustion model and soot formation model for direct-injection diesel engines. Proceedings of the Institution of Mechanical Engineers, Part D: Journal of Automobile Engineering, 216(6), 495-504.

[2.99] Cheng, X., Chen, L., Yan, F., & Dong, S. (2013). Study on soot formation characteristics in the diesel combustion process based on an improved detailed soot model. Energy Conversion and Management, 75, 1-10.

[2.100] Cheng, X., Chen, L., Hong, G., Yan, F., & Dong, S. (2014). Modeling study of soot formation and oxidation in DI diesel engine using an improved soot model. Applied thermal engineering, 62(2), 303-312.

[2.101] Cheng, X., Jv, H., & Wu, Y. (2008, January). Application of a phenomenological soot model for diesel engine combustion. In Internal Combustion Engine Division Spring Technical Conference (Vol. 48132, pp. 205-214).

[2.102] Kong, S. C., Sun, Y., & Rietz, R. D. (2007). Modeling diesel spray flame liftoff, sooting tendency, and NO x emissions using detailed chemistry with phenomenological soot model.

[2.103] Tao, F., Liu, Y., RempelEwert, B. H., Foster, D. E., Reitz, R. D., Choi, D., & Miles, P. C. (2005). Modeling the effects of EGR and injection pressure on soot formation in a high-speed direct-injection (HSDI) diesel engine using a multi-step phenomenological soot model. SAE transactions, 263-283.

[2.104] Vishwanathan, G., & Reitz, R. D. (2010). Development of a practical soot modeling approach and its application to low-temperature diesel combustion. Combustion Science and Technology, 182(8), 1050-1082.

[2.105] Singh, J., Balthasar, M., Kraft, M., & Wagner, W. (2005). Stochastic modeling of soot particle size and age distributions in laminar premixed flames. Proceedings of the Combustion Institute, 30(1), 1457-1465.

[2.106] Balthasar, M., & Kraft, M. (2003). A stochastic approach to calculate the particle size distribution function of soot particles in laminar premixed flames. Combustion and Flame, 133(3), 289-298.

[2.107] Aubagnac-Karkar, D., El Bakali, A., & Desgroux, P. (2018). Soot particles inception and PAH condensation modelling applied in a soot model utilizing a sectional method. Combustion and Flame, 189, 190-206.

[2.108] Netzell, K., Lehtiniemi, H., & Mauss, F. (2007). Calculating the soot particle size distribution function in turbulent diffusion flames using a sectional method. Proceedings of the Combustion Institute, 31(1), 667-674

[2.109] Frenklach, M., & Wang, H. (1991, January). Detailed modeling of soot particle nucleation and growth. In Symposium (International) on Combustion (Vol. 23, No. 1, pp. 1559-1566). Elsevier.

[2.110] Frenklach, M. (2002). Method of moments with interpolative closure. Chemical Engineering Science, 57(12), 2229-2239.

[2.111] Lee, J., Sung, N. W., & Huh, K. Y. (2011). Prediction of soot particle size distribution for turbulent reacting flow in a diesel engine. International Journal of Engine Research, 12(2), 181-189.

[2.112] Duvvuri, P. P., Sukumaran, S., Shrivastava, R. K., & Sreedhara, S. (2019). Modeling soot particle size distribution in diesel engines. Fuel, 243, 70-78.

[2.113] Aubagnac-Karkar, D., Michel, J. B., Colin, O., Vervisch-Kljakic, P. E., & Darabiha, N. (2015). Sectional soot model coupled to tabulated chemistry for Diesel RANS simulations. Combustion and Flame, 162(8), 3081-3099.

[2.114] Frenklach, M. (1985). Computer modeling of infinite reaction sequences: a chemical lumping. Chemical engineering science, 40(10), 1843-1849.

[2.115] McGraw, R. (1997). Description of aerosol dynamics by the quadrature method of moments. Aerosol Science and Technology, 27(2), 255-265.

[2.116] Hong, S., Wooldridge, M. S., Im, H. G., Assanis, D. N., & Pitsch, H. (2005). Development and application of a comprehensive soot model for 3D CFD reacting flow studies in a diesel engine. Combustion and Flame, 143(1-2), 11-26.

[2.117] Zhong, B. J., Dang, S., Song, Y. N., & Gong, J. S. (2012). 3-D simulation of soot formation in a direct-injection diesel engine based on a comprehensive chemical mechanism and method of moments. Combustion Theory and Modelling, 16(1), 143-171.

[2.118] Wu, S., Zhou, D., & Yang, W. (2019). Implementation of an efficient method of moments for treatment of soot formation and oxidation processes in three-dimensional engine simulations. Applied Energy, 254, 113661.

[2.119] Ibrahim, F., Mahmood, W. M. F. W., Abdullah, S., & Mansor, M. R. A. (2017). Comparison of simple and detailed soot models in the study of soot formation in a compression ignition diesel engine (No. 2017-01-1006). SAE Technical Paper.

[2.120] Karlsson, A., Magnusson, I., Balthasar, M., & Mauss, F. (1998). Simulation of soot formation under diesel engine conditions using a detailed kinetic soot model. SAE transactions, 1430-1440.

[2.121] Wu, S., Lao, C. T., Akroyd, J., Mosbach, S., Yang, W., & Kraft, M. (2020). A joint moment projection method and maximum entropy approach for simulation of soot formation and oxidation in diesel engines. Applied Energy, 258, 114083.

[2.122] Dempsey, A., Curran, S., Storey, J., Eibl, M., Pihl, J., Prikhodko, V., ... & Parks, J. (2014). Particulate matter characterization of reactivity controlled compression ignition (RCCI) on a light duty engine (No. 2014-01-1596). SAE Technical Paper

[2.123] Prikhodko, V. Y., Curran, S. J., Barone, T. L., Lewis, S. A., Storey, J. M., Cho, K., ... & Parks, J. E. (2010). Emission characteristics of a diesel engine operating with in-cylinder gasoline and diesel fuel blending. SAE International Journal of Fuels and Lubricants, 3(2), 946-955.

[2.124] Kolodziej, C., Wissink, M., Splitter, D., Hanson, R., Reitz, R. D., & Benajes, J. (2013). Particle size and number emissions from RCCI with direct injections of two fuels (No. 2013-01-1661). SAE Technical Paper.

[2.125] Storey, J. M., Curran, S. J., Lewis, S. A., Barone, T. L., Dempsey, A. B., Moses-DeBusk, M., ... & Northrop, W. F. (2017). Evolution and current understanding of physicochemical characterization of particulate matter from reactivity controlled compression ignition combustion on a multicylinder light-duty engine. International Journal of Engine Research, 18(5-6), 505-519.

[2.126] Benajes, J., García, A., Monsalve-Serrano, J., & Boronat, V. (2017). An investigation on the particulate number and size distributions over the whole engine map from an optimized combustion strategy combining RCCI and dual-fuel diesel-gasoline. Energy Conversion and Management, 140, 98-108.

[2.127] Zhang, Y., Ghandhi, J., & Rothamer, D. (2014). Comparison of particulate size distributions from advanced and conventional combustion-part I: CDC, HCCI, and RCCI. SAE International Journal of Engines, 7(2), 820-834.

[2.128] García, A., Monsalve-Serrano, J., Villalta, D., & Fogué-Robles, Á. (2022). Detailed analysis of particulate emissions of a multi-cylinder dual-mode dual-fuel engine operating with diesel and gasoline. Fuel, 330, 125578.

[2.129] Agarwal, A. K., Singh, A. P., & Kumar, V. (2021). Particulate characteristics of low-temperature combustion (PCCI and RCCI) strategies in single cylinder research engine for developing sustainable and cleaner transportation solution. Environmental pollution, 284, 117375

[2.130] Fang, W., Kittelson, D. B., & Northrop, W. F. (2017). Dilution Sensitivity of Particulate Matter Emissions from Reactivity-Controlled Compression Ignition Combustion. Journal of Energy Resources Technology, 139(3).

[2.131] Agarwal, A. K., Singh, A. P., & Kumar, V. (2021). Particulate characteristics of low-temperature combustion (PCCI and RCCI) strategies in single cylinder research engine for developing sustainable and cleaner transportation solution. Environmental pollution, 284, 117375

[2.132] Srivastava, D. K., Agarwal, A. K., & Gupta, T. (2011). Effect of engine load on size and number distribution of particulate matter emitted from a direct injection compression ignition engine. Aerosol and Air Quality Research, 11(7), 915-920.

[2.133] Lu, T., Cheung, C. S., & Huang, Z. (2012). Effects of engine operating conditions on the size and nanostructure of diesel particles. Journal of Aerosol Science, 47, 27-38.

[2.134] Di, Y., Cheung, C. S., & Huang, Z. (2009). Experimental study on particulate emission of a diesel engine fueled with blended ethanol–dodecanol–diesel. Journal of Aerosol Science, 40(2), 101-112.

[2.135] Young, L. H., Liou, Y. J., Cheng, M. T., Lu, J. H., Yang, H. H., Tsai, Y. I., ... & Lai, J. S. (2012). Effects of biodiesel, engine load and diesel particulate filter on nonvolatile particle number size distributions in heavy-duty diesel engine exhaust. Journal of hazardous materials, 199, 282-289.

[2.136] Virtanen, A. K., Ristimäki, J. M., Vaaraslahti, K. M., & Keskinen, J. (2004). Effect of engine load on diesel soot particles. Environmental science & technology, 38(9), 2551-2556.

[2.137] Guan, C., Cheung, C. S., Li, X., & Huang, Z. (2017). Effects of oxygenated fuels on the particle-phase compounds emitted from a diesel engine. Atmospheric Pollution Research, 8(2), 209-220.

[2.138] Zhang, Z. H., & Balasubramanian, R. (2014). Influence of butanol–diesel blends on particulate emissions of a non-road diesel engine. Fuel, 118, 130-136.

[2.139] Lapuerta, M., Martos, F. J., & Herreros, J. M. (2007). Effect of engine operating conditions on the size of primary particles composing diesel soot agglomerates. Journal of aerosol science, 38(4), 455-466.

[2.140] Agarwal, A. K., Srivastava, D. K., Dhar, A., Maurya, R. K., Shukla, P. C., & Singh, A. P. (2013). Effect of fuel injection timing and pressure on combustion, emissions and performance characteristics of a single cylinder diesel engine. Fuel, 111, 374-383

[2.141] Desantes, J. M., Bermúdez, V., García, J. M., & Fuentes, E. (2005). Effects of current engine strategies on the exhaust aerosol particle size distribution from a heavy-duty diesel engine. Journal of Aerosol Science, 36(10), 1251-1276.

[2.142] Xu, Z., Li, X., Guan, C., & Huang, Z. (2014). Effects of injection timing on exhaust particle size and nanostructure on a diesel engine at different loads. Journal of aerosol science, 76, 28-38.

[2.143] Li, X., Xu, Z., Guan, C., & Huang, Z. (2014). Effect of injection timing on particle size distribution from a diesel engine. Fuel, 134, 189-195.

[2.144] Zhu, R., Miao, H., Wang, X., & Huang, Z. (2013). Effects of fuel constituents and injection timing on combustion and emission characteristics of a compression-ignition engine fueled with diesel-DMM blends. Proceedings of the combustion institute, 34(2), 3013-3020.

[2.145] Wang, T., Liu, J., Sun, P., Ji, Q., Gao, W., & Yang, C. (2020). Influence of injection parameters on combustion, gaseous emissions and particle size distribution of a CRDI diesel engine operating with PODE/diesel blends. Fuel, 281, 118733.

[2.146] Mohiuddin, K., Kwon, H., Choi, M., & Park, S. (2021). Effect of engine compression ratio, injection timing, and exhaust gas recirculation on gaseous and particle number emissions in a light-duty diesel engine. Fuel, 294, 120547.

[2.147] Geng, L., Xiao, Y., Li, S., Chen, H., & Chen, X. (2021). Effects of injection timing and rail pressure on particulate size-number distribution of a common rail DI engine fueled with fischer-tropsch diesel synthesized from coal. Journal of the energy institute, 95, 219-230.

[2.148] Zhou, X., Qian, W., Pan, M., Huang, R., Xu, L., & Yin, J. (2020). Potential of n-butanol/diesel blends for CI engines under post injection strategy and different EGR rates conditions. Energy Conversion and Management, 204, 112329.

[2.149] Duan, X., Xu, Z., Sun, X., Deng, B., & Liu, J. (2021). Effects of injection timing and EGR on combustion and emissions characteristics of the diesel engine fuelled with acetone–butanol–ethanol/diesel blend fuels. Energy, 231, 121069.

[2.150] Li, X., Guan, C., Luo, Y., & Huang, Z. (2015). Effect of multiple-injection strategies on diesel engine exhaust particle size and nanostructure. Journal of Aerosol Science, 89, 69-76.

[2.151] Zhou, X., Qian, W., Pan, M., Huang, R., Xu, L., & Yin, J. (2020). Potential of n-butanol/diesel blends for CI engines under post injection strategy and different EGR rates conditions. Energy Conversion and Management, 204, 112329.

[2.152] Ye, P., Sun, C., Lapuerta, M., Agudelo, J., Vander Wal, R., Boehman, A. L., ... & Daw, S. (2016). Impact of rail pressure and biodiesel fueling on the particulate morphology and soot nanostructures from a common-rail turbocharged direct injection diesel engine. International Journal of Engine Research, 17(2), 193-208.

[2.153] Xu, Z., Li, X., Guan, C., & Huang, Z. (2014). Effects of injection pressure on diesel engine particle physico-chemical properties. Aerosol Science and Technology, 48(2), 128-138.

[2.154] McTaggart-Cowan, G. P., Jones, H. L., Rogak, S. N., Bushe, W. K., Hill, P. G., & Munshi, S. R. (2005, January). The effects of high-pressure injection on a compression-ignition, direct injection of natural gas engine. In Internal combustion engine division fall technical conference (Vol. 47365, pp. 161-173).

[2.155] Pagán, J. (1999). Study of particle size distributions emitted by a diesel engine. SAE transactions, 557-562.

[2.156] Wang, T., Liu, J., Sun, P., Ji, Q., Gao, W., & Yang, C. (2020). Influence of injection parameters on combustion, gaseous emissions and particle size distribution of a CRDI diesel engine operating with PODE/diesel blends. Fuel, 281, 118733.

[2.157] Kittelson, D. B., Arnold, M., & Watts, W. F. (1999). Review of diesel particulate matter sampling methods: Final Report. University of Minnesota, Minneapolis, MN, 63.

[2.158] Pan, S., Li, X., Han, W., & Huang, Y. (2017). An experimental investigation on multi-cylinder RCCI engine fueled with 2-butanol/diesel. Energy Conversion and Management, 154, 92-101.

[2.159] Pan, S., Liu, X., Cai, K., Li, X., Han, W., & Li, B. (2020). Experimental study on combustion and emission characteristics of iso-butanol/diesel and gasoline/diesel RCCI in a heavy-duty engine under low loads. Fuel, 261, 116434.

[2.160] Benajes, J., Garcia, A., Monsalve-Serrano, J., & Boronat, V. (2017). Particulates size distribution of reactivity controlled compression ignition (RCCI) on a medium-duty engine fueled with diesel and gasoline at different engine speeds. SAE International Journal of Engines, 10(5), 2382-2391.

[2.161] Qian, Y., Zhang, Y., Wang, X., & Lu, X. (2017). Particulate matter emission characteristics of a reactivity controlled compression ignition engine fueled with biogas/diesel dual fuel. Journal of Aerosol Science, 113, 166-177.

[2.162] Saxena, M. R., & Maurya, R. K. (2021). Influence of fuel injection pressure and injection timing on nanoparticle emission in light-duty gasoline/diesel RCCI engine. Particulate Science and Technology, 39(5), 641-650.

[2.163] Saxena, M. R., & Maurya, R. K. (2020). Influence of direct injection timing and mass of port injected gasoline on unregulated and nano-particle emissions from RCCI engine. Fuel, 282, 118815.

[2.164] Saxena, M. R., & Maurya, R. K. (2018). Effect of fuel injection strategy on nano-particle emissions from RCCI engine (No. 2018-01-1709). SAE Technical Paper.

[2.165] Saxena, M. R., & Maurya, R. K. (2020). Experimental investigation of combustion stability and particle emission from CNG/diesel RCCI engine (No. 2020-01-0810). SAE Technical Paper

[2.166] Singh, A. P., Sharma, N., Kumar, V., & Agarwal, A. K. (2021). Experimental investigations of mineral diesel/methanol-fueled reactivity controlled compression ignition engine operated at variable engine loads and premixed ratios. International Journal of Engine Research, 22(7), 2375-2389.

[2.167] Singh, A. P., Kumar, V., & Agarwal, A. K. (2021). Evaluation of reactivity controlled compression ignition mode combustion engine using mineral diesel/gasoline fuel pair. Fuel, 301, 120986.

[2.168] Agarwal, A. K., Singh, A. P., & Kumar, V. (2022). Reactivity controlled compression ignition engine fueled with mineral diesel and butanol at varying premixed ratios and loads. Journal of Energy Resources Technology, 144(2).

[2.169] Anderson, J., Giechaskeiel, B., Munoz-Bueno, R., Sandbach, E., & Dilara, P. (2007). Particle Measurement Programme (PMP) light-duty Inter-Laboratory Correlation Exercise (ILCE_LD) final report. Report EUR 24561 EN, European Commission, Joint Research Centre. Institute for Environment and Sustainability, Ispra, Italy.

[2.170]Burtscher, H., Baltensperger, U., Bukowiecki, N., Cohn, P., Hüglin, C., Mohr, M., ... & Weingartner, E. (2001). Separation of volatile and non-volatile aerosol fractions by thermodesorption: instrumental development and applications. Journal of Aerosol Science, 32(4), 427-442.

[2.171] Kawai, T., Lee, J. H., Goto, Y., & Odaka, M. (2003). Influence of Thermo-Denuder Dimensions on Nano-particle Measurement (No. 2003-01-2018). SAE Technical Paper.

[2.172] Etikyala, S., Koopmans, L., & Dahlander, P. (2019). Particulate emissions in a GDI with an upstream fuel source (No. 2019-01-1180). SAE Technical Paper

[2.173] Das, D., Gaur, V., & Verma, N. (2004). Removal of volatile organic compound by activated carbon fiber. Carbon, 42(14), 2949-2962.

[2.174] Giechaskiel, B., Dilara, P., Sandbach, E., & Andersson, J. (2008). Particle measurement programme (PMP) light-duty inter-laboratory exercise: comparison of different particle number measurement systems. Measurement Science and Technology, 19(9), 095401.

[2.175] Giechaskiel, B., Carriero, M., Martini, G., Krasenbrink, A., & Scheder, D. (2009). Calibration and validation of various commercial particle number measurement systems. SAE International Journal of Fuels and Lubricants, 2(1), 512-530.

[2.176] Swanson, J., & Kittelson, D. (2010). Evaluation of thermal denuder and catalytic stripper methods for solid particle measurements. Journal of Aerosol Science, 41(12), 1113-1122.

[2.177] Dekati, L. "Sampling automotive exhaust with a thermodenuder." Dekati Ltd., Technical Note (2001).

[2.178] Fierz, M., & Burtscher, H. (2003). Separation of solid and volatile fraction by thermodesorption and hot dilution. PMP report CH6.

[2.179] Park, D., Kim, S., Choi, N. K., & Hwang, J. (2008). Development and performance test of a thermo-denuder for separation of volatile matter from submicron aerosol particles. Journal of aerosol science, 39(12), 1099-1108.

[2.180] Fierz, M., Vernooij, M. G., & Burtscher, H. (2007). An improved low-flow thermodenuder. Journal of Aerosol Science, 38(11), 1163-1168.

[2.181] Huffman, J. A., Ziemann, P. J., Jayne, J. T., Worsnop, D. R., & Jimenez, J. L. (2008). Development and characterization of a fast-stepping/scanning thermodenuder for chemically-resolved aerosol volatility measurements. Aerosol Science and Technology, 42(5), 395-407

[2.182] An, W. J., Pathak, R. K., Lee, B. H., & Pandis, S. N. (2007). Aerosol volatility measurement using an improved thermodenuder: Application to secondary organic aerosol. Journal of Aerosol Science, 38(3), 305-314.

[2.183] Wehner, B., Philippin, S., & Wiedensohler, A. (2002). Design and calibration of a thermodenuder with an improved heating unit to measure the size-dependent volatile fraction of aerosol particles. Journal of Aerosol Science, 33(7), 1087-1093.

[2.184] Rönkkö, T., Arffman, A., Karjalainen, P., Lähde, T., Heikkilä, J., Pirjola, L., ... & Keskinen, J. (2011). Diesel exhaust nanoparticle volatility studies by a new thermodenuder with low solid nanoparticle losses. Technology, 43(24), 9501-9506

[2.185] Stevanovic, S., Miljevic, B., Madl, P., Clifford, S., & Ristovski, Z. (2015). Characterisation of a commercially available thermodenuder and diffusion drier for ultrafine particles losses.

[2.186] Giechaskiel, B., Arndt, M., Schindler, W., Bergmann, A., Silvis, W., & Drossinos, Y. (2012). Sampling of non-volatile vehicle exhaust particles: A simplified guide. SAE International Journal of Engines, 5(2), 379-399.

[2.187] Fuchs, N. A., Daisley, R. E., Fuchs, M., Davies, C. N., & Straumanis, M. E. (1965). The mechanics of aerosols. Physics Today, 18(4), 73.

[2.188] Kulkarni, P., Baron, P. A., & Willeke, K. (Eds.). (2011). Aerosol measurement: principles, techniques, and applications. John Wiley & Sons.

[2.189] Abarham, M., Hoard, J., Assanis, D., Styles, D., Curtis, E. W., & Ramesh, N. (2010). Review of soot deposition and removal mechanisms in EGR coolers. SAE International Journal of Fuels and Lubricants, 3(1), 690-704.

[2.190] Lin, J. S., & Tsai, C. J. (2003). Thermophoretic deposition efficiency in a cylindrical tube taking into account developing flow at the entrance region. Journal of Aerosol Science, 34(5), 569-583.

[2.191] Talbot, L. R. K. R. W. D. R., Cheng, R. K., Schefer, R. W., & Willis, D. R. (1980). Thermophoresis of particles in a heated boundary layer. Journal of fluid mechanics, 101(4), 737-758

[2.192] Giechaskiel, B., & Drossinos, Y. (2010). Theoretical investigation of volatile removal efficiency of particle number measurement systems. SAE International Journal of Engines, 3(1), 1140-1151.

[2.193] Swanson, J., & Kittelson, D. (2010). Evaluation of thermal denuder and catalytic stripper methods for solid particle measurements. Journal of Aerosol Science, 41(12), 1113-1122.

[2.194] Giechaskiel, B., Vanhanen, J., Väkevä, M., & Martini, G. J. A. S. (2017). Investigation of vehicle exhaust sub-23 nm particle emissions. Aerosol Science and Technology, 51(5), 626-641.

[2.195] Amanatidis, S., Ntziachristos, L., Giechaskiel, B., Katsaounis, D., Samaras, Z., & Bergmann, A. (2013). Evaluation of an oxidation catalyst ("catalytic stripper") in eliminating volatile material from combustion aerosol. Journal of Aerosol Science, 57, 144-155.

[2.196] Lähde, T., Rönkkö, T., Happonen, M., Söderström, C., Virtanen, A., Solla, A., ... & Keskinen, J. (2011). Effect of fuel injection pressure on a heavy-duty diesel engine nonvolatile particle emission. Environmental science & technology, 45(6), 2504-2509.

[2.197] RÖnkkÖ, T., Virtanen, A., Kannosto, J., Keskinen, J., Lappi, M., & Pirjola, L. (2007). Nucleation mode particles with a nonvolatile core in the exhaust of a heavy duty diesel vehicle. Environmental science & technology, 41(18), 6384-6389.

[2.198] Zhang, Z. H., & Balasubramanian, R. (2014). Influence of butanol–diesel blends on particulate emissions of a non-road diesel engine. Fuel, 118, 130-136.

[2.199] Heikkila, J., Virtanen, A., Ronkko, T., Keskinen, J., Aakko-Saksa, P., & Murtonen, T. (2009). Nanoparticle emissions from a heavy-duty engine running on alternative diesel fuels. Environmental Science & Technology, 43(24), 9501-9506.

[2.200] Ajtai, T., Pintér, M., Utry, N., Kiss-Albert, G., Gulyás, G., Pusztai, P., ... & Bozóki, Z. (2016). Characterisation of diesel particulate emission from engines using commercial diesel and biofuels. Atmospheric Environment, 134, 109-120.

[2.201] Graves, B. M., Koch, C. R., & Olfert, J. S. (2017). Morphology and volatility of particulate matter emitted from a gasoline direct injection engine fuelled on gasoline and ethanol blends. Journal of Aerosol Science, 105, 166-178.

[3.1] Ansys, 2019, ANSYS® Forte. Release 2019 R3. Forte Theory, Ansys Inc., Canonsburg, PA.

[3.2] Beale, J. C., & Reitz, R. D. (1999). Modelling spray atomization with the Kelvin-Helmholtz/Rayleigh-Taylor hybrid model. Atomization and sprays, 9(6).

[3.3] Abani, N., & Reitz, R. D. (2007). Unsteady turbulent round jets and vortex motion. Physics of Fluids, 19(12), 125102.

[3.4] Abani, N., Munnannur, A., & Reitz, R. D. (2007, January). Reduction of numerical parameter dependencies in diesel spray models. In Internal Combustion Engine Division Fall Technical Conference (Vol. 48116, pp. 163-174).

[3.5] Hou, S., & Schmidt, D. P. (2006). Adaptive collision meshing and satellite droplet formation in spray simulations. International Journal of Multiphase Flow, 32(8), 935-956

[3.6] Ra, Y., & Reitz, R. D. (2009). A vaporization model for discrete multi-component fuel sprays. International Journal of Multiphase Flow, 35(2), 101-117.

[3.7] Han, Z., & Reitz, R. D. (1997). A temperature wall function formulation for variable-density turbulent flows with application to engine convective heat transfer modeling. International journal of heat and mass transfer, 40(3), 613-625.

[3.8] Yakhot, V., & Orszag, S. A. (1986). Renormalization group analysis of turbulence. I. Basic theory. Journal of scientific computing, 1(1), 3-51.

[3.9] Han, Z., & Reitz, R. D. (1995). Turbulence modeling of internal combustion engines using RNG κ-ε models. Combustion science and technology, 106(4-6), 267-295.

[3.10] Kong, S. C., Han, Z., & Reitz, R. D. (1995). The development and application of a diesel ignition and combustion model for multidimensional engine simulation. SAE transactions, 502-518.

[3.11] Saxena, M. R., & Maurya, R. K. (2021). Influence of fuel injection pressure and injection timing on nanoparticle emission in light-duty gasoline/diesel RCCI engine. Particulate Science and Technology, 39(5), 641-650.

[3.12] Cambustion Ltd. (2015). DMS 500 User Manual, Version 4.04.

[3.13] Cengel, R. A. (2008). Introduction to thermodynamics and heat transfer. McGraw-Hill.

[3.14] Giechaskiel, B., Arndt, M., Schindler, W., Bergmann, A., Silvis, W., & Drossinos, Y. (2012). Sampling of non-volatile vehicle exhaust particles: A simplified guide. SAE International Journal of Engines, 5(2), 379-399.

[3.15] Rana, S., Saxena, M. R., & Maurya, R. K. (2021). Development and characterization of aerosol conditioning devices for solid ultrafine particle measurement from diesel engines: A review. SAE Technical Paper, (2021-01-0615).

[3.16] Guo, C., Yu, T., Yang, Y., Gui, H., Hu, J., & Liu, J. (2023). Design and evaluation of a volatile particle remover combining hot dilution and a thermodenuder. Instrumentation Science & Technology, 1-20.

[3.17] Heywood, J. B. (2018). Internal combustion engine fundamentals. McGraw-Hill Education

[3.18] Gatowski, J. A., Balles, E. N., Chun, K. M., Nelson, F. E., Ekchian, J. A., & Heywood, J. B. (1984). Heat release analysis of engine pressure data. SAE transactions, 961-977.

[3.19] Littera, D., Cozzolini, A., Besch, M., Thiruvengadam, A., & Gautam, M. (2011). High Temperature Sampling System for Real Time Measurement of Solid and Volatile Fractions of Exhaust Particulate Matter. SAE International Journal of Engines, 4(2), 2477-2489.

[3.20] Gainey, B., Longtin, J. P., & Lawler, B. (2019). A guide to uncertainty quantification for experimental engine research and heat release analysis. SAE International Journal of Engines, 12(5), 509-290.

[3.21] Petitpas, G., McNenly, M. J., & Whitesides, R. A. (2017). A framework for quantifying measurement uncertainties and uncertainty propagation in HCCI/LTGC engine experiments. SAE International Journal of Engines, 10(3), 1275-1296.

[3.22] Maurya, R. K., & Agarwal, A. K. (2013). Investigations on the effect of measurement errors on estimated combustion and performance parameters in HCCI combustion engine. Measurement, 46(1), 80-88.

[3.23] Holmén, B. A., & Qu, Y. (2004). Uncertainty in particle number modal analysis during transient operation of compressed natural gas, diesel, and trap-equipped diesel transit buses. Environmental science & technology, 38(8), 2413-2423.

[3.24] Li, X., Xu, Z., Guan, C., & Huang, Z. (2014). Particle size distributions and OC, EC emissions from a diesel engine with the application of in-cylinder emission control strategies. Fuel, 121, 20-26.

[3.25] Giechaskiel, B., Lähde, T., Melas, A. D., Valverde, V., & Clairotte, M. (2021). Uncertainty of laboratory and portable solid particle number systems for regulatory measurements of vehicle emissions. Environmental Research, 197, 111068.

[3.26] Hall, D. E., Stradling, R. J., Zemroch, P. J., Rickeard, D. J., Mann, N., Heinze, P., ... & Szendefi, J. (2000). Measurement of the number and size distribution of particle emissions from heavy duty engines (No. 2000-01-2000). SAE Technical Paper.

[3.27] Kirchner, U., Vogt, R., & Maricq, M. (2010). Investigation of EURO-5/6 level particle number emissions of European diesel light duty vehicles (No. 2010-01-0789). SAE Technical Paper.

[4.1] Li, X., Xu, Z., Guan, C., & Huang, Z. (2014). Effect of injection timing on particle size distribution from a diesel engine. Fuel, 134, 189-195.

[4.2] Maurya, R. K., 2018, Characteristics and Control of Low Temperature Combustion Engines: Employing Gasoline, Ethanol and Methanol, Springer, New York.

[4.3] Sarathy, S. M., Oßwald, P., Hansen, N., & Kohse-Höinghaus, K. (2014). Alcohol combustion chemistry. Progress in energy and Combustion Science, 44, 40-102.

[4.4] Dayma, G., Ali, K. H., & Dagaut, P. (2007). Experimental and detailed kinetic modeling study of the high pressure oxidation of methanol sensitized by nitric oxide and nitrogen dioxide. Proceedings of the Combustion Institute, 31(1), 411-418.

[4.5] Sjöberg, M., & Dec, J. E. (2007). EGR and intake boost for managing HCCI low-temperature heat release over wide ranges of engine speed. SAE Transactions, 65-77.

[4.6] Inagaki, K., Fuyuto, T., Nishikawa, K., Nakakita, K., & Sakata, I. (2006). Dual-fuel PCI combustion controlled by in-cylinder stratification of ignitability (No. 2006-01-0028). SAE Technical Paper.

[4.7] Paykani, A., Kakaee, A. H., Rahnama, P., & Reitz, R. D. (2016). Progress and recent trends in reactivity-controlled compression ignition engines. International Journal of Engine Research, 17(5), 481-524.

[4.8] Kumar, K., & Sung, C. J. (2011). Autoignition of methanol: experiments and computations. International Journal of Chemical Kinetics, 43(4), 175-184.

[4.9] Heidarabadi, S., Khoshbakhti Saray, R., & Neshat, E. (2021). Detailed kinetic study on methane/diesel RCCI combustion. International Journal of Engine Research, 22(8), 2422-2441.

[4.10] Ebrahimi, M., Najafi, M., Jazayeri, S. A., & Mohammadzadeh, A. R. (2018). A detail simulation of reactivity-controlled compression ignition combustion strategy in a heavy-duty diesel engine run on natural gas/diesel fuel. International journal of engine research, 19(7), 774-789.

[4.11] Saxena, S., & Bedoya, I. D. (2013). Fundamental phenomena affecting low temperature combustion and HCCI engines, high load limits and strategies for extending these limits. Progress in Energy and Combustion Science, 39(5), 457-488.

[4.12] Nieman, Derek E., Adam B. Dempsey, and Rolf D. Reitz. "Heavy-duty RCCI operation using natural gas and diesel." SAE International Journal of Engines 5.2 (2012): 270-285

[4.13] Jia, Z., & Denbratt, I. (2015). Experimental investigation of natural gas-diesel dual-fuel RCCI in a heavy-duty engine. SAE International Journal of Engines, 8(2), 797-807

[4.14] Poorghasemi, K., Saray, R. K., Ansari, E., Irdmousa, B. K., Shahbakhti, M., & Naber, J. D. (2017). Effect of diesel injection strategies on natural gas/diesel RCCI combustion characteristics in a light duty diesel engine. Applied Energy, 199, 430-446.

[4.15] Musculus, M. P., Dec, J. E., & Tree, D. R. (2002). Effects of fuel parameters and diffusion flame lift-off on soot formation in a heavy-duty DI diesel engine. SAE Transactions, 1467-1489.

[4.16] He, C., Ge, Y., Tan, J., You, K., Han, X., & Wang, J. (2010). Characteristics of polycyclic aromatic hydrocarbons emissions of diesel engine fuelled with biodiesel and diesel. Fuel, 89(8), 2040-2046.

[4.17] Storey, J. M., Curran, S. J., Lewis, S. A., Barone, T. L., Dempsey, A. B., Moses-DeBusk, M., ... & Northrop, W. F. (2017). Evolution and current understanding of physicochemical characterization of particulate matter from reactivity controlled compression ignition combustion on a multicylinder light-duty engine. International Journal of Engine Research, 18(5-6), 505-519.

[4.18] Lucachick, G., Curran, S., Storey, J., Prikhodko, V., & Northrop, W. F. (2016). Volatility characterization of nanoparticles from single and dual-fuel low temperature combustion in compression ignition engines. Aerosol Science and Technology, 50(5), 436-447.

[4.19] Northrop, W. F., Madathil, P. V., Bohac, S. V., & Assanis, D. N. (2011). Condensational growth of particulate matter from partially premixed low temperature combustion of biodiesel in a compression ignition engine. Aerosol Science and Technology, 45(1), 26-36.

[4.20] Prikhodko, V. Y., Curran, S. J., Barone, T. L., Lewis, S. A., Storey, J. M., Cho, K., ... & Parks, J. E. (2010). Emission characteristics of a diesel engine operating with in-cylinder gasoline and diesel fuel blending. SAE International Journal of Fuels and Lubricants, 3(2), 946-955.

[4.21] Appel, J., Bockhorn, H., & Frenklach, M. (2000). Kinetic modelling of soot formation with detailed chemistry and physics: laminar premixed flames of C2 hydrocarbons. Combustion and flame, 121(1-2), 122-136.

[4.22] Frenklach, M., & Wang, H. (1991, January). Detailed modeling of soot particle nucleation and growth. In Symposium (International) on Combustion (Vol. 23, No. 1, pp. 1559-1566). Elsevier

[4.23] Lee, J., Sung, N. W., & Huh, K. Y. (2011). Prediction of soot particle size distribution for turbulent reacting flow in a diesel engine. International Journal of Engine Research, 12(2), 181-189

[4.24] Fenimore, C. P., & Jones, G. W. (1967). Oxidation of soot by hydroxyl radicals. The Journal of physical chemistry, 71(3), 593-597.

[4.25] Tao, F., Reitz, R. D., Foster, D. E., & Liu, Y. (2009). Nine-step phenomenological diesel soot model validated over a wide range of engine conditions. International Journal of Thermal Sciences, 48(6), 1223-1234.

[4.26] Saxena, M. R., & Maurya, R. K. (2016). Effect of butanol blends on nano particle emissions from a stationary conventional diesel engine. Aerosol and Air Quality Research, 16(9), 2255-2266.

[4.27] Tan, P. Q., Hu, Z. Y., Lou, D. M., & Li, B. (2009). Particle number and size distribution from a diesel engine with Jatropha biodiesel fuel (No. 2009-01-2726). SAE Technical Paper.

[4.28] Kittelson, D. B. (1998). Engines and nanoparticles: a review. Journal of aerosol science, 29(5-6), 575-588.

[4.29] Abdul-Khalek, I., Kittelson, D., & Brear, F. (1999). The influence of dilution conditions on diesel exhaust particle size distribution measurements. SAE transactions, 563-571.

[4.30] Kawai, T., Goto, Y., & Odaka, M. (2004). Influence of dilution process on engine exhaust nano-particles (No. 2004-01-0963). SAE Technical Paper.

[4.31] RÖnkkÖ, T., Virtanen, A., Kannosto, J., Keskinen, J., Lappi, M., & Pirjola, L. (2007). Nucleation mode particles with a nonvolatile core in the exhaust of a heavy duty diesel vehicle. Environmental science & technology, 41(18), 6384-6389.

[4.32] Filippo, A. D., & Maricq, M. M. (2008). Diesel nucleation mode particles: semivolatile or solid?. Environmental science & technology, 42(21), 7957-7962.

[4.33] Saxena, M. R., & Maurya, R. K. (2018). Effect of fuel injection strategy on nano-particle emissions from RCCI engine (No. 2018-01-1709). SAE Technical Paper.

[4.34] Montajir, R. M., Kawai, T., Goto, Y., & Odaka, M. (2005). Thermal conditioning of exhaust gas: potential for stabilizing diesel nano-particles (No. 2005-01-0187). SAE Technical Paper.

[4.35] Zhang, Y., Ghandhi, J., & Rothamer, D. (2014). Comparison of particulate size distributions from advanced and conventional combustion-part I: CDC, HCCI, and RCCI. SAE International Journal of Engines, 7(2), 820-834

[4.36] Benajes, J., García, A., Monsalve-Serrano, J., & Boronat, V. (2017). An investigation on the particulate number and size distributions over the whole engine map from an optimized combustion strategy combining RCCI and dual-fuel diesel-gasoline. Energy Conversion and Management, 140, 98-108.

[4.37] Storey, J., Curran, S., Dempsey, A., Lewis, S., Walker, N. R., Reitz, R., & Wright, C. (2015). The contribution of lubricant to the formation of particulate matter with reactivity-controlled compression ignition in light-duty diesel engines. Emission Control Science and Technology, 1, 64-79

[4.38] Saxena, M. R., & Maurya, R. K. (2020). Influence of direct injection timing and mass of port injected gasoline on unregulated and nano-particle emissions from RCCI engine. Fuel, 282, 118815.

[4.39] Park, S., Wang, Y., Chung, S. H., & Sarathy, S. M. (2017). Compositional effects on PAH and soot formation in counterflow diffusion flames of gasoline surrogate fuels. Combustion and Flame, 178, 46-60

[4.40] Fang, W., Kittelson, D. B., & Northrop, W. F. (2017). Dilution Sensitivity of Particulate Matter Emissions From Reactivity-Controlled Compression Ignition Combustion. Journal of Energy Resources Technology, 139(3).

[4.41] Dempsey, A., Curran, S., Storey, J., Eibl, M., Pihl, J., Prikhodko, V., ... & Parks, J. (2014). Particulate matter characterization of reactivity-controlled compression ignition (RCCI) on a light duty engine (No. 2014-01-1596). SAE Technical Paper.

[4.42] Bambha, R. P., Dansson, M. A., Schrader, P. E., & Michelsen, H. A. (2013). Effects of volatile coatings and coating removal mechanisms on the morphology of graphitic soot. Carbon, 61, 80-96.

[4.43] Rothenbacher, S., Messerer, A., & Kasper, G. (2008). Fragmentation and bond strength of airborne diesel soot agglomerates. Particle and fibre toxicology, 5, 1-7.

[4.44] Harris, S. J., & Maricq, M. M. (2002). The role of fragmentation in defining the signature size distribution of diesel soot. Journal of Aerosol Science, 33(6), 935-942.

[4.45] Li, J., Yang, W., & Zhou, D. (2017). Review on the management of RCCI engines. Renewable and Sustainable Energy Reviews, 69, 65-79.

[4.46] Han, W., Lu, Y., Jin, C., Tian, X., Peng, Y., Pan, S., ... & Zhong, Y. (2020). Study on influencing factors of particle emissions from a RCCI engine with variation of premixing ratio and total cycle energy. Energy, 202, 117707

[4.47] Nithyanandan, K., Lin, Y., Donahue, R., Meng, X., Zhang, J., & Chia-fon, F. L. (2016). Characterization of soot from diesel-CNG dual-fuel combustion in a CI engine. Fuel, 184, 145-152

[4.48] Bischof, O. F. (2015). Recent developments in the measurement of low particulate emissions from mobile sources: A review of particle number legislations. Emission Control Science and Technology, 1, 203-212.

[4.49] Storey, J. M., Curran, S. J., Lewis, S. A., Barone, T. L., Dempsey, A. B., Moses-DeBusk, M., ... & Northrop, W. F. (2017). Evolution and current understanding of physicochemical characterization of particulate matter from reactivity-controlled compression ignition combustion on a multicylinder light-duty engine. International Journal of Engine Research, 18(5-6), 505-519.

[4.50] Zhou, H., Li, X., & Lee, C. F. F. (2019). Investigation on soot emissions from diesel-CNG dual-fuel. International journal of hydrogen energy, 44(18), 9438-9449.

[4.51] Saxena, M. R., & Maurya, R. K. (2020). Experimental investigation of combustion stability and particle emission from CNG/diesel RCCI engine (No. 2020-01-0810). SAE Technical Paper